Characterisation of mass-to-light ratios in early-type galaxies through strong gravitational lensing

Dissertation
presented for the degree of

Doctor of Philosophy in Space Sciences

Judith Biernaux

Liège, 2018

Université de Liège

Faculté des Sciences

Département d'Astrophysique, de Géophysique et d'Océanographie

Supervisor:

Pr. Pierre Magain

Members of the Jury:

Pr. Denis Grodent as president

Dr. Damien Hutsemékers as secretary

Pr. Frédéric Courbin

Pr. Pierre Magain

Dr. Dominique Sluse

Dr. Olivier Wertz

This work is supported by the FRIA grant of the FNRS.

À Léa, Hugo et Marius.
Soyons toujours curieux comme un enfant.

Summary

Strong gravitational lensing produces multiple, distorted images of a background source that can be traced back to the projected surface density of the lens producing the deflection. If the lens is a galaxy of which the brightness profile can be studied, its dark matter proportion and distribution can be estimated by comparing its luminosity profile to its total mass profile inferred from lensing. We conduct such an analysis on elliptical lensing galaxies. Dark matter in elliptical galaxies has been investigated through various proxies, from planetary nebulae velocities to stellar kinematics, yielding discrepant conclusions and indicating the currently poor understanding of this topic.

Lensing galaxies appear surrounded by point-like or diffuse lensed signal, or both, that can get mixed with galaxy flux, restricting the galaxy light profile analysis to its small inner portions. We use accurate point spread functions (PSFs) from Chantry et al. (2010) and Sluse et al. (2012) to subtract the point-like source images and we build a new diffuse lensed signal subtraction technique. We design shape parameters measurement methods based on the computation of isophotes. We measure each parameter individually to avoid local minima in the parameters space. We show that this new technique is more stable than classical fitting algorithms in the specific conditions of gravitational lensing images. We apply it to H-band HST/NICMOS images of eight early-type lensing galaxies from the CASTLES survey and provide an accurate determination of their light profiles.

We then use gravitational lensing formalism to retrieve the galaxies total mass profile. We rank the ability to reproduce the observed astrometry and time delay constraints of three types of density profiles, each based on a different assumption on the dark matter distribution: isothermal profiles, "mass-follows-light" de Vaucouleurs profiles and the sum of a de Vaucouleurs plus a Navarro-Frenk-White halo. We find that in most cases, adding a halo to the best-fitting H-band de Vaucouleurs (to a scaling factor) does not improve the fit, leaning towards the absence of dark halos. Unfortunately, lens modelling is prone to well-known degeneracies and is sensitive to local minima in its high-dimensional parameters space. This ranking is thus not conclusive enough, and we choose a more robust quantity to investigate dark halos, that is, the galaxies mass-to-light ratios M/L at their Einstein radii $r_{\rm Ein}$. The latter is quite model-independent, and so is the mass comprised within it. We use fluxes from the H-band de Vaucouleurs profiles determined above. More specifically, we plot M/L for each one of our eight galaxies as a function of their $r_{\rm Ein}$ in units of half-light radii $r_{\rm eff}$, and characterise the M/L behaviour with galacto-centric distance, as it is expected to increase from the centre out for a galaxy embedded in a dark matter halo.

Interestingly, we observe that the opposite is true for our sample: we find that the highest M/L values are achieved for the smallest $r_{\rm Ein}/r_{\rm eff}$ values, but large uncertainties affecting our measurements make it impossible to bring out conclusive results. Moreover, the sample turns out to be unevenly distributed between small and large $r_{\rm Ein}/r_{\rm eff}$, with more points inwards, whereas outermost regions are more relevant to this research. Although we do not find evidence for the existence of dark matter halos around early-type galaxies, these uncertainties make it impossible to provide secure evidence against it. The present work highlights the importance of a high-quality determination of the PSF and of the brightness profile, defining leads to more accurate, bias-free studies of early-type galaxies mass-to-light ratios.

Résumé

Les mirages gravitationnels forts produisent des images multiples et déformées d'une source d'arrière-plan, qui renseignent sur le profil de densité de surface projeté de la lentille à l'origine du phénomène. Si celle-ci est une galaxie dont le profil de luminosité peut être étudié, sa distribution et sa proportion de matière sombre peuvent être obtenues en le comparant au profil de masse totale obtenu grâce à la modélisation du mirage. Nous appliquons ce procédé à des galaxies elliptiques. La matière sombre dans celles-ci peut être étudiée via différents indicateurs, des distributions de vitesses de nébuleuses planétaires à celles des étoiles, mais les résultats obtenus jusqu'ici sont contradictoires et montrent à quel point ce sujet est encore peu compris.

Les lentilles gravitationnelles fortes apparaissent entourées d'images défléchies d'une source d'arrière-plan, ponctuelles, diffuses, ou les deux à la fois, qui peuvent être superposées au signal de la galaxie lentille et restreindre l'analyse de sa luminosité à de petites régions proches de son centre. Nous utilisons des fonctions d'étalement du point (PSF) précises obtenues par Chantry et al. (2010) et Sluse et al. (2012) pour soustraire ces images ponctuelles, et nous mettons au point une soustraction du signal diffus. Nous proposons de nouvelles méthodes de mesure des paramètres structuraux des galaxies sur base du calcul de leurs isophotes. Nous mesurons chaque paramètre individuellement pour pallier au problème des minima locaux. Nous démontrons que cette technique est plus stable que les algorithmes classiques d'ajustement de modèles dans les conditions spécifiques des images de lentilles. Nous l'appliquons à un échantillon d'images HST/NICMOS dans la bande H de huit galaxies elliptiques lentilles de la base de données CASTLES, et nous obtenons une expression de leurs profils de luminosité.

Nous utilisons ensuite le formalisme des mirages gravitationnels pour obtenir leurs profils de masse. Nous ajustons trois types de profils de masse et analysons leur capacité à reproduire les observations (astrométrie et délais temporels). Chacun de ces types de profil est défini par une hypothèse différente sur leur distribution de matière sombre: des profils isothermes, des profils de de Vaucouleurs où la luminosité trace la masse totale, et enfin une combinaison d'un de Vaucouleurs et d'un halo Navarro-Frenk-White. Nous observons que dans la plupart des cas, ajouter un halo de matière sombre au de Vaucouleurs obtenu dans la bande H (à un facteur multiplicatif près) n'améliore pas la qualité de l'ajustement, ce qui semble favoriser l'absence de halos. Malheureusement, l'ajustement de modèles sur des lentilles gravitationnelles souffre de dégénérescences bien connues et est sensible à l'existence de minima locaux dans l'espace des paramètres. Cette analyse n'est donc pas suffisamment conclusive et nous choisissons un paramètre plus fiable pour rechercher les halos de matière sombre, à savoir, le rapport masse-luminosité M/L des galaxies au sein de leurs rayons d'Einstein r_{Ein}. Ce dernier ne dépend quasiment pas du modèle, et il en va de même pour la masse comprise au sein de celui-ci. Nous calculons le flux des galaxies dans la bande H à l'aide des profils de de Vaucouleurs déterminés précédemment. Plus précisément, nous portons en graphique le M/L de chaque galaxie en fonction de leur r_{Ein} en unités de rayon effectif r_{eff}, et analysons le comportement de M/L avec la distance galactocentrique. Une augmentation de M/L devrait être observée vers l'extérieur des galaxies abritant un halo de matière sombre.

Curieusement, nous observons le contraire au sein de notre échantillon : les M/L les

plus élevés sont obtenus pour les plus petits $r_{\mathrm{Ein}}/r_{\mathrm{eff}}$, mais d'importantes incertitudes de mesure nous empêchent de produire un résultat conclusif. De plus, l'échantillon s'avère mal distribué entre les grandes et petites valeurs de $r_{\mathrm{Ein}}/r_{\mathrm{eff}}$, avec plus de points vers le centre des galaxies, alors que l'extérieur est plus pertinent dans une telle recherche. Bien que nous n'obtenions aucune preuve en faveur de l'existence de halos de matière sombre autour des galaxies elliptiques, ces incertitudes nous empêchent de prouver leur absence. Ce travail souligne l'importance d'une excellente détermination des PSF et des profils de luminosité, ouvrant ainsi des pistes pour des études plus précises et moins biaisées des M/L de galaxies elliptiques.

"The only thing I know is that I know nothing."

Socrates (470 BC - 399 BC)

"When you have eliminated the impossible, whatever remains, however improbable, must be the truth."

Sherlock Holmes, in *"The Sign of the Four"*, Arthur Conan Doyle (1859 - 1930)

"Science is competitive, aggressive, demanding. It is also imaginative, inspiring, uplifting. You can do it, too."

Vera Rubin (1928 - 2016)

Acknowledgements

The present work has been made possible thanks to many collaborations. I cannot believe how many colleagues and friends have invested their time and energy in my research. I have plenty of thanks to formulate.

First and foremost, I am infinitely thankful to my supervisor Pierre Magain, for his continuous support during these past four (five!) years. I have learnt more than I can tell under his guidance in all aspects of academia. Thank you for always going out of your way to keep the office mood bright, even in rough times, like raptor attacks. I am also thankful to Dominique Sluse, for his precious insights along the way, for proofreading all my writings, for teaching me everything I know about Python or lens modelling, and for always replying so quickly to my e-mails. His input to this work is invaluable. I further wish to acknowledge all the members of the jury and the thesis committee for the precious time they devoted to this work.

To Virginie Chantry, thank you for passing on your knowledge, your motivation, and your hard drive :-) You dealt with the teething problems of this work, put me on track and gave me a head start. To Sandrine Sohy, thank you so much for your help not only in programming the image processing tools, but also in all practical aspects of this work, from fixing doors to replacing dead batteries. If Sandrine cannot fix it, it cannot be fixed. Thanks also to Alain Detal for the computer maintenance. To Angela and all the secretaries of the department, thank you for taking charge of all our paperwork: nothing would happen without your help in this building! To all my colleagues from the first floor, thank you for all the lovely moments, drinks and lunchtimes.

I cannot even begin to describe how thankful I am to Clémentine. We met on day one and you are still by my side today, you deserve a medal for putting up with me this long! Thank you for your considerable help in this work but also for your constant friendship, for helping me find my way on campus, for sharing my Star Wars fandom and for helping me fight all the raptors. You are the best office mate anyone could ever hope for.

I have been blessed with many wonderful friends during this experience. Thank you to all the former PhD students who taught me how to navigate through the pits and traps we all face! To Gaël, Cyrielle and Laëtitia, thank you SO MUCH for passing us that coffee machine. Caffeination has been essential to Science, and the machine will solemnly be handed to generations of PhD students. To Martin, for supervising said coffee machine,

for being even clumsier than me, and for the deep philosophical conversations about life and stuff... To Elsa, for sharing my Disney enthusiasm (culture, should I say) and for letting me call you "Frenchie". To my dear sweet Françoise, and thank you for your priceless help with the cover! To Manu, Galien, Sébastien, both Sylvain's, and Aurore, for the unforgettable moments over lunch and tea and for organising the most crowded coffee breaks in History. To Maïté and Audrey L., for their limitless wisdom on what being a PhD student entails. Thanks to Ludivine, Audrey, Marie-Julie, Antoine, Élo, Jérem, Alain, and to everyone from my year group I am forgetting, you all kept me sane (well, as sane as possible) and I am forever grateful for your kind friendship.

Talking about friendships, I wish to thank all of my great friends outside the University who have been with me during this amazing experience: thank you Mimi, Anna, Barbara (gracias!), Braulio (gracias también!), Ludo, Arnaud, Dominik, Nathan, my yoga friends and my krav maga buddies.

I am thankful for every single opportunity I have been provided with during these four years: thank you Pierre and Guy for letting me teach some of your classes. Thank you Lyne, Andrea and especially Luca for letting me supervise, at least partly, your master theses, and for showing forgiveness when having to use my not so user-friendly pieces of code. Thank you to Manu Jehin, to Réjouisciences, to Méla, to Denis, to Arnaud and to Yaël for all the wonderful outreach experiences. Bringing science out of our offices is undoubtedly the most fulfilling experience I have had so far, and thank you for being a part of it.

I owe a gigantic thank you to all my family (including our four-legged friends!), none of this would have been possible without you. Thank you Mom and Dad for encouraging me to pursue this path. Thank you Mom for feeding me proper food during the exam crunch times (and at all other times, really) and for taking such good care of me. Thank you Dad for helping me out with Python and Bash and for basically delivering on anything I ever needed. Thanks to my brother and sister for their kindness and for making the best gin tonic. Thank you also for bringing to this world Léa, Hugo and Marius, the loveliest nephews anyone could ever wish for, who are always there to take me back to the real world. My thoughts go to my inspiring grandmother, you left us too soon.

Then there is Tristan. I am SO grateful for you being in my life. You may not even realise how helpful you have been. A million thank you for listening to me talking about my day everyday, for putting up with my every mood, for actively participating to this work by proofreading, optimising bits of codes, teaching me the rubber duck method (it is a thing!), listening to my talks, I could go on. It would take a whole other thesis just to list everything you did for me. Thank you!

My last acknowledgement goes to everyone who proofread this manuscript: Pierre, Dominique, Clem, Ludo, Martin, Tristan and all the jury members. It goes without saying that any remaining mistake should be entirely attributed to me.

Thank you to anyone who is reading this. I deeply hope it contributes to any science

endeavours you might be needing this for. It is the hope of any PhD student to produce a thesis that is not destined to collect dust on a shelf, but instead, to inspire future work.

Contents

List of Figures

List of Tables

1 Introduction: the scene and the protagonists

This Chapter provides some background to the questions this thesis is addressing and puts it into a scientific context. It sets the scene for the protagonists: elliptical galaxies, gravitational lensing and dark matter, that are briefly presented in the next few Sections. The present work falls into the scope of extragalactic astrophysics. More specifically, it aims at contributing to shedding some light on the distribution of dark matter in elliptical galaxies, and by that means, fuelling the open discussions about galaxy formation. The specific questions this work is tackling are stated at the end of this Chapter.

1.1 Elliptical galaxies

The discussion in this Section is inspired by Spinrad (2005), Mo et al. (2010) and Eichner (2013).

1.1.1 General description

Galaxies are gathering of stars and gas. They are the building blocks of the large structures in the Universe. In the 1920's, Edwin Hubble, who participated a lot in the understanding of extragalactic astrophysics, built a classification of galaxies based on their apparent shape. The Hubble sequence separates spiral galaxies, like our Milky Way, from elliptical galaxies. By then, it was thought that galaxies evolve from ellipticals to spirals, and they were respectively called early-type and late-type galaxies. These terms are still used today, even though it is thought that spirals and ellipticals form through different mechanisms.

Elliptical galaxies have a three-dimensional ellipsoid shape with stars distributed on roughly random orbits around the centre, as opposed to the group rotation of spiral galaxies. Their luminosity distribution, that is, their intensity as a function of the distance to

Figure 1.1: A diagram of the Hubble sequence. Elliptical galaxies occupy the left part of the fork, with ellipticity increasing from left to right. Spirals are divided into barred spirals (*bottom*) and non-barred spirals (*top*), and are more reeled from left to right. Credit: Ville Koistinen, Caltech.

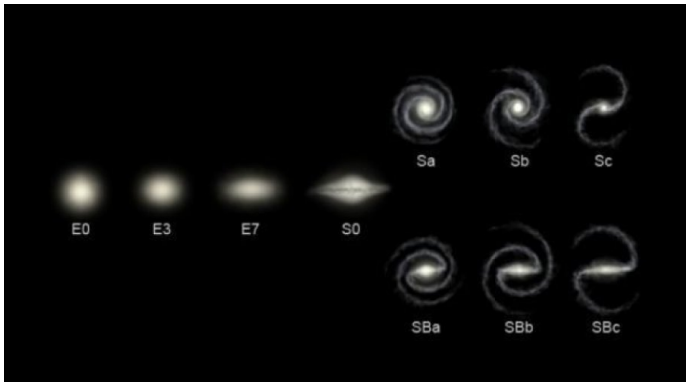

their centre, can be described by a de Vaucouleurs profile (de Vaucouleurs 1948):

$$I(r) = I_0 \exp\left(-k\left(\frac{r}{r_{\text{eff}}}\right)^{1/4}\right) \tag{1.1}$$

where I_0 is the central intensity, r is the galacto-centric radius, and r_{eff} is the half-light radius or effective radius, that is, the radius of the circle enclosing half the total luminosity. k is a normalisation constant that is equal to 7.669 approximately. In fact, this expression is valid for a circular galaxy. It can be generalised to elliptical galaxies. In that case, $r_{\text{eff}} = \sqrt{(a_{\text{eff}} b_{\text{eff}})}$, where a_{eff} and b_{eff} are the respective semi-major and semi-minor axes of the apparent 2-D ellipse enclosing half the total light. The de Vaucouleurs law has empirically proved to be a good fit for most elliptical galaxies, but it can be generalised to the Sérsic law (Sérsic 1963):

$$I(r) = I_{\text{eff}} \exp\left(-k\left(\frac{r}{r_{\text{eff}}}\right)^{1/n} - 1\right) \tag{1.2}$$

where n is called the Sérsic index and is a parameter of the profile. However, when studying light profiles of elliptical galaxies, it is inconvenient to have an exponent as a parameter, as a small error on n could translate into a large error on $I(r)$. Adopting a Sérsic profile instead of a de Vaucouleurs broadens the scope of galaxies the profile can fit but the gain in generalisation may not be worth the extra complication. Besides the intensity distribution and the half-light radius, the morphology of an elliptical galaxy is characterised by an orientation angle, that corresponds to the angle between the semi-major axis of the galaxy and the horizontal axis. It is also described by its ellipticity ε, which is linked to the axes ratio, $\varepsilon = 1 - b/a$.

It is worth noticing that both the Sérsic and the de Vaucouleurs profiles are empirical laws, meaning that they have been verified observationally, but there is no physical reason as to why the light content of a galaxy should take on that configuration. Moreover, even though their overall structure resembles a 3-D ellipsoid, they are observed as 2-D objects because of their extragalactic distance. Therefore, their ellipticity undergoes a projection,

Figure 1.2: A sketch of an elliptical light distribution. The position angle is noted PA and the ellipticity ε is defined based on the ratios of the semi-minor (b) and major (a) axes.

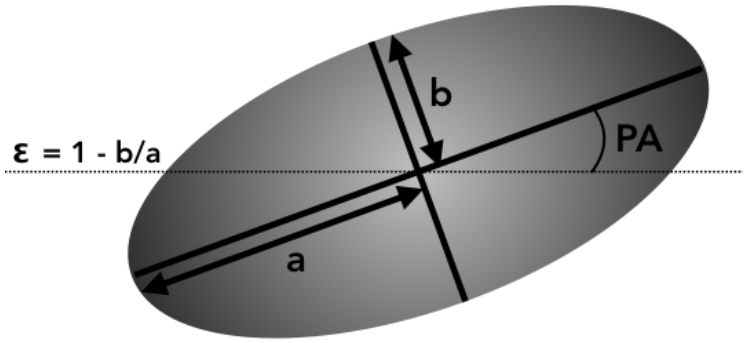

and the observed morphology parameters might be quite different from the physical properties of the galaxy. In fact, their actual 3-D structure may also deviate from a perfect ellipsoid structure. The loci of equal brightness, called the isophotes, may display some twisting along one of the axes, and their shape may be a little more box-like (boxy) or disk-like (disky) than an elliptical ring. Like any model, the de Vaucouleurs law is but an approximation, and its accuracy is sufficient as part of this work.

1.1.2 Formation of elliptical galaxies

It has been observed that elliptical galaxies are most often found in dense environments (Dressler 1980). This may be an indication that they form in these dense environments. It has been logically suggested that they form through mergers of smaller, possibly spiral galaxies (Toomre 1977, Lacey and Cole 1993). The process implies two galaxies colliding, gravitationally interacting and their stars being re-distributed into the rather homogenous structure of an elliptical galaxy. Such collisions are being observed in the Universe, like the Mice galaxies NGC 4676 or the Antennae galaxies NGC 4038-9. Some elliptical galaxies, like NGC 474, display unusual shell-shaped structures, that can be attributed to tidal interactions during the merger process (Turnbull et al. 1999).

During a merger, more specifically in the late stages of the process, the gravitational potential of the resulting galaxy undergoes some chaotic changes. The stars trapped in this potential are re-arranged in random orbits, even if they started with an orderly group rotation. This is called violent relaxation, and such random energy orbits are observed in elliptical galaxies. Moreover, the gas content of both (or more) protagonists collides and condenses into regions of very high star formation rate. This process rapidly consumes the gas content of the merger, which explains how little gas we observe in elliptical galaxies. For both these reasons, it seems logical that elliptical galaxies are the product of mergers, although most of this evidence is rather circumstantial.

The details of the merger process is not fully understood yet. Another galaxy formation scenario has been considered, that is, the monolithic collapse. It consists of the contraction of a gas region into a star formation burst region. If the scenario does not

Figure 1.3: *Left*: composite visible and near infrared image of the Antennae galaxy, an ongoing merger of two spiral galaxies. The pink regions point out clouds of gas, whereas blue regions are star formation nests. *Right*: visible wavelength image of the Mice galaxies, characterised by a spectacular tidal tail. Credit for both images: NASA/Hubble Space Telescope, resp. WFPC2/WFC3/ACS and ACS.

include energy dissipation from the gas cloud through radiation, the star formation occurs prior to or in the early phases of the galaxy formation, and there is virtually no stellar evolution during the life of the galaxy. If dissipation is permitted, then the star formation timescale is compatible to that of the whole collapse process, and some stellar evolution can be seen in the early life of the ellipticals. Mergers can also be separated into dissipative and dissipationless cases, although in a merger scenario, most of the star formation occurs before the merger itself, as the merging galaxies have evolved beforehand. In all cases, the merger scenario is usually favoured as the correct one for elliptical galaxies formation. One of the reasons for this is that in the monolithic collapse case, the formation time scales are either too large (in the dissipationless scenario, most galaxies should have formed too early in the Universe) or too short (in the dissipative scenario, most galaxies are still forming today) compared to observations.

Simulations (e.g: Dubinski 1998, Mo et al. 2010, and references therein) have shown that in most cases, the result of merging two disk or spiral galaxies resembles an elliptical galaxy. Moreover, it seems that dissipation is essential in reproducing properties of low-mass ellipticals, such as their size, their low ellipticity, their high level of isotropy and their high central velocities. Conversely, dissipative mergers remnants do not match some observational characteristics of massive, luminous ellipticals, such as their on average higher boxiness and shallower core (Cox et al. 2006). As a result, it seems that low-mass elliptical galaxies stem from dissipative mergers, whereas massive elliptical galaxies originate in dissipationless or "dry" mergers.

Besides simulations, few observational tests are able to conclusively validate or invalidate one of the two formation models (monolithic collapse or merger). For example, it could be argued that under the merger hypothesis, since progenitors have evolved beforehand, and possibly over the whole course of their life, the resulting stellar population would include stars of various ages. On the other hand, the monolithic collapse predicts a single starburst, and thus all stars should have the same age in the newly formed galaxy. Unfortunately, a merger scenario that happens early in the Universe and that allows for little to no star formation afterwards would yield a similar "mono-age" stellar population.

Some issues with the merger scenario have been pointed out (Forbes 1999, Keselman and Nusser 2012). Burkert et al. (2008) have used high-quality kinematics data from the SAURON spectrograph (Emsellem et al. 2004) to show that two different merger scenarios are required to explain kinematics correlations in rather round or rather flattened galaxies. They conclude that it is possible that only some families of ellipticals form by merging, which is in agreement with the simulations discrepancy mentioned earlier.

To sum up, even though the merger scenario is more often considered to have produced most elliptical galaxies, the wide variety of their stellar population and of their stellar kinematics makes it almost impossible for one scenario to cover all the possibilities, and in general, elliptical galaxies formation is not completely understood yet. Nevertheless, some trends in the elliptical galaxies stellar populations can be brought out.

1.1.3 Stars in elliptical galaxies

Elliptical galaxies display very little to no star formation and a scarce interstellar medium of gas and dust. On top of that, they tend to harbour older, lower-mass stars[1]. These factors give elliptical galaxies a redder colour (spectral energy distribution, or SED) than their spiral counterparts, with no emission lines. The stellar content of an elliptical galaxy is described by the initial ingredients of its stellar population, that is, the age, mass and chemical composition of its individual stars. These initial ingredients are best described by the initial mass function of the stellar population, or IMF. It defines the initial number N of stars at a given mass m. In other words, it helps counting massive stars compared to low-mass stars. There are a variety of mathematical expressions of galaxies IMF, but the most common ones are the Salpeter IMF (Salpeter 1955) and the Kroupa IMF (Kroupa 2002). They express $N(m)$ as a power law (Salpeter) or a combination of power laws (Kroupa). A Salpeter IMF favours more low-mass stars compared to massive ones, whereas for Kroupa, fewer low-mass stars are expected. The IMF has an impact on the luminosity of a galaxy: massive stars are much brighter (per units of mass) but have a much shorter lifespan than low-mass stars. They also tend to display higher energies, giving the galaxy a bluer colour. The luminosity of a star is not only driven by its mass or age: its chemical composition has an impact too. If a star has more metals, that is, any element heavier than helium, it will appear redder. The higher the metallicity of a star, the cooler its temperature (at a given mass), and the redder its spectrum. Therefore, the light we observe from an elliptical galaxy depends not only on the IMF of its stellar content, but also on its age and metallicity. Many studies have attempted to determine the correct IMF for elliptical galaxies, and that question is still open today. Cappellari et al. (2013) have shown it might depend on the mass range of the galaxy.

Finally, the stellar population of a galaxy can be characterised by a mass-to-light ratio or M/L. The M/L of an object compares its total mass to its luminosity. These quantities are most often expressed both in solar units. For that reason, the Sun has a M/L of unity. A massive star, that is for example 10 times more massive than the Sun, can be more than

[1] A star is considered massive if its mass exceeds approximately 8 solar masses ($M_\odot$)

a thousand times brighter than the Sun, which gives it a M/L lower than unity. A low mass star, on the other hand, can have a M/L ratio that is higher than unity. This quantity also depends on the wavelength at which it is measured. The light content of a galaxy depends mostly on its stellar population, and its mass content can be affected by other objects, like dust or dead star remnants, that do not emit (much) light but can be quite massive. Most of all, the M/L ratio of a galaxy is influenced by its dark matter content.

1.2 Dark matter

The discussion in this Section is largely based on Binney and Merrifield (1998), Spinrad (2005) and Longair (2006).

1.2.1 Missing matter in the Universe

Any two massive objects share a gravitational interaction. The movement of any celestial body is influenced by its gravitational environment. For example, the orbit of the Earth is mostly determined by its gravitational interactions with the Sun, but also, to some extent, with the Moon, and all the planets and small bodies passing by at any given moment. In the 19th century, Urbain Le Verrier, a French astronomer, observed irregular movements in the orbit of Uranus. He attributed this abnormality to gravitational interactions with a yet unobserved neighbouring planet, thereby predicting the existence of Neptune.

Such a reasoning has been applied later to extragalactic objects. It has been suggested that the gravitational pull from all matter in galaxies, or all galaxies in a cluster, would be insufficient to maintain the structure of said object, and that they should crumble apart. In 1933, Fritz Zwicky was amongst the first astronomers to study extragalactic nebulae, which are nowadays called galaxies. He applied a straightforward equilibrium theorem to the nearby Coma cluster of galaxies. The virial theorem states that for a gravitationally bound system at a state of dynamical equilibrium, the kinetic energy T is half as large as its gravitational potential energy U:

$$T = \frac{1}{2}|U| \tag{1.3}$$

For a galaxy cluster, we have:

$$|U| \approx \frac{GM^2}{R} \quad , \quad T \approx \frac{3}{2}M\langle v_{\mathrm{LOS}}^2\rangle \tag{1.4}$$

where M is the mass of the cluster, R is its radius, G is the gravitational constant[2] and $\langle v_{\mathrm{LOS}}\rangle$ is the average velocity of the galaxies in the cluster. Zwicky measured the velocity of galaxies near the edge of the cluster. In fact, he estimated it using their Doppler shifts: this only gives access to the velocity component along the line of sight (LOS) (Zwicky

[2] $6.6740810^{-11} m^3 kg^{-1} s^{-2}$

1933). Under the assumption that velocities are isotropically distributed, $\langle v^2 \rangle = 3\langle v_{\mathrm{LOS}}^2 \rangle$. He used this relation to estimate the virial mass of the cluster, and found out that it had to be at least 400 times larger than the luminous mass estimate. He was the first to hypothesise the existence of dark matter in galaxy clusters: an invisible form of matter that interacted gravitationally with normal matter, and seemed to largely outweigh it.

The next major step in the study of dark matter was taken by Vera Rubin in the 1970s. She brought to light an anomaly that would be later known as the galaxy rotation problem: using a method similar to the one used in Zwicky (1933), she measured the rotation velocity of spiral galaxies. As illustrated in Figure 1.4, because of the Doppler effect, light emitted from a source moving away from the observer appears too red, and if the source is moving towards the observer, too blue. To be more specific, the spectral lines of a spinning galaxy are blueshifted in the regions moving towards the observer, and redshifted in the regions moving away. Vera Rubin and her collaborators Kent Ford and Norbert Thonnard quantified this effect in 21 spiral galaxies, using lines in the visible spectrum, mostly from hydrogen.

Figure 1.4: *Left*: an illustration of how to produce velocity curves of a spiral galaxy based on the Doppler effect. The regions moving towards the observer, at the bottom of the image, are blueshifted, and the regions moving away from the observer, redshifted. *Right*: a sketch of the trend in observed galactic velocity curves (red) showing a plateau in the outskirts, as opposed to what should be expected in classic Newtonian dynamics based on the estimated "luminous" mass (dashed blue).

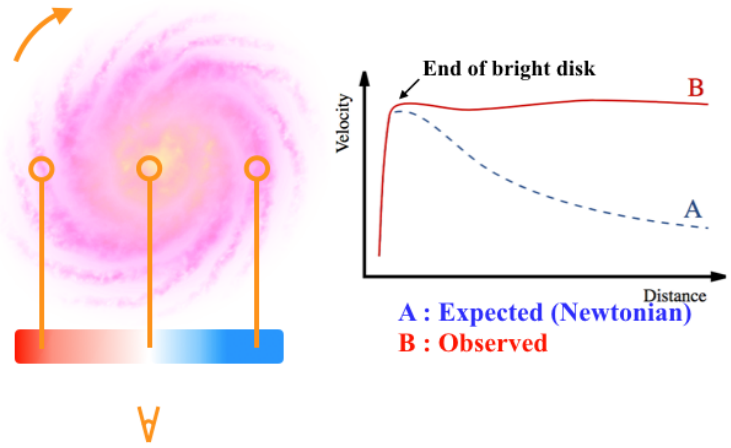

As a first approximation, the rotation speed v_{rot} of a point mass in a galaxy at a distance d from its centre depends on the mass enclosed within a circle of radius d, $v_{\mathrm{rot}} \approx \sqrt{GM(d)/d}$. The mass can be traced by the luminosity, as they both come from the stars and gas in the galaxy. In that case, as the luminosity increases from the centre out, the rotation speed should increase too. Then, after the end of the luminous disk, the luminosity drops, the mass stops increasing ($M(d) \approx constant$) and the rotation speed is thus expected to drop, $v_{\mathrm{rot}} \approx d^{-1/2}$. However, Rubin observed a continuous rise, up to a plateau for some objects, even at large distances from the galaxy core, where almost no light is left. These results were published in Rubin et al. (1980), and Figure 1.5 shows the rotation curves these authors obtained. If Newtonian dynamics is correct, this rise and plateau imply that there is some mass at large distances that does not emit light but that

participates in the gravitational potential of the galaxy. It was suggested that spiral galaxies are enclosed in a large halo of dark matter. The velocity curve discrepancy showed that the total dark matter content outweigh the total luminous mass content by a factor of six on average for their sample. A similar result was almost simultaneously obtained in radio wavelengths, first on M31 by Roberts (1966) and then on farther galaxies by Rogstad and Shostak (1972) and Bosma (1981). Persic et al. (1996) provided rotation curves for nearly a thousand galaxies, in the optical and radio wavelengths: most galaxies needed an amount of dark matter between five and ten times as large as the light content to match the outermost velocities. There was no doubt left on the existence of extended dark matter halos around spiral galaxies.

Figure 1.5: Rotation curves for 21 spiral galaxies as published in Rubin et al. (1980). None of them display the expected decrease in the outer regions.

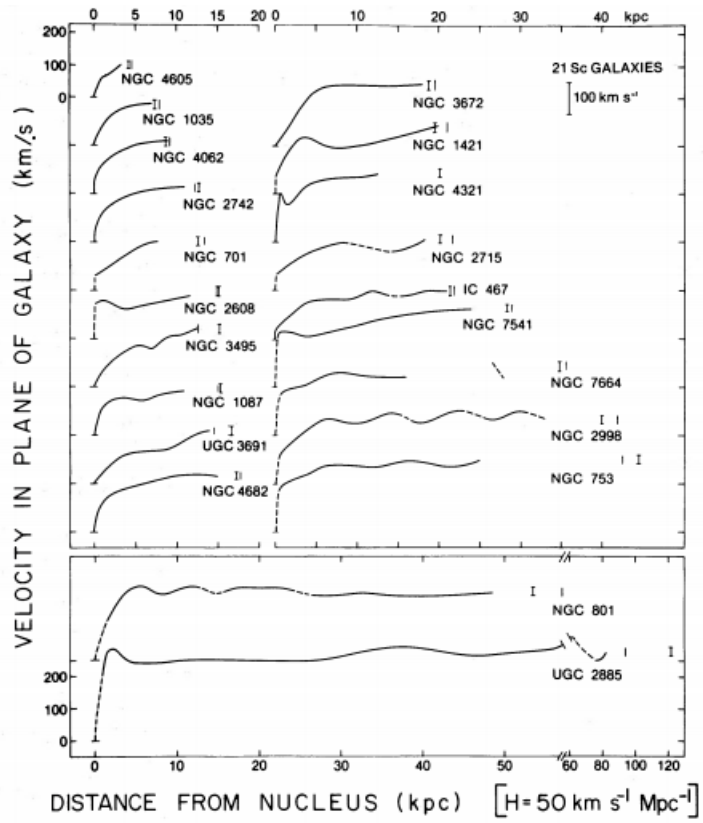

The discovery of dark matter in extragalactic objects constituted a major advance for cosmology too. In fact, the best-fitting model to explain the evolution of the Universe so far uses dark matter as one of its main ingredients to explain most large structure formation mechanisms. It is appropriately named the ΛCDM model, which stands for "Λ cold dark matter". The very young Universe was generally homogenous, although it presented some very small density fluctuations. These anisotropies affected normal matter as much as dark matter. Yet, normal matter is able to interact with radiation, which was dominant at this epoch. That interaction tended to smooth the matter density perturbations. Dark matter, on the other hand, does not interact with light, so its density fluctuations remained as the Universe expanded. Ultimately, these original anisotropies acted as tiny

gravitational wells, attracting more and more matter with time and seeding the structures we observe today, such as clusters and galaxies (Blumenthal et al. 1984). The large scale organisation of the Universe would not have had enough time to form if there was no dark matter, as the initial density fluctuations would not have been able to condense soon enough. These small anisotropies have left an imprint in the Cosmic Microwave Background (CMB)[3] in the form of temperature fluctuations. Since the 1990s, three space missions have been dedicated to their measurement, as they give access to the cosmological density parameters, which are basically the breakdown of the Universe into its main ingredients. The ΛCDM model is the best-fitting model to the temperature anisotropies power spectrum. From the most recent CMB satellite, Planck (Planck Collaboration et al. 2013), it has been inferred that dark matter makes up for 25% of the mass-energy density of the Universe, whereas normal matter accounts for about 5%. Even though dark matter seems dominant on cosmological scales, its very nature remains unknown.

1.2.2 The nature of dark matter

Many candidates have been suggested to play the part of dark matter, from dead stars to exotic particles, but none has measured up to the issue. The possibility of massive, compact stellar remnants inhabiting the outskirts of galaxies has been contemplated: brown dwarfs, neutron stars, black holes... Such objects do not emit much radiation, but they could be detected by microlensing (see Section 1.3.4). Some surveys of such objects have been conducted on the Milky Way and neighbouring galaxies, but their results have been discrepant or inconclusive (see e.g C. Renault 1997, D.P. Bennett 1997, S. Calchi Novati 2013, 2014).

Even though some of the dark matter content could be baryonic[4], the search is headed towards some new, exotic, unknown particle. Some dark matter particle candidates stem from breaches in the standard model, like axions, supersymmetry particles, or any hypothetical Weakly Interacting Massive Particle (WIMP). Large scale experiments such as the well-known Large Hadron Collider (LHC) in Geneva have been built to try and break down elementary particles into even smaller contents up until the discovery of new matter ingredients. There are even some theories involving extra spatial dimensions conferring new levels of energy to ordinary particles (see Bertone et al. 2005, for an extensive review).

To summarise, dark matter is the name of some gravitational anomalies observed in astronomy, that highlight a problem of missing matter. It is needed to explain a great deal of observations, in clusters, galaxies, and cosmology in general. It is expected to account for more matter in the Universe than ordinary matter. As it does not interact with light, the study of its nature is undoubtedly a major challenge for modern science.

[3]The CMB is the remnant of the Universe first light that was emitted when its opacity dropped after the recombination. Its trace can be observed in the microwave spectral domain, in any direction in the Universe.

[4]Baryons are the family of elementary particles that make up ordinary matter, such as protons and neutrons.

1.2.3 Dark matter in elliptical galaxies

The next Subsection is inspired among others by Capaccioli et al. (2002) and references therein.

Rotation curves provide strong evidence for the existence of dark matter halos in spiral galaxies since the 1970s. The situation is far less clear for elliptical galaxies. The computation of a velocity curve in an early-type galaxy is not as straightforward as for a spiral: the stars inhabiting them tend to have a random distribution of orbits instead of a group rotation. Moreover, they are depleted of cold gas, so that the lines most often used as tracers, such as the 21-cm hydrogen line, are difficult to observe.

In the 1980s, amongst the first studies focusing on elliptical galaxies, Fabricant et al. (1980) pioneered in using X-ray brightness measurement as a tracer of their total mass. Their target was the giant elliptical M87. Such massive and bright galaxies sometimes have a hot corona of X-ray-emitting gas, probably originating from stellar mass loss and heated by supernovae (Forman et al. 1985). Assuming hydrostatic equilibrium, the temperature profile $T(r)$ of this gaseous halo can be linked to the galactic mass profile $M(r)$. Some analyses of more ellipticals have led to very high mass-to-light ratio, of about 10 or higher (Fabricant et al. 1980, Trinchieri et al. 1986), meaning a high density of dark matter in the corona. Similar results have been obtained more recently thanks to the Chandra and XMM-Newton X-ray telescopes (Humphrey et al. 2006, O'Sullivan et al. 2007). However, this result is tightly dependent on the hydrostatic equilibrium hypothesis. Diehl and Statler (2007) stated that if that condition is not met, the mass estimates from X-ray analyses are overestimated.

Besides neutral hydrogen, some other objects found in ellipticals can be used to trace velocity as a function of galacto-centric distance. For example, Huchra and Brodie (1987) measured velocities of globular clusters in M87 and obtained a mass-to-light ratio of about 10, in agreement with X-rays results. Planetary nebulae make good candidates for probing the kinematics of outer regions of ellipticals, thanks to some strong emission lines, particularly the [O III] line at 500.7 nm. Capaccioli et al. (2002) compiled a sample of elliptical galaxies studied with planetary nebulae, where the average M/L at $4r_{\mathrm{eff}}$ reaches 7.12 ± 2.78, in mild agreement with X-ray results. Romanowsky et al. (2003) traced velocities of dozens of planetary nebulae in three intermediate-luminosity elliptical galaxies. They obtained (line-of-sight) kinematics information out to approximately $4r_{\mathrm{eff}}$. Their velocity measurements show a clear decrease with galacto-centric distance, compatible with dark matter halo-free models. However, the authors point out that since the Doppler effect method only gives access to the line-of-sight component of the velocity, that decrease can also correspond to highly anisotropic orbits. In that case, the observable component of the velocity would decrease, even though the total velocity may remain constant, like in spiral galaxies, which would indicate a dark matter halo. Two years later, Dekel et al. (2005) produced spiral mergers simulations results, indicating that the stellar orbit in the resulting galaxy would indeed display a high anisotropy. The validity of planetary nebulae conclusions is still being debated (see e.g. Napolitano et al. 2009, De Lorenzi et al. 2009).

Figure 1.6: Results from Romanowsky et al. (2003). The graphs show the line-of-sight velocity dispersion profiles for their three targets. The error bars correspond to 1σ uncertainties on each axis. Predicted profiles are shown by the dashed lines for a singular isothermal halo, and by the dotted lines for a constant mass-to-light ratio profile. This is a reproduction of their Figure 4.

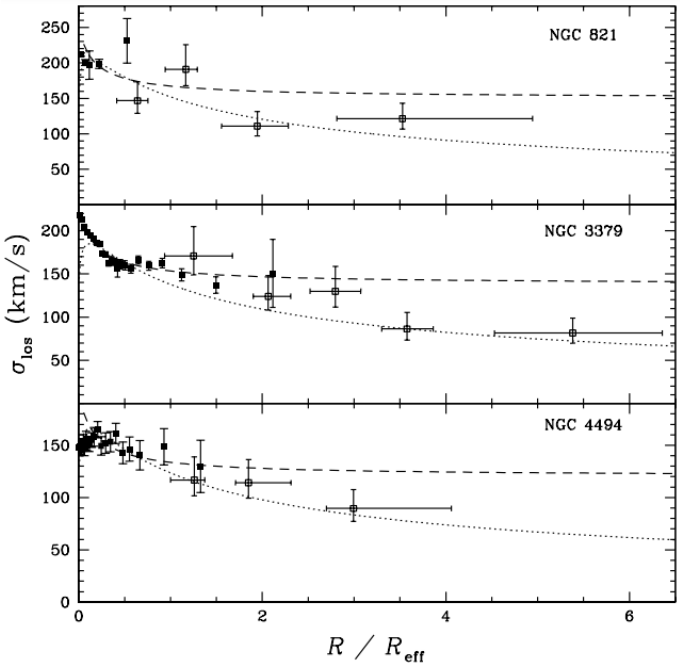

Even though early-type galaxies lack neutral hydrogen, their kinematics can be studied by stellar velocities using the same line of reasoning: the line-of-sight velocity dispersion can be measured using the Doppler effect. Early kinematics studies include Binney et al. (1990), van der Marel et al. (1990) and Saglia et al. (1992), who obtained good fits on velocity dispersions with dynamical models assuming a constant mass-to-light ratio, meaning no dark matter halo. Some dynamical models studies combining spectroscopy, lensing and/or photometry observations have yielded core mass-to-light ratios close to roughly 1.5 at r_{eff} (Pierini et al. 2002, Cappellari et al. 2006a, Grillo et al. 2008, Ferreras et al. 2008), which is coherent with little to no dark matter in the core. However, the same anisotropy issue as in planetary nebulae remain, and this degeneracy between anisotropy and gravitational potential makes it uncertain to draw any firm conclusion. Other early works have yielded discrepant results (see e.g. Saglia et al. 1993, Bertin et al. 1994, Carollo et al. 1995, de Paolis et al. 1995).

In particular, thanks to the SAURON spectrograph, stellar kinematics for about 50 elliptical galaxies have been mapped out, but stars are usually located within one half-light radius, where the search for dark matter halos is slightly less relevant. The SAURON data have yielded a dark matter fraction of about 30% within r_{eff} (Cappellari et al. 2006a), with significant scatter, by comparing the mass evaluated from dynamical models to the mass of the estimated stellar population, based on photometry or spectroscopy. Data from other instruments have given similar results (see e.g. Thomas et al. 2007, and references therein). Weijmans et al. (2008) have combined SAURON data to 21-cm hydrogen line

data for one elliptical galaxy, NGC 2974. The hydrogen line measurements cover larger galacto-centric distances than stellar kinematics. They have found a higher mass-to-light ratio in the outer parts than in the inner parts, suggesting not only the presence of dark matter, but also its organisation in the form of a halo. Many kinematics-based studies have yielded similar results (Pu et al. 2010, Chae et al. 2014, Yıldırım et al. 2016, Smith et al. 2017).

In fact, kinematics and dynamical studies have shown some peculiar scaling relations in elliptical galaxies dark matter halos. Cappellari et al. (2015) have combined data from the SLUGGS (Usher et al. 2012) and ATLAS3D (Cappellari et al. 2011) surveys, mapping out stellar kinematics to four half-light radii. Using dynamical models with few hypotheses on the dark halos to determine the mass profile of 14 galaxies, they have found a remarkable fit of the singular isothermal profile[5], with very little scatter, regardless of the mass or rotation of the galaxy. It is almost as if the dark matter and the luminous matter had conspired to organise the total mass profile into the same form in all galaxies, with stars dominating the inner parts and dark matter, the outer parts. This observation is therefore referred to as the bulge-halo conspiracy (Remus et al. 2013, Dutton and Treu 2014, Cappellari et al. 2015, Janz et al. 2016), and is an odd behaviour of dark matter in a ΛCDM Universe. McGaugh et al. (2016) have reported a tight correlation between the luminous content and the radial acceleration of stars in over 100 early-type galaxies. Their sample covers a wide range of mass and size. This implies that the rotation of a galaxy is entirely defined by its ordinary matter content, highlighting one more time the odd behaviour of dark matter halos in elliptical galaxies.

Dynamical studies of velocity dispersions are a powerful tool. Many of them have concluded to the existence of dark matter halos, although the behaviour of dark matter in such halos seems a little odd. One weakness of such studies is that they often rely on hypotheses on the spatial distribution of velocities. Gravitational lensing, on the other hand, gives direct access to the mass profile of any galaxy, regardless of its type, age, stellar population or spectrum. It also makes it possible to probe regions that usually spread farther out than stellar kinematics. The study of dark matter halos in elliptical galaxies through gravitational lensing is the focus of this work. The mechanisms and formulation of gravitational lensing are discussed in Section 1.3. It consists in observing light rays bent by the gravitational potential of a galaxy and quantifying this deflection to characterise the galaxy mass profile.

1.3 Gravitational lensing

In short, gravitational lensing is the deflection of light rays by gravity. It yields to the formation of "mirages", or illusionary images of astronomical objects. The next Section, describing this phenomenon in further detail, is widely based on the following references: Narayan and Bartelmann (1996), Binney and Merrifield (1998), Courbin (1999), Burud (2001), Chantry (2009), Eulaers (2012), Eichner (2013). Some of the historical discussion

[5] See Chapter 4 for further information about the singular isothermal profile.

about the origins of gravitational lensing is inspired by Valls-Gabaud (2006), Renn and Tilman (2000) and Siegfried (2015).

1.3.1 Early history of gravitational lensing

As early as in the 18th century, the possibility of an interaction between gravity and light rays was considered, notably by Isaac Newton, who wrote in his 1704 "Opticks" : "*Do not Bodies act upon Light at a distance, and by their action bend its Rays; and is not this action strongest at the least distance?*". Newton did not try to quantify any such deflection nor did he perform any experiment to verify it. The paternity of the first gravitational lensing calculation is attributed to the German astronomer Johan Soldner in 1804. However, some records of Henry Cavendish and John Michell writing about the mathematics of "the bending of a ray of light which passes near the surface of any body by the attraction of that body" have been dug up by Frank Watson Dyson in 1921. The exact publication date of the Cavendish-Michell paper is unknown, but has been narrowed down to between 1783 and 1804 (Valls-Gabaud 2006). Johann Soldner is widely considered as the first author to actually study the gravitational deflection of a light ray in his paper "On the deflection of a light ray from its straight motion due to the attraction of a world body which it passes closely". He writes that a light ray passing by the limb of the Sun would undergo a deviation that is close to an arcsecond (a 3600th of a degree).

The work of Soldner was conducted in the context of Newtonian gravity. At the beginning of the 20th century, Albert Einstein starts building up his well-known theory of general relativity, a new mathematical context for gravity. Along with completing the theory of general relativity, Einstein studies the deviation of a light ray passing close to the solar limb and obtains a value close to the double of the Soldner estimate. The next step by then was to actually observe this phenomenon, that is, the shift of the apparent position of a star near the Sun by the angle predicted by Einstein. The brightness of the Sun makes it impossible to distinguish faint stars close to its limb. In 1919, Arthur Eddington and his team took advantage of a solar eclipse to try and measure such a deflection. He led an expedition to the island of Principe as another team was sent to Brazil, aiming at measuring positions of stars during the eclipse. Despite uncertainties because of difficult weather conditions, both teams are said to have confirmed the predicted value of the deflection. This observation is considered to be crucial evidence at this time for Einstein's theory of general relativity. Regardless of the 1919 eclipse expeditions results, Einstein had little faith that this phenomenon could be observed for other stars and was reluctant to pursue any research on gravitational lensing. He changed his mind thanks to the support of Rudi Mendl, a Czech engineer who supposedly encouraged Einstein to publish the famous 1936 paper "Lens-like action of a star by the deviation of light in the gravitational field" (Einstein 1936).

The mathematics derived by Albert Einstein are of course still valid today. However, by then, only stars had been contemplated as lenses. Fritz Zwicky suggested in a couple of 1937 papers (Zwicky 1937a,b) that galaxies would be more efficient as gravitational lenses, because their masses, sizes and mutual distances are of a more suitable magni-

tude to produce multiple images. The interest for gravitational lenses wore down until the 1960s. In 1963, a Dutch astronomer named Maarten Schmidt identified the first quasar (Schmidt 1963) using optical and radio telescopes. Quasars are distant galaxies that harbour an active nucleus, consisting of a supermassive black hole accreting matter in the shape of a disk. The intense friction in this disk produces an enormous quantity of energy, making quasars the brightest objects in the Universe. This property, along with their distance, makes them an excellent source for an observable gravitational lens. The larger the distance, the higher the probability of a lensing mass on the line-of-sight. Around the same time, three astrophysicists independently revived the interest for gravitational lensing. In 1963, the USSR scientist Yu Klimov provided a mathematical description of lensing by galaxies (Klimov 1963a,c,b). In a 1964 paper, Sidney Liebes studied the probability of a stellar lens detection (Liebes 1964). The same year, Sjur Refsdal published two papers on the subject: the first one proposes a geometrical optics description of a point-mass lens. The second one highlights the possibility of using gravitational lensing observations to measure the Hubble parameter, giving for the first time a cosmological application to this phenomenon (Refsdal 1964b,a). This use of lensing is discussed in Subsection 1.3.5.

Finally, in 1979, the first observation of gravitational lensing of a quasar by a galaxy is confirmed. Dennis Walsh, Bob Carwell and Ray Weymann observed a pair of twin quasars, with the same spectrum at the same redshift, separated by a short distance (Walsh et al. 1979). They suggested immediately upon discovery that this twin object was in fact two images of the same background quasar formed through gravitational lensing. Shortly after, the elliptical galaxy responsible for the lensing had been identified by Stockton (1980). The second lensing candidate was discovered that same year (Weymann et al. 1980). Nowadays, dozens of gravitational lensing observations of various morphologies are known, and their study is at the core of many astrophysical papers.

1.3.2 The deflection angle

General relativity predicts that a dense object bends the space-time continuum in its vicinity. This deformation affects the path of a light ray passing close to the object. When deflected light rays reach an observer, they can produce multiple, distorted images of their source. The dense object is called a gravitational lens. The background source is often a quasar, and the lens can be a galaxy, or a cluster of galaxies. In this work, we are focusing on galaxy lensing. A simple sketch of the deflection is shown on Figure 1.7. The deflection angle $\hat{\alpha}$ on a light ray passing by a mass M at a distance ξ is:

$$\hat{\alpha} = \frac{4GM}{c^2\xi} \tag{1.5}$$

where G is the gravitational constant and c the speed of light.

Figure 1.7: The deflection of a light ray (black arrow) by a mass M. O is the observer, ξ is the impact parameter.

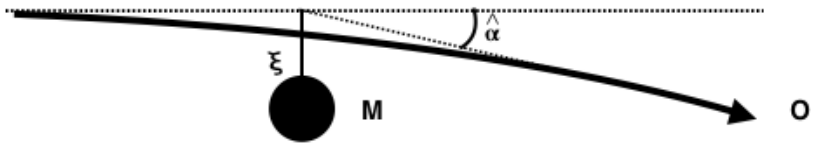

Figure 1.8: A diagram of gravitational lensing by a lens L of a light ray emitted by a source S into an image I as seen by the observer O. Credit: Chantry (2009)

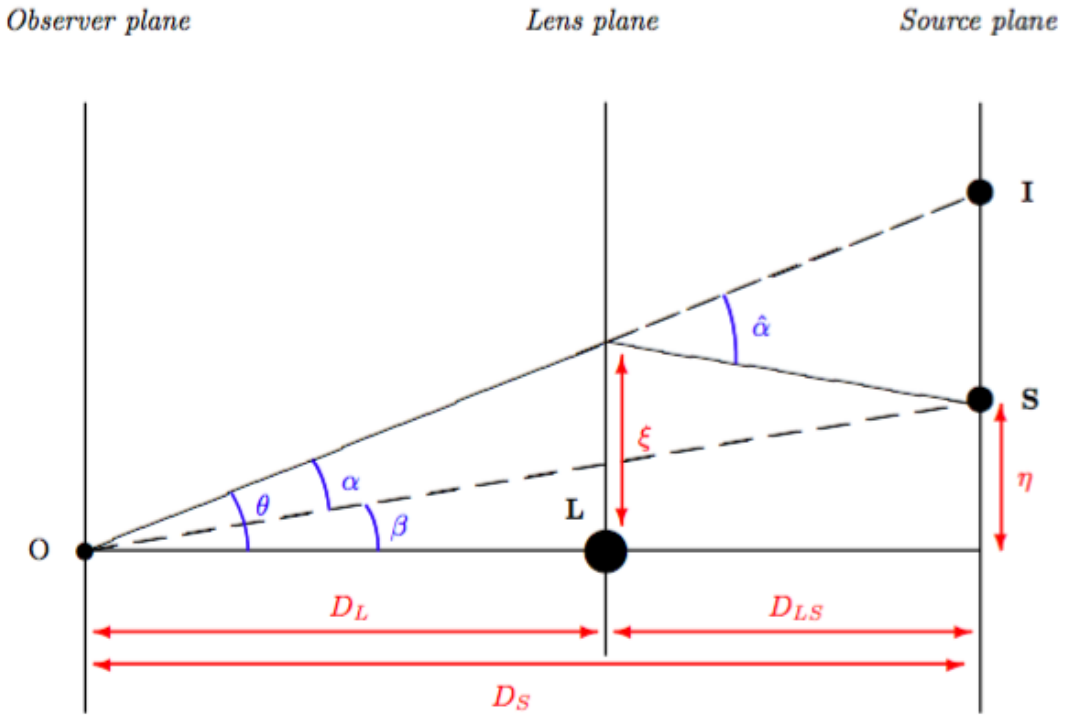

1.3.3 The lens equation

Let us consider first a point-like mass M. The aim is to express the deflection angle as a function of observables quantities. Figure 1.8 represents the situation of an observer O observing the image I of a source S lensed by L. D_{L}, D_{S} and D_{LS} are the respective distances between the observer, the lens, and the source. At cosmological scales, it can be assumed that these distances are much larger than the typical size of a galaxy. This yields two reasonable working hypotheses: first, the thin lens approximation, which means that all the mass of the lens is concentrated in a plane at a distance D_{L}. The same approximation is tacitly assumed for the background source. Second, the small-angle approximation makes it possible to approach a few trigonometrical functions of the angles by the size of the angles themselves. α is the apparent angle between the source and its lensed image, as measured by the observer, whereas $\hat{\alpha}$ is that same angle, as measured from the lens plane.

They are linked by the following equation :

$$\alpha = \frac{D_{\mathrm{LS}}}{D_{\mathrm{S}}}\hat{\alpha} \tag{1.6}$$

β is the angular position of the source and θ is the angular position of the lensed image, both as seen by the observer. θ is usually the only observable angle. ξ is the distance from the lens to the intersection between the light ray and the lens plane.

Under the small-angle hypothesis, using trigonometry, we have :

$$\theta D_{\mathrm{S}} = \beta D_{\mathrm{S}} + \hat{\alpha} D_{\mathrm{LS}} \tag{1.7}$$

that can be rewritten using Equation 1.6 as:

$$\beta = \theta - \alpha(\theta) \tag{1.8}$$

The latter relation is named the lens equation. These relations are valid under the assumption that the mass M is point-like, which is unphysical. For an extended lens with a circular symmetry, we can rewrite Equation 1.5:

$$\hat{\alpha}(\xi) = \frac{4GM(\xi)}{c^2 \xi} \tag{1.9}$$

where $M(\xi)$ is the mass enclosed in a radius ξ in the lens plane. For a more general case, let us consider a thin lens with a projected surface mass density of $\Sigma(\boldsymbol{\xi})$. The angles and positions are two-dimensional vectors on the sky plane. The expression of the deflection angle becomes a two-dimensional integral in the lens plane :

$$\hat{\boldsymbol{\alpha}}(\boldsymbol{\xi}) = \frac{4G}{c^2} \iint \frac{\Sigma(\boldsymbol{\xi}')(\boldsymbol{\xi} - \boldsymbol{\xi}')}{|\boldsymbol{\xi} - \boldsymbol{\xi}'|^2} d\boldsymbol{\xi}' \ . \tag{1.10}$$

The lens equation becomes vectorial too,

$$\boldsymbol{\beta} = \boldsymbol{\theta} - \boldsymbol{\alpha}(\boldsymbol{\theta}) \ . \tag{1.11}$$

Geometry links the impact parameter $\boldsymbol{\xi}$ to the observable $\boldsymbol{\theta}$ as $\boldsymbol{\xi} = D_{\mathrm{L}}\boldsymbol{\theta}$. A simple substitution makes it possible to express the deflection angle $\boldsymbol{\alpha}$ as a function of the observable $\boldsymbol{\theta}$, according to Equation 1.6:

$$\boldsymbol{\alpha}(\boldsymbol{\theta}) = \frac{D_{\mathrm{LS}}}{D_{\mathrm{S}}}\, \hat{\boldsymbol{\alpha}}(\boldsymbol{\theta}) = \frac{4G}{c^2} \frac{D_{\mathrm{L}} D_{\mathrm{LS}}}{D_{\mathrm{S}}} \iint \frac{\Sigma(\boldsymbol{\theta}')(\boldsymbol{\theta} - \boldsymbol{\theta}')}{|\boldsymbol{\theta} - \boldsymbol{\theta}'|^2} d\boldsymbol{\theta}' \ . \tag{1.12}$$

Let Σ_{crit} be the critical density defined as:

$$\Sigma_{\mathrm{crit}} = \frac{c^2}{4\pi G} \frac{D_{\mathrm{S}}}{D_{\mathrm{L}} D_{\mathrm{LS}}} \ . \tag{1.13}$$

The critical density depends only on constants. The ratio of the projected surface mass density $\Sigma(\boldsymbol{\theta})$ and the critical density is called the convergence $\kappa(\boldsymbol{\theta})$.

$$\kappa(\boldsymbol{\theta}) = \frac{\Sigma(\boldsymbol{\theta})}{\Sigma_{\mathrm{crit}}} \ . \tag{1.14}$$

If we substitute the convergence for the density in Equation 1.12, we get

$$\boldsymbol{\alpha}(\boldsymbol{\theta}) = \frac{1}{\pi} \iint \kappa(\boldsymbol{\theta}') \frac{(\boldsymbol{\theta} - \boldsymbol{\theta}')}{|\boldsymbol{\theta} - \boldsymbol{\theta}'|^2} d\boldsymbol{\theta}' \tag{1.15}$$

where the integrand bears resemblance to the derivative $\boldsymbol{\nabla}_{\boldsymbol{x}} \ln|\boldsymbol{x}| = \boldsymbol{x}/|\boldsymbol{x}|^2$. If we define a quantity labelled $\phi(\boldsymbol{\theta})$ such that $\boldsymbol{\nabla}_{\boldsymbol{\theta}}\phi(\boldsymbol{\theta}) = \boldsymbol{\alpha}(\boldsymbol{\theta})$:

$$\phi(\boldsymbol{\theta}) = \frac{1}{\pi} \iint \kappa(\boldsymbol{\theta}') \ln|\boldsymbol{\theta} - \boldsymbol{\theta}'| d\theta' \ . \tag{1.16}$$

In fact, $\phi(\boldsymbol{\theta})$ is linked to the convergence by a Poisson equation :

$$\nabla^2_{\theta}\phi(\boldsymbol{\theta}) = 2\kappa(\boldsymbol{\theta}) \tag{1.17}$$

and it can be seen as the effective gravitational potential of the lens. To be more specific, the mass of the lens generates a Newtonian gravitational potential. Just like the projected surface density of the lens $\Sigma(\boldsymbol{\xi})$ is the projection of the lens (volumetric) density on the lens plane along the line of sight, the effective gravitational potential can be linked to the "common" Newtonian potential by an integration along the line of sight. Using that effective gravitational potential, we can finally formulate the lens equation in its most common form:

$$\boldsymbol{\beta} = \boldsymbol{\theta} - \boldsymbol{\nabla}_{\boldsymbol{\theta}}\phi(\boldsymbol{\theta}) \tag{1.18}$$

The lens equation builds a link between the observable positions of the lensed images and the mass distribution of the lens. Most often, the challenge is to go back from the observed images configuration to the lens physical mass profile. This is called lens modelling. Gravitational lensing images can have multiple appearances, from multiple points to closed, symmetric rings.

1.3.4 Gravitational lensing images

Figure 1.8 only shows the formation of one image I. However, in the cases we are focusing on, two or four images of the background source are observed. Because of the relative distances, multiple quasar images are most often point-like. The number of images depends on the relative positions of the protagonists. Nevertheless, quasar host galaxies are extended sources, and may sometimes yield extended images. A remarkable case of extended lensed image happens if the lens has circular symmetry, and if the observer, the lens and the source are exactly aligned: it produces a ring-shaped image around the lens. In that configuration $\beta = 0$ and equation 1.11 simplifies into a scalar form:

$$\theta = \alpha(\theta) = \hat{\alpha}(\xi)\frac{D_{\mathrm{LS}}}{D_{\mathrm{S}}} \tag{1.19}$$

and the angular radius of that ring θ is denoted θ_{Ein}, as such a ring is named an Einstein ring. Given Equation 1.5 and noticing $\xi = D_{\mathrm{L}}\theta$, we get:

$$\theta_{\mathrm{Ein}} = \sqrt{\frac{4GM}{c^2}\frac{D_{\mathrm{LS}}}{D_{\mathrm{S}}D_{\mathrm{L}}}} \tag{1.20}$$

where M is the mass of the lens enclosed in the Einstein radius. In realistic cases, under the approximation that the lens is sufficiently symmetrical, the average density of the lens inside the Einstein radius is the mass M divided by the surface of a circle of radius $\theta_{\rm Ein}$:

$$\Sigma(\theta_{\rm Ein}) = \frac{M}{\pi(D_{\rm L}\theta_{\rm Ein})^2} \tag{1.21}$$

and by substituting Equation 1.20 in Equation 1.21, it can be seen that it exactly corresponds to the critical density. Therefore, the lens mass inside the Einstein radius can be expressed in terms of constants, of the distances and of $\theta_{\rm Ein}$. When the perfect alignment criterion between the observer, lens and source is not met, partial rings or arcs can be observed, and constraints about the mass can be inferred too. That is also the case with multiply imaged sources, where as a rule of thumb, the Einstein radius is often well approximated by the average between the galacto-centric angular positions of the sources (Mediavilla et al. 2016).

Besides deforming and multiplying images of the source, gravitational lensing may lead to a change in the total flux the observer receives. In fact, the surface brightness of the source is conserved, but the apparent surface of the source is not. Since it can be larger than the apparent surface of the non-lensed source, a lensed image can be even brighter than the original source. The magnification μ is thus simply linked to their apparent surface ratio,

$$\mu(\boldsymbol{\theta}) = \left[\det \frac{\partial \boldsymbol{\beta}(\boldsymbol{\theta})}{\partial \boldsymbol{\theta}}\right]^{-1} . \tag{1.22}$$

This determinant can be positive, negative or null. If it is null, then the magnification

Figure 1.9: A sketch of the critical curves (*left*) and the caustics (*right*) for a lens with an elliptical mass distribution. The numbers indicate the number of images that are formed if the source is located in these regions. The colours correspond to matching positions in the source plane and in the lens plane: for example, a source placed near the blue part of the caustics will produce an image located near the blue parts of the critics. The inner caustic matches the outer critical curve, and vice-versa. Credit: Chantry (2009).

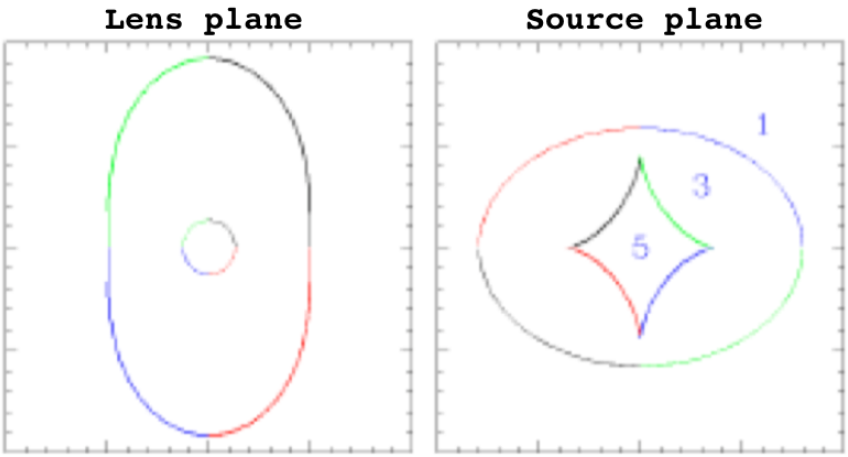

diverges. The ensemble of points from the lens plane where the amplification diverges are called the critical curves. Their projection in the source plane are called the caustics. An infinite magnification is of course non-physical: the magnification actually diverges for

point-like sources only, and no source is truly point-like, the background quasar always has a physical extension. In a more general case, the total magnification is the integral of $\mu(\boldsymbol{\theta})$ on the whole surface of the source, and is always finite. The magnification can also be expressed in terms of two other parameters:

$$\mu(\boldsymbol{\theta}) = \frac{1}{(1 - \kappa(\boldsymbol{\theta})) - \gamma^2} \tag{1.23}$$

where κ is the convergence and γ is called the shear. Gravitational lensing produces distorted images, and this distortion can be summed up into two effects: the convergence isotropically changes the size of the image, and the shear stretches it along a tangential dimension. In fact, the shear accounts for tidal perturbations of the lens gravitational field, whether it is intrinsic to the lens or due to the presence of an extra deflector in its vicinity. Any deflector along the line of sight adds to the shear parameter.

Figure 1.10: A sketch of the effect of the convergence κ (*right*) and the shear γ (*left*) on a ring. κ isotropically resizes it, while γ distorts it along a tangential direction.

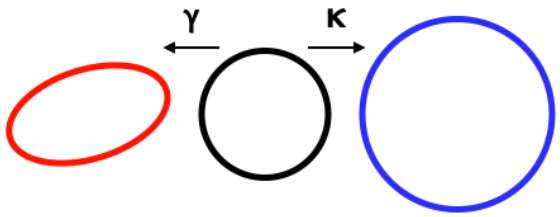

Because the intrinsic property of the background quasar are unknown, the magnification factor μ cannot be absolutely determined. The best we can do is to measure the ratio between the fluxes in all the images of the source and use it as a constraint on the magnification.

So far, it has been shown that lensing can produce images that are multiple, distorted and/or magnified. Sometimes, only one or two of these effects can be observed. The magnitude of each effect defines three classes of gravitational lensing:

- Strong lensing: in this case, we observe multiple images, and in case of high symmetry, arcs and Einstein rings. The lenses can be galaxy clusters, or galaxies of about $10^{10} - 10^{12}\ M_\odot$. It is the case we are focusing on in this work. With these masses, the images are typically separated by distances of the order of one arcsecond.

- Weak lensing: as the name suggests, the mechanisms at work are the same as for strong lensing, but to a smaller magnitude. No multiple images are observed. The distortions are less obvious and can only be inferred statistically, by observing many objects in a large field. The lens is usually a diffuse galaxy cluster.

- Microlensing: the shape of the image is unchanged, but its flux varies over time. To be more specific, it happens when two distorted images of a background source are

formed so close to one another that they cannot be resolved, but only the magnification is observable. It can happen at smaller scales than the two other classes of lensing: for example, when a star passes in front of a bright object, the flux measured form that bright object increases. As the star passes by, the magnification varies. This phenomenon is sometimes used to detect exoplanets. On a cosmological distance scale, microlensing might happen on top of a strong lensing situation. If a quasar is lensed by a galaxy, the movement of stars in the lensing galaxy might cause a change in the magnification of one of the multiple source images.

1.3.5 Time delays

The multiple images of a lensed background quasar take different optical paths up to the observer. For that reason, each image may take a different time to reach the observer. If the quasar shows intrinsic variability, the change in the flux might not manifest simultaneously in all images: there is a time delay in each pair of images. In fact, the contribution to the time delay between two images of a lensed quasar, say A and B, is twofold. First, there is a geometrical component, due to the actual difference in optical paths. Second, a relativistic property of light rays is that their speed changes when they move through gravitational potentials: they are slowed down when the potential is stronger. This is the Shapiro effect (Shapiro 1964). In a gravitational lensing configuration, light rays that cross different regions of the lens potential undergo different Shapiro decelerations.

By identifying the lens equation (1.11) to the definition of the effective potential gradient $\boldsymbol{\nabla}_{\boldsymbol{\theta}}\phi(\boldsymbol{\theta})$, we get:

$$(\boldsymbol{\theta} - \boldsymbol{\beta}) - \boldsymbol{\nabla}_{\boldsymbol{\theta}}\phi(\boldsymbol{\theta}) = 0 \tag{1.24}$$

This equation can be turned into a more general gradient:

$$\boldsymbol{\nabla}_{\boldsymbol{\theta}}\left[\frac{1}{2}(\boldsymbol{\theta} - \boldsymbol{\beta})^2 - \phi(\boldsymbol{\theta})\right] = 0 \tag{1.25}$$

The term between brackets is related to the expression of the time delay. Its first part is related to the extra distance compared to an unlensed ray path. Its second part is linked to the effective gravitational potential and the Shapiro effect. This gradient yields the time-delay function, describing the arrival time t of a lensed image at a position $\boldsymbol{\theta}$:

$$t(\boldsymbol{\theta}) = \frac{1 + z_\mathrm{l}}{c}\frac{D_\mathrm{L} D_\mathrm{S}}{D_\mathrm{LS}}\left[\frac{1}{2}(\boldsymbol{\theta} - \boldsymbol{\beta})^2 - \phi(\boldsymbol{\theta})\right] + C \tag{1.26}$$

where z_l is the lens redshift and C is a constant. The multiplication by the factor including the redshift accounts for the time stretching. The difference between a pair of images $t(\boldsymbol{\theta}_\mathbf{A}) - t(\boldsymbol{\theta}_\mathbf{B})$ eliminates C and yields:

$$\begin{aligned}\Delta t_{AB} &= t(\boldsymbol{\theta}_\mathrm{B}) - t(\boldsymbol{\theta}_\mathrm{A}) \\ &= \frac{1 + z_\mathrm{l}}{c}\frac{D_\mathrm{L} D_\mathrm{S}}{D_\mathrm{LS}}\left[\frac{1}{2}(\boldsymbol{\theta}_\mathbf{B} - \boldsymbol{\beta}_\mathrm{B})^2 - \frac{1}{2}(\boldsymbol{\theta}_\mathrm{A} - \boldsymbol{\beta}_\mathrm{A})^2 + \phi(\boldsymbol{\theta}_\mathrm{A}) - \phi(\boldsymbol{\theta}_\mathrm{B})\right]\end{aligned} \tag{1.27}$$

Let us conclude the mathematical discussion on time delays by noticing that interestingly enough, Equation 1.25 is in fact an expression of the Fermat principle, stating that the optical path length must be an extremum of the light travel time: $\nabla_\theta t = 0$.

The time delays between pairs of images can be measured by monitoring the flux from both images as continuously as possible. This measurement yields a light curve for each image, and the analysis of this light curve gives access to the offset between a significant flux change in both images. This can be conducted for as many images as available, as illustrated of the four images of HE0435-1223 as an example on Figure 1.11.

Figure 1.11: The light curves of the four lensed images of a quadruply-imaged quasar, HE0435-1223, based on observations between 2003 and 2016. This lens is part of the sample studied here and is described in further detail in Chapter 2. These light curves have been obtained and analysed by Bonvin et al. (2017) and this figure an excerpt from their Figure 2. The shift between the light curves cannot be made out by the naked eye. For example, the time delay between A and B is approximately 13 days.

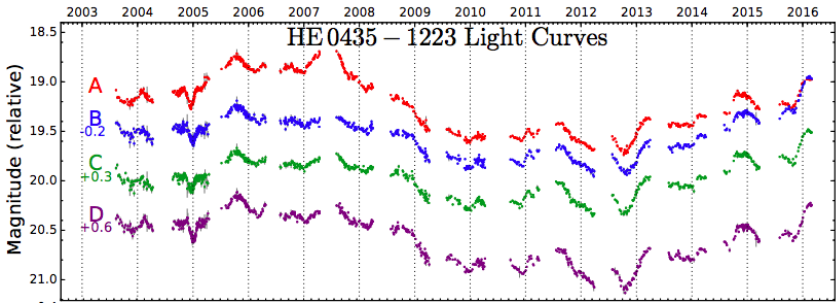

If an accurate measurement of time delays is available, gravitational lensing can be used to determine the value of the Hubble constant H_0, that is related to the rate of expansion of the Universe. Indeed, the distances involved in Equation 1.27 are inversely proportional to the Hubble constant, and the rest of the terms mostly are observable quantities. A detailed process to calculate H_0 from time delays in gravitational lensing has first been introduced by Refsdal (1964a) and still is nowadays widely applied, including programs like COSMOGRAIL (COSmological MOnitoring of GRAvItational Lenses, Bonvin et al. 2016) or H0LiCOW (H_0 Lenses in COSMOGRAIL's Wellspring, Suyu et al. 2017). However, this lies beyond the scope of this work: time delays will only be used as constraints for lens modelling.

1.3.6 Gravitational lensing and dark matter in early-type galaxies

In this work, we are using gravitational lensing to study the physical mass content and distribution of the lens. It boils down to solving the lens equation (Equation 1.11) assuming a model for $\kappa(\theta)$ and fine-tuning it to yield the best reproduction of the observables. We focus on quadruply imaged quasars, and we use as many constraints as possible: the astrometry of the lensing observation (galaxy and sources positions), time delays, and other constraints specific to each mass model. More details about this process are given in Section 4.2. We choose not to use the flux ratios as constraints, as they may be affected

by microlensing uncertainties.

Previous studies of dark matter in ellipticals using gravitational lensing have yielded a variety of results. Choosing a mass model that includes dark matter usually produces better results than a "mass-follows-light" model (Gavazzi et al. 2008, Lagattuta et al. 2010, Thomas et al. 2011). In fact, some lensing results have shown that elliptical galaxies may contain even more dark matter than spirals (Gavazzi et al. 2008, Thomas et al. 2009). On the other hand, it has also been argued that the dark matter fractions from lensing do not match cosmological ΛCDM predictions (e.g. Keeton 2002). What is more, gravitational lens modelling suffers from a few degeneracy issues (see Chapter 4, Section 4.2.) In this work, we aim at comparing the goodness-of-fit from "mass-follows-light" models to that from classical models including spiral-like dark matter halos. The objectives are defined in Section 1.4.

1.4 Objectives

This work is tackling the following issue: are elliptical galaxies embedded in extended dark matter halos, as it seems to be the case for their spiral counterparts? To answer that question, we aim at measuring mass-to-light ratios of a sample of ellipticals within their Einstein radii. These ratios compare the luminous content of galaxies, that is, stars and gas, to their total mass, luminous and dark. If the mass-to-light ratio of an object is close to unity, then its luminosity content tends to be equal to its total mass: it does not include any dark matter. On the contrary, the higher the mass-to-light ratio, the more dark matter the object contains. It thus gives a rough idea of the dark matter fraction of the sample galaxies.

Since we are considering this value within the Einstein radius, we can infer some information about the extension of the dark matter content. Indeed, if the Einstein radius is equal to several half-light radii, that means that we are probing a region of the galaxy that extends beyond the stellar bulge. What is more, the evolution of our galaxies mass-to-light ratios with galacto-centric distance should be of great interest. Assuming that galaxies are embedded in dark halos, their mass-to-light ratios should increase the farther out we probe. In this study, we have but one mass-to-light ratio at one galacto-centric distance per galaxy. Nevertheless, since each one of our galaxies has a different Einstein radius, we are probing a variety of distances. Plotting our galaxies mass-to-light ratios versus their Einstein radii should show the trend of its behaviour with galacto-centric distance. If the mass-to-light ratio does not significantly increase after a few half-light radii, it would dispute the existence of dark matter halos around the members of our sample. This characterisation of mass-to-light ratios in early-type galaxies is the main purpose of this work. It will be pursued in two main steps: on the one hand, computing an accurate light profile of the lensing galaxies and on the other hand, modelling their density profile. Eventually, these two results should give direct access to the mass-to-light ratios.

First, we are tackling the light profile study. We aim at fitting a de Vaucouleurs profile to images of the sample galaxies. However, some constraints, coming from the very na-

ture of gravitational lensing images, hinder that operation. Indeed, these images contain a mixture of lensed signal from a background quasar and actual signal from the lens itself. Lensed signal can appear in two forms, point-like (sources) or diffuse (arcs). We must make sure to properly separate these from the lens signal, and we do so by designing two subtraction methods, one for each kind of lensed signal. For that purpose, we need an excellent understanding of the instrumental profile, also known as the point-spread function (PSF), of our images. Since this work enters into the continuity of the PhD thesis of Virginie Chantry (Chantry 2009), we use PSF results from that study. The authors of this work and of related papers (Chantry et al. 2010, Sluse et al. 2012) have used and improved a specific PSF determination method, namely the MCS algorithm (Magain et al. 1998, 2007), that is particularly well suited for gravitational lensing images, where usually no point-like star is available to help computing the PSF.

We also design new techniques to fit the de Vaucouleurs model to our data set. Indeed, gravitational lensing images still entail some specific difficulties: despite a careful lensed signal subtraction, some diffuse signal might remain farther out around the lens. Also, uncertainties coming from to the point-source subtraction may produce artefacts in lensing systems that are highly asymmetric, as it is the case for one of our galaxies. Both these phenomena limit the modelling to the inner regions of the galaxy and the measurements to small parts of the lens. On top of that, in lensing images, the galaxy is usually quite small compared to the size of the PSF. All these factors may cause classical fitting techniques, that consist in minimising a merit function in the parameters space, to perform poorly on such images. We therefore propose a technique that is as robust as possible for studying the shape parameters of lensing galaxies and that is able to work around the above-mentioned artefacts (Biernaux et al. 2016).

Second, we focus on the mass profile determination. This is where the lensing formalism takes part. We use the *lensmodel* application from the GRAVLENS package (Keeton 2011) to fit mass models to our lenses, so that they best reproduce the observed image configuration. We use astrometry results from Chantry (2009), Chantry et al. (2010), Sluse et al. (2012), and we take into account all the available information, that is, time delays measurements, if any, and the influence of the environment (other deflectors). We test a variety of mass models, considering different hypotheses on the distribution of dark matter in the lens: halos or "mass-follows-light". These mass models are compared in terms of goodness-of-fit. However, as lens modelling is a complex problem, that includes a large number of parameters (thus sensitive to the existence of local minima in the parameters space) and some degeneracies, we choose to focus on the mass-to-light ratio as a more conclusive parameter to investigate the dark content of early-type galaxies.

We then compute the total mass content of each lens within its Einstein radius, as the latter depends very little on the chosen model. By integrating the best-fitting light profile in an aperture of a radius equal to the Einstein radius, we get the corresponding light content. It is then pretty straightforward to compute the mass-to-light ratio for each mass model case. These values are plotted as a function of the Einstein radius, expressed in units of half-light radii. They are compared to theoretical mass-to-light ratios, corresponding to a variety of scenarios regarding the dark matter content of elliptical galaxies,

their IMFs, and their metallicity. The behaviour of the mass-to-light ratio of our elliptical galaxies with galacto-centric distance is also analysed, as it is expected to increase from the centre out in the presence of a dark matter halo.

This work is structured as follows. Chapter 2 gives an overview of the data sample, and gives some background information about the PSF and astrometry results we used from Chantry (2009), Chantry et al. (2010) and (Sluse et al. 2012). Chapter 3 then exposes the details of our light profile study, step per step, from the lensed signal subtraction to the de Vaucouleurs fitting. Chapter 4 explains the various cases we considered for the mass profiles, as well as our results regarding lens modelling. The comparison of light and mass profiles, to compute the mass-to-light ratios, as well as the computation of the theoretical mass-to-light ratios, are explained in Chapter 5, where our results are also presented and discussed. Eventually, some concluding remarks are provided in Chapter 6.

2 Data sample selection and data pre-processing

In this Chapter, the criteria for selecting our sample of gravitational lensing systems are explained. We used astrometry results from Chantry et al. (2010) and Sluse et al. (2012). We also used their determination of the PSFs. Some parts of the following Chapter have first been published in Biernaux et al. (2016).

2.1 The data

2.1.1 Selecting the data sample

Eight gravitational lensing systems are selected from the CASTLES database[1] (Muñoz et al. 1998). They have been chosen amongst a larger sample of lenses, which were previously processed in Chantry et al. (2010) and Sluse et al. (2012). Their full sample has been reduced to a subsample of eight systems because of the following criteria. First, we choose to focus on quadruply lensed sources, so as to maximise the number of constraints on the mass profile. Since the light profile of the lens is to be studied too, the redshifts of each lens and source have to be securely known, and systems with multiple lenses of similar luminosity are excluded. The images were obtained with the NIC2 camera of the NICMOS instrument onboard the HST between 1997 and 2004 in the near infrared H-band. The angular scale of these images is 0.075 arcseconds per pixel. Detailed information about each observation session can be found in Chantry et al. (2010) and Sluse et al. (2012).

Previous processing of these data in Chantry et al. (2010) and Sluse et al. (2012) includes a thorough determination of the PSF for each data frame, using the MCS algorithm, explained in Section 2.2. These very detailed PSFs have not only given access to accurate astrometry, but also made it possible to clearly distinguish the deflected images from the

[1] https://www.cfa.harvard.edu/castles/

Table 2.1: A list of the systems included in the data sample, their coordinates and redshifts. These values are taken from Sluse et al. (2012) and Chantry et al. (2010), but more specific references are provided in the text.

System	*# frames*	*Source redshift*	*Lens redshift*	*RA (J2000)*	*DEC (J2000)*
MG0414+0534	13	2.64	0.96	04:14:37.73	+05:34:44.3
HE0435-1223	4	1.689	0.46	04:38:14.9	−12:17:14.4
RXJ0911+0551	4	2.80	0.77	09:11:27.50	+05:50:52.0
SDSS0924+0219	8	1.524	0.359	09:24:55.87	+02:19:24.9
PG1115+080	4	1.72	0.351	11:18:17.00	+07:45:57.7
SDSS1138+0314	4	2.44	0.45	11:38:03.70	+03:14:58.0
B1422+231	4	3.62	0.354	14:24:38.09	+22:56:00.6
WFI2033-4723	4	1.66	0.664	20:33:42.08	-47:23:43.0

lensing galaxy. The main results of this previous processing, i.e. the PSFs and the astrometry, have been used as a starting point for the present work. Some comments about the characteristics of each one of our lenses are given below.

MG0414+0534: this quadruple system was discovered by Hewitt et al. (1992) in the radio wavelengths, and the lens was observed shortly after by Schechter and Moore (1993). Falco et al. (1997), McLeod et al. (1998) and Ros et al. (2000) obtained accurate astrometry, confirmed its lensing nature and identified an extra deflector, respectively in visible, near infrared and radio frequencies. This extra object is included in the lens modelling. Its redshift was measured by Tonry and Kochanek (1999).

HE0435-1223: HE 0435-1223 was discovered by Wisotzki et al. (2002). Its redshift was measured by Morgan et al. (2005), Ofek et al. (2006a) and later confirmed by Eigenbrod et al. (2006b). Momcheva (2009) discovered it to be part of a group, which has to be taken into account when modelling the lensing potential. This rich group was extensively studied by Sluse et al. (2017). Time delays for this lens were first measured by Courbin et al. (2011), then confirmed and refined by Bonvin et al. (2017).

RXJ0911+0551: this highly asymmetrical system was first discovered by Bade et al. (1997) and later confirmed as a quadruple lens by Burud et al. (1998), and suspected to be a member of a cluster. This was later confirmed by Kneib et al. (2000a) and complicates the study of its lensing potential. Three out of the four images lie very close to each other to form the *A* component, while the *B* component lies at a considerable angular distance of almost $3''$ from *A*. Its time delays were measured by Hjorth et al. (2002), then by Burud et al. (2001), and eventually confirmed by Eulaers and Magain (2011).

SDSS0924+0219: this system was discovered by Inada et al. (2003). Many teams attempted a measurement of its time delays, but the study of its light curves is greatly complicated by anomalous flux ratios. This uncertainty is attributed to microlensing (Keeton et al. 2006a, Saha et al. 2006). Its lens redshift was measured by Ofek et al. (2006b).

PG1115+080: first identified by Weymann et al. (1980), then by Kneib et al. (2000b), this quadruple lens is part of a group at a redshift of $z = 0.31$ (Tonry 1998, Grant et al. 2004, Momcheva et al. 2006). Its time delays were first measured by Schechter et al. (1997) and confirmed by Barkana (1997). However, it was then analysed by Eulaers and Magain (2011), who showed that different processing methods lead to different results. Eventually, Shimanovskaya et al. (2015a) and Shimanovskaya et al. (2015b) provided a new estimate of its time delays and a critical analysis of results obtained so far: their results are in agreement with those of Eulaers and Magain (2011) using the numerical fit method described in Burud et al. (2001). Bonvin et al. (2018) re-analysed existing light curves together with new data and acquired precise time delays that are in agreement with those from Burud et al. (2001). For that reason, we chose their published results of $\Delta t_{AC} = 11.7 \pm 2.2$ and $\Delta t_{BC} = 23.8 \pm 3.0$.

SDSS1138+0314: this lens was discovered by Inada et al. (2008). Its redshifts were measured by Eigenbrod et al. (2006b).

B1422+231: this lensing system was discovered by Patnaik et al. (1992) and, shortly after, extensively studied by Lawrence et al. (1992) and Remy et al. (1993). Its redshift reaches $z = 0.35$ and it is also part of a group of galaxies (Impey et al. 1996, Kundic et al. 1997, Tonry 1998, Grant et al. 2004, Momcheva et al. 2006).

WFI2033-4723: this lensed quasar, at a redshift $z = 1.66$ was discovered by Morgan et al. (2004), and is part of a rather crowded environment, that takes part into its lensing potential. The redshift of the lens was measured by both Ofek et al. (2006b) and Eigenbrod et al. (2006b), and their results came into an agreement. Its time delays were accurately measured by Vuissoz et al. (2008).

For readability, in all further discussion, the names of the systems will be shortened to the first part of their identification. WFI2033-4723 will be noted WFI2033 and so on.

2.1.2 Pre-processing

After selection, a classical pre-processing of the images is conducted. Since we are directly using the PSFs, astrometry, and some image processing results of Chantry et al. (2010) and Sluse et al. (2012), this step is reduced to a simpler task. One could even wonder why bother re-processing the HST/NICMOS images at all. Upon re-analysing these works, we identified a likely source of systematic errors: the sky background was found to be systematically underestimated, attributing too much luminosity to the galaxy. We thus carry out a whole pre-processing routine to correct from that bias.

The first step consists in correcting the HST/NICMOS images for the cosmic rays, for hot, saturated, poorly dark-corrected or flat-field-corrected pixels, and for pixels affected by readout errors. This is performed by identifying those pixels thanks to a data quality map provided in the HST/NICMOS data package. Their error is set up to a warning value

in the σ-map, giving them no weight in the subsequent operations, and their value is interpolated between their immediate neighbours.

Then, the sky background value is determined in the form of a constant value and individually computed for each frame. This is achieved by calculating the average intensity of object-free zones, that is, areas where there is no intensity gradient caused, for example, by the presence of the galaxy, the sources, any arc, or other object. Since the NICMOS detector is divided into four cells, four different sky background values have to be computed, one for each cell. This operation is conducted separately on each data frame. These constants are then subtracted directly from the intensity of each pixel. The background sky of the resulting images is analysed to make sure no gradients are left in the subtraction. On average, the magnitude of the underestimation of the sky in Chantry et al. (2010) and Sluse et al. (2012) reaches about 12%.

The final step of this pre-processing is to extract the region of the image that is relevant to this study, that is, a part of the image that contains the lens, the lensed images, and some "comfortable room" that includes undisturbed background. That last step is conducted so that the astrometry results from Chantry et al. (2010) and Sluse et al. (2012) are respected. The steps of the pre-processing are shown as an example on HE0435 in Figure 2.1.

2.2 The MCS algorithm

The theoretical background to this Section is largely based on Chantry (2009).

Determining accurate PSFs for the images in our sample is necessary for achieving a good point sources subtraction, and for a precise measurement of the lenses shape parameters. Like many authors who have processed lenses in the framework of the COSMOGRAIL project (Chantry et al. 2010, Courbin et al. 2011, Sluse et al. 2012), we use the MCS deconvolution algorithm (Magain et al. 1998, 2007, Chantry and Magain 2007). The MCS algorithm is a deconvolution and PSF determination method that stands for Magain, Courbin and Sohy and has been introduced in Magain et al. (1998). The motivation behind this technique is the observation that most deconvolution methods aim at a PSF with an infinite resolution, meaning that the sampling step should become infinitely small. This generally violates the sampling theorem and introduces artefacts when deconvolving signal from a detector, leading to irrelevant information being added to actual signal from the source. The MCS algorithm aims at a finite resolution for the deconvolved image, solving this inconsistency with the sampling theorem.

2.2.1 The sampling theorem

The sampling theorem states that *"A function that contains no frequencies higher than ν_0 is completely determined by giving its ordinates at a series of points spaced $(2\nu_0)^{-1}$ seconds apart"* (Shannon 1949). In other words, a continuous signal that has a Fourier

Figure 2.1: The pre-processing steps applied to one of the HST/NICMOS images of HE0435. *From left to right, top to bottom*: (1) original HST/NICMOS image, (2) after data quality map correction, (3) after sky subtraction and (4) after extraction. The images are displayed in units of electrons, all with the same intensity scale cuts. They display the same orientation as when captured by the instrument.

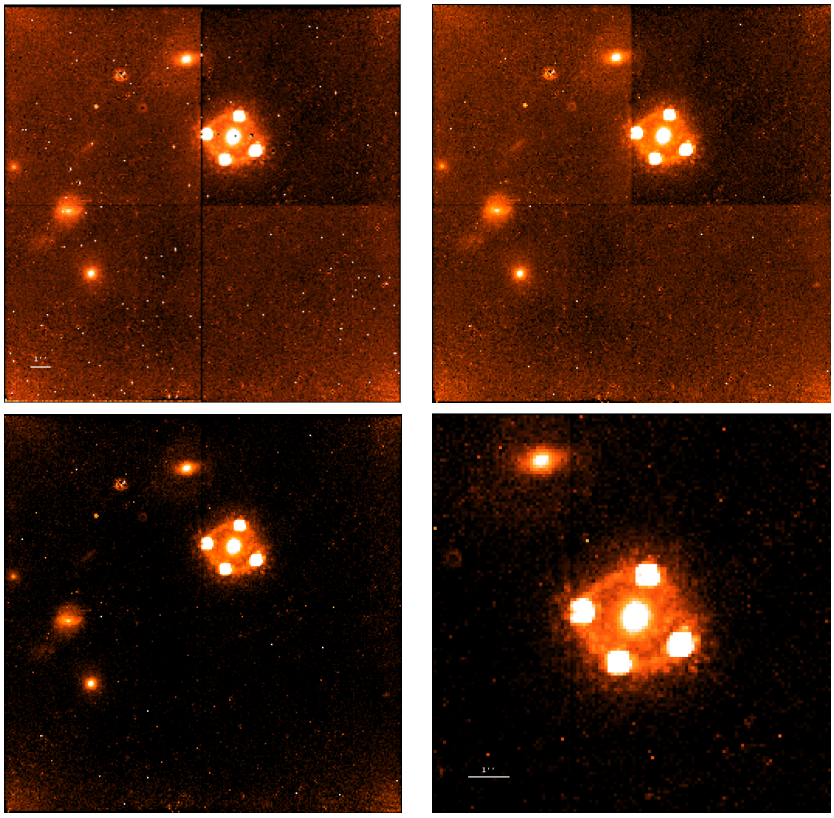

transform equal to zero for all frequencies higher than ν_0 can only be reconstructed if it is sampled with a frequency higher than or equal to $2\nu_0$. That minimum sampling frequency is called the cut-off frequency, ν_c. An alternative way to phrase it is that the sampling step needs to be smaller than $1/2\nu_0$. If the sampling frequency is too low, below ν_c, or the sampling step, too large, above $1/\nu_c$, the signal components with frequencies higher than ν_c are no longer distinguishable from those with frequencies lower than ν_c. That phenomenon is called aliasing, and it is illustrated on Figure 2.2. On that example, the sampled function is a sum of three sines terms, with three distinct frequencies. The function has been constructed so that its Fourier transform does not have frequencies above $\nu_0 = 5.0\ Hz$, so it cannot be sampled with a step higher than $\Delta_t = 1/(2\nu_0) = 0.1\ s$. When it is well sampled, the Fourier transform shows the three peaks corresponding to the three frequencies. When it is sampled with a too large step, the higher frequencies are not recovered in the Fourier transform and mixed with lower frequencies.

Figure 2.2: An illustration of aliasing. On the upper panels, a sum of three sines terms is well sampled and all the three frequencies distinctly appear in its Fourier transform. On the lower panels, it is under-sampled, and the higher frequencies are badly represented, or even missing.

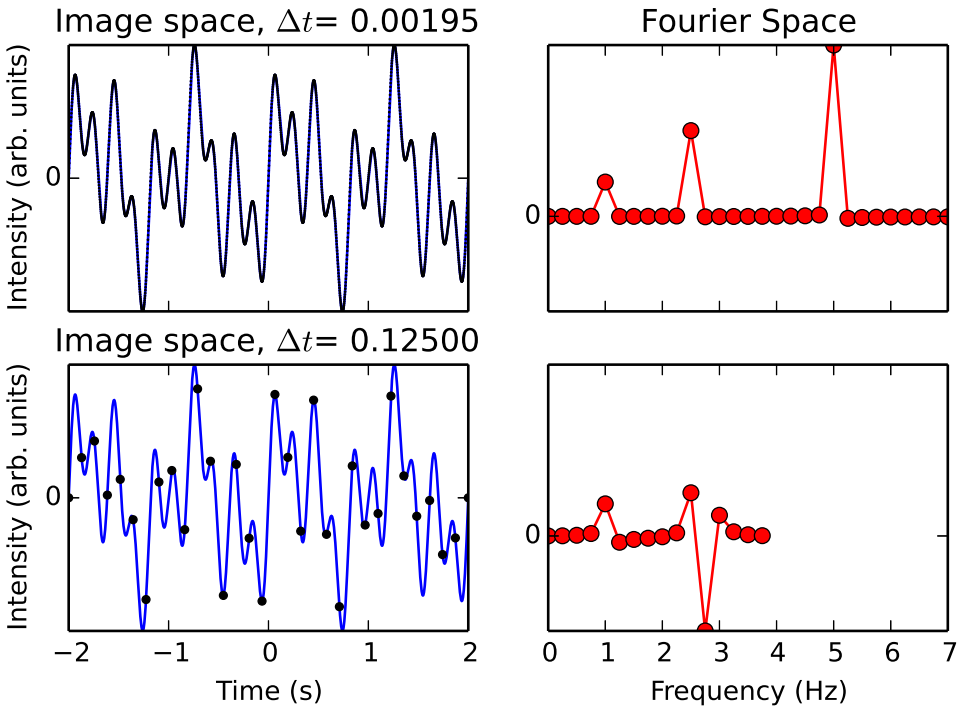

2.2.2 Some common deconvolution methods

Any signal, depending on an $\boldsymbol{x}$ coordinate on a detector is affected by an instrumental profile. An observation $D(\boldsymbol{x})$ is actually the original signal $F(\boldsymbol{x})$ affected by the PSF $T(\boldsymbol{x})$ and the noise $N(\boldsymbol{x})$:

$$D(\boldsymbol{x}) = [F(\boldsymbol{x}) * T(\boldsymbol{x})] + N(\boldsymbol{x}) \tag{2.1}$$

In the case of HST/NICMOS images, $T(\boldsymbol{x})$ would be the diffraction figure of a point source through the optics of the camera, and $N(\boldsymbol{x})$ would come from the statistics of photons counting and readout noise from the CCD. Deconvolving the signal consists in inverting Equation 2.1, which does not have a unique solution, especially in the presence of noise. There are nonetheless many different deconvolution techniques, and they all include some regularisation criterion in order to select one of the possible solutions of Equation 2.1.

A convolution in the image space becomes a simple product in the Fourier space. Thus, the Fourier transform of Equation 2.1 becomes:

$$\bar{D}(\boldsymbol{\nu}) = \left[\bar{F}(\boldsymbol{\nu}) \cdot \bar{T}(\boldsymbol{\nu})\right] + \bar{N}(\boldsymbol{\nu}) \tag{2.2}$$

where $\boldsymbol{\nu}$ is the coordinate in Fourier space, and where $\bar{D}(\boldsymbol{\nu})$, $\bar{F}(\boldsymbol{\nu})$, $\bar{T}(\boldsymbol{\nu})$ and $\bar{N}(\boldsymbol{\nu})$ are the respective Fourier transforms of $D(\boldsymbol{x})$, $F(\boldsymbol{x})$, $T(\boldsymbol{x})$ and $N(\boldsymbol{x})$. The inversion problem in the

Fourier space becomes:

$$\bar{F}(\boldsymbol{\nu}) = \frac{\bar{D}(\boldsymbol{\nu}) - \bar{N}(\boldsymbol{\nu})}{\bar{T}(\boldsymbol{\nu})} \tag{2.3}$$

provided that $\bar{T}(\boldsymbol{\nu})$ is different from zero. The problem is that $\bar{T}(\boldsymbol{\nu})$ tends towards zero at high frequencies, so the term $\bar{N}(\boldsymbol{\nu})/\bar{T}(\boldsymbol{\nu})$ diverges at high frequencies, which are precisely the relevant frequencies when trying to increase the image resolution. That problem can be reduced by applying a filter to the data that attenuates high frequencies. This is called the Wiener filter and it can be written in the Fourier space with the following form:

$$\bar{\Phi}(\boldsymbol{\nu}) = \frac{\left|\bar{B}(\boldsymbol{\nu})\right|^2}{\left|\bar{B}(\boldsymbol{\nu})\right|^2 + \left|\bar{N}(\boldsymbol{\nu})\right|^2} \tag{2.4}$$

with

$$\bar{B}(\boldsymbol{\nu}) = \bar{F}(\boldsymbol{\nu}) \cdot \bar{T}(\boldsymbol{\nu}) \ . \tag{2.5}$$

In the theoretical case of data without noise, the filter becomes equal to unity. Unfortunately, $\bar{B}(\boldsymbol{\nu})$ and $\bar{N}(\boldsymbol{\nu})$ can only be estimated by examining the power spectrum of $\bar{D}(\boldsymbol{\nu})$, trying to separate $\left|\bar{B}(\boldsymbol{\nu})\right|^2$ from $\left|\bar{N}(\boldsymbol{\nu})\right|^2$ and fitting models on each component (noise and actual data). This is all highly uncertain as the noise term often cannot be represented accurately by an analytical function.

One might try and pose the problem a little differently, by defining a merit function to minimise, in order to find the best-fitting deconvolved signal based on a least-square criterion. That means, the following expression, representing the deviation between the data and the convolved signal, needs to be minimised:

$$\left(\frac{D(\boldsymbol{x}) - [F(\boldsymbol{x}) * T(\boldsymbol{x})]}{\sigma(\boldsymbol{x})}\right)^2 \ . \tag{2.6}$$

One can recognise the form of a χ^2 expression. Since most data are sampled (images in pixels, time series in frequencies, ...) this function can be written as a discrete sum:

$$\chi^2 = \sum_{i=1}^{N} \left[\frac{d_i - \left[\sum_{j=1}^{N} t_{ij} f_j\right]}{\sigma_i}\right]^2 \tag{2.7}$$

with N the total number of samples, d_i the measurement in the i^{th} sample, σ_i an estimation of the uncertainty on that measurement, t_{ij} the intensity in the j^{th} sample of the PSF centred in the i^{th} sample and f_j the original signal in the j^{th} sample. In image processing in particular, f_j is the intensity in the j^{th} pixel, i.e. the number of photons hitting the j^{th} pixel, but it can also be seen as the probability that a photon is detected in the j^{th} pixel of the detector, under the assumption that the intensity distribution is normalised:

$$\sum_{i=1}^{N} f_i = 1 \ . \tag{2.8}$$

This formulation implies a positivity constraint on the f_i, as they represent a probability distribution for the intensities. To solve an inverse problem, a reasonable criterion is to

pick, amongst all the solutions, the one containing the minimum amount of information, since it would be the most inclusive one. The information content of a function can be approximated by its entropy H (Shannon 1949):

$$H = -\sum_{i=1}^{N} f_i \ln f_i \ . \tag{2.9}$$

To minimise the information content of the solution, its entropy should be maximised: that is called the maximum entropy deconvolution method. In practice, it is often implemented by minimising a function Φ depending on the f_i and a Lagrange parameter λ:

$$\Phi = \chi^2 - \lambda H \tag{2.10}$$

2.2.3 The MCS algorithm and its extensions

Both these methods, as well as most other deconvolution methods that are not mentioned in this work (e.g., the Richardson-Lucy algorithm, see Richardson (1972) and Lucy (1974)) suffer from a major weakness: they attempt to violate the sampling theorem. Indeed, let us assume an image with a correct sampling step, that is, not larger than $1/{\nu_c}^2$. The deconvolution process aims at increasing its resolution, that is, recovering higher frequencies of its Fourier transform. The cut-off frequency is increased, so the correct sampling step is decreased, and the image is no longer correctly sampled. Such deconvolution algorithms aim at an infinite resolution, as if the image was seen by a perfect instrument, that means, an infinitely small pixel size, which is certainly not feasible. In astronomical images, it is not uncommon to encounter point-like images of stars, i.e. sources with an angular diameter much smaller than the sampling interval, so their image can never be perfectly recovered. This contradiction leads to the ringing phenomenon, that is, ring-like artefacts appearing around point sources or sharp edges (see Figure 2.3).

A solution to that issue was proposed by Magain et al. (1998). The idea is to not deconvolve by the total PSF $T(\boldsymbol{x})$ but by a narrower PSF, so that the deconvolved image still has its own PSF because its resolution is not infinite. We have:

$$T(\boldsymbol{x}) = R(\boldsymbol{x}) * S(\boldsymbol{x}) \tag{2.11}$$

with $S(\boldsymbol{x})$ the narrower PSF and $R(\boldsymbol{x})$ the deconvolved frame PSF. In practice, $R(\boldsymbol{x})$ is chosen by the user, so that the deconvolved data is well sampled: the image of a point source on the deconvolved image has a full width at half maximum (FWHM) of at least two pixels. The size of those pixels is most often chosen to be half the linear pixel size of the original image, so that there is an improvement in the spatial resolution. For further detail, the reader is encouraged to turn to Magain et al. (1998).

The MCS algorithm has since then been extended to images of crowded fields, where no point-source (star) is sufficiently isolated to get an estimate of the total PSF $T(\boldsymbol{x})$

[2] In practice, in image processing, the cut-off frequency ν_c can be seen as $2\nu_0$ with ν_0 being the highest frequency at which it the Fourier transform of the data emerges from the noise (Magain et al. 1998)

Figure 2.3: An illustration of the ringing phenomenon in image processing. *Left*: reference image. *Right*: under-sampled image, where the ringing artefacts are visible. Credit: Umnov et al. (2015)

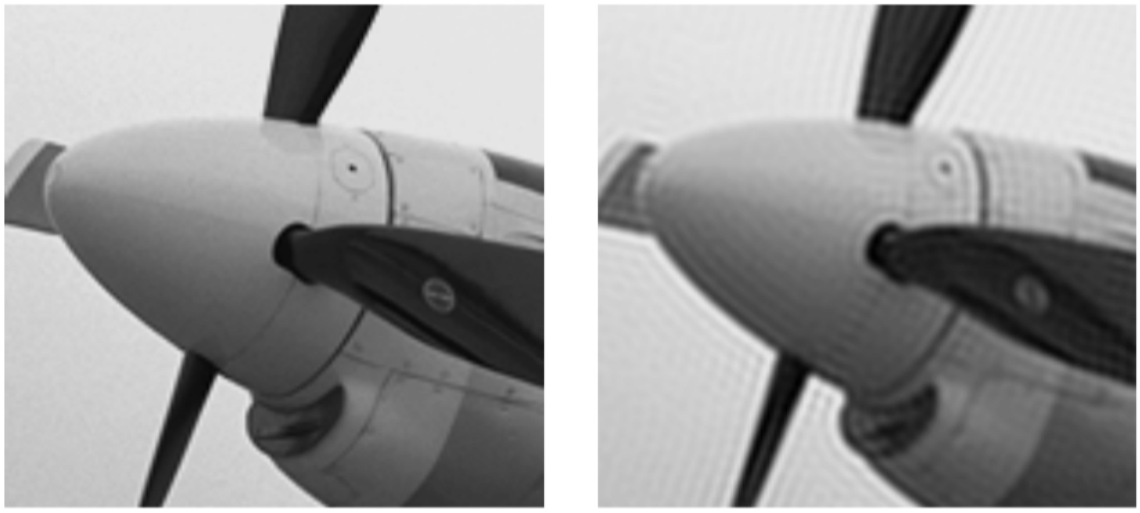

(Magain et al. 2007). In short, the proposed approach is to use the prior knowledge that the image is but the sum of point sources and a diffuse background:

$$F(\boldsymbol{x}) = H(\boldsymbol{x}) + \sum_{k=1}^{M} a_k R(\boldsymbol{x} - \boldsymbol{c_k}) \tag{2.12}$$

where $H(\boldsymbol{x})$ corresponds to the diffuse component and M is the number of point sources. The function to minimise has a similar form to Equation 2.10, combining a χ^2 term and this expression of $F(\boldsymbol{x})$. In the case of blended point sources, as in crowded fields, a bump in the wings of a PSF could be interpreted by this fit as a neighbouring point source, or as an integral part of the PSF, or even as a mixture of both. Such bumps in the PSF wings are most often not physical, so to make sure they are interpreted correctly, the MCS algorithm is applied iteratively: first, the PSF is approximated by an appropriate function, for example, a sum of Gaussians, that is fitted to the point sources based on a common χ^2 criterion. This yields an approximate value for the a_i and c_i, which are in fact the intensities and positions of the centres of the point sources. Second, a numerical component is added to that analytical estimate, first to its central regions, and then progressively to its outer regions. In doing so, the centres of the PSFs are securely obtained, so the bumpy artefacts in their wings do not appear.

Gravitational lensing images are complex astronomical images, as they are a mixture of point-like and diffuse sources. A further extension to the MCS method has been proposed in Chantry and Magain (2007). Their motivation was that as the NIC2 camera field of view is quite small, there are often no isolated point sources (stars) available to determine the PSF shape. They developed an iterative implementation of the MCS algorithm, called ISMCS, where a simultaneous deconvolution of all images of the same object (in the same filter) is performed, while each individual image has its own PSF. The first step is to find an approximate form for these PSFs, as in the crowded fields MCS method, for

example using the TinyTim software (Hook and Krist 1997, Krist and Hook 1997). Let us call it $S_0(\boldsymbol{x})$. It is also shown in Chantry and Magain (2007) that TinyTim PSFs are not accurate enough to obtain satisfactory deconvolution results on gravitational lensing HST/NICMOS images. The iteration steps are the following:

- First, an improved PSF $S_1(\boldsymbol{x})$ is determined (one for each individual image) by adding a numerical correction to $S_0(\boldsymbol{x})$. That component corresponds in part to a genuine improvement of the PSF shape, but also includes diffuse structures wrongly attributed to the PSF, for example due to the arcs passing "under" the multiple point-like images of the background quasar.

- Second, a simultaneous deconvolution is carried out with $S_1(\boldsymbol{x})$, so as to obtain a first approximation of the diffuse component $H(\boldsymbol{x})$, noted $H_1(\boldsymbol{x})$. However, some of the diffuse background was wrongly attributed to $S_1(\boldsymbol{x})$.

- By subtracting $H_1(\boldsymbol{x})$ to the original images, after re-convolving it, we obtain a new version of the original data frames, with less contamination by the diffuse components. This whole cycle constitutes one iteration. Let us denote these new images $D_1(\boldsymbol{x})$.

- The cycle resumes by determining a new PSF $S_2(\boldsymbol{x})$ on $D_1(\boldsymbol{x})$. Since they are less contaminated by the diffuse background, the new PSFs contain less non-point-like signal. The cycle is repeated until no significant improvement on the PSFs is observed, usually between 3 and 5 times.

Upon development, ISMCS has been successfully tested on the Cloverleaf gravitational lens, H1413+117 (Hazard et al. 1984, Magain et al. 1988, Chantry and Magain 2007). It is very well suited to gravitational lensing images, as it consists in iteratively subtracting a diffuse component, including any non-point-like object, such as galaxies and lensed arcs, until convergence to an image of the point sources. Moreover, it has the important advantage to not violate the sampling theorem. For both these reasons, we choose to use those PSFs as a starting point for this work.

3 Analysis of the light distributions of the lensing galaxies

This Chapter presents the study of the lensing galaxies light profiles. More specifically, the purpose is to recover the shape and intensity parameters for a de Vaucouleurs profile that best fits each lens. These parameters have to be accurately measured, as they will be used in the next phases of the work. On the one hand, they will be used to constrain a constant mass-to-light ratio profile for the total galaxy density when fitting the lensing observations, in Chapter 4. On the other hand, they will be used to compute the light content of the galaxies within their Einstein radii.

To investigate the shape of an early-type galaxy, a de Vaucouleurs law is most often fitted directly onto the data frames, taking the PSF into account. The most straightforward way to proceed would be to generate a synthetic de Vaucouleurs two-dimensional image, convolve it by the PSF and adjust its parameters until a goodness-of-fit criterion is met, e.g. a χ^2 minimisation. This classical fitting method has a major issue: since all the parameters are fitted simultaneously, it boils down to finding the minimum of a χ^2 surface in a space that has as many dimensions as there are parameters. However, even the most simple, circular de Vaucouleurs profile has at least 4 parameters: the galaxy centre coordinates, one scaling parameter in size and one in intensity. The process is thus prone to getting stuck into a local minimum. We adopt a different approach, that is, to determine each parameter separately, as independently from each other as possible.

Because of the lensed images, whether point-like or diffuse, measuring the morphology of lensing galaxies is noticeably more complex than for non-lensing galaxies. Discriminating background quasar signal from actual, relevant lens signal is crucial. Lensed images constitute a parasite signal that has to be subtracted from the actual galaxy signal. This process often leaves large uncertainties or even some remaining (diffuse) lensed components, limiting the region of interest to small, inner parts of the galaxy. This may cause classical fitting techniques such as GALFIT (Peng et al. 2002, 2010) to perform poorly on such images. To make sure this contaminating signal impacts our results as little as possible, we develop two multi-step subtraction processes for both these compo-

nents, detailed respectively in Section 3.1 and 3.2. The shape parameters measurement methods are presented in Section 3.3, tested in Section 3.4 and the error calculations are discussed in Section 3.5. Eventually, the results are discussed in Section 3.6. These results were first published in Biernaux et al. (2016) and Biernaux et al. (2017). Most of the material presented here can be found in these papers.

3.1 Subtraction of the sources

A subtraction of the point-like lensed images of the background quasar, a.k.a the sources, is conducted on the images[1]. This is performed following four steps. First, the original image is deconvolved using the MCS-determined PSF, as explained in Chapter 2. After deconvolution, a frame picturing only the four deconvolved lensed images is created (upper right panel of Figure 3.1). They are represented with a Gaussian profile of a two-pixel FWHM, the final PSF of the deconvolved image. This synthetic frame does not include any diffuse component, such as lensed arcs, a background sky or the lens galaxy. It is then convolved by the PSF. The resulting frame depicts the four lensed images as if they were observed through the HST/NICMOS instrument without light from the intervening galaxy and sky background (lower left panel of Figure 3.1). Eventually, this last image is subtracted from the original image. The final result is an image of the lensing galaxy and arcs without the point sources and at the HST/NICMOS resolution (lower right panel of Figure 3.1). The results for each system are shown in Figure 3.2.

[1]The input of the sources subtraction is the pre-processed images, that is, after correction for hot, saturated, poorly dark-corrected or flat-field-corrected pixels and for pixels affected by large readout errors, after sky subtraction and region of interest extraction.

Figure 3.1: Four-step point sources subtraction on one of the frames of HE0435 as an example. *From left to right, top to bottom*: (1) original image, (2) synthesised image of the four deconvolved sources, (3) synthesised image of the four re-convolved sources and (4) result of the subtraction of (3) from (1).

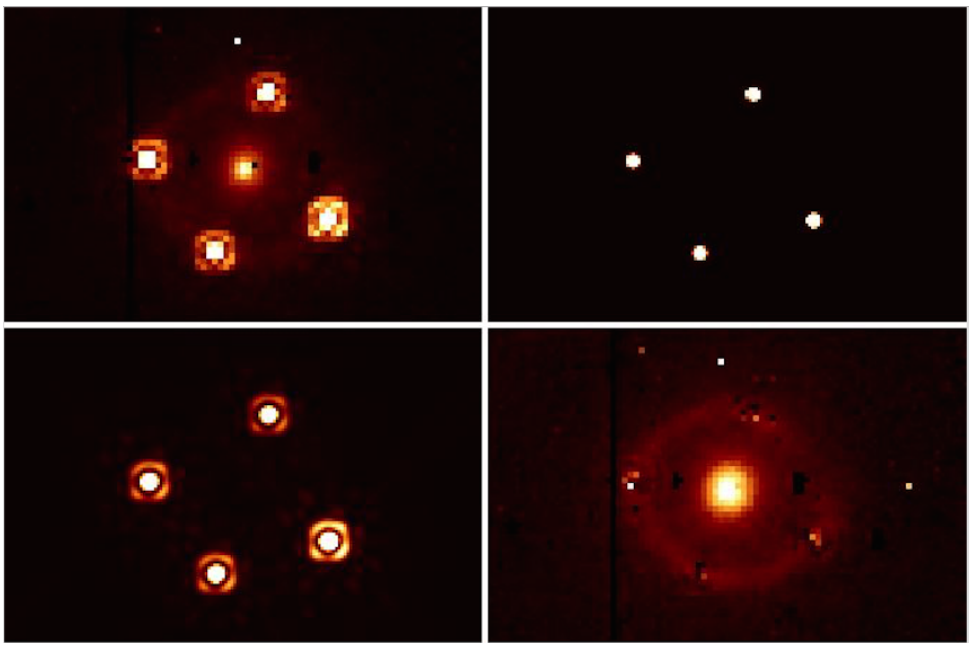

Figure 3.2: *From left to right for each row, top to bottom*: one of the HST images before subtraction, MCS-deconvolved image and resulting image after subtracting the deflected background source images at the HST resolution. Only one data frame is shown per system.

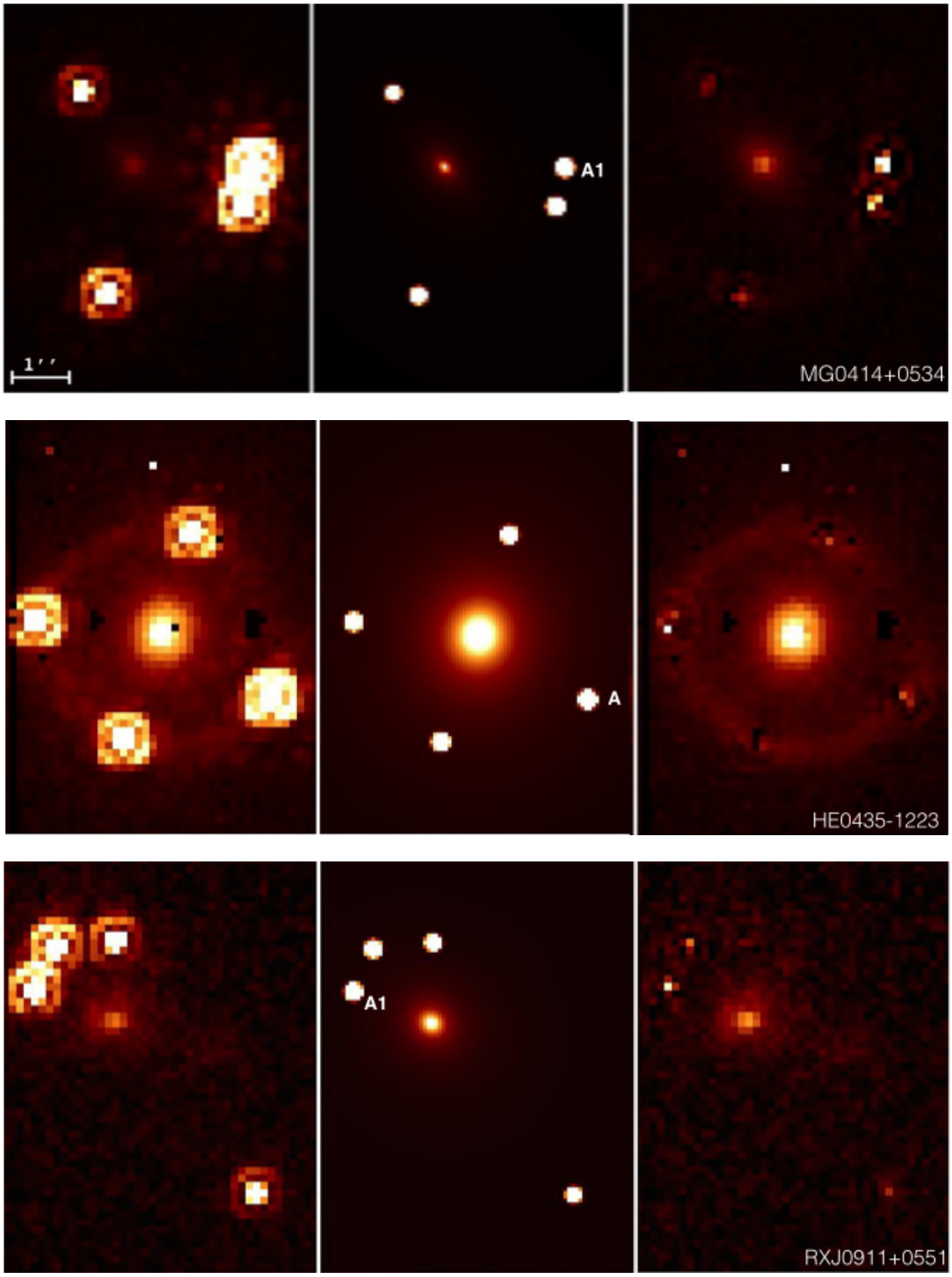

Figure 3.2: Continued.

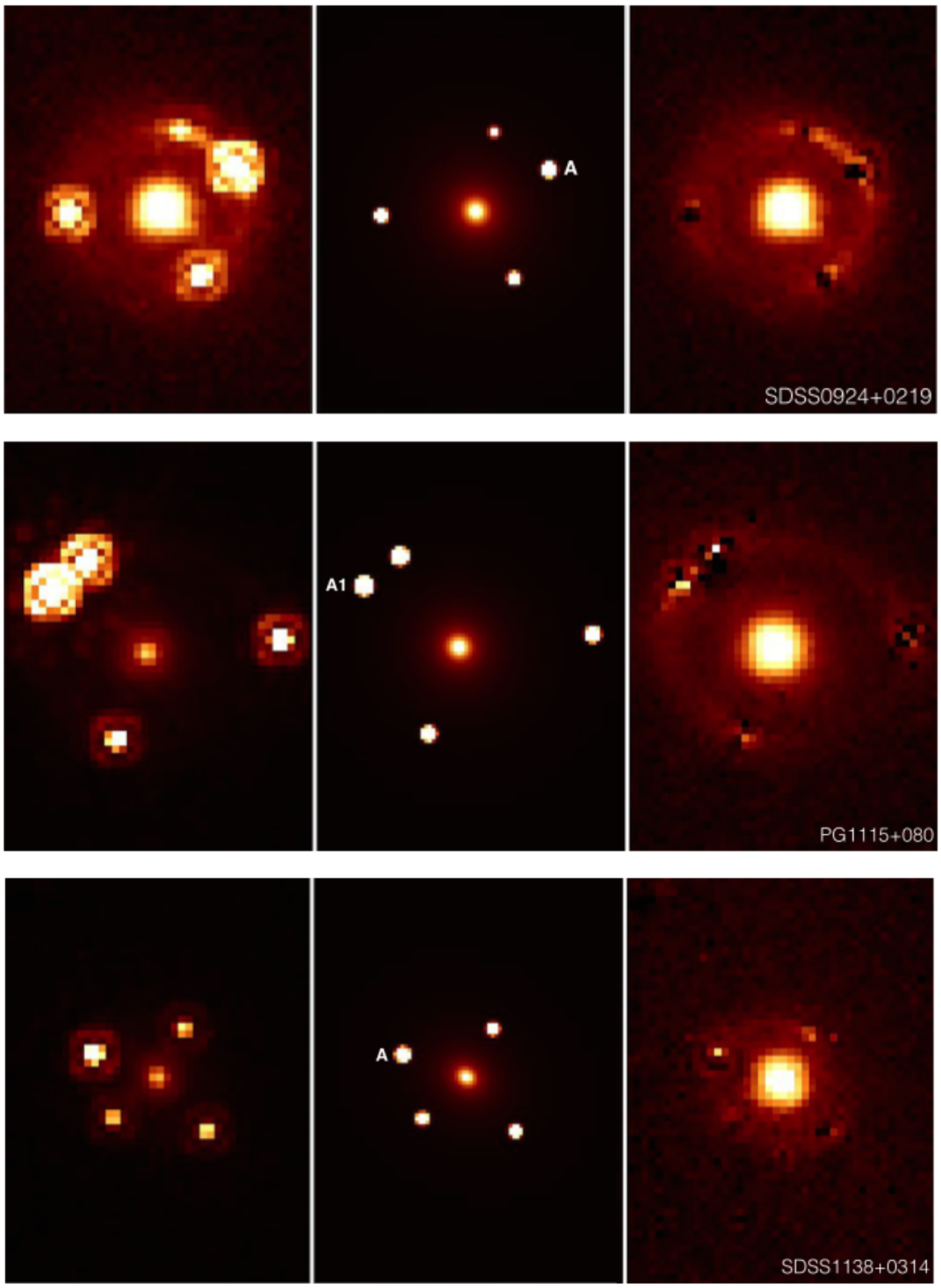

Figure 3.2: Continued.

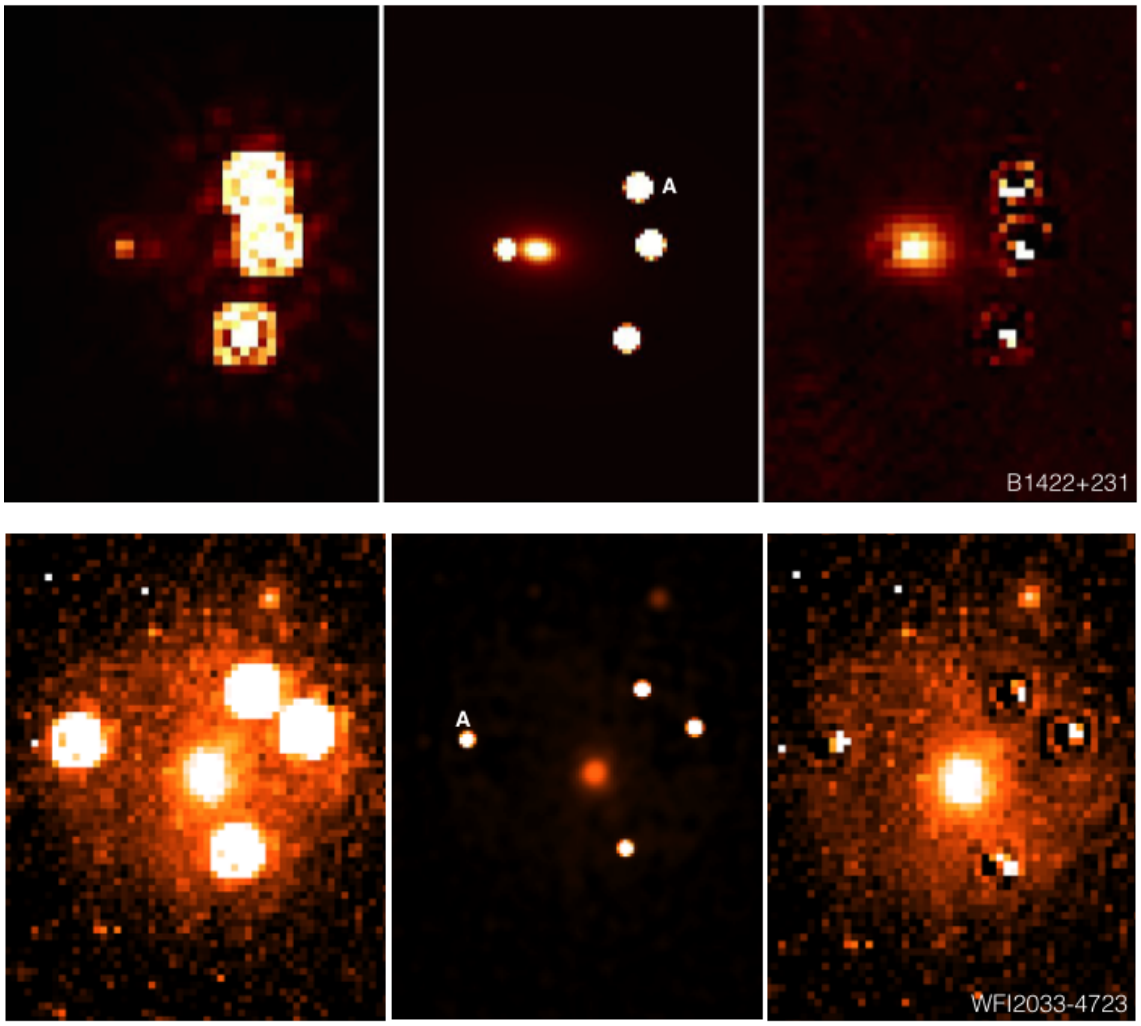

3.2 Subtraction of the arc

After the point sources subtraction, some diffuse lensed signal, in the form of arcs or a ring surrounding the lenses, may remain as a nuisance to the study of the galaxies light profile. The uncertainties in the outer regions of the galaxy restrain the study of the light profile to its inner regions. However, the value of $r_{\rm eff}$ is sensitive to the wings of the galaxy light profile, so they ought to be taken into account. We design a method to subtract that signal, in order to be able to encompass more of the outer parts of the galaxy in the fitting region.

Similarly to the sources subtraction, we aim at building an image of the arc and at directly subtracting it from the original data frame. We formulate only one simple hypothesis: because the arc consists of an image of the background galaxy, its light distribution displays, to the first order, the same properties of radial symmetry. In other words, along a galacto-centric radius, the arc should have a symmetric light distribution on either side of its maximum intensity.

We thus locate the maximum intensity of the arc with respect to the centre of our lens. We choose to work in a galacto-centric coordinate system. For a few azimuthal coordinates α (typically about 200, evenly distributed around the whole ring), we locate the pixel with the highest intensity in the arc. This yields an ensemble of ($r_{\rm max}$; α) data points, $r_{\rm max}$ being the distance between that pixel and the galactic centre. To refine the location of $r_{\rm max}$, we fit a constant plus a linear combination of sines up to the second order on these data points:

$$r_{\rm max}(\alpha) = r^0_{\rm max} + a_1 sin(\alpha) + a_2 sin(\alpha^2) \ , \tag{3.1}$$

where $r^0_{\rm max}$ is the average of $r_{\rm max}$. We actually conduct this operation separately on pieces of the arc between pairs of point sources. We exclude coordinates where PSF subtraction has been performed. We thus get a function $r_{\rm max}(\alpha)$ that locates the centre of symmetry of the arc light profile at any angle. We divide the arc image into sectors of various sizes along the angular coordinate, as shown in the top panel of Figure 3.3. Within each sector, we require $r_{\rm max}$ to not vary more than a few percents. However, should $r_{\rm max}(\alpha)$ be nearly constant, the maximum angular width of a sector is set to a value chosen by the user, typically around 20 degrees. The width of sectors is therefore a parameter of the arc subtraction process, but its influence on the arc subtraction is negligible compared to the other sources of systematics considered in our error calculation (Section 3.5).

The next step consists in collapsing the 2-D image of the arc into 1-D radial profiles. This is done sector by sector, by re-scaling the length of each row of pixels of the same angular coordinate, also called traces, so that they get the exact same $r_{\rm max}$. We thus get one value of $r_{\rm max}$ per sector. Then, the re-scaled traces are summed and averaged. The resulting radial profile of a sector (crosses in the bottom panel of Figure 3.3) corresponds to the sum of the galaxy and the arc radial profiles, the latter showing up as a "bump" around $r_{\rm max}$. We model the lensing galaxy profile $I(r)$ as a de Vaucouleurs law,

$$I(r) = I_0 \exp\left(-k\left(\frac{r}{r_{\rm eff}}\right)^{1/4}\right) \tag{3.2}$$

Figure 3.3: *Top*: sketch of the division of an image of HE0435 into sectors along the angular coordinates. *Bottom*: collapsed radial profile of a sector from HE0435. The crosses represent the measured intensity along the radial coordinate. The solid line shows the best-fitting de Vaucouleurs profile regarding the residuals maximum symmetry criterion.

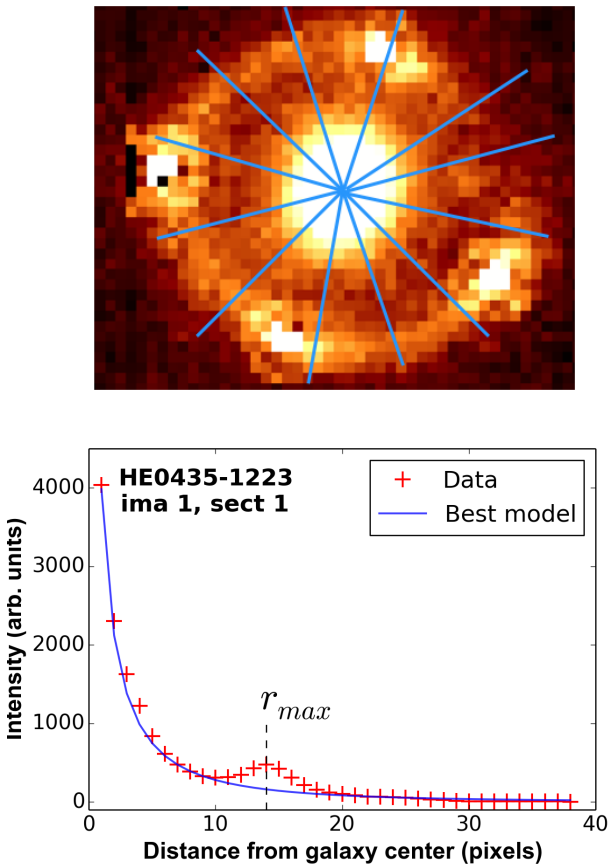

where I_0 is the central pixel intensity, r_{eff} the half-light radius and k the normalisation constant. This expression is valid for a centred light distribution, which is the case in our galacto-centric coordinate system. We use as a validity criterion that the de Vaucouleurs profile parameters maximise the symmetry of the residuals in a given region of interest around r_{max}. The solid curve on the bottom panel of Figure 3.3 gives an example of the galactic profile giving the most symmetric residuals wings around r_{max}. Those residuals act as data points for the arc radial light profile modelling. The size of the region of interest around r_{max} is also a parameter of the process: the larger the better, but not so large that we mistakenly consider parts of the image where there should be no arc.

Although it is valid to the first order, the hypothesis of symmetry around r_{max} may not always apply perfectly. Moreover, our symmetry criterion is more stable when restricted closer to the arc maximum, where the signal clearly dominates the noise. To extend the arc estimate to lower intensities, we fit a de Vaucouleurs law on each of the arc wings. We then compute a linear combination (per wing) of the fitted values and the data points, with weights so that the data points dominate around r_{max} and the fitted values dominate closer to the wings (see Figure 3.4). That way we obtain a numerical profile that is a close approximation of the true arc radial light distribution.

Figure 3.4: Two examples of numerical radial profile computation for the arc in one sector of HE0435 and one of SDSS1138. The stars represent the wings data points, the crosses, the best-fitting de Vaucouleurs models for each wing. The solid line shows the linear combination that acts as the arc numerical profile.

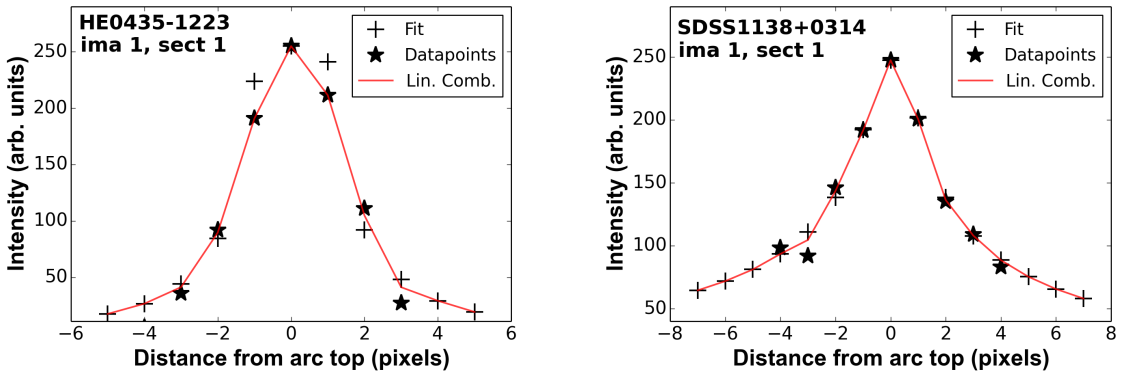

Finally, for each trace within the sector, we scale that numerical profile to better fit the radial intensities of each angular coordinate. We repeat the process on each sector, yielding for each one a numerical radial profile of the arc. We end up with as many arc profiles as traces, each corresponding to a single angular coordinate. We thus have a map of the arc intensity as a function of galacto-centric coordinates $I_{\rm arc}(r, \alpha)$. To reconstruct a 2-D image of the arc in cartesian coordinates, we compute the intensity of each pixel by interpolating on its direct neighbours on the $I_{\rm arc}(r, \alpha)$ map. We can eventually subtract that 2-D image from the data frame.

The arc subtraction is performed on each individual image of four out of eight galaxies in our sample. The results of this process are shown in Figure 3.5. Three of the remaining four systems do not show any visible diffuse lensed signal contaminating the galaxy light, there is no significant "bump" in their radial profile, so no arc subtraction is conducted on their images. For the last system, WFI2033, the arc should be present given the symmetry of the system. However, the expected "bump" in the outer wings of the lens profile does not appear clearly. We reckon it might be more diffuse, especially if the host galaxy of the background quasar is rather spread out. A lensing galaxy that has large outer wings in its light profile might hide the characteristic bump, particularly if the latter is flattened because it is the image of a diffuse galaxy. It is therefore challenging to detect and to subtract. It seems to be the case for this specific system. All subtraction attempts on WFI2033 given a variety of subdivisions in sectors and of functions $r_{\rm max}(\alpha)$ turned out to be fruitless. The probable arc peak $r_{\rm max}$ could not be properly determined. For that reason, no arc subtraction was conducted on that system, and this is to be kept in mind when discussing its results. Once all the lensed signal, both point-like and diffuse, has been subtracted from the data frames, we can proceed to the shape parameters measurements.

Figure 3.5: *Left*: HST/NICMOS data frames from our sample. *Right*: resulting images after the lensed signal subtraction, both sources and arcs. Only one data frame is shown per system and only for the systems on which the arc subtraction has been conducted.

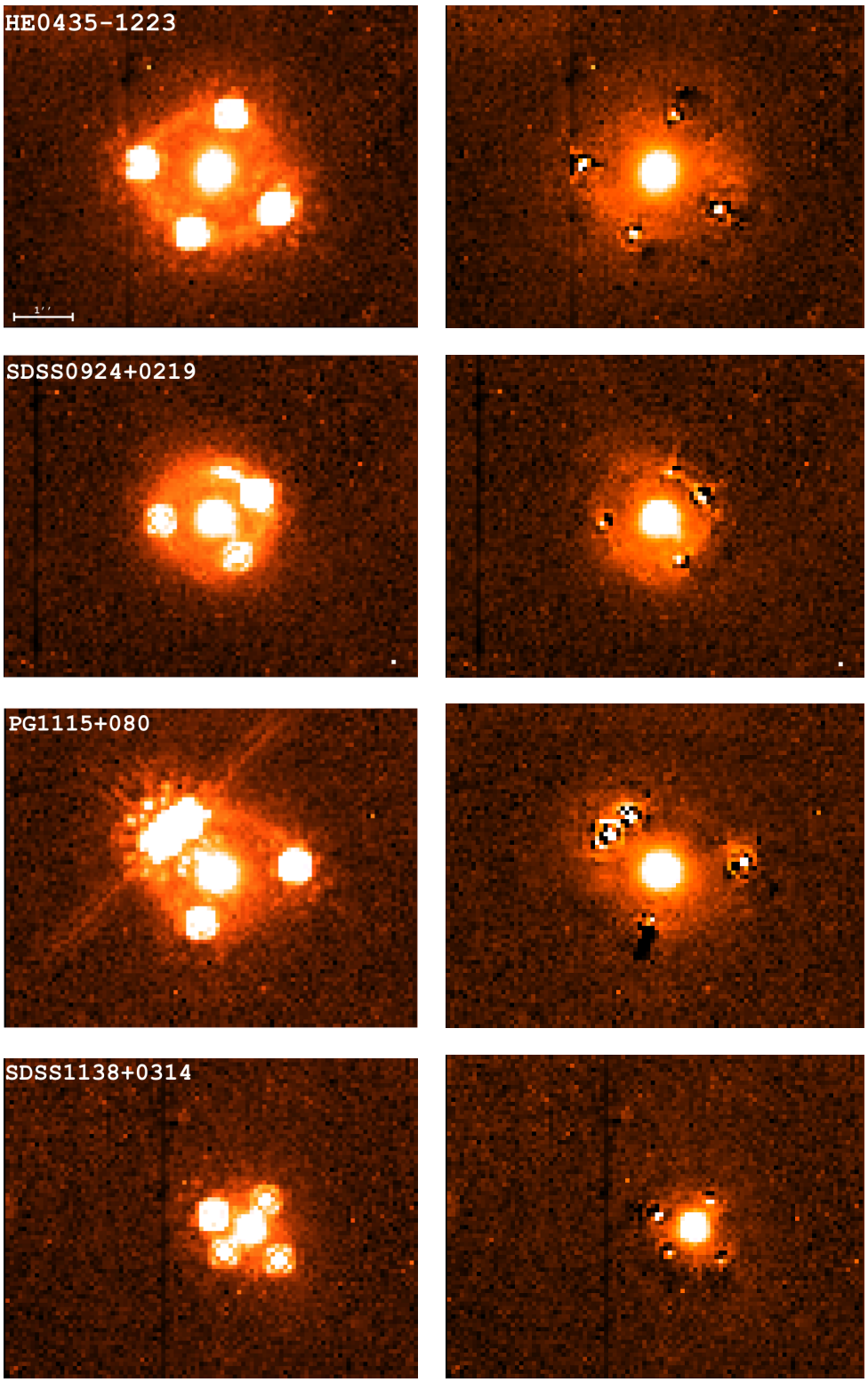

3.3 Measurement of the shape parameters

In this Section, we explain how we characterise the galaxy morphology and describe our measurement methods. We want to determine the parameters as independently from each other as possible. For each system, the measurements are individually conducted on all the data frames, then averaged over all frames. The methods described hereafter are applied directly to the PSF-convolved data frames. The results are eventually corrected from the convolution, as described in Section 3.3.3.

3.3.1 Measurement of the position angle

The position angle (PA) of a galaxy is defined as the orientation angle of its semi-major axis with respect to the horizontal axis. To measure it, we construct a circular mask divided into four quadrants. A mask is an image consisting of null pixels, except from a chosen area where the pixels have an arbitrary intensity of one. Pixels that are only partially included in the chosen area are given an intensity equal to the fraction of their surface included in the area. To do so, the mask is created with a sampling step eight times smaller than the data frames and then re-binned linearly to the NIC2 spatial resolution. The radius of the mask is chosen visually. It should be large enough to include as much galaxy signal as possible without reaching the parasite signal from the remaining arcs. It typically reaches the approximate size of the galaxy semi-minor axis.

The mask centre is aligned with the galaxy centre. This operation reveals two zones, A and B, on the elliptical luminosity distribution (Figure 3.6, top panel). The average intensities within zones A and B, $\bar{I}_{\mathrm{A}}$ and $\bar{I}_{\mathrm{B}}$, are respectively computed, as well as their difference, labelled Δ. The mask is then rotated around its centre and the operation is repeated for each rotation angle of the mask α. A plot of Δ versus α reveals the position angle, which is the value of α that maximises Δ (Figure 3.6, bottom panel). A 90° uncertainty remains at that point, but it is removed when the ellipticity is known. It should be pointed out that the measurement of the PA is carried out directly on the data frames prior to any rotation. The PA on the data frame is corrected a posteriori from the instrument orientation angle to obtain a PA on the sky.

The choice of the mask radius potentially changes the result of the measurement. To determine whether that is the case, the measurement is conducted with masks of various radii. Figure 3.7 shows the average PA measured on the four data frames of HE0435 with masks of radii from four to nine pixels. Their error bars correspond to the standard error on the mean, noted σ_{rand}. It can be seen that regardless of the mask radius, within a reasonable range excluding the rings and arcs, the measured PA is the same within its error bar. The radius of the mask thus has no significant influence on the measured PA. The PA measurement results for all systems are given in Table 3.1

Figure 3.6: *Top*: a sketch of the PA measurement method. The grey area depicts an elliptical luminosity distribution. The thick red circle and lines picture four quadrant-shaped masks defining two zones, labelled A and B. The mask rotates around its centre. For each mask orientation angle α, the average intensities $\bar{I}_A$ and $\bar{I}_B$ are computed within each couple of quadrants, as well as their difference Δ. *Bottom*: a plot of Δ versus α for one of the data frames of HE0435. The value of α for which Δ reaches a maximum indicates the PA of the galaxy. The second maximum is redundant, 180° further.

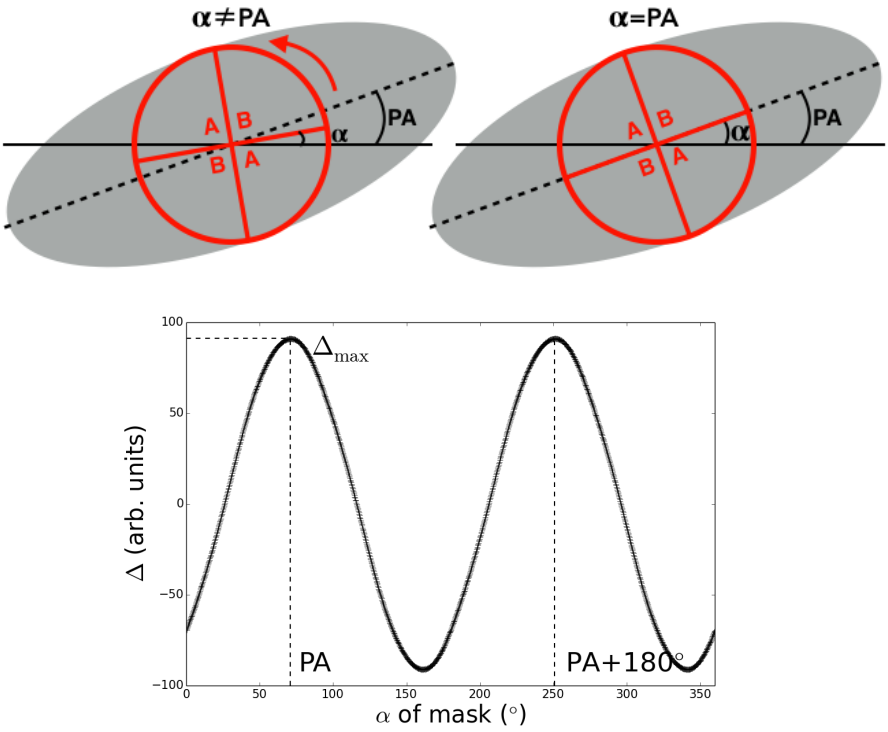

Figure 3.7: Effect of the mask radius on the measurements of PA on HE0435 as an example. The horizontal axis shows the radius of the mask r_{mask} in pixels and the vertical axis, the measured PA. Error bars correspond to the standard error on the mean. The blue line is a linear regression on PA(r_{mask}), showing a slope that is not significantly different from zero, therefore the PA measurement does not depend on the mask radius.

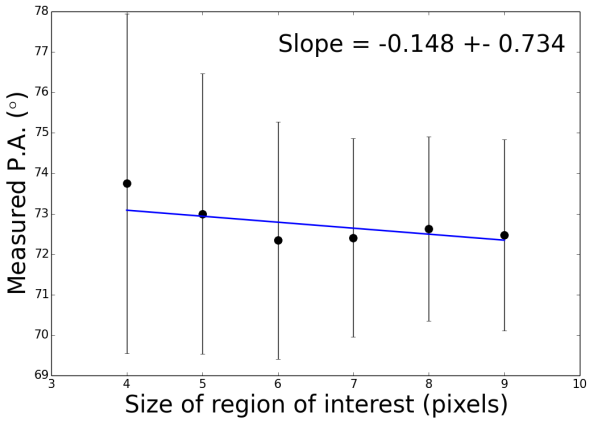

3.3.2 Measurement of the ellipticity

We also use a mask to measure the galaxy ellipticity. It is defined as the following expression, depending on the ratio between the semi-major and semi-minor axes a and b:

$$\varepsilon = 1 - \frac{b}{a} \tag{3.3}$$

Several ring-shaped masks of increasing ellipticity ε_i are successively applied to the frame. The masks are created in the same way as in Section 3.3.1, except that they are elliptical ring-shaped instead of circular and aligned according the PA measured as described above. The isolated ring-shaped parts of the galaxy are divided into four quadrants, as illustrated in Figure 3.8 (top panel) by the labels A and B. The average intensities within areas A and B, $\bar{I}_\mathrm{A}$ and $\bar{I}_\mathrm{B}$, are computed at each step, as well as their difference Δ. When the mask has the same ellipticity as the galaxy, it shapes out an isophote. Thus, at that very step, $\Delta = 0$. Plotting Δ versus the ellipticity ε_i of the mask and determining the intersection between this curve and $\Delta = 0$ gives the ellipticity of the galaxy (bottom panel of Figure 3.8.) Once again, the ellipticity measurement does not depend on the semi-minor axis of the mask, as shown in Figure 3.9. As a test, the measurement is conducted on the four frames of HE0435 with masks of increasing semi-minor axes, from four to eight pixels, and the result remains constant within the standard error on the mean. However, the last data point, corresponding to an inner semi-minor axis of eight pixels, has a dramatic error bar and an odd value for ε. This is because the outer semi-major axis of the ring-shaped masks reaches about 12 pixels and encloses some signal from the leftover artefacts after sources and arc subtraction. Therefore, the masks should be chosen not to include such signal.

The elliptical ring-shaped masks are characterised by some thickness. Usually, the difference between the inner and outer semi-minor axes is three pixels. The ellipticity and PA of each isophote may differ, because twisting can be observed in elliptical luminosity profiles (Liller 1960, 1966). The isophotes twisting within the thickness of the ring cannot be detected on the frame, particularly because of pixelation. Therefore, by considering a rather thick ring, we can safely assume that the ellipticity of the profile is averaged over the few isophotes included in the mask. The ellipticity measurement results for all systems are given in Table 3.1

Figure 3.8: *Top*: a sketch of the ellipticity measurement method. The grey area sketches the luminosity distribution of the galaxy. The thick red rings and lines represent the ring-shaped masks split into quadrants, defining two zones, labelled A and B. The ellipticity of the mask increases, from $\varepsilon_i = 0$ to $\varepsilon_i = \varepsilon$, with ε the galaxy ellipticity. For each ε_i, the average intensities in zones A and B, $\overline{I}_A$ and $\overline{I}_B$, are computed, as well as their difference Δ. *Bottom*: a plot of Δ versus ε_i for one of the data frames of HE0435 as an example. The value of ε_i for which $\Delta = 0$ indicates the ellipticity of the galaxy.

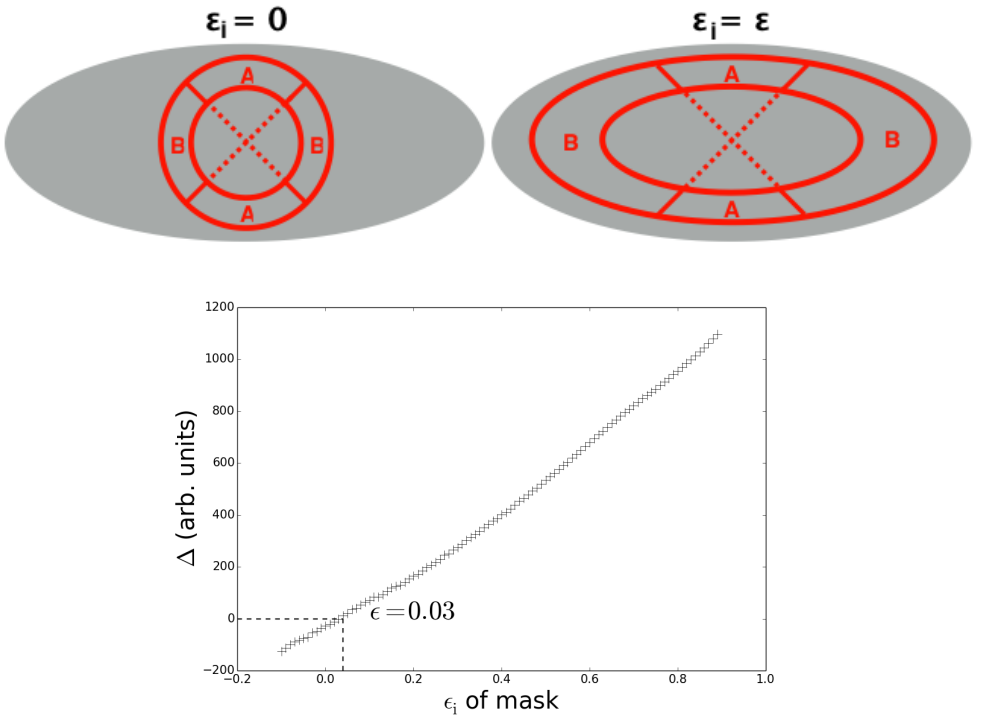

Figure 3.9: Effect of the mask radius on the measurements of ε on HE0435 as an example. The horizontal axis shows the semi-minor axis of the mask b_{mask} in pixels, the vertical axis, the measured ε. Error bars correspond to the standard error on the mean. The blue line is a linear regression on $\varepsilon(b_{\text{mask}})$, showing a slope that is not significantly different from zero, therefore the ε measurement does not depend on the mask radius.

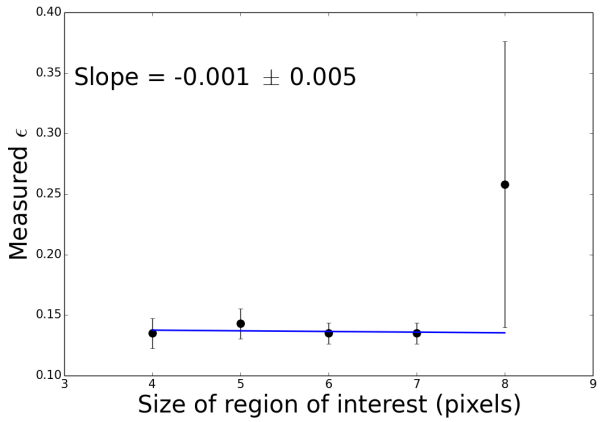

3.3.3 Measurement of the half-light radius

The last structural parameter to be measured is the half-light radius of the galaxy. This parameter is especially important since it gives an estimate of the size of the galaxy luminous component. For a hypothetically circular galaxy, the luminosity profile is usually represented by the Sérsic profile (Sérsic 1963, Prugniel and Simien 1997):

$$I = I_{\text{eff}} \exp\left(-k\left(\left(\frac{r}{r_{\text{eff}}}\right)^{1/n} - 1\right)\right) \tag{3.4}$$

where I_{eff} is the surface brightness at the half-light radius. For an elliptical luminosity profile, $r = \sqrt{ab}$, where a and b are the semi-major and semi-minor axes of the isophotes. The constant k is a normalisation constant that can be expressed as a function of the exponent n (Prugniel and Simien 1997):

$$k = 2n - \frac{1}{3} + \frac{0.009876}{n} \,. \tag{3.5}$$

In this work, we use the specific case of $n = 4$, i.e. the de Vaucouleurs law. This law empirically proved to be a good representation of the luminosity profile of elliptical galaxies. By calculating the natural logarithm of Equation 3.4 with $n = 4$ we get

$$\ln I = \ln I_{\text{eff}} - k\left(\frac{r}{r_{\text{eff}}}\right)^{1/4} - k \tag{3.6}$$

which is in fact a linear relationship between $\ln I$ and the radial coordinate $r^{1/4}$ where the slope depends on the half-light radius. The half-light radius measurement procedure is based on this linear relationship between $\ln I$ and $r^{1/4}$. We therefore call it the linear regression method, hereafter LRM. It makes it possible not only to determine the half-light radius, but also to correct the shape parameters measurement from the PSF.

Since the ellipticity and PA of the (convolved) galaxy are already known (see Sections 3.3.1 and 3.3.2), we can apply elliptical ring-shaped masks to the frame with the same ellipticity and PA as the galaxy. Those shape out one-pixel wide isophotes of increasing radii. The intensity I of each isophote is measured and $\ln I$ is plotted versus the radial coordinate $r^{1/4}$, where $r = \sqrt{ab}$. The central couple of pixels is not considered when constructing this plot. Indeed, their intensities are very sensitive to the position of the centre with respect to the pixel grid, and actual galaxy profiles often differ from the de Vaucouleurs law at the very centre (Kormendy et al. 2009). Moreover, the centre is also the region where the convolution by the PSF most strongly affects the shape of the galaxy.

A synthetic galaxy model is produced for each lens galaxy, i.e. a two-dimensional image of an elliptical de Vaucouleurs profile. For higher accuracy, the model is computed on a 2*2 finer pixel grid and then later resampled to the original pixel grid. This model is convolved by the PSF, using a classical FFT algorithm[2]. Its ellipticity and PA are measured the same way as described above. The input synthetic values of PA and ellipticity

[2] see Chapter 12.4 of Press et al. (1992)

are tuned until their convolved values match those measured on the HST/NICMOS data.

Afterwards, we produce its ($\ln I$; $r^{1/4}$) plot (Figure 3.11). The input synthetic half-light radius is then tuned until it minimises the χ^2 between the HST/NICMOS data points and the convolved model radial profile in the ($\ln I$; $r^{1/4}$) space. Because we do not have any information about I_0 at that point, for each try, the convolved model logarithmic profile is translated by a constant that is an average of the difference between matching data points from the convolved model and the data frame radial profiles. The whole shape parameters fine-tuning is repeated iteratively until convergence and eventually, the input parameters of the synthetic model yield the deconvolved values of the shape parameters of the lens. A diagram of this loop is given in Figure 3.10 for visualisation.

Figure 3.10: A visualisation of the $r_{\rm eff}$ measurement method that includes the correction for the PSF. PA_0, ε_0 and $r_{\rm eff,0}$ are the input parameters of the initial synthetic de Vaucouleurs model. The latter is convolved by the PSF, which changes its parameters into PA_0^c, ε_0^c and affects its $\ln I$ vs $r^{1/4}$ profile. PA_0, ε_0 and $r_{\rm eff,0}$ are tuned until PA_0^c and ε_0^c are equal to the parameters of the (PSF-affected) HST/NICMOS data frame, PA and ε, and until the χ^2 is minimal between the $\ln I$ vs $r^{1/4}$ profiles of the model and the data. When that condition is met, the input parameters of the synthetic de Vaucouleurs are the HST/NICMOS values corrected from the PSF.

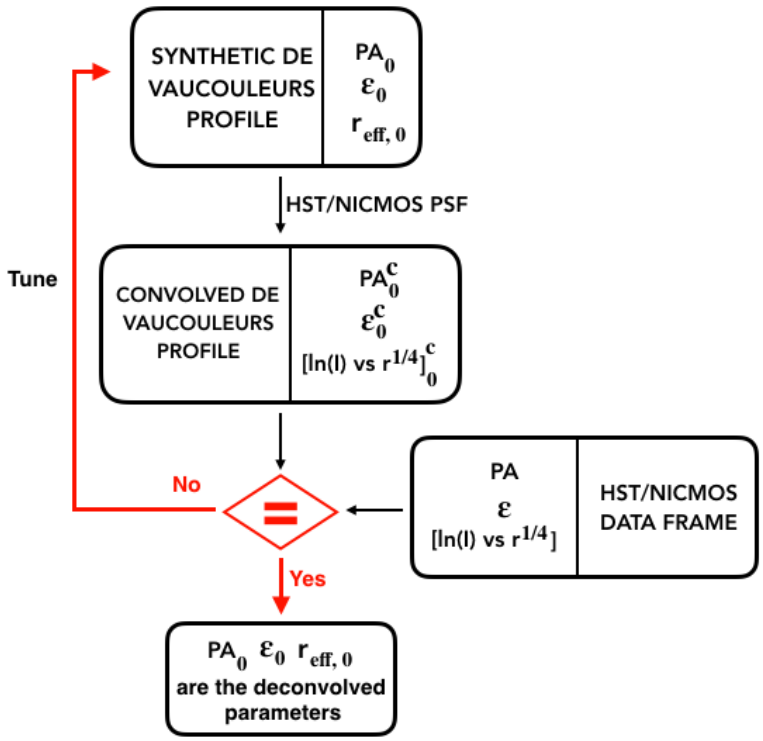

This iterative step is a major difference with previous MCS-based works. Indeed, in Chantry et al. (2010) and Sluse et al. (2012), a two-dimensional model was fitted on the data frames, whereas our method focuses on radial profiles for the measurement of $r_{\rm eff}$. Thanks to the subtraction of the arc, more data points can be taken into account for the $r_{\rm eff}$ measurement; we can consider a portion of the galaxy with a radius that is one or two pixels larger than before any arc subtraction, corresponding to an average increase of 37%

Figure 3.11: Plots of ($\ln I$; $r^{1/4}$) as used in the measurement of the galaxies half-light radii. The radial coordinate r is in pixels. The error bars on $\ln I$ are the standard errors on the mean within each isophote. The solid line shows a linear regression for visualisation, it is not used in the measurement itself. Only one data frame is shown for each system.

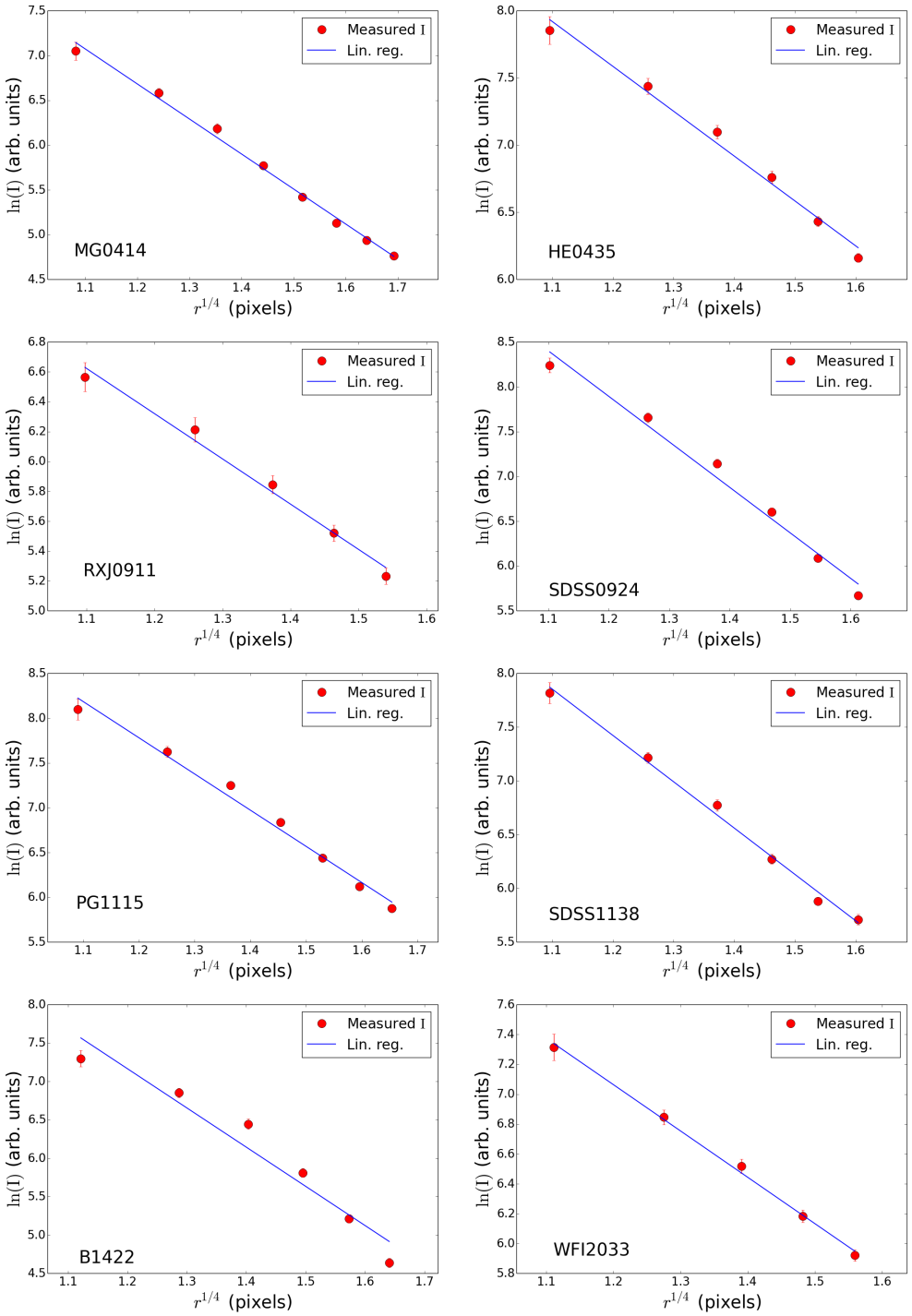

of the galaxy surface considered. Although this may seem like a small increase, it is of considerable importance because the $r_{\rm eff}$ value is highly sensitive to the wings of the de Vaucouleurs profile. Moreover, because the convolution mostly affects the central regions of the galaxy, we choose to ignore the first couple of pixels from the centre out, hence the interest in reaching as far out from the galactic centre as possible. The $r_{\rm eff}$ measurement results for all systems are given in Table 3.1

3.4 Testing the linear regression method

In this Section, we test the robustness of the LRM. We compare it to the commonly used galaxy profile-fitting code GALFIT (Peng et al. 2002, 2010). The GALFIT algorithm consists in fitting a convolved model directly on a data frame and in optimising it by minimising a χ^2 value. This methodology is similar to the one used by many galaxy profile-fitting softwares, such as IMFITFITS (McLeod et al. 1998), setting this comparison in an interesting context. Schechter et al. (2014) have mentioned the discrepancies between MCS-based image processing and other methods, regarding the measurement of the half-light radius of lensing galaxies. MCS-based studies seem to get higher half-light radii than the TinyTim-based studies. The following test takes place in an investigation of the discrepancies noted by Schechter et al. (2014).

We perform the half-light radius measurement with both the LRM and GALFIT on sets of simulations. We examine the impact of three factors on the $r_{\rm eff}$ results: the size of the fitting region, the signal-to-noise ratio (S/N) and the size of the galaxy compared to the PSF. We also investigate how the use of an incorrect Sérsic index affects the shape measurements. Indeed, the widely used de Vaucouleurs profile is but a specific case of the Sérsic profile, and the effect of using a de Vaucouleurs law on a physical profile that might have a different exponent is of great interest, since there could be a scatter in the observed Sérsic indices (Kormendy et al. 2009, Bolton et al. 2012). Mock galaxies are built using a circularly symmetric Sérsic luminosity profile. They are convolved using a typical NIC2 PSF of approximately two-pixels FWHM. Some noise is added, considering both photon noise and a Gaussian background sky noise. The peak S/N is calculated considering the maximum signal at the peak of the convolved Sérsic profile.

Measuring the half-light radius with GALFIT means that only the parameters $r_{\rm eff}$ and the central brightness of the galaxy are free. The coordinates of the centre are constrained in a small domain around the actual values[3]. We use the same PSF for GALFIT and for the LRM. GALFIT requires a 1σ error image as input: we use an image of the total noise, thus taking both photon noise and background noise into account. Even though GALFIT is built to optimise the value of n, we choose to set it to $n = 4$, because we are investigating the discrepancies between the de Vaucouleurs models.

[3]See user manual at *http://users.obs.carnegiescience.edu/peng/work/galfit/galfit.html*

3.4.1 Effect of n

First, we build a mock galaxy using a Sérsic profile with an index $n = 3$. We choose a fixed value for its half-right radius of ten pixels, which is a typical value for the systems in our sample (see Section 3.6). We label it $r_{\rm eff,true}$ as opposed to the notation $r_{\rm eff}$ assigned to the measured values. We choose a S/N of 800, which is unrealistically high. We only modify the region over which the fit is carried out, from a radius of 1 $r_{\rm eff,true}$ to 5 $r_{\rm eff,true}$. To test the impact of the choice of n on the measurement of $r_{\rm eff}$, we perform the fit using the purposely incorrect value of $n = 4$. For each set of values of $\{S/N$, size of fitting region$\}$, five iterations of the random noise generation are conducted, in order to calculate a dispersion error bar $\sigma_{\rm rand}$ on $r_{\rm eff}$.

The top panel of Figure 3.12 shows the resulting $r_{\rm eff}$ of both methods, for an unrealistically high S/N. One can see that when using the incorrect $n = 4$, GALFIT overestimates the half-light radius by a factor that depends on the size of the fitting region. For inner regions of the galaxy, the overestimation reaches 1.7, and it only goes down to 1.4, even when probing out to 5 $r_{\rm eff,true}$. The 1.4 overestimation factor seems to be a convergence limit for GALFIT. In contrast, the LRM is able to find the correct $r_{\rm eff}$ when probing at least 4 $r_{\rm eff,true}$. For the inner regions, the overestimation factor in the LRM reaches roughly 1.45, less than the 1.7 factor that GALFIT displays. This simulation shows how robustly the LRM behaves regarding the Sérsic index. It also points out how using the de Vaucouleurs law can have consequences on the measurement of $r_{\rm eff}$ on profiles that have different Sérsic indices. Those consequences turn out to be even more important for gravitational lensing images, since the fitting is often restricted to inner parts of the galaxy, where the overestimation factor is the highest.

3.4.2 Effect of the S/N

We then perform the fit using the correct $n = 3$ Sérsic profile. Let us only consider the $n = 3$ measurements in Figure 3.12. By comparing the top, middle and bottom panels, one can see that when the S/N decreases, the GALFIT bias increases. The limit value of this overestimation when probing outer regions ranges from 3% to 7% when the S/N varies from 800 to 50. The intermediate value of 170 is the typical S/N of the frames of our sample. At this ratio, the GALFIT overestimate reaches 6% for a 5-$r_{\rm eff,true}$ fitting region and 9% for a 1-$r_{\rm eff,true}$ fitting region. It appears that even in the "best conditions", i.e. with the highest S/N and the correct n and when probing a large fitting region, GALFIT still slightly overestimates $r_{\rm eff}$ by about 3%.

That is not the case for the linear regression method. A change in the S/N within the explored range did not cause any change in the measured $r_{\rm eff}$ larger than 2%, regardless of the size of the fitting region. For a S/N similar to the one of our NIC2 data, the largest error on $r_{\rm eff}$ in the LRM reaches only 0.3%. The fact that GALFIT converges to a too high value of $r_{\rm eff}$ may come from the processing of the PSF. Indeed, when the measurement is performed directly on the deconvolved mock galaxy, it reaches the right value. GALFIT deconvolves a portion of the input frame that is chosen by the user. It is suggested (see

user manual) to choose a convolution box that is as large as possible, although the larger the box, the more time-consuming the process. The plots in Figure 3.12 were obtained using the largest possible convolution box, that is, the total size of the frame. When the size of the convolution box is equal to that of the fitting box, the overestimate of the half-light radius (with the correct n) reaches 10%.

Figure 3.12: Results of the measurement of $r_{\mathrm{eff}}/r_{\mathrm{eff,true}}$ by GALFIT and the LRM, as a function of the size of the fitting area, for various S/Ns. The simulated galaxy is a Sérsic profile with $n = 3$ and a half-light radius of 10 pixels. The left-hand panels show the result from GALFIT, the right-hand panel, from the LRM. The top panels correspond to S/N = 800, the middle panels, S/N = 170, the bottom panels, S/N = 50. The vertical axis is the measured $r_{\mathrm{eff}}/r_{\mathrm{eff,true}}$. The horizontal line represents $r_{\mathrm{eff}}/r_{\mathrm{eff,true}} = 1$. The horizontal axis shows the size of the fitting region in units of $r_{\mathrm{eff,true}}$, ranging from 1 $r_{\mathrm{eff,true}}$ to 5 $r_{\mathrm{eff,true}}$. The black circles are the results for an $n = 4$ model, the blue diamonds, for the correct value $n = 3$. Because they are sometimes smaller than the symbol size, the σ_{rand} error bars do not always appear.

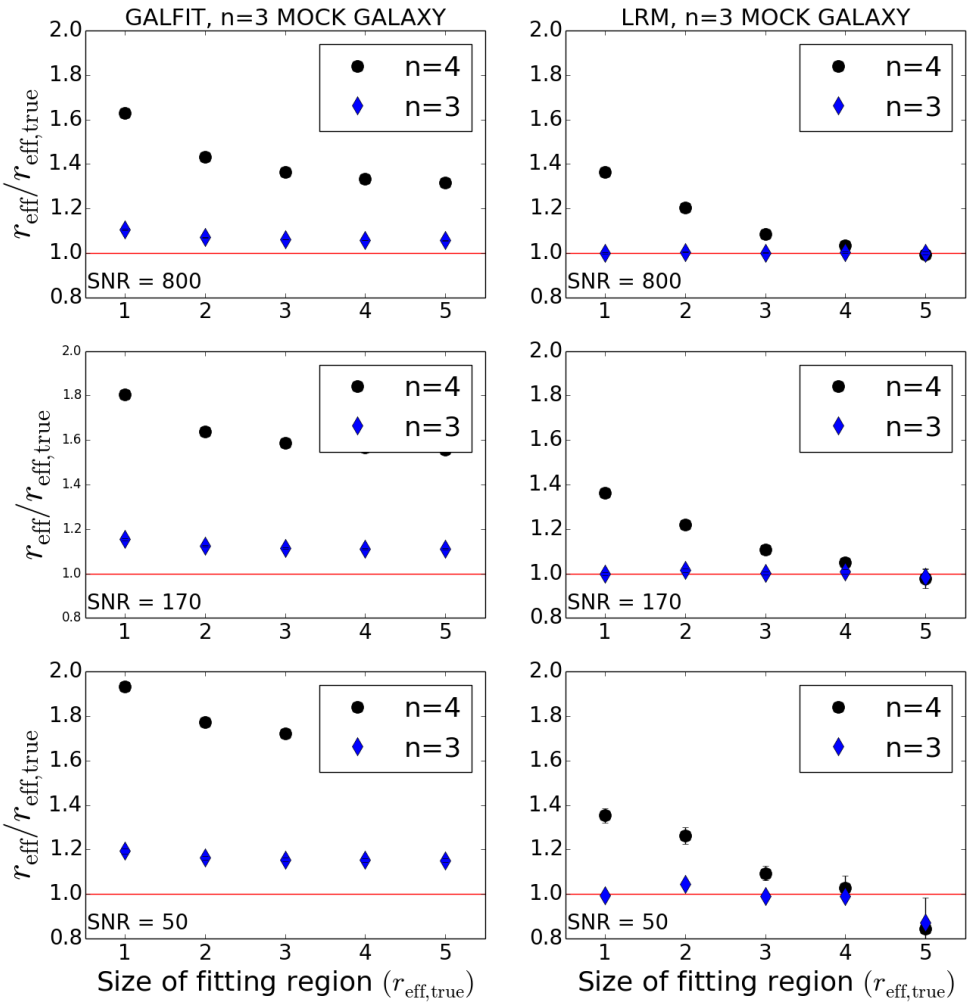

3.4.3 Effect of the size of the galaxy

We now set S/N = 800 and $n = 3$ but only modify the half-light radius $r_{\text{eff,true}}$. The purpose of this set of tests is to examine how both methods behave for galaxies that are not much larger than the width of the PSF.

First, we probe a 1-$r_{\text{eff,true}}$ region. Figure 3.13 shows that the smaller the galaxy, the higher the GALFIT overestimate. The largest bias is achieved for the smallest galaxy and reaches about 18%. However, when probing a large enough region of 3 $r_{\text{eff,true}}$, the size of the galaxy seems to matter less for GALFIT, because the overestimation factor varies between 1.08 and 1.06. In contrast, the LRM performs remarkably well, regardless of the size of the galaxy and of the fitting region. This demonstrates that the LRM is particularly well suited to studying lensing galaxies, which are in general relatively compact and where lensed images close to the galaxies restrain their analysis to small inner regions. Furthermore, it is shown here that it is capable of handling galaxies that are not much larger than the PSF.

Figure 3.13: Results of the measurement of $r_{\text{eff}}/r_{\text{eff,true}}$ by GALFIT and the LRM as a function of $r_{\text{eff,true}}$, in pixels. The S/N is set to 800. The black circles correspond to a fitting region of $1r_{\text{eff,true}}$ in size and the blue diamonds, of $3r_{\text{eff,true}}$. Because they are sometimes smaller than the symbol size, the σ_{rand} error bars do not always appear.

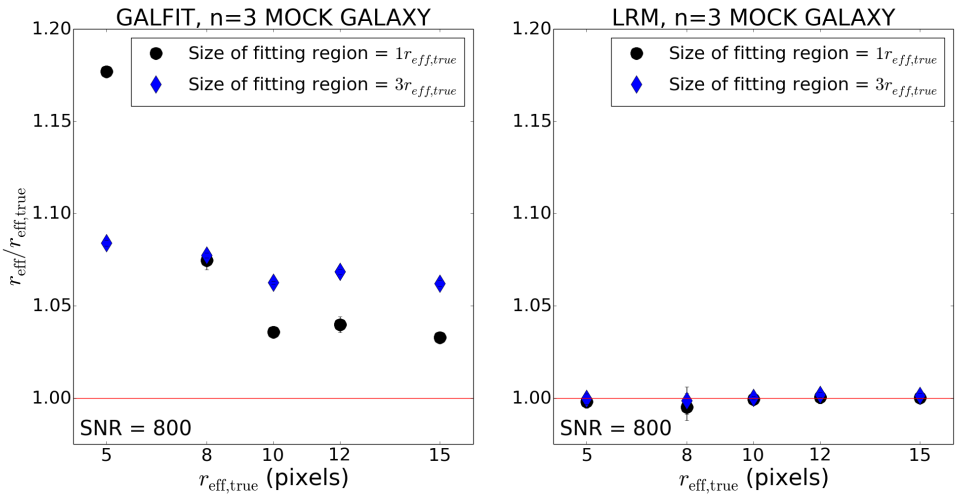

3.4.4 Test on mock galaxies with $n = 4$

In previous sections, we perform tests on mock galaxies with a Sérsic index $n = 3$. However, the expected Sérsic index for ellipticals is most often $n = 4$. The purpose of the simulation is only to test the behaviour of both methods in the same conditions, so that the Sérsic index of the mock galaxy does not affect our conclusion. To make sure that is the case, we performed identical tests with mock galaxies corresponding to a de Vaucouleurs profile, $n = 4$. We followed the same prescription as earlier, but for a de Vaucouleurs profile. Specifically, we convolved the profiles and added random Gaussian noise. Their

half-light radii were measured with both methods, with $n = 3$ and $n = 4$ profiles.

Figure 3.14: Results of the measurement of $r_{\mathrm{eff}}/r_{\mathrm{eff,true}}$ by GALFIT and the LRM as a function of the size of the fitting area, for various S/Ns. The simulated galaxy is a Sérsic profile with $n = 4$ and a half-light radius of 12 pixels. The left-hand panels show the result from GALFIT, the right-hand panel, from the linear regression method. The top panels correspond to S/N = 800, the middle panels to S/N = 170, the bottom panels, to S/N = 50. The vertical axis is the measured $r_{\mathrm{eff}}/r_{\mathrm{eff,true}}$. The horizontal line represents $r_{\mathrm{eff}}/r_{\mathrm{eff,true}} = 1$. The horizontal axis shows the size of the fitting region in units of $r_{\mathrm{eff,true}}$, ranging from 1 $r_{\mathrm{eff,true}}$ to 5 $r_{\mathrm{eff,true}}$. The blue diamonds are the results for an $n = 3$ model and the black circles for the correct value $n = 4$. Because they are sometimes smaller than the symbol size, the σ_{rand} error bars do not always appear.

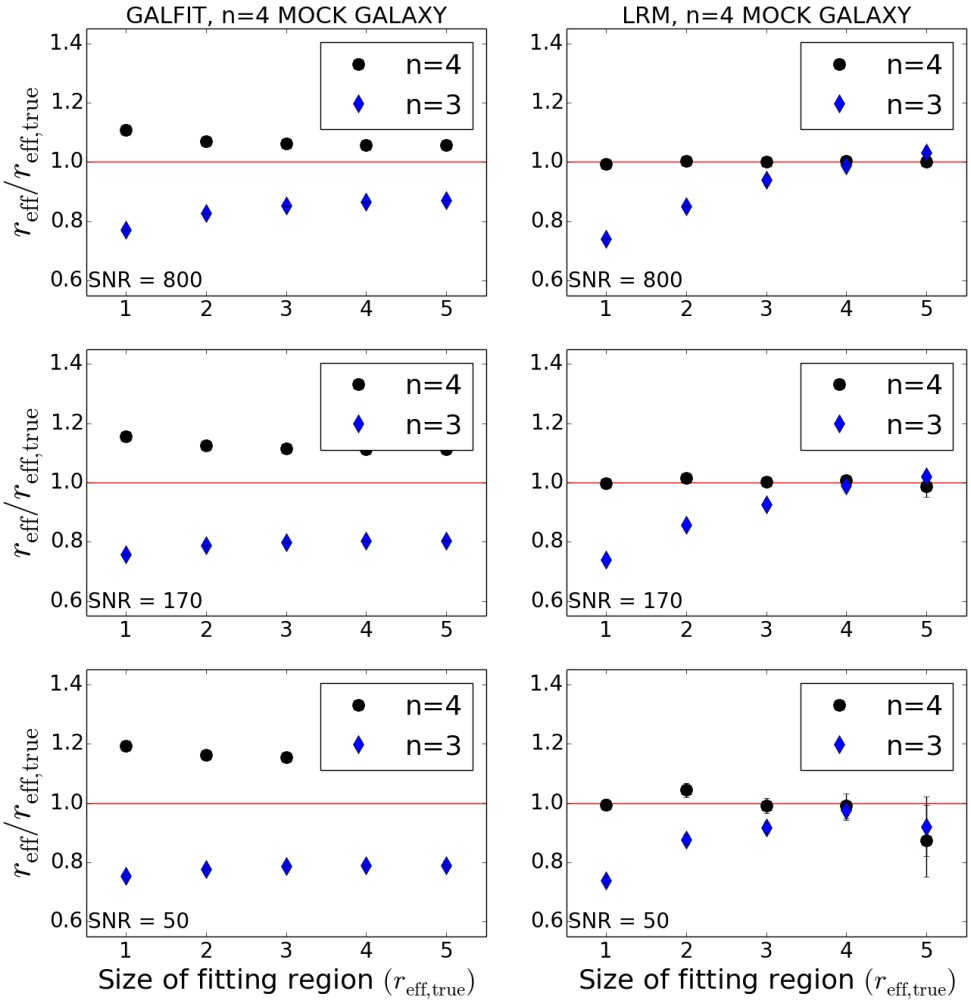

The conclusions are similar to those of the test on mock galaxies with $n = 3$; only this time, the use of a Sérsic index that is too low leads to underestimating the half-light radius. We first consider the S/N = 800 case. When using $n = 3$, GALFIT underestimates the half-light radius by a factor depending on the fitting region. The larger the fitting region, the lower the underestimation, ranging between 13% and 23%. Those negative biases are,

however, less important than the positive bias observed in the test with the $n = 4$ model on $n = 3$ mock galaxies. The same is true for the LRM: using a too low Sérsic index leads to an underestimation that depends on the size of the fitting region. It reaches 26% for the innermost regions. This bias is not smaller than that of GALFIT; however, as opposed to GALFIT, the linear regression method reaches the correct half-light radius even with a Sérsic index that is too low, when probing out to at least 4 $r_{\rm eff}$. When using the right n, the method converges towards the correct value, regardless of the fitting region, whereas GALFIT still slightly overestimates the half-light radius by about 5%

When studying $n = 4$ mock galaxies, there seems to be a slightly stronger dependency on the value of the S/N than with $n = 3$ galaxies, for both GALFIT and the LRM. Indeed, when comparing the top, middle and bottom panels for GALFIT, it can be seen that the bias increases when the S/N decreases. For example, for a 2-$r_{\rm eff}$ fitting region using the correct $n = 4$, the GALFIT overestimation reaches 7%, 12% and 16% for the three considered S/Ns. The bias changes a little too for the LRM method, as there is a slight overestimation from 0.5% for the best SNR to 4% for the worst. However, the method still converges to the correct value.

In summary, those tests show that more robust results are obtained with our technique. The linear regression method behaves better than GALFIT regarding the critical aspects of image processing, such as the S/N or the fitting region. We have also shown that this method depends less on the knowledge of n than GALFIT. However, our simulations have a domain of validity. In particular, the PSF we used here was (1) perfectly known, which is not usually the case for actual observations and (2) free of any noise. Neither the behaviour of GALFIT nor that of the LRM in cases where there are uncertainties on the true PSF has been investigated in this work.

3.5 Error calculation

Each measurement is conducted on all the frames of each system. The mean results and their $\sigma_{\rm rand}$ have been computed. What still needs to be taken into account are the systematic errors caused by four major factors: the determination of the background sky value, of the galaxy centre coordinates, the subtraction of the sources (i.e. the determination of their positions and intensities) and of the arc. Each of these error sources is studied individually. For readability, the approach will be explained in detail first for the sky background. A similar approach is used to estimate the error bars coming from the other error factors.

The background sky is calculated based on the average intensity of object-free zones on the data frames, $I_{\rm sky} = \langle I_{\rm j} \rangle$ (see Section 2.1.2). A 1σ error bar on its value, $\sigma_{\rm sky}$, is computed using the standard error on the mean:

$$\sigma_{\rm sky} = \sqrt{\frac{\sum_{j=1}^{m} (I_{\rm j} - I_{\rm sky})^2}{m(m-1)}} \tag{3.7}$$

where m is the number of measurements for each background sky value (that is, the number of object-free zones on each data frame), I_j is the individual value of the background sky for each zone and I_{sky} the average of those m values.

The pre-processing and the shape parameters measurements are conducted twice. Once with the correct values I_{sky} of the background sky, and once with too high a value of $I_{sky} + \sigma_{sky}$. The resulting shape parameters are thus affected by the error propagation from the background sky. The difference between this value of ε, for example, and the original one, gives the error bar on ε coming from the background sky. The same is true for both other shape parameters.

The same error calculation process is applied for all other sources of systematics. We consider the 1σ error bar on the galaxy centre coordinates from Chantry et al. (2010), Sluse et al. (2012), Courbin et al. (2011) and Eigenbrod et al. (2006a). The measurements are conducted first using the published astrometry, then using centre coordinates shifted by their 1σ error bar. As for the error propagation from the sources, a 1σ dispersion error bar has been calculated on their positions and intensities amongst all the frames of each system. The sources subtraction is conducted once using the correct values of their X-positions, and once using a wrong value, shifted by an offset of the same magnitude as their error bars. The same is done with the Y-positions and intensities of the sources. These transformations are only operated on one of the four point sources, the one closest in projection to the galaxy, because modifying it would have the strongest effect on the galaxy.

The process remains the same for the arc subtraction. A 1σ error image of the arc is computed by propagating the individual pixels uncertainties[4] at each step of the arc construction: the stacking and collapsing of traces within each sector, the fitting of a de Vaucouleurs law with the residuals symmetry criterion, the linear combination between this fit and arc data points, the re-scaling on individual traces and the 2-D reconstruction of the arc. Then, we conduct the measurement of the shape parameters twice, once after a subtraction of the correct arc image, and once deliberately subtracting too much arc, adding the 1σ value for each pixel in the arc image. We find that the arc subtraction did not cause any noticeable error on the measurement of the PA nor of ε.

Eventually, since all the error sources are assumed to be independent, the quadratic sum of all the errors on each structural parameter is computed, leading to the total error bars given in Table 3.1.

[4]Each pixel of the data frame is affected by an uncertainty on its intensity, that is an output of the HST/NICMOS pipeline data reduction or that can be inferred from the data quality map and the photon noise.

3.6 Results

Figure 3.15 shows the best-fitting 2-D de Vaucouleurs models for each system, together with their residuals map. In the majority of cases, a slight overestimation of the central luminosity of the galaxy can be noticed. Indeed, the de Vaucouleurs model reaches a cusp at the centre, and that is why the first couple of pixels have been ignored in most shape parameters measurements. The results of these measurements are given in Table 3.1 along with their error budget. For all further discussion, the half-light radius $r_{\rm eff}$ is noted $\theta_{\rm eff}$ when referring to its angular value in arcseconds. To discuss the discrepancies noted by Schechter et al. (2014), values of $\theta_{\rm eff}$ measured from a variety of references, with MCS or other deconvolution algorithms, are given in Table 3.2.

3.6.1 Comparison with previous works

The first apparent reason for the differences between MCS and IMFITFITS $\theta_{\rm eff}$ values is the use of a different deconvolution algorithm. As explained in Magain et al. (1998) and Chantry and Magain (2007), MCS is well suited to gravitational lensing images, because it consists in iteratively subtracting a diffuse component, including any non-point-like object, such as galaxies and lensed arcs, until convergence to an image of the point sources. Moreover, it has the important advantage of not violating the sampling theorem. Chantry et al. (2010) and Sluse et al. (2012) used the MCS method to determine the PSF because TinyTim PSFs proved not to be accurate enough to model the point sources (Chantry and Magain 2007, Chantry et al. 2010). Using an incorrect PSF produces artefacts due to bad point source subtraction. It also introduces errors in the determination of the parameters of the model, since it has to be convolved by the PSF before comparison with the data. The use of a different fitting method may explain the discrepancies between MCS and IMFITFITS results, too. The background sky processing in the IMFITFITS work may also have been different, since it may have been subtracted before the fitting, as in this work. In Chantry et al. (2010) and Sluse et al. (2012), some sky had been subtracted directly from the data frames, and during the deconvolution, a numerical background was fitted to subtract any remaining signal. This method leads to a bias in the sky levels. Finally, our simulations have shown that classical galaxy profile fitting methods like IMFITFITS depend rather strongly on the fitting area. The choice of different regions of interests between MCS- and IMFITFITS-based works would explain part of the discrepancies as well.

However, the present values of $\theta_{\rm eff}$ seem to be in better agreement with the IMFITFITS values, even though we used MCS PSFs. The differences between our measurements and the values reported in Chantry et al. (2010) and Sluse et al. (2012) come mainly from the different shape parameter measurement procedures. In those works, the shape parameters were all measured simultaneously, since a de Vaucouleurs model was fitted on the data frames. The problem with such a method, the possible existence of local minima, was one of the motivations for this work. Furthermore, we do not use a two-dimensional profile on the frames, but rather a radial profile to determine the shape parameters of the convolved profile and then implement an iterative method to correct from the PSF. Together with the

better estimation of the background sky, those differences explain the major discrepancies between the past MCS and present values. For one system, WFI2033, our half-light radius is larger than the one determined by Vuissoz et al. (2008), also using an MCS method. As mentioned in Section 3.2, the arc subtraction could not be properly performed on its images because the bump corresponding to the visible arc is so diffuse that the process does not detect it. It can be assumed that some contamination from the arc remains, overestimating the half-light radius.

Another discrepancy between previous MCS works and the present result is the direct subtraction of the lensed signal (arc and sources) at the NIC2 resolution from the original images, which is specific to this work. It significantly increases the visibility of the lensing galaxy as shown in Figure 3.2 and it makes disentangling the luminosity from the galaxy and from other components easier. Nevertheless, this pre-processing has its own drawbacks. In particular, in the case of B1422, a point source appeared close in projection to the elliptical galaxy. Distinguishing the light from that specific point source and from the galaxy pixels on top of it is extremely uncertain. The PSF subtraction produces spurious artefacts in regions where the lensing galaxy is bright, yielding systematic errors in our half-light radius measurement. This problem is treated by using a mask cancelling the value of the ill pixels. It should be pointed out that in such cases, classical fit methods may not be able to accurately separate the point source from the luminous disk either.

Finally, discrepancies remain between the IMFITFITS works and the present, too. They come from the use of a different PSF, the instabilities in their fitting methods and their stronger dependency on the fitting area.

Not taking the arc into account leads to an overestimate of θ_{eff} of about 11% in the case of our sample. Even though the arc subtraction constitutes an improvement to the measurement of θ_{eff}, it comes with a few weaknesses. It may produce some residual noise or artefacts on individual pixels values. We take that into account by computing the error maps of the reconstructed arc image and by including it in the θ_{eff} error bars. Another inconvenience of this arc subtraction is that it requires a lot of human intervention at each step, mostly for verification purposes, and is therefore very time-consuming. Since each system presents a different arc, each one with its own specificities linked to its position, the point sources positions and the configuration of the system, building a quicker, more automated version of the arc subtraction may lead to the loss of some precision.

Figure 3.15: *Left to right*: data frame after arc and point source subtraction, best model and residuals for each system. The circle depicts the region of interest for the measurement of $r_{\rm eff}$. The residual maps correspond to a $\pm 3\sigma$ scale, white corresponding to $> 3\sigma$ and black, $< 3\sigma$. Only one data frame is shown for each system.

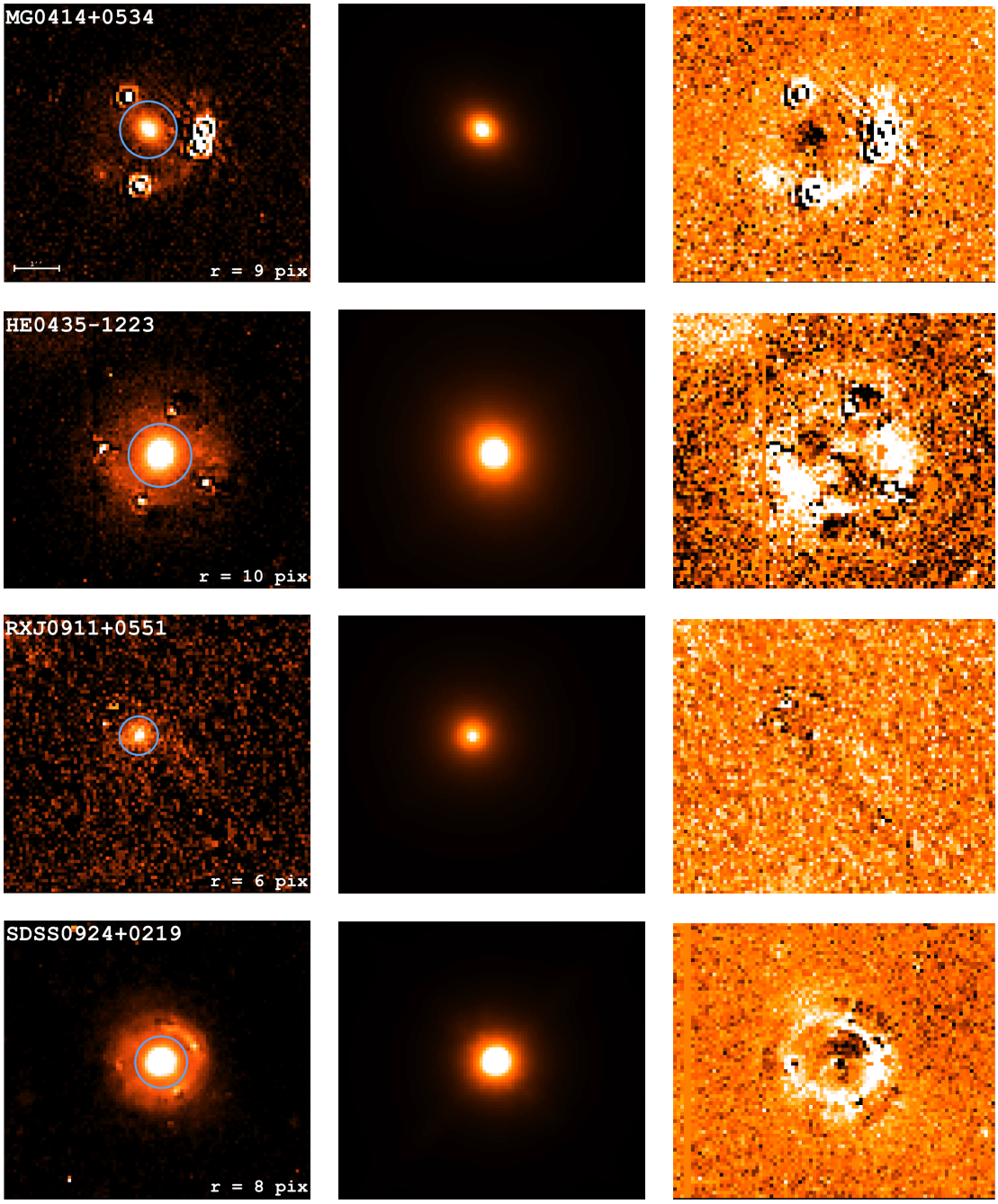

Figure 3.15: Continued.

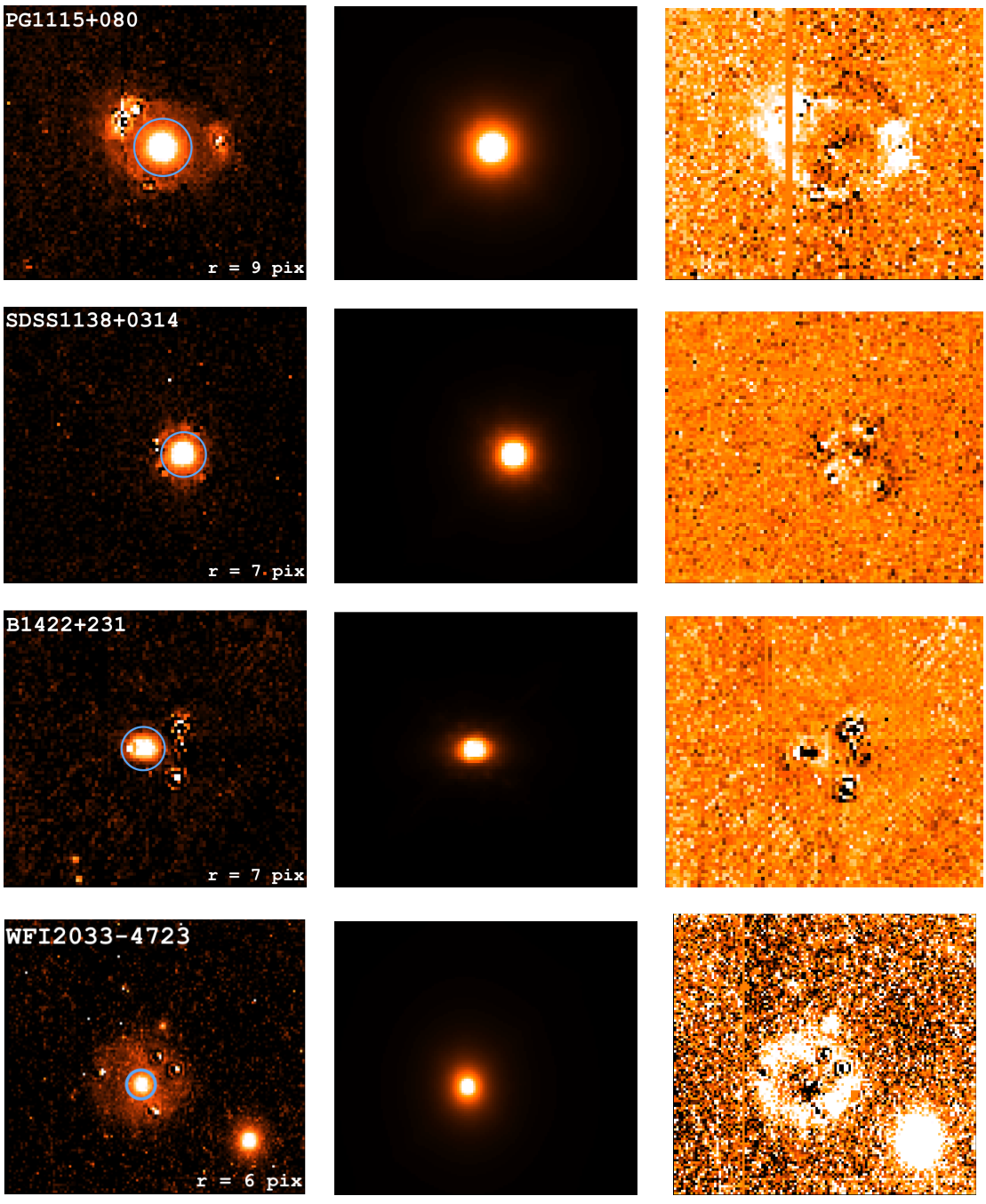

Table 3.1: Respective values of σ_{rand} and systematic errors. Systematic errors sources are, in order: the background sky, the $x-$ and $y-$positions of the point sources, their intensities, the galaxy centre coordinates and the arc subtraction.

System	*Parameter*	*Measured value*	σ_{rand}	σ_{sky}	σ_{xs}	σ_{ys}	σ_{Is}	σ_{xg}	σ_{yg}	σ_{arc}	*Total error*
	θ_{eff} (")	**0.660**	0.044	0.010	0.029	0.029	0.028	0.017	0.073	N.A.	**0.100**
MG0414+0534	ε	**0.150**	0.032	0.003	0.020	0.020	0.030	0.006	0.020		**0.056**
	PA (°)	**-13.556**	4.032	0.097	0.000	0.000	0.250	0.417	1.930		**4.498**
	θ_{eff} (")	**0.872**	0.008	0.001	0.026	0.027	0.034	0.030	0.034	0.034	**0.076**
HE0435	ε	**0.218**	0.019	0.023	0.060	0.060	0.050	0.005	0.010		**0.103**
	PA (°)	**22.086**	2.452	3.000	1.000	2.000	0.750	0.750	0.188		**4.602**
	θ_{eff} (")	**0.869**	0.106	0.018	0.105	0.102	0.063	0.077	0.007	N.A.	**0.207**
RXJ0911+0551	ε	**0.128**	0.020	0.001	0.045	0.045	0.015	0.005	0.005		**0.069**
	PA (°)	**-49.345**	2.413	0.125	0.250	0.250	0.250	0.688	0.219		**2.558**
	θ_{eff} (")	**0.253**	0.012	0.031	0.009	0.009	0.009	0.007	0.025	0.043	**0.062**
SDSS0924+0219	ε	**0.090**	0.013	0.004	0.020	0.020	0.020	0.033	0.014		**0.051**
	PA (°)	**-24.449**	4.983	0.065	0.000	0.250	0.250	9.641	1.828		**11.011**
	θ_{eff} (")	**0.443**	0.012	0.041	0.032	0.032	0.032	0.017	0.047	0.033	**0.092**
PG1115+080	ε	**0.035**	0.014	0.143	0.001	0.001	0.001	0.060	0.068		**0.169**
	PA (°)	**42.322**	8.647	0.125	0.250	0.250	0.250	0.000	1.344		**8.762**
	θ_{eff} (")	**0.199**	0.005	0.000	0.002	0.002	0.005	0.008	0.039	0.075	**0.085**
SDSS1138+0314	ε	**0.000**	0.024	0.055	0.040	0.040	0.010	0.033	0.023		**0.092**
	PA (°)	**90.584**	3.884	0.000	8.000	0.250	0.500	2.594	3.438		**9.896**
	θ_{eff} (")	**0.107**	0.012	0.014	0.030	0.026	0.027	0.015	0.014	N.A.	**0.056**
B1422+231	ε	**0.258**	0.048	0.011	0.045	0.035	0.065	0.033	0.000		**0.105**
	PA (°)	**-53.570**	1.366	0.130	0.000	2.250	0.250	0.344	1.156		**2.909**
	θ_{eff} (")	**0.923**	0.116	0.091	0.054	0.059	0.054	0.016	0.042	N.A.	**0.182**
WFI2033-4723	ε	**0.075**	0.057	0.002	0.000	0.000	0.000	0.053	0.005		**0.078**
	PA (°)	**-22.412**	17.710	0.000	0.219	0.375	0.031	0.438	10.219		**20.456**

Table 3.2: Comparison between the values of the half-light radii measured in the present work and in previous studies. The values from this work are almost systematically lower than from previous studies, probably owing the lensed signal subtraction. The more accurate MCS PSFs and the higher degree of robustness of the LRM also explain the observed differences.

System	*Method*	$\theta_{\rm eff}$ (")	*Reference*
MG0414+0534	Present	0.660 ± 0.100	Present work
	IMFITFITS	0.77 ± 0.14	(1)
HE0435	Present	0.872 ± 0.076	Present work
	MCS	1.5 ± 0.08	(2)
	IMFITFITS	0.86 ± 0.04	(3)
RXJ0911+0551	Present	0.869 ± 0.207	Present work
	MCS	1.02 ± 0.01	(4)
	IMFITFITS	0.67 ± 0.06	(1)
SDSS0924+0219	Present	0.253 ± 0.062	Present work
	MCS	0.5 ± 0.05	(5)
	IMFITFITS	0.436 ± 0.004	(6)
	IMFITFITS	0.31 ± 0.02	(7)
PG1115+080	Present	0.443 ± 0.092	Present work
	MCS	0.92 ± 0.01	(4)
	IMFITFITS	0.47 ± 0.02	(1)
SDSS1138+0314	Present	0.199 ± 0.085	Present work
	MCS	0.86 ± 0.03	(8)
B1422+231	Present	0.107 ± 0.056	Present work
	MCS	0.41 ± 0.02	(4)
	IMFITFITS	0.31 ± 0.09	(1)
WFI2033-4723	Present	0.923 ± 0.182	Present work
	MCS	0.61 ± 0.02	(9)

References. (1) Kochanek et al. (2000); (2) Courbin et al. (2011); (3) Kochanek et al. (2006); (4) Sluse et al. (2012); (5) Eigenbrod et al. (2006a); (6) Keeton et al. (2006b); (7) Morgan et al. (2006); (8) Chantry et al. (2010); (9) Vuissoz et al. (2008).

3.6.2 Residual curvature test

We conduct a visual test to assess how well the de Vaucouleurs model represents the physical luminosity profiles of our lenses. The best model of each galaxy (the one appearing in Figure 3.15) is convolved by the corresponding PSF; its logarithmic radial

profile ($\ln I$; $r^{1/4}$) is plotted and subtracted from that of the data. If any residual curvature remains, it could mean that $n \neq 4$, n being the Sérsic index. As can be seen in Figure 3.16, the test shows little or no curvature at all for four cases (MG0414, HE0435, RXJ0911 and PG1115). This provides validation to the de Vaucouleurs model hypothesis. Three cases display some residual "upwards" curvature, which may indicate that their Sérsic index might be slightly higher than 4 (SDSS0924, SDSS1138 and WFI2033). For WFI2033, this conclusions might be biased by the possible overestimate of the inner wings flux coming from the lack of arc subtraction. B1422 displays a significant downwards curvature. This system in particular had to endure an extra treatment, as we applied a mask with null weights for some sources subtraction-induced ill pixels (see Section 3.6.1). However, in spite of that treatment, some artefacts from the sources subtraction may remain on the B1422 data frames. As can be seen in Table 3.1, the uncertainties coming from the positions and intensities of the sources are high for that system, and it has particularly large relative error bars. We therefore consider it less conclusive regarding the de Vaucouleurs profile test than the other systems.

3.7 Conclusion

The luminosity profiles of eight lensing galaxies have been analysed with a newly designed method, independent of classical galaxy fitting methods. Each shape parameter has been estimated individually in order to keep the results as free as possible of any influence from the other parameters. A careful pre-processing that is specific to gravitational lensing images has been implemented, including a subtraction of the lensed signal. It has increased the visibility of the galaxy and made the shape parameters measurements more secure. A highly detailed study of the systematic errors has given reliable error bars. By being tested versus GALFIT regarding various aspects of image processing (the PSF, the S/N, the portion of the galaxy that can be studied) and properties of the fitted galaxy luminosity profile (the use of an incorrect Sérsic index n), the LRM has proved to be less n-dependent and better suited to studying small galaxies compared to the PSF. For that reason, it is particularly relevant when analysing lensed images, because they comprise tricky diffuse components that restrict the study of the lens luminosity profile to its inner regions. Thanks to the residual curvature test, we have also verified that the de Vaucouleurs profile satisfactorily represents the physical light distribution of the elliptical galaxies in our sample. Nevertheless, even though we measured shape parameters independently of the Sérsic index n, the latter should be measured too in order to complete the characterisation of the lensing galaxies. A possible improvement of the LRM is expanding it to the measure of n as well.

These results are to be used to constrain the lenses mass profiles, when using constant mass-to-light ratio models to characterise it. Further on, the integrated luminosity of the lenses within their Einstein radii will be computed, using these best-fitting de Vaucouleurs models. This is discussed in the next Chapters.

Figure 3.16: Plots of the residual curvature when the ($\ln I$; $r^{1/4}$) radial profile of the convolved best de Vaucouleurs model has been subtracted from that of the data frame. SDSS0924, SDSS1138 and WFI2033 display a slight residual upwards curvature. B1422 displays a significant downwards curvature. On average, the de Vaucouleurs profile is a satisfactory representation of the galaxies.

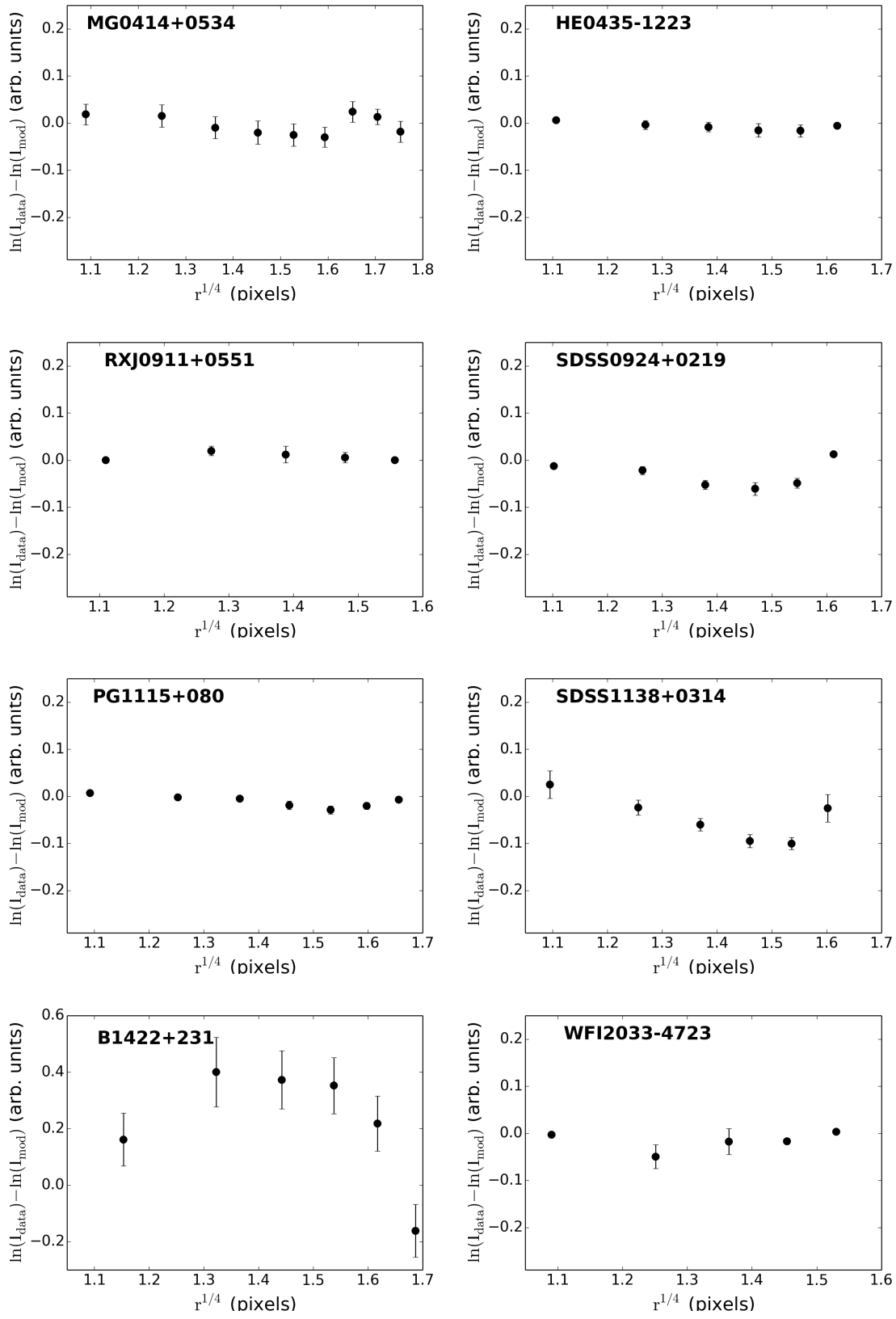

4 Analysis of the mass distributions of the lensing galaxies

In this Chapter, we explain the process and results of fitting a mass profile to our sample of gravitational lensing observations. We chose a widely-used open-access tool to solve the lens equation, the *lensmodel* package (Keeton 2001, 2011). Given a mathematical expression of the lens density profile, it computes its lensing potential and tunes its parameters to best render the observables.

We consider three different mass profiles, with a variety of assumptions regarding their dark matter content. They are fitted on the lensing observables, that is, the sources and lens positions and the time delays when available. In some cases, when we consider a constant mass-to-light ratio profile, we use additional constraints coming from the study of the lenses light profile. We have chosen not to consider the flux ratios between the source images, as they are most likely affected by microlensing from the stars within the lens and by dust extinction (Courbin 2003). Flux ratios may therefore vary with time and are deemed too uncertain for this study. More details about each profile are given in Section 4.1, and some issues of the fitting process itself are discussed in Section 4.2.

The goodness-of-fit is to be compared between mass profiles as a first step towards answering the main question of this study, that is, whether or not elliptical galaxies are embedded in dark matter halos. This comparison is but a first step and should not be used to draw any firm conclusion on the existence of halos around our lenses. Indeed, on the one hand, our fits are sometimes quite poorly constrained, as we have few observational constraints compared to the high number of parameters of our models. On the other hand, gravitational lens modelling is subject to a few degeneracies and to the existence of local minima in a high-dimensional parameters space. This matter is discussed in Section 4.4. Therefore, another quantity will be used to try and detect dark matter halos around the lensing galaxies, that is, their mass-to-light ratios as a function of the galacto-centric distance. To compute it, the Einstein radius needs to be calculated, as it is presented in Section 4.3.

4.1 The mass profiles

We are considering three families of mass profiles corresponding to three different hypotheses regarding the dark content of our galaxies. First, we are considering the singular isothermal ellipsoid model or SIE (Kormann et al. 1994). An isothermal profile is most often a "good place to start" when modelling a galaxy, as it is a general, simple expression of a symmetrical mass distribution. Many observations, like spiral galaxies rotation curves or elliptical galaxies dynamics, tend to be in agreement with an isothermal profile (Keeton 2001). Its definition boils down to a simple condition:

$$\rho(r) \sim \frac{1}{r^2} \tag{4.1}$$

where r is a radial coordinate. The actual proportionality can be expressed exactly, for example depending on the velocity dispersion σ_v^2 of the mass distribution: $\rho(r) = \sigma_v^2/2\pi G r^2$ where G is the gravitational constant. This expression is valid for a spherical mass distribution, but can be generalised to an elliptical mass distribution through a manipulation of the r coordinate, such as $r^2 = x^2 + (y^2/q^2)$, with q the projected axis ratio of the 2-D ellipse ($q = b/a$). It is called "singular" because it reaches a singularity at $r = 0$. To avoid the divergence of ρ at the central $r = 0$ coordinate, a core radius s can be introduced, and the density profile becomes $\rho(r) = \rho_0/(s^2 + r^2)$, with ρ_0 the proportionality constant.

In the case of lens modelling, the parametrisation affects the convergence $\kappa(\xi)$, where $\xi^2 = x^2 + \frac{y^2}{q^2}$. For any power law model with a core radius s, the convergence is (Keeton 2011):

$$\kappa(\xi) = \frac{1}{2}\frac{b^{2-\alpha}}{(s^2 + \xi^2)^{1-\alpha/2}} \tag{4.2}$$

with b the scaling factor. For singular models, s reaches 0 and for isothermal models, $\alpha = 1$. Thus,

$$\kappa(\xi) = \frac{1}{2}\frac{b}{\xi}. \tag{4.3}$$

The associated two-dimensional gravitational potential for a power law model can be written in the following form (Keeton 2011):

$$\phi = x\phi_x + y\phi_y - b\ q\ s\ \ln[\sqrt{(\delta + s)^2 + (1 - q^2)x^2}] + b\ q\ s\ \ln[s(1 + q)]$$

where

$$\begin{aligned} \phi_x &= \frac{b\ q}{\sqrt{1 - q^2}} \arctan\left(\frac{\sqrt{1 - q^2}x}{\delta + s}\right) \\ \phi_y &= \frac{b\ q}{\sqrt{1 - q^2}} \operatorname{arctanh}\left(\frac{\sqrt{1 - q^2}y}{\delta + q^2 s}\right) \end{aligned} \tag{4.4}$$

and $\delta^2 = q^2(s^2 + x^2 + y^2)$. For singular models, this becomes:

$$\phi = x\phi_x + y\phi_y$$

$$\phi_x = \frac{b\,q}{\sqrt{1-q^2}} \arctan\left(\frac{\sqrt{1-q^2}x}{\delta}\right)$$
$$\phi_y = \frac{b\,q}{\sqrt{1-q^2}} \operatorname{arctanh}\left(\frac{\sqrt{1-q^2}y}{\delta}\right) . \tag{4.5}$$

The fact that this profile is singular does not impair the model fitting because our lens modelling tool requires a finite core radius.

The SIE model corresponds to an isolated, symmetrical lens. No galaxy is ever truly isolated, as other massive objects in its vicinity, or along the line of sight, can add some perturbation to the gravitational potential responsible for the lensing phenomenon. To account for this effect, we add an external tidal perturbation term, that is called the shear γ. The shear might be coarsely described, for visualisation purposes, as an "extra" ellipticity that is not the galaxy intrinsic ellipticity but that represents the deformation of the galaxy potential coming from its environment. Since both these angular terms correspond to a similar mathematical representation, they are difficult to separate, leading to a slight degeneracy, as discussed in Section 4.2 (Keeton et al. 1997, Keeton 2001). One has to keep this in mind when examining results from the models.

What is more, considering an isothermal slope for the mass profile of a lensing galaxy might seem like a very rough approximation. Most studies show that elliptical galaxies light profiles are well fitted by a de Vaucouleurs law, but little is known about how their dark matter content might be distributed. Most dynamical studies indicate that the SIE model tends to fit elliptical galaxies quite satisfactorily. For example, Cappellari et al. (2015) have mapped out the stellar velocities of 14 fast rotating elliptical galaxies, to find out that their observations were well rendered by an isothermal density profile for the total content of the galaxies, that is, the sum of dark and baryonic matter. This highlights a suspicious observation that somehow, dark matter and luminous matter have conspired to sum up to an isothermal profile, where stars dominate in the bulge, and dark matter in the outer parts, as stated in Chapter 1. This so-called bulge-halo conspiracy is not predicted by the ΛCDM dark matter halo formation models (Remus et al. 2013, Dutton and Treu 2014, Cappellari et al. 2015, Janz et al. 2016). Aside from dynamical modelling of galaxies, hydrodynamical simulations support the SIE model as a good representation of early-type galaxies. This arrangement of the total density profile might stem from the formation history of ellipticals, where early processes steepen the inner slope of their density profile, before mergers and accretion flatten them out (van de Ven et al. 2009a, Mandelbaum et al. 2009, Remus et al. 2013, Xu et al. 2016, 2017). Nonetheless, the SIE profile is one of the most straightforward mass profiles to model and constitutes a good start.

To move beyond the SIE profile, we consider another distribution of matter, that closely follows the light profile to a factor of scaling. We have extensively studied the structural parameters of the de Vaucouleurs profile that best describes the light content of the lenses: in our second case, we try and model their total density profiles with a de Vaucouleurs (DVC) law. In that "mass-follows-light" situation, the convergence κ is

expressed as (Keeton 2011):

$$\kappa(\xi) = \kappa_0 \exp[-k * (\xi/r_{\rm eff})^{1/4}] \tag{4.6}$$

with $k = 7.67$, the same numerical normalisation constant as in the light profile (Equation 3.5) and κ_0, a scaling parameter. This law also tends towards a cusp close to the centre of the lens. We set the parameters of the mass profiles to the values measured on the light profile, allowing the scaling parameter κ_0 to be free. This is a constant mass-to-light ratio model along the galacto-centric distance axis, but the constant can be higher than 1. To be more specific, we use the observed values of the three structural parameters we have just measured, that is, $\varepsilon \pm \sigma_\varepsilon$, $PA \pm \sigma_{PA}$ and $\theta_{\rm eff} \pm \sigma_{\theta_{\rm eff}}$ as additional observational constraints to the fit. They contribute as an extra term in the χ^2 computation, that increases the further the model steps away from the constraint. We also add a shear term for that de Vaucouleurs model. The associated deflection potential has to be computed numerically for its elliptical form, but for a circular profile, analytical solutions have been obtained and can be found for example in Maoz and Rix (1993) and Cardone (2004). In *lensmodel*, the circular gravitational potential is implemented as follows:

$$\phi(r) = \kappa_0 \frac{40320}{k^8} \frac{r_{\rm eff}^2}{r} \left[1 - \exp(-u)\left(1 + u\left(1 + \frac{u}{2}\left(1 + \frac{u}{3}\left(1 + \frac{u}{4}\left(1 + \frac{u}{5}\left(1 + \frac{u}{6}\left(1 + \frac{u}{7}\right)\right)\right)\right)\right)\right)\right)\right] \tag{4.7}$$

with $u = k(r/r_{\rm eff})^{1/4}$. Then, the lensing properties of any circularly symmetric profile can be generalised to elliptical symmetry through a few 1-D integrals that can be found in Schramm (1990) or Keeton (2001).

Finally, we consider one more case: we use a combination of a de Vaucouleurs profile and of a Navarro-Frenk-White (NFW) profile (Navarro et al. 1996), noted DVC+NFW. The NFW profile stems from N-body cosmological simulations conducted to investigate the average structure of dark matter halos in the ΛCDM model around objects of various masses ranging from galaxy clusters to dwarf galaxies. It is widely used to represent dark matter halos. The mass density of an NFW profile is expressed as:

$$\rho(r) = \frac{\rho_s}{(r/r_{\rm s})(1 + (r/r_{\rm s}))^2} \tag{4.8}$$

where ρ_s and r_s are the halo scaling parameters. It is therefore also singular. The lensing properties of a spherical NFW model can be found in Bartelmann (1996), Meneghetti et al. (2001) and Golse and Kneib (2002). The projected surface mass density κ has the following form:

$$\kappa = 2\kappa_s \frac{1 - \mathcal{F}(x)}{x^2 - 1} \tag{4.9}$$

with $\kappa_s = \rho_s r_{\rm s}/\Sigma_{cr}$, $x = r/r_{\rm s}$, and $\mathcal{F}(x)$ is the following:

$$\mathcal{F}(x) = \begin{cases} \frac{1}{\sqrt{x^2-1}} \tan^{-1}(\sqrt{x^2-1}), & \text{if } x > 1 \\ \frac{1}{\sqrt{1-x^2}} \tanh^{-1}(\sqrt{1-x^2}), & \text{if } x < 1 \\ 1, & \text{if } x = 1. \end{cases} \tag{4.10}$$

The deflection potential for the spherical case is:

$$\phi(r) = 4\kappa_s r_s \frac{\ln(x+2) + \mathcal{F}(x)}{x} \ . \tag{4.11}$$

For an elliptical NFW, one can replace the radial coordinate r by the elliptical coordinate ξ we have been using. However, as that would produce a model that cannot be solved analytically, *lensmodel* offers an alternative implementation (Keeton 2001, 2011),

$$\phi(\xi) = 2\kappa_s r_s^2 \left[\ln^2\left(\frac{\xi}{2}\right) - \text{arctanh}^2\left(\sqrt{1-\xi^2}\right) \right] \tag{4.12}$$

which can be solved analytically (Meneghetti et al. 2001, Golse and Kneib 2002). We are focusing on spherical dark matter halos, as adding an ellipticity parameter to the NFW contribution to the potential would require more constraints for the model to be viable. Even so, the NFW model adds two free parameters (κ_s and r_s) to the list, which may hinder the convergence of our poorly constrained problem. For that reason, over a second phase, we conduct the fit with an extra bound on the NFW halo. Indeed, its scaling radius can be linked to the galaxy virial radius through the dark matter concentration parameter c_{dm} (e.g. Leier et al. (2012), Brimioulle et al. (2013)):

$$c_{dm} = \frac{R_{200}}{r_s} \tag{4.13}$$

where R_{200} denotes the virial radius. In this case, the virial radius is defined so that the average density inside a sphere of that radius is equal to $200\rho_{\text{crit}}$, where ρ_{crit} is the critical density of the Universe $3H^2/8\pi G$. The virial radius approximately separates the inner region where the galaxy is virialised, that is, in dynamical equilibrium, from the outer region where material is still in infall (Cole and Lacey 1996, White 2001, Brimioulle et al. 2013). From simulations, a plausible value for c_{dm} in early-type galaxies is around 8 (more specifically 8.4 in Table 1 from van de Ven et al. (2009b)). On the other hand, Kravtsov (2013) showed that the virial radius can be systematically linked to the half-light radius of galaxies of most types through a linear scaling relation: $r_{\text{eff}} = 0.015\, R_{200}$. This relation has been inferred over a vast sample of galaxies of all morphologies, detailed in Section 3 of Kravtsov (2013). Eliminating R_{200} from both relations, we find a linear relation between r_s and r_{eff}, the scaling factor reaching approximately 8 (7.954). We use this extra constraint in the second DVC+NFW fits on our sample. For readability, we note these scaled halos NFW*, as opposed to unscaled NFW. This proportionality factor between r_s and r_{eff} is but approximative and the scatter on the factor is probably important. To ensure this is not a problem, we conducted the DVC+NFW* fit on one of the systems (HE0435) and changed the proportionality factor by 50% (once increasing it, once decreasing it). It produced very little change in the results: the χ^2 value changed by 2%, the structural parameters by between 2% (for r_{eff}) and 7% (for ε), and the Einstein radius by not more that 0.03%.

These three families of mass profiles are each characterised by one general assumption on the dark matter content of the lens. The pure de Vaucouleurs model assumes a constant mass-to-light ratio along the whole lens radius while both others allow it to increase with galacto-centric distance. If the assumption of the pure de Vaucouleurs case is too strict, then adding a dark matter halo to the mass profile should increase the quality of the fit.

4.2 Solving the lens equation

Fitting a mass model to a gravitational lensing observation mostly consists in solving the lens equation:

$$\boldsymbol{\beta} = \boldsymbol{\theta} - \nabla\phi(\boldsymbol{\theta}) \tag{4.14}$$

with $\boldsymbol{\beta}$ the source position and $\boldsymbol{\theta}$ the image position, given an expression for the two-dimensional gravitational potential $\phi(\boldsymbol{\theta})$. This operation is often impossible to solve analytically, as the potential gradient of a physical lens, that is not too simplified, involves functions that can only be computed numerically. We therefore use the *lensmodel* software package, which implements a simplification strategy to solve the lens equation. The trick is to reverse the equation, and to solve it from the image plane to the source plane. Each position in the image plane $\boldsymbol{\theta}$ can be mapped to a corresponding source position $\boldsymbol{\beta}(\boldsymbol{\theta})$. In doing so, the algorithm builds up a tiling of the image plane, or lens plane, where each tile I_j corresponds to a single tile in the source plane S_j, mapping out a similar tiling of the source plane (see Figure 4.1). In the end, this simultaneous tiling contains all the information needed to solve the lens equation: the number of source plane tiles $(S_\mathrm{j}, S_\mathrm{k}, ...)$ covering one specific source position gives the number of images this source yields, and the corresponding image plane tiles $(I_\mathrm{j}, I_\mathrm{k}...)$ gives an estimation of their positions, that only needs to be refined further on (Keeton 2011). There is much more than this strategy to the *lensmodel* package. For example, the resolution of the tiling increases closer the critical curves.

Given some observables and a particular expression of ϕ depending on some parameters, the fit is conducted and these parameters are fine-tuned using a χ^2 criterion. The χ^2 minimisation is performed using the Nelder-Mead (or downhill simplex) method (Nelder and Mead 1965, Press et al. 1992). In our cases, the observables that take part into the χ^2 term are the image positions, the galaxy position, the measured time delays when available and other constraints that depend on the mass model we consider: the morphological parameters observed in the H-band for the DVC model and the scaling relation for the DVC+NFW*. When we do take time delays into account, we conduct the fit twice, assuming two values of the Hubble constant H_0 to translate angular distances into luminosity distances, each at the border of the likely domain where H_0 lies (Riess et al. 2005, Sandage et al. 2006). We do so in order to make sure that the choice of its value does not bias our conclusion. Let us point out that if another deflector of comparable mass has been identified in the vicinity of the line of sight, we include it in our fit as a singular isothermal sphere (SIS).

Gravitational lens modelling may seem rather easy to put into operation, given a few reasonable assumptions. However, in practice, it is prone to some specific issues. First, even within non-restrictive hypotheses, the lens models quickly reach a high level of complexity and an important number of parameters, especially when taking external perturbations or more than one deflector into account. As a result, the parameters space often contains local minima and any χ^2 minimisation algorithm might get stuck in one of them. To avoid such an issue, for each of the fits we perform, we start by exploring a deliberately broad region of the parameters space and by computing a grid of models. That way, a coarse estimate of the parameters can be obtained, and the model is progressively

Figure 4.1: An illustration of the *lensmodel* tiling strategy for a circular lens profile (Keeton 2011). The top panel shows the tiling in the image plane. The bold curves are the critical curves. The middle figure shows the distortion of the image plane by the lens mapping process, with an artificial height to make the features apparent. The bottom panel shows the projected tiling in the source plane. Some tiles overlap each other, indicating multiply-imaged regions. A sample source is placed on the source plane, together with its intersections with the distorted surface as well as its image positions.

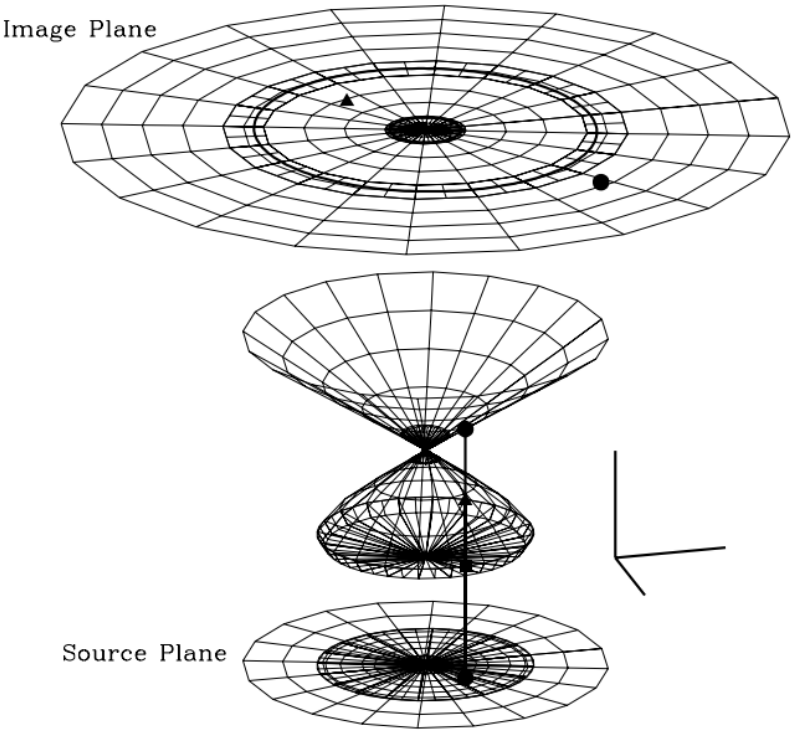

refined within a smaller portion of the parameters space. After this refinement, we double check that the minimal χ^2 we found is not local by re-exploring a significant portion of the χ^2 surface, changing one parameter at a time.

Second, strong lensing observations generally provide a small number of constraints per system, since there are at best four images of the source, each with their positions, time delays and flux ratios. In such a situation, it is common to find more than one density profile that can reproduce the observation and few conclusions can be drawn on the physical nature of the lens. This is called a degeneracy. Some seem quite intuitive: for example, the effects of the intrinsic ellipticity of a lens can be hard to distinguish from an external tidal deformation, coming from the lens environment. This is a degeneracy between parameters. To break it, we need to add a constraint on one of these two parameters, for example by setting the ellipticity of the lens to its observed value for the light profile (Courbin 2003, Schneider and Sluse 2013). Some other degeneracies exist between models themselves, the best-known one being the mass-sheet degeneracy (MSD). First shown by Falco et al. (1985), it stems from a family of transformations of the convergence $\kappa(\boldsymbol{\theta})$ that leaves most of the observables unchanged:

$$\kappa_\lambda(\boldsymbol{\theta}) = \lambda\,\kappa(\boldsymbol{\theta}) + (1 - \lambda) \tag{4.15}$$

Indeed, any of the κ_λ convergences will produce the same image positions, flux ratios and

image distortions. The only affected lensing observable is the product $H_0\,\Delta t$ that will be rescaled into $\lambda\,H_0\,\Delta t$. This corresponds to physically adding a sheet of constant mass density, within the galaxy, its environment, or along the line-of-sight (Falco et al. 1985, Schneider and Sluse 2013). In practice, when including constraints from extended lensed images, like Einstein rings, a great deal of degeneracies can be broken, but the MSD still remains even in this case (Falco et al. 1985, Schneider and Sluse 2013, 2014, Unruh et al. 2017). In some of our fits, we use time delays as a constraint and assume a value for H_0. In that case, we should not worry about MSD. However, in cases where we do not take time delays into account, this degeneracy still exists even though we make assumptions on H_0. The lensing studies that are most sensitive to the MSD are the ones that use lens modelling to place bounds on the Hubble constant (see e.g. Saha 2000, Wucknitz 2002, Schneider and Sluse 2013).

On top of the MSD, there are some other mathematical transformations that leave some observables unchanged (see e.g. Gorenstein et al. 1988, Liesenborgs et al. 2009, Liesenborgs and De Rijcke 2012). Most of them consist in adding a constant to the potential or rescaling it by a constant and leave a subset of the observables unchanged. In fact, the MSD has been shown to be a specific case of a broader families of transformations, called the source-position transformations (SPT), that leave all observables unchanged except for time delays between pairs of images. The SPT has been highlighted by Schneider and Sluse (2014) and then studied in further detail by Unruh et al. (2017) and Wertz and Orthen (2018). Its impact on time delays has been characterised by Wertz et al. (2017). A given convergence profile $\kappa(\boldsymbol{\theta})$ yields a mapping relation between the image plane ($\boldsymbol{\theta}$) to the source plane ($\boldsymbol{\beta}$):

$$\boldsymbol{\beta} = \boldsymbol{\theta} - \boldsymbol{\alpha}(\boldsymbol{\theta}) \tag{4.16}$$

where $\boldsymbol{\alpha}(\boldsymbol{\theta})$ is defined by a deflection potential. To be more specific, if i and j are indices denoting individual source images, the observables constraints are only the relative positions of pairs of images:

$$\boldsymbol{\theta_i} - \boldsymbol{\alpha}(\boldsymbol{\theta_i}) = \boldsymbol{\theta_j} - \boldsymbol{\alpha}(\boldsymbol{\theta_j}) \tag{4.17}$$

for all $i \neq j$, since all multiple images $\boldsymbol{\theta_i}$ come from the same source at the position $\boldsymbol{\beta}$. The situation thus boils down to a mapping $\boldsymbol{\theta_i}(\boldsymbol{\theta_1})$. The question addressed in Schneider and Sluse (2014) is the following: is there a deflection law $\hat{\boldsymbol{\alpha}}(\boldsymbol{\theta})$ that preserves the mapping $\boldsymbol{\theta_i}(\boldsymbol{\theta_1})$ for a single source ? If so, then it must satisfy the following condition:

$$\boldsymbol{\theta_i} - \hat{\boldsymbol{\alpha}}(\boldsymbol{\theta_i}) = \boldsymbol{\theta_j} - \hat{\boldsymbol{\alpha}}(\boldsymbol{\theta_j}). \tag{4.18}$$

It must then correspond to an image plane - source plane mapping $\hat{\boldsymbol{\beta}} = \boldsymbol{\theta} - \hat{\boldsymbol{\alpha}}(\boldsymbol{\theta})$. The two mappings given by $\boldsymbol{\alpha}(\boldsymbol{\theta})$ and $\hat{\boldsymbol{\alpha}}(\boldsymbol{\theta})$ correspond to the same observed images. Therefore, any bijective source-position transformation $\hat{\boldsymbol{\beta}}(\boldsymbol{\beta})$ defines a deflection law $\hat{\boldsymbol{\alpha}}(\boldsymbol{\theta})$ that is equivalent to $\boldsymbol{\alpha}(\boldsymbol{\theta})$, leaving the strong lensing observables unchanged. The particular case of $\hat{\boldsymbol{\beta}} = \lambda\boldsymbol{\beta}$ corresponds to the MSD transformation.

Actually, not every SPT leads to a corresponding density distribution $\hat{\boldsymbol{\kappa}}(\boldsymbol{\theta})$, because the Jacobian matrix of this transformation $(\partial\hat{\boldsymbol{\beta}}/\partial\boldsymbol{\theta})$ is not necessarily symmetric, and therefore cannot always be expressed as the gradient of a potential. Nevertheless, it has been shown by Unruh et al. (2017) that provided that its asymmetrical terms are small enough, that

is, provided that $\hat{\boldsymbol{\alpha}}(\boldsymbol{\theta})$ has a sufficiently small curl term, there can be a curl-free deflection law that is so similar to $\hat{\boldsymbol{\alpha}}(\boldsymbol{\theta})$ that their difference is smaller than the astrometric accuracy of the observations. The SPT is in this case a "quasi-invariance" of the observables.

The source-position degeneracy and its particular case, the MSD, only affect the time delay observations. Fortunately for this study, these degeneracies mostly hinder studies that aim at measuring the Hubble constant from gravitational lensing time delay modelling. In this work, we are mostly affected by "local" degeneracies between parameters, like the ellipticity-shear degeneracy, unless we do not include a time delay measurement constraint in the fit. For that reason, one must keep in mind a satisfactory χ^2 is not a definitive proof of the veracity of a model.

4.3 Einstein radii calculations

As explained in Chapter 1, the Einstein radius can be roughly seen as the average between the galacto-centric angular positions of the sources (Mediavilla et al. 2016). The mathematical definition of the Einstein radius depends on the integrated mass $M(\theta_{\mathrm{Ein}})$ and on the ratio between the distances separating the protagonists. It is therefore little dependent on the choice of the model:

$$\theta_{\mathrm{Ein}} = \sqrt{\frac{4GM(\theta_{\mathrm{Ein}})}{c^2}\frac{D_{LS}}{D_L D_S}} \tag{4.19}$$

The *lensmodel* package is provided with a simple command that computes the Einstein radius of a given model. By definition, at the Einstein radius, $\kappa(\theta_{\mathrm{Ein}}) = 1$. The tool progressively integrates the model up until $\kappa(\theta)$ reaches a value of one. The resulting Einstein radii are given in Table 4.2 along with an error bar. The error was calculated as follows.

The uncertainty on the Einstein radius θ_{Ein} comes from the uncertainties on the parameters of the model. The latter can be evaluated as a function of the χ^2 variation (Press et al. 1992). More specifically, the covariance matrix of the parameters can be computed based on the theoretical definition of its terms, using the derivatives of χ^2 with respect to these parameters. To evaluate these derivatives, we calculate how the χ^2 value increases with an infinitesimal variation on each parameter. This was conducted on each best-fitting model using a Python program (developed by Clémentine Hauret): the best-fitting parameters would be shifted by a small offset, the χ^2, re-calculated, and these values used to approximate the derivative of the χ^2 with respect to each parameter. Then, these approximate derivatives would be used to compute the covariance matrix (see Chapter 14 of "Numerical Recipes" (Press et al. 1992) for detailed calculation). This yields the error bar on each parameter of the lens model, σ_i. These error bars are the ones given in Table 4.2.

What we aim at here is an error bar on the Einstein radius, $\sigma_{\theta_{\mathrm{Ein}}}$. To propagate the σ_i on the Einstein radius calculation, we re-conduct it with the parameters shifted by their error bars, or a fraction of these error bars if they are quite large, one at a time. As a

result, we obtain a list of $\theta_{\rm Ein}$ matching a list of χ^2, that is basically, a function $\chi^2(\theta_{\rm Ein})$. We fit a parabola on this function, and find the value of $\theta_{\rm Ein}$ for which $\chi^2 = \chi^2_{\rm best} + 1.0$, with $\chi^2_{\rm best}$ the value of the best-fitting χ^2, the one given in Table 4.2. The increment of unity of the χ^2 corresponds to an uncertainty of 68.3% on the parameter in a one-degree of freedom problem (Press et al. 1992), as that is the case here, since our only parameter is $\theta_{\rm Ein}$. We eventually reach the value of $\sigma_{\theta_{\rm Ein}}$ by computing the difference between the best-fitting $\theta_{\rm Ein}(\chi^2_{\rm best})$ and $\theta_{\rm Ein}(\chi^2_{\rm best} + 1.0)$. That is how the $\sigma_{\theta_{\rm Ein}}$ values shown in Table 4.2 were obtained.

4.4 Results of lens modelling

The results of the fits are given in multiple forms. Table 4.2 shows the χ^2, shear terms and $\theta_{\rm Ein}$ values for each fit. Table 4.3 shows the overlap between the lenses structural parameter in each best-fitting model as well as with the H-band light profile structural parameters. Figure 4.2 is a plot visualisation of Table 4.3. Finally, one-dimensional convergence profiles are plotted in Figure 4.3. They are computed by averaging the two-dimensional $\kappa(\boldsymbol{\theta})$ map azimuthally. These Tables and Figures are given in Section 4.5. For readability, relevant excerpts of Table 4.2 are given in the text when needed. In these excerpts as well as in Section 4.5, when a reduced χ^2 is marked with a cross, it is because the model has zero degrees of freedom. A reduced χ^2 cannot be computed and the χ^2 is simply copied.

Let us remind that every time an extra deflector contributing to the total lensing gravitational potential has been identified along the line of sight, i.e., if its position is (sufficiently well) known, it is added to the model in the form of a SIS model. In that case, the environment of the lens is not only taken into account through the shear parameters, but actually incorporated into the lens model as a companion. This is the case for all systems but SDSS1138 and SDSS0924. What is more, even for the systems where time delay measurements were available, we have conducted fits excluding them from our constraints. The comparison between studies of the same system with and without its time delay constraints make it possible to understand how important these constraints are in the process of model fitting.

First, Tables 4.2, 4.3 and Figure 4.2 show that the value of the Hubble parameter does not change which model fits each system best. In these Tables and Figure, $H1 = 73.24\ km/s/Mpc$ (Riess et al. 2005) and $H2 = 62.3\ km/s/Mpc$ (Sandage et al. 2006). This ensures that the conclusions of this study are not biased by a choice of cosmological parameter. Switching from $H1$ to $H2$ does sometimes change some parameters values but not the ranking of the models in terms on goodness-of-fit (Excerpt 1). Therefore, for all further discussion, the time delays-constrained models will be considered under the $H_0 = H1$ hypothesis. The DVC+NFW* mass model has not been considered with the $H2$ value of the Hubble constant: after confirming by a test on HE0435 that changing the value of the Hubble constant did not change the conclusions on the DVC+NFW* either, we have chosen to skip redundant lens modelling operations.

Excerpt 1

System	*Model*	χ^2	
		$H_0 = 73.24\ kms^{-1}Mpc^{-1}$	$H_0 = 62.3\ kms^{-1}Mpc^{-1}$
HE0435	SIE	6.74	8.50
	DVC	29.97	63.85
	DVC+NFW	12.73	15.93
RXJ0911	SIE	2.01	3.63
	DVC	131.24	196.51
	DVC+NFW	17.44	14.30
PG1115	SIE	9.21	5.62
	DVC	3.53	3.22
	DVC+NFW	2.50	2.40
B1422	SIE	25.49	24.70
	DVC	60.78	58.27
	DVC+NFW	42.48	41.97
WFI2033	SIE	85.12	124.78
	DVC	205.98	310.26
	DVC+NFW	94.32	94.29

4.4.1 The SIE versus the "mass-follows-light" lens models

The χ^2 results from Table 4.2 (Excerpt 2) show that at the exception of SDSS0924, PG1115 and SDSS1138, the SIE model yields the best reduced χ^2. It is able to reproduce astrometry and time delays constraints, even though the structural parameters this models gives most often mismatch their observed H-band counterpart (Figure 4.2). The DVC lens model yields highly unsatisfactory χ^2 values for RXJ0911, B1422 and WFI2033, which happen to be the systems displaying the highest asymmetry in the sources positions. The resulting DVC shape parameters for these systems lie quite far away from their H-band counterparts, increasing the χ^2. In fact, for these three systems without time delays as well as for the first two when taking Δt into account, the DVC yields a suspiciously large[1] shear parameter, highlighted in bold in Excerpt 2. In the case of elliptical models, the shear parameter is prone to suffer from a degeneracy with the lenses intrinsic ellipticity and this may affect the quality of the fit.

Conversely, the DVC model comes in first for PG1115 in terms of χ^2 and the resulting shape parameters perfectly match their H-band counterpart, although the shear parameter seems, once again, quite large. The fact that the SIE model is the best-fitting model for all but one of our time delay-constrained systems tends to favour the hypothesis that early-type galaxies carry a halo of dark matter, as supported by dynamical studies and simulations (Cappellari et al. 2015, Xu et al. 2016, 2017). Let us however notice that, although many observation support the SIE as a good representation of galaxies, it is a simplistic approximation of a matter distribution. It might therefore yield only a superficial level of understanding of the lens mass profile, but it is accurate enough to compute

[1] A shear parameter above ~ 0.35 may indicate that the intrinsic ellipticity of the lens is ill-fitted, that an extra deflector lies along the line-of-sight, or that the chosen mass model does not represent the lens satisfactorily.

its total mass content, as is the goal in this work.

Excerpt 2

System	*Model*	Δt	χ^2	Reduced χ^2	γ
MG0414	SIE	No	2.08	2.08†	0.08
	DVC		23.53	11.77	0.16
HE0435	SIE	Yes	6.74	2.25	0.06
	DVC		29.97	5.99	0.11
RXJ0911	SIE	Yes	2.01	0.67	0.32
	DVC		131.24	26.25	**0.37**
SDSS0924	SIE	No	5.44	5.44	0.07
	DVC		14.56	4.85	0.11
PG1115	SIE	Yes	9.21	3.07	0.22
	DVC		3.53	0.71	**0.40**
SDSS1138	SIE	No	1.18	1.18	0.09
	DVC		0.98	0.33	0.17
B1422	SIE	Yes	25.49	8.50	0.13
	DVC		60.78	12.16	**0.35**
WFI2033	SIE	Yes	85.12	28.37	0.23
	DVC		205.98	41.20	0.29

4.4.2 The DVC+NFW(*) versus the "mass-follows-light" lens models

In the majority of cases, adding an NFW halo to a DVC produces little to no change in the results, neither in the χ^2 value (Excerpt 3) nor in the structural parameters, whether the scaling bound on the NFW is present or not. For most cases, as can be seen from Figure 4.3, the magnitude scaling of the NFW (NFW*) halo might seem a little odd, as it does not clearly dominate the de Vaucouleurs, even at several Einstein radii. To quantify that, the dark matter fraction ($f_{\rm DM}$) within $\theta_{\rm eff}$ and $\theta_{\rm Ein}$ have been computed for these composite models and are given in Table 4.1. They have been obtained by integrating two-dimensional $\kappa(\boldsymbol{\theta})$ maps within a circular aperture of a radius equal to $\theta_{\rm eff}$ or $\theta_{\rm Ein}$.

For most cases, like PG1115 or all models without time delays, the resulting $f_{\rm DM}$ is tiny, indicating that the DVC is sufficient to render the observations. However, for RXJ0911 it reaches around 70% , which lies in a plausible range (Cappellari et al. 2006a, Oguri et al. 2014, Leier et al. 2016, Xu et al. 2017). In fact, RXJ0911 is the only system for which adding a halo significantly improves the quality of the fit with and without time delays. Its χ^2 value is reduced, so is its shear parameter, and its $\kappa(\boldsymbol{\theta})$ profile seems physical. For two other systems, WFI2033 and HE0435, the addition of a halo improves the fit as well and yields a plausible $f_{\rm DM}$, but only when adding the time delay constraints. Although the $f_{\rm DM}$ and the $\kappa(\boldsymbol{\theta})$ also seem acceptable for the NFW model of B1422, its reduced χ^2 is not lower than that of the DVC, so it does not improve the DVC fit.

The computation of $f_{\rm DM}$ makes it possible to highlight how important the time delay constraints can be in lens modelling. In general, the ranking between best-fitting and worst-fitting χ^2 for one lens does not change when discarding time delays. The structural

parameters are slightly affected, but not to a significant magnitude. However, it can be seen that including the time delay constraints changes the $\kappa(\boldsymbol{\theta})$ profile and increases the f_{DM} of the resulting models, as can bee seen from Table 4.1 (it is particularly visible for HE0435, B1422, PG1115 and WFI2033). This observation issues a warning for models where no time delay values were available: since they are poorly constrained and likely subject to degeneracies like the MSD, they should be handled with caution, especially these with the most parameters, that is the composite DVC+NFW(*) models.

Excerpt 3

System	*Model*	Δt ?	χ^2	Reduced χ^2
MG0414	DVC	No	23.53	11.7
	DVC+NFW		23.53	23.53†
	DVC+NFW*		23.53	23.53
HE0435	DVC	Yes	29.97	5.99
	DVC+NFW		12.73	4.24
	DVC+NFW*		9.46	2.37
RXJ0911	DVC	Yes	131.24	26.25
	DVC+NFW		17.44	5.81
	DVC+NFW*		30.56	7.64
SDSS0924	DVC	No	14.56	4.85
	DVC+NFW		14.56	14.56
	DVC+NFW*		14.56	7.28
PG1115	DVC	Yes	3.53	0.71
	DVC+NFW		2.50	0.83
	DVC+NFW*		2.42	0.61
SDSS1138	DVC	No	0.98	0.33
	DVC+NFW		0.98	0.98
	DVC+NFW*		0.98	0.49
B1422	DVC	Yes	60.78	12.16
	DVC+NFW		42.48	14.16
	DVC+NFW*		41.46	10.37
WFI2033	DVC	Yes	205.98	41.20
	DVC+NFW		94.32	31.44
	DVC+NFW*		98.02	24.51

Table 4.1: Dark matter fractions of composite DVC+NFW and DVC+NFW* models within θ_{Ein} and θ_{eff}

System	*Model*	$f_{\mathrm{DM}}(\theta_{\mathrm{Ein}})$ *in %*	$f_{\mathrm{DM}}(\theta_{\mathrm{eff}})$ *in %*
MG0414	DVC+NFW, NoΔt	17.61	11.96
	DVC+NFW*, NoΔt	16.1	9.56
HE0435	DVC+NFW, NoΔt	2.51	2.25
	DVC+NFW*, NoΔt	46.61	38.06
	DVC+NFW, $H1$	99.90	99.89
	DVC+NFW*, $H1$	52.29	43.49
RXJ0911	DVC+NFW, NoΔt	80.76	76.08
	DVC+NFW*, NoΔt	83.79	78.83
	DVC+NFW, $H1$	77.12	72.35
	DVC+NFW*, $H1$	68.81	62.16
SDSS0924	DVC+NFW, NoΔt	0.02	0.01
	DVC+NFW*, NoΔt	0.01	1E-03
PG1115	DVC+NFW, NoΔt	0.02	0.01
	DVC+NFW*, NoΔt	0.05	0.02
	DVC+NFW, $H1$	13.65	9.01
	DVC+NFW*, $H1$	9.04	3.61
SDSS1138	DVC+NFW, NoΔt	0.15	0.04
	DVC+NFW*, NoΔt	0.06	0.02
B1422	DVC+NFW, NoΔt	3.14	1.13
	DVC+NFW*, NoΔt	0.03	0.01
	DVC+NFW, $H1$	80.79	59.13
	DVC+NFW*, $H1$	99.90	99.40
WFI2033	DVC+NFW, NoΔt	0.11	0.09
	DVC+NFW*, NoΔt	0.07	0.06
	DVC+NFW, $H1$	50.39	44.78
	DVC+NFW*, $H1$	50.69	45.89

4.5 Complete Tables and Figures

Table 4.2: Results of the lens modelling. χ^2 value, number of degrees of freedom (d.o.f), reduced χ^2 value, shear magnitude γ and orientation angle θ_γ (as all models contain an external perturbation term) and Einstein radius.

System	*Model*	χ^2	*# d.o.f*	*Reduced* χ^2	γ, θ_γ	$\theta_{\rm Ein}('')$
Without taking the Δt into account						
MG0414	SIE	2.08	0	2.08†	0.08, -55.94°	1.175 ± 0.001
	DVC	23.53	2	11.77	0.16, -76.23°	1.173 ± 0.001
	DVC+NFW	23.53	0	23.53†	0 .16, -76.10°	1.173 ± 0.001
	DVC+NFW*	23.53	1	23.53	0.16, -75.75°	1.173 ± 0.001
HE0435	SIE	8E-05	0	8E-05†	0.06, 19.04°	1.201 ± 0.001
	DVC	3.71	2	1.86	0.12, 19.10°	1.198 ± 0.001
	DVC+NFW	3.71	0	3.71†	0 .11, 18.96°	1.198 ± 0.001
	DVC+NFW*	3.62	1	3.62	0.08, 18.78°	1.199 ± 0.001
RXJ0911	SIE	8E-05	0	8E-05†	0.33, 9.25°	1.083 ± 0.001
	DVC	63.02	2	31.51	0.38, 8.91°	1.086 ± 0.001
	DVC+NFW	15.20	0	15.20†	0 .23, 8.72°	1.178 ± 0.001
	DVC+NFW*	12.41	1	12.41	0.19, 8.72°	1.145 ± 0.001
SDSS0924	SIE	5.44	1	5.44	0.07, 68.00°	0.874 ± 0.001
	DVC	14.56	3	4.85	0.11, 77.36°	0.873 ± 5E-04
	DVC+NFW	14.56	1	14.56	0.11, 77.35°	0.873 ± 0.001
	DVC+NFW*	14.56	2	7.28	0.11, 77.34°	0.873 ± 0.001
PG1115	SIE	0.09	0	0.09†	0.38, 69.59°	1.135 ± 4E-04
	DVC	3.53	2	1.77	0.30, 55.47°	1.137 ± 0.001
	DVC+NFW	1.53	0	1.53†	0 .31, 55.32°	1.137 ± 0.001
	DVC+NFW*	1.53	1	1.53	0.31, 55.32°	1.137 ± 0.001
SDSS1138	SIE	1.18	1	1.18	0.09. 31.88°	0.665 ± 0.001
	DVC	0.98	3	0.33	0.17, 32.59°	0.663 ± 0.001
	DVC+NFW	0.98	1	0.98	0.17, 32.58°	0.663 ± 0.001
	DVC+NFW*	0.98	2	0.49	0.17, 32.60°	0.663 ± 0.001
B1422	SIE	4.19	0	4.19†	0.14, -49.11°	0.771 ± 0.002
	DVC	12.38	2	6.19	0.58, 40.76°	0.761 ± 0.002
	DVC+NFW	12.35	0	12.35†	0 .58, 40.67°	0.763 ± 0.002
	DVC+NFW*	12.35	1	12.35	0.59, 40.71°	0.761 ± 0.002
WFI2033	SIE	60.98	0	60.98†	0.21. 10.19°	1.124 ± 0.001
	DVC	77.43	2	38.72	0.36, 9.72°	1.111 ± 2E-04
	DVC+NFW	77.43	0	77.43†	0.36, 9.72°	1.111 ± 0.001
	DVC+NFW*	77.44	1	77.44	0.36, 9.72	1.111 ± 0.001

Continued on next page

Table 4.2 – Continued

System	*Model*	χ^2	*# d.o.f*	Reduced χ^2	γ, θ_γ	$\theta_{\rm Ein}('')$
With Δt, $H_0 = 73.24\ kms^{-1}Mpc^{-1}$ (Riess et al. 2005)						
HE0435	SIE	6.74	3	2.25	0.06, 21.23°	1.200 ± 0.001
	DVC	29.97	5	5.99	0.11, 17.00°	1.198 ± 0.002
	DVC+NFW	12.73	3	4.24	0.09, 16.14°	1.200 ± 1E-04
	DVC+NFW*	9.46	4	2.37	0.07, 19.31°	1.199 ± 1E-04
RXJ0911	SIE	2.01	3	0.67	0.32, 9.52°	1.094 ± 0.001
	DVC	131.24	5	26.25	0.37, 9.20°	1.046 ± 0.001
	DVC+NFW	17.44	3	5.81	0.25, 8.67°	1.169 ± 0.001
	DVC+NFW*	30.56	4	7.64	0.24, 8.48°	1.184 ± 0.001
PG1115	SIE	9.21	3	3.07	0.22, 63.06°	1.135 ± 0.001
	DVC	3.53	5	0.71	0.40, 53.14°	1.137 ± 0.001
	DVC+NFW	2.50	3	0.83	0.31, 53.90°	1.139 ± 0.001
	DVC+NFW*	2.42	4	0.61	0.30, 54.70°	1.138 ± 0.001
B1422	SIE	25.49	3	8.50	0.13, -49.00°	0.771 ± 0.002
	DVC	60.78	5	12.16	0.35, -51.55°	0.692 ± 0.001
	DVC+NFW	42.48	3	14.16	0.20, -54.34°	0.832 ± 3E-04
	DVC+NFW*	41.46	4	10.37	0.21, -54.27°	0.826 ± 3E-04
WFI2033	SIE	85.12	3	28.37	0.23, 12.03°	1.119 ± 0.001
	DVC	205.98	5	41.20	0.29, 14.31°	1.113 ± 4E-04
	DVC+NFW	94.32	3	31.44	0.21, 11.48	1.118 ± 0.001
	DVC+NFW*	98.02	4	24.51	0.21, 11.81	1.121 ± 0.001
With Δt, $H_0 = 62.3\ kms^{-1}Mpc^{-1}$ (Sandage et al. 2006)						
HE0435	SIE	8.50	3	2.83	0.07, 17.93°	1.200 ± 0.001
	DVC	63.85	5	12.77	0.11, 16.99°	1.199 ± 0.002
	DVC+NFW	15.93	3	5.31	0.09, 16.80°	1.200 ± 1E-04
RXJ0911	SIE	3.63	3	1.21	0.34, 8.89°	1.062 ± 0.001
	DVC	196.51	5	39.30	0.37, 9.06°	0.998 ± 0.001
	DVC+NFW	14.30	3	4.77	0.21, 8.77°	1.184 ± 0.001
PG1115	SIE	5.62	3	1.87	0.25, 62.51°	1.137 ± 0.001
	DVC	3.22	5	0.64	0.42, 47.69°	1.141 ± 0.001
	DVC+NFW	2.40	3	0.80	0.26, 54.43°	1.139 ± 0.001
B1422	SIE	24.70	3	8.23	0.13, -48.90°	0.771 ± 0.002
	DVC	58.27	5	11.65	0.39, -52.49°	0.693 ± 0.001
	DVC+NFW	41.97	3	13.99	0.20, -54.34°	0.832 ± 3E-04
WFI2033	SIE	124.78	3	41.59	0.24, 13.23°	1.116 ± 6E-04
	DVC	310.26	5	62.05	0.29, 15.30	1.111 ± 4E-04
	DVC+NFW	94.29	3	31.43	0.18, 11.57	1.120 ± 0.001

Table 4.3: Best-fitting structural parameters of the lens models compared to the parameters measured in the H-band, noted in bold. A visualisation of this Table is given in Figure 4.2. "N.A." stands for "not applicable", as the SIE model uses a different scaling parameter than $\theta_{\rm eff}$.

System	*Model*	ε	*PA* (°)	$r_{\rm eff}('')$
MG0414	**H-band**	**0.150 ± 0.056**	**−13.556 ± 4.498**	**0.660 ± 0.100**
	SIE	0.240 ± 0.020	89.980 ± 2.410	N.A.
	DVC	0.047 ± 0.038	-13.935 ± 4.934	0.674 ± 0.069
	DVC+NFW	0.044 ± 0.030	-13.889 ± 2.020	0.669 ± 0.092
	DVC+NFW*	0.034 ± 0.030	-13.678 ± 2.020	0.677 ± 0.092
HE0435	**H-band**	**0.218 ± 0.103**	**22.086 ± 4.602**	**0.872 ± 0.076**
	SIE, No Δt	0.090 ± 0.060	12.270 ± 2.630	N.A.
	DVC, No Δt	0.185 ± 0.091	13.907 ± 1.119	0.872 ± 0.078
	DVC+NFW, No Δt	0.187 ± 0.067	13.877 ± 1.299	0.864 ± 0.067
	DVC+NFW*, No Δt	0.207 ± 0.067	13.916 ± 1.299	0.863 ± 0.067
	SIE, $H1$	0.120 ± 0.030	13.420 ± 1.630	N.A.
	DVC, $H1$	0.000 ± 0.005	22.122 ± 4.883	0.909 ± 0.080
	DVC+NFW, $H1$	0.218 ± 0.103	22.029 ± 4.655	0.871 ± 0.074
	DVC+NFW*, $H1$	0.240 ± 0.103	13.943 ± 4.655	0.864 ± 0.074
	SIE, $H2$	0.050 ± 0.030	10.300 ± 1.630	N.A.
	DVC, $H2$	0.000 ± 0.003	22.615 ± 7.268	0.974 ± 0.135
	DVC+NFW, $H2$	0.220 ± 0.103	22.116 ± 4.655	0.872 ± 0.074
RXJ0911	**H-band**	**0.128 ± 0.069**	**−49.345 ± 2.558**	**0.869 ± 0.207**
	SIE, No Δt	0.250 ± 0.020	-73.470 ± 2.730	N.A.
	DVC, No Δt	0.223 ± 0.015	-59.902 ± 1.953	1.395 ± 0.110
	DVC+NFW, No Δt	0.337 ± 0.037	-52.109 ± 2.187	1.083 ± 0.173
	DVC+NFW*, No Δt	0.329 ± 0.037	-51.630 ± 2.037	0.994 ± 0.039
	SIE, $H1$	0.230 ± 0.010	-69.860 ± 1.880	N.A.
	DVC, $H1$	0.272 ± 0.015	-69.963 ± 1.666	1.665 ± 0.152
	DVC+NFW, $H1$	0.323 ± 0.024	-52.462 ± 1.892	1.113 ± 0.161
	DVC+NFW*, $H1$	0.278 ± 0.024	-54.138 ± 1.892	0.820 ± 0.161
	SIE, $H2$	0.300 ± 0.010	-77.530 ± 1.880	N.A.
	DVC, $H2$	0.360 ± 0.015	-77.499 ± 1.666	1.581 ± 0.152
	DVC+NFW, $H2$	0.340 ± 0.024	-51.927 ± 1.892	1.071 ± 0.161
SDSS0924	**H-band**	**0.090 ± 0.051**	**−24.449 ± 11.011**	**0.253 ± 0.062**
	SIE	0.110 ± 0.090	-53.810 ± 9.160	N.A.
	DVC	0.190 ± 0.011	-45.174 ± 4.532	0.255 ± 0.027
	DVC+NFW	0.190 ± 0.011	-45.257 ± 3.173	0.255 ± 0.022
	DVC+NFW*	0.191 ± 0.011	-45.083 ± 3.173	0.255 ± 0.022

Continued on next page

Table 4.3 – Continued

System	*Model*	ε	*PA* (°)	$r_{\rm eff}('')$
PG1115	**H-band**	**0.035 ± 0.169**	**42.322 ± 8.762**	**0.443 ± 0.092**
	SIE, No Δt	0.200 ± 0.569	-77.306 ± 9.121	N.A.
	DVC, No Δt	0.000 ± 0.093	42.322 ± 9.160	0.441 ± 0.087
	DVC+NFW, No Δt	0.000 ± 0.021	42.342 ± 9.227	0.456 ± 0.013
	DVC+NFW*, No Δt	0.000 ± 0.021	42.344 ± 9.227	0.456 ± 0.013
	SIE, $H1$	0.140 ± 0.186	-82.324 ± 12.032	N.A.
	DVC, $H1$	0.000 ± 0.077	42.299 ± 9.012	0.449 ± 0.087
	DVC+N FW, $H1$	0.032 ± 0.093	41.639 ± 5.357	0.448 ± 0.076
	DVC+NFW*, $H1$	0.008 ± 0.093	42.357 ± 5.357	0.442 ± 0.076
	SIE, $H2$	0.109 ± 0.186	-83.006 ± 12.032	N.A.
	DVC, $H2$	0.000 ± 0.077	42.320 ± 9.012	0.451 ± 0.087
	DVC+NFW, $H2$	0.020 ± 0.102	42.138 ± 5.357	0.444 ± 0.102
SDSS1138	**H-band**	**0.000 ± 0.092**	**90.584 ± 9.896**	**0.199 ± 0.085**
	SIE	0.050 ± 0.110	37.400 ± 10.700	N.A.
	DVC	0.006 ± 0.011	89.465 ± 9.743	0.202 ± 0.077
	DVC+NFW	0.006 ± 0.010	89.496 ± 9.758	0.202 ± 0.003
	DVC+NFW*	0.006 ± 0.010	89.461 ± 9.758	0.202 ± 0.003
B1422	**H-band**	**0.258 ± 0.105**	**−53.570 ± 2.909**	**0.107 ± 0.056**
	SIE, No Δt	0.270 ± 0.070	-57.670 ± 1.380	N.A.
	DVC, No Δt	0.304 ± 0.095	-54.875 ± 2.384	0.139 ± 0.050
	DVC+NFW, No Δt	0.300 ± 0.080	-55.081 ± 2.367	0.130 ± 0.053
	DVC+NFW*, No Δt	0.311 ± 0.093	-54.977 ± 2.097	0.128 ± 0.019
	SIE, $H1$	0.280 ± 0.040	-57.580 ± 0.980	N.A.
	DVC, $H1$	0.753 ± 0.032	-52.619 ± 0.356	0.334 ± 0.029
	DVC+NFW, $H1$	0.260 ± 0.130	-53.554 ± 3.604	0.108 ± 0.069
	DVC+NFW*, $H1$	0.258 ± 0.130	-53.588 ± 3.604	0.079 ± 0.069
	SIE, $H2$	0.280 ± 0.040	-57.580 ± 0.980	N.A.
	DVC, $H2$	0.740 ± 0.032	-52.711 ± 0.356	0.338 ± 0.029
	DVC+NFW, $H2$	0.260 ± 0.130	-53.554 ± 3.604	0.108 ± 0.069
WFI2033	**H-band**	**0.075 ± 0.094**	**−22.412 ± 20.456**	**0.923 ± 0.182**
	SIE, No Δt	0.198 ± 0.061	15.938 ± 3.152	N.A.
	DVC, No Δt	0.450 ± 0.018	5.190 ± 0.351	0.859 ± 0.123
	DVC+NFW, No Δt	0.449 ± 0.069	5.156 ± 0.813	0.858 ± 0.118
	DVC+NFW*, No Δt	0.449 ± 0.069	5.141 ± 0.813	0.859 ± 0.118
	SIE, $H1$	0.045 ± 0.011	-66.600 ± 12.392	N.A.
	DVC, $H1$	0.184 ± 0.017	-79.986 ± 1.181	1.849 ± 0.201
	DVC+NFW, $H1$	0.166 ± 0.111	13.593 ± 6.928	1.162 ± 0.119
	DVC+NFW*, $H1$	0.110 ± 0.111	21.438 ± 6.928	1.396 ± 0.119
	SIE, $H2$	0.147 ± 0.011	-84.995 ± 12.392	N.A.
	DVC, $H2$	0.284 ± 0.017	-78.060 ± 1.181	1.968 ± 0.201
	DVC+NFW, $H2$	0.156 ± 0.111	15.93 ± 6.928	1.158 ± 0.119

Figure 4.2: Visualisation of the overlap between best-fitting parameters of all models, for each galaxy. The parameters plotted here with their error bars are given in Table 4.3.

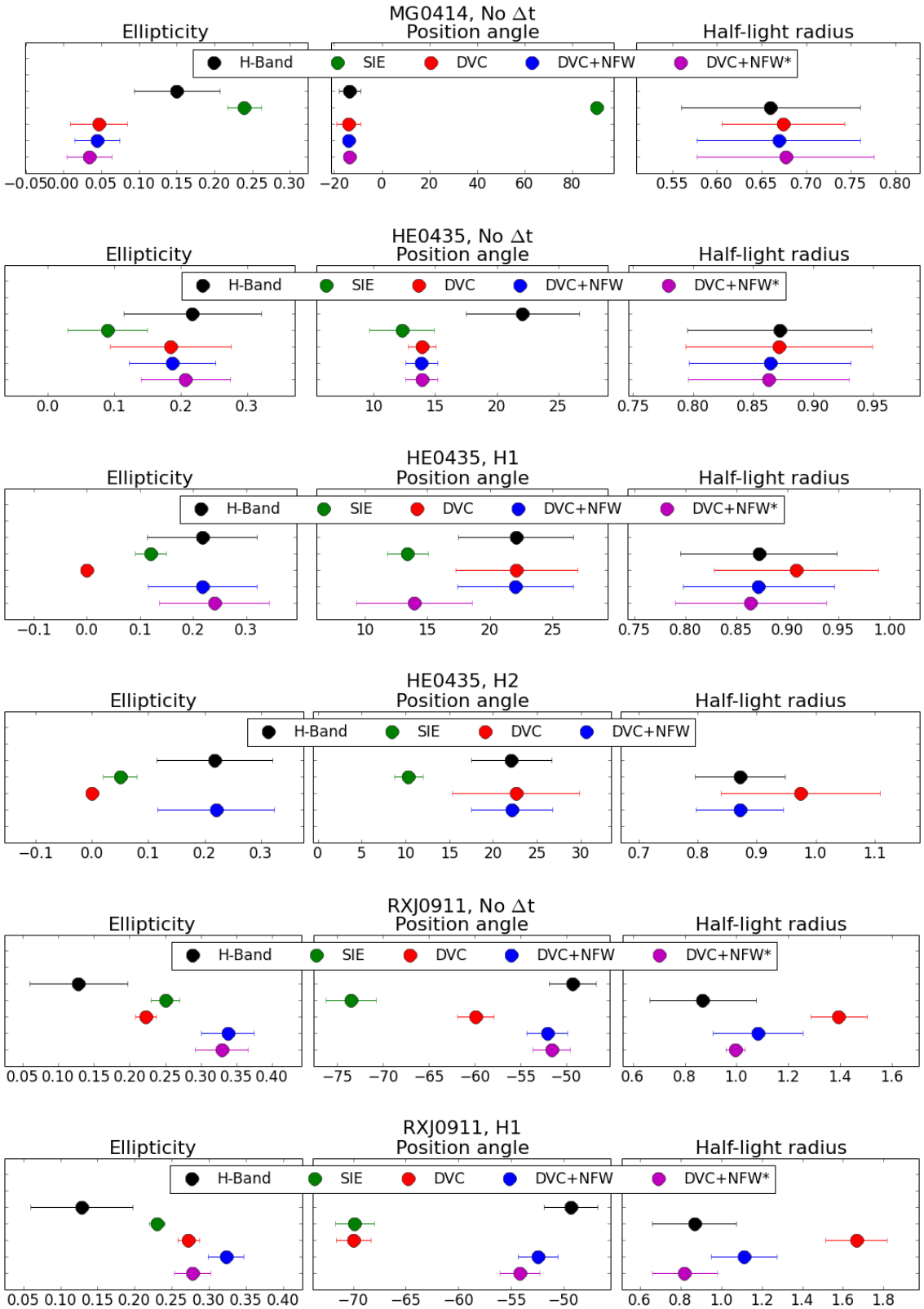

Figure 4.2: Continued.

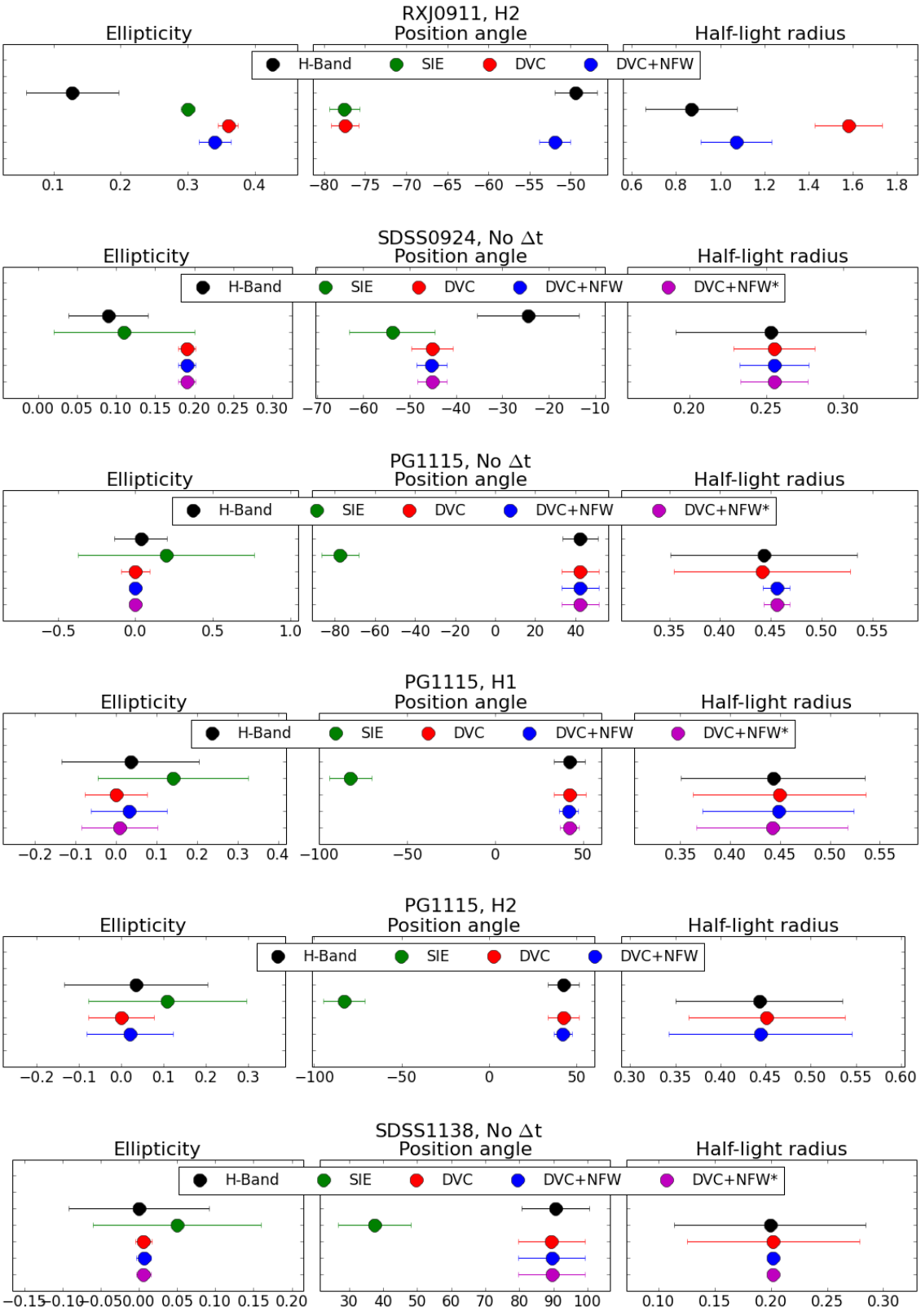

Figure 4.2: Continued

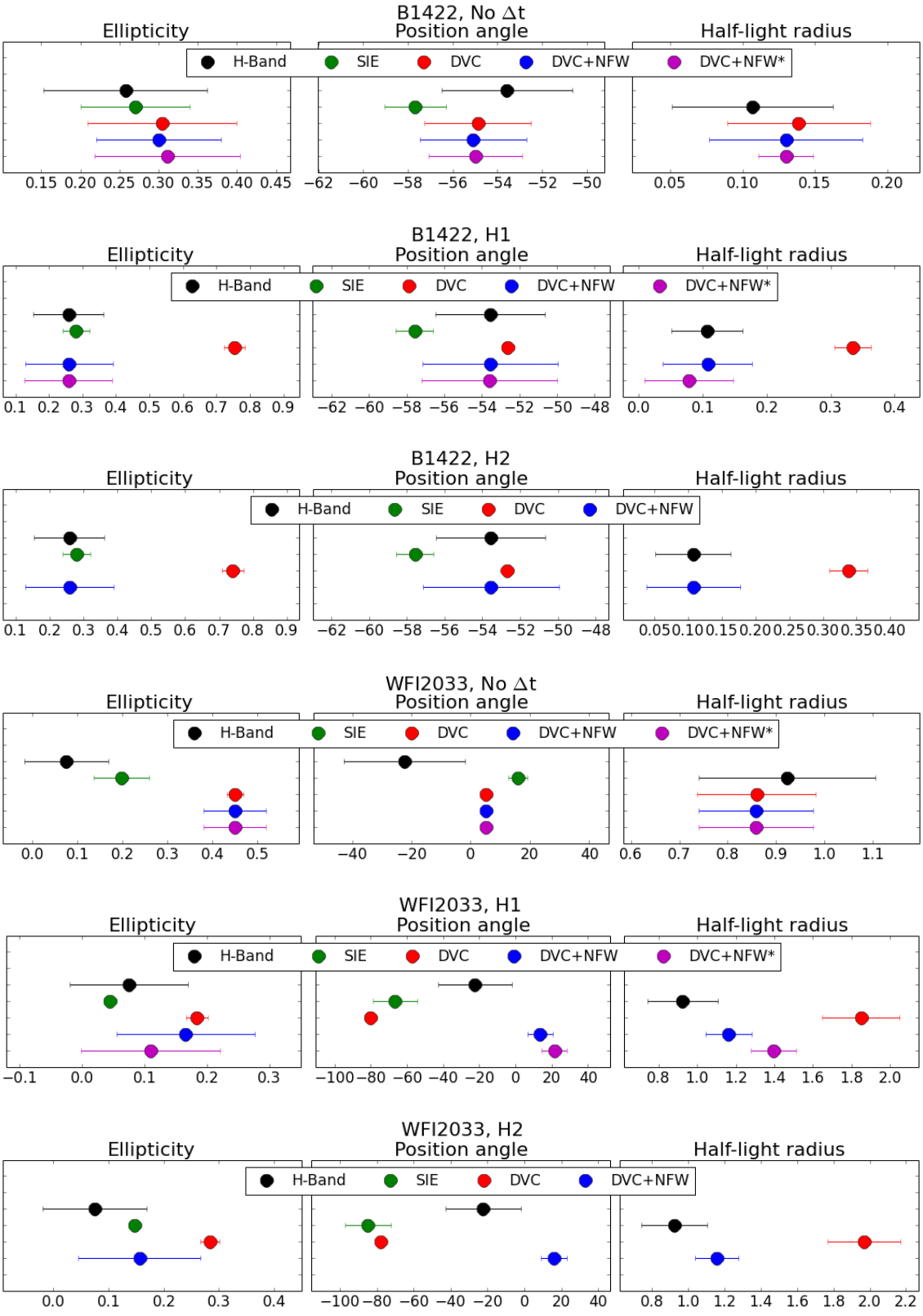

Figure 4.3: Comparison of best-fitting convergence profiles $\kappa(r)$ with and without halos. Each row corresponds to a system. The left column corresponds to unconstrained NFW halos, the right column, to NFW* halos with a scaling radius proportional to the half-light radius of the luminous counterpart. The corresponding dark matter fraction within $\theta_{\rm eff}$ ($f_{\rm DM}(\theta_{\rm eff})$) is given on each panel. The full red line shows the convergence profile of the DVC only mass model. The dash-dotted blue line shows that of the DVC as a part of a composite DVC + NFW(*) mass model, and the dashed black line, that of the NFW (NFW*) component. Two vertical green lines respectively indicate the half-light radius (dashed) and the Einstein radius (full) of the lens.

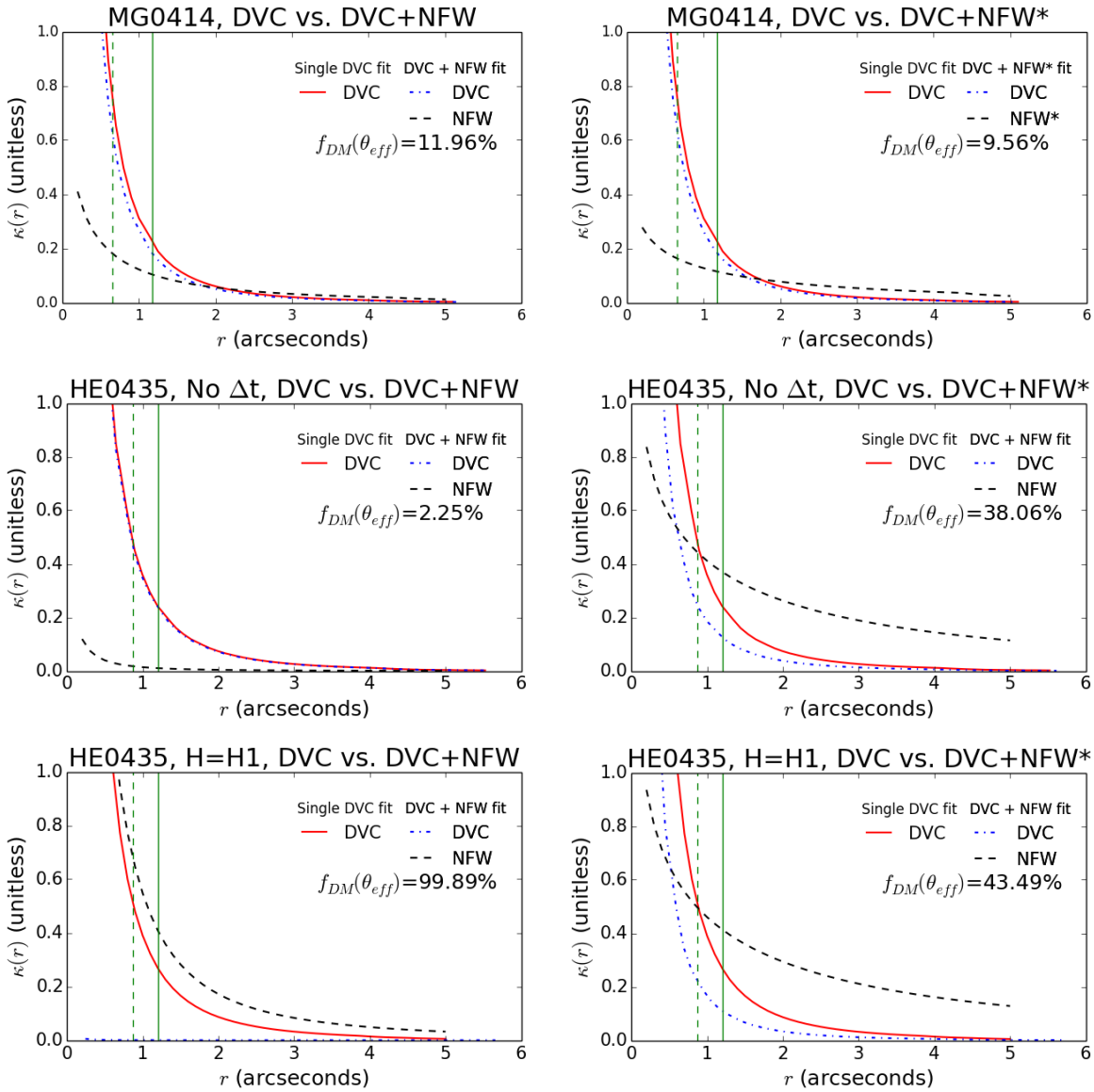

Figure 4.3: Continued.

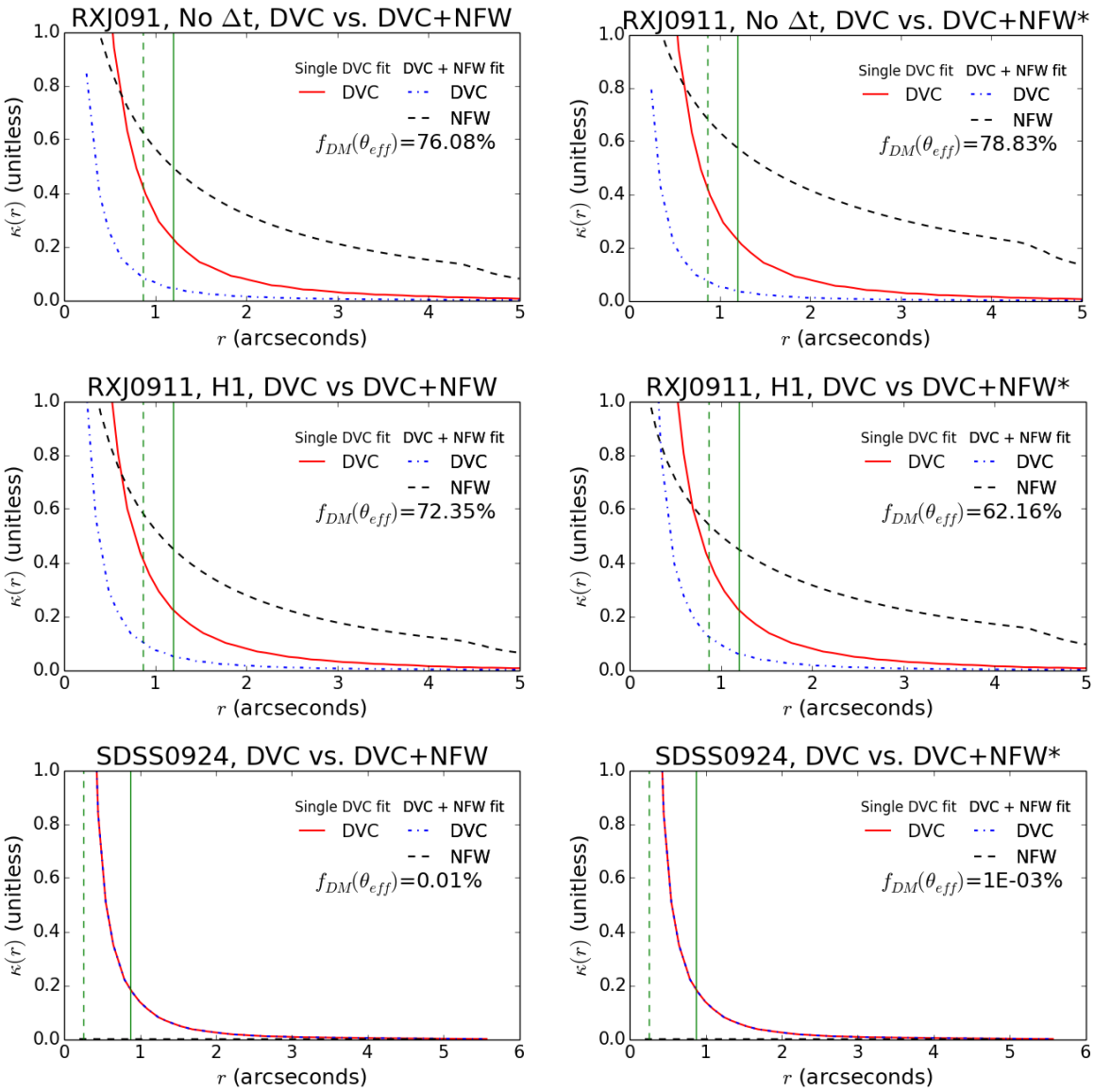

Figure 4.3: Continued.

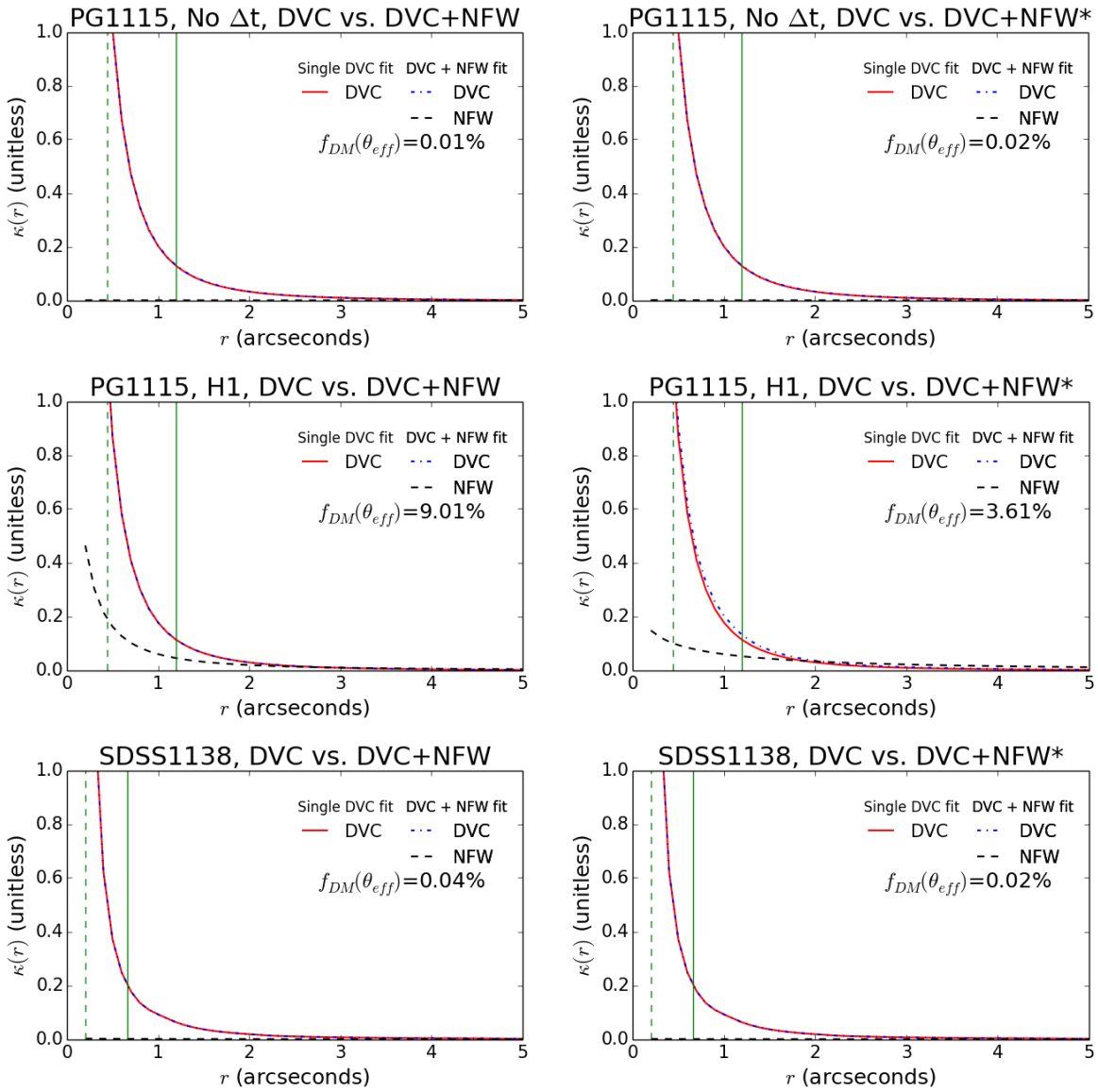

Figure 4.3: Continued.

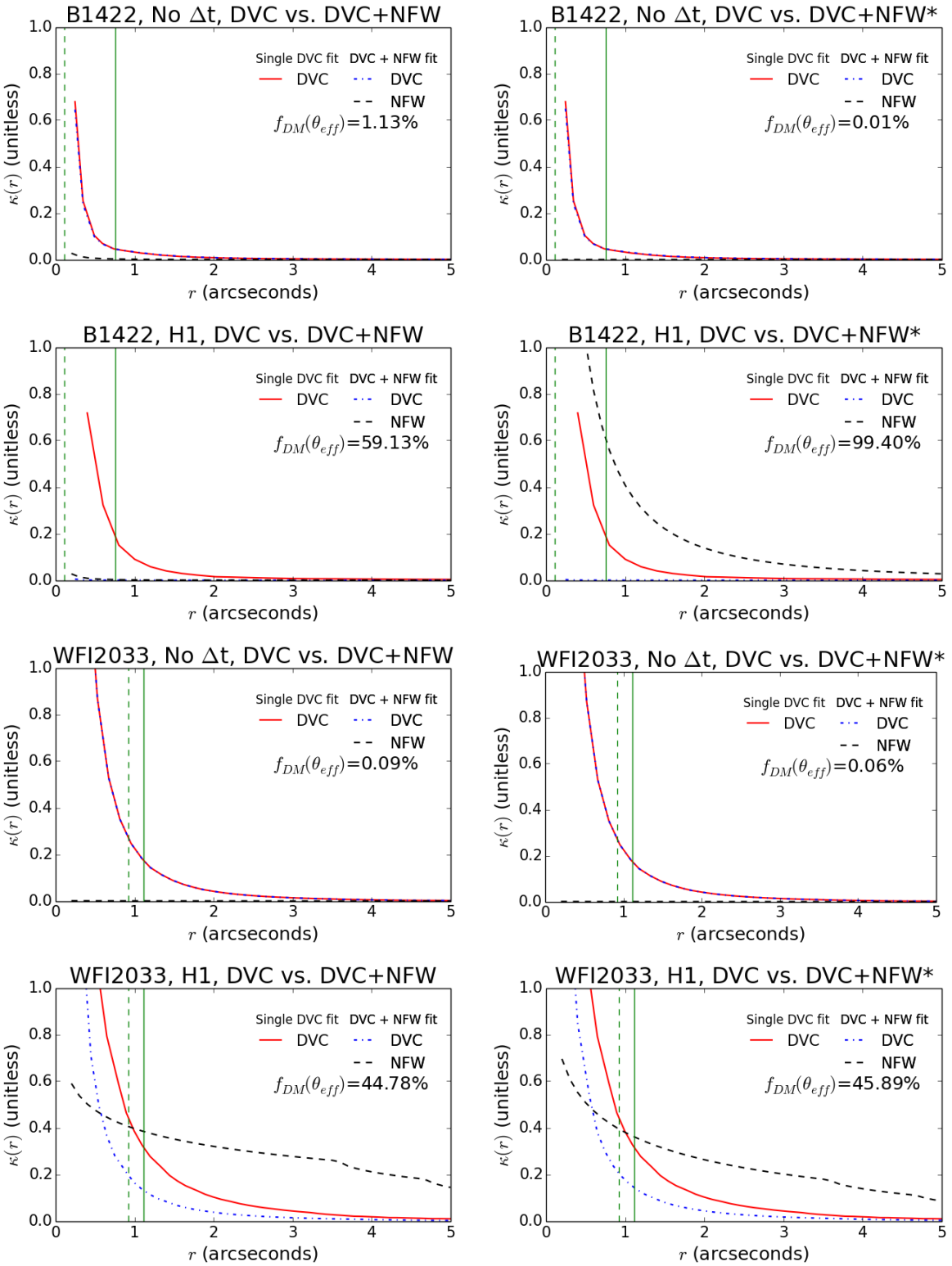

4.6 Conclusion

We conducted several fits on our observations, taking all the necessary precautions regarding local minima and considering several mass models, each corresponding to some different assumptions on the dark matter distribution. We have observed that the SIE model works best in the majority of cases. There is one system, PG1115, for which the DVC model produces a better fit than the SIE, favouring a constant mass-to-light ratio lensing galaxy. We have also noticed that at the exception of three out of eight cases, adding an NFW(*) dark matter halo does not change (nor improve) the quality of the fit. This means that the lenses are equally well described by a constant mass-to-light ratio model than by a composite model with a classical halo, making it difficult to bring out any conclusion on the existence of such halos around our lenses. This might trigger doubt towards the existence of dark matter halos around early-type galaxies, but the dispersed character of the results as well as the scatter in the dark matter fractions indicate that using the fit comparison to assess the existence of dark matter halos around ellipticals is untrustworthy. What is more, we only have a low number of constraints on our models and they are probably affected by degeneracies. This calls for an investigation of the dark matter content of early-type galaxies through a more robust proxy.

The mass within the Einstein radius is the most accurate mass measurement that can be obtained for lensing galaxies (Oguri et al. 2014, Schneider and Sluse 2014). It is quite robust as it depends very little on the mass models and on the assumptions we make for the fits, as can be seen from the results in Table 4.2, where θ_{Ein} has nearly the same value for all models of a system. For that reason, we consider it to be the most appropriate measurement of the total matter content in our galaxies. Comparing it to its light content, through the mass-to-light ratios, should give a model-independent indication of our galaxies dark matter content. This work is conducted in Chapter 5.

5 Mass-to-light ratios and search for dark matter halos

The mass-to-light ratio of a galaxy yields first-hand information on its dark matter content. A surplus of M compared to L can indicate that the mass includes a contribution from matter that does not emit (much) light, whether it is dust, gas, low-mass stars like brown dwarfs, or dark matter.

We compute the mass-to-light ratio of our galaxies within their Einstein radii. In order to do so, we first need to determine the total H-band surface flux and the total mass within an aperture of a radius equal to the Einstein radius. The details of this process along with an estimation of its uncertainty are given in Sections 5.1 and 5.2. We then compare these results to theoretical M/L inferred from stellar population evolutionary models. We also compute approximate theoretical M/L ratios for a combination of a stellar component and a dark matter halo. The details and validity of this comparison are discussed in Section 5.3.

Beyond its very value, the behaviour of M/L with the galacto-centric distance is at the centre of this study. The original question was whether or not elliptical galaxies are embedded in dark matter halos like their spiral equivalent. It is reasonable to consider that the M/L of a galaxy with an extended dark matter halo should increase the farther out we probe. Such an increase over the various galacto-centric distances in our sample would be a clue for the existence of halos around its members.

5.1 Determination of flux within θ_{Ein}

The quantity we are aiming at is the total flux of the lens in the H-band within its Einstein radius. It is computed by integrating the brightness profile of the lens in a circular aperture centred on the lens itself, of a radius equal to $\theta_{\rm Ein}$. This operation is conducted on a two-dimensional image of the deconvolved light profile of the lens that is built based on its

best-fitting H-band de Vaucouleurs profile. It is the best approach to its true form that we can get: it is obviously not affected by the instrumental profile and by the lensed signal, and neither does it have cosmic rays, nor ill, hot, and poorly corrected pixels. However, at this stage, one crucial parameter remains unknown: the scaling factor I_0. Similarly to what is performed for the shape parameters, we aim at a simple, 1-D measurement method for I_0. We scan a wide interval of I_0 values and refine it until it minimises the translation constant between the model and the data radial profiles in the $(\ln I \; r^{1/4})$ space. Once in possession of the correct I_0 value, we can produce an image of the deconvolved galaxy profile, which is thus our best model of the lensing galaxy brightness distribution. The best-fitting models and residuals shown on Figure 3.15 actually include the I_0 parameter already.

This image of the best brightness distribution model is used to integrate the H-band flux F_{H} within the Einstein radius. The integration yields, after correcting for the DN to erg/cm^2/s/Å conversion (taking into account the instrument gain, sensitivity, and the exposure time), the flux in the instrumental bandpass wavelengths, F_λ. However, because of the object redshift, there is an offset between the lens spectrum and that bandpass. This offset is corrected through a K-correction, that is computed based on an elliptical galaxy template spectrum synthesised using the *Pégase* software (Fioc and Rocca-Volmerange 1997). The K-correction consists in a factor K such that $F_{\mathrm{H}} = KF_\lambda$, where F_λ is the measured flux and F_{H} is the corrected H-band flux. K is obtained through a linear interpolation of the logarithm of the flux in the synthetic spectrum, between the redshifted instrument wavelength and the actual rest-frame H-band wavelength. The K-correction makes it possible to obtain a true, galaxy H-band flux from part of the galaxy emission that actually originates in a lower wavelength. The validity of such a process depends on the degree of trust we put in the template spectrum. We used results from evolutionary models of galaxies from Fioc and Rocca-Volmerange (1997), where the authors computed galaxy spectra across the Hubble sequence, based on a stellar population, a nebular continuum and emission lines. The only source of uncertainty they do not take into account in their results is the combined effect of extinction and metallicity. However, these factors mostly affect metal-enriched ellipticals, and we do not assume our sample to fall into that category.

Finally, the K-corrected H-band flux is expressed in solar units, using a value of the solar flux in the H-band $F_{\mathrm{H},\odot}$ (Colina et al. 1996, Mann and von Braun 2015) corrected for the lens distance, using the WMAP cosmology parameters (Lewis 2008) ($\Omega_\Lambda = 0.73$, $\Omega_m = 0.27$). Since we considered two values for the Hubble constant, $F_{\mathrm{H},\odot}$ depends on that choice too. The whole process is shown in Table 5.1, where the integrated flux before and after K-correction is given, as well as its conversion in solar units. It is shown as an example for the SIE models, with time delays if any had been measured. The exact same process is applied using each Einstein radius given in Table 4.2, for both Hubble constant values, but is not shown in Table 5.1 for readability. Instead, all the flux measurement results are added in Table A1 as appendices at the end of this work.

The error bar on F_{H} takes a variety of factors into account. A similar procedure to that for the shape parameters error calculation (Section 3.5) is put into operation. On top of

the dispersion among the data frames of each system, we consider sources of systematic errors, conduct the $F_{\rm H}$ measurement with their values shifted by an offset equal to their 1σ error bar, and get their contribution to the total $F_{\rm H}$ error budget. This time, the sources of systematic errors include the sky subtraction, the arc subtraction and the determination of point sources positions and intensities. We also do take into account the effect from a miscalculation of the shape parameters. We find the errors on the PA and ε did not influence the $F_{\rm H}$ measurement. On the other hand, the half-light radius and central intensity parameter I_0 are tightly correlated: an overestimated $\theta_{\rm eff}$ would give an underestimated I_0 and yield a wrong result for the integrated flux. To quantify this effect, we conduct the $F_{\rm H}$ measurement starting from the I_0 determination with a set of parameters that include an overestimate value of $\theta_{\rm eff} + 1\sigma_{\theta_{\rm eff}}$. Because we already compute an error bar on $F_{\rm H}$ from the point source positions and intensities and from the sky and arc subtraction, the $\sigma_{\theta_{\rm eff}}$ value we use here only combines its dispersion and its error bars from the galaxy centre position ($\sigma_{\rm rand}$, $\sigma_{\rm xg}$ and $\sigma_{\rm yg}$ in Table 3.1).

On top of that, we add a contribution to the error bar on $F_{\rm H}$ coming from the uncertainty on $\theta_{\rm Ein}$. In fact, we are using $F_{\rm H}$ to compute a mass-to-light ratio. We are aiming at one M/L ratio per mass model, and are therefore computing one M and one L, or $F_{\rm H}$, per mass model. Even though the value of $\theta_{\rm Ein}$ changes very little with the mass model, we consider each $\theta_{\rm Ein}$ value individually, along with its uncertainty. We conduct the flux integration in an aperture of a radius equal to $\theta_{\rm Ein}$, and then to $\theta_{\rm Ein} + 1\sigma_{\theta_{\rm Ein}}$ to estimate the propagation of that error on $F_{\rm H}$. Eventually, since all the error sources are considered independent form each other, they are all summed up quadratically to yield the total error bar.

The error budget is given in Table 5.2 on the SIE case for $H_0 = H1$, as an example. Time delay constraints are included if available.

5.2 Determination of mass within θ_{Ein}

By definition, the average surface density reaches the critical density at the Einstein radius of a lens:

$$\Sigma_{cr} = \frac{c^2}{4\pi G}\frac{D_{\rm S}}{D_{\rm LS}D_{\rm L}} \ . \tag{5.1}$$

The mass within the Einstein radius is then quite straightforward to compute, as it is the product of the average surface density within $\theta_{\rm Ein}$ and the surface of the circular aperture of radius $\theta_{\rm Ein}$,

$$M(\theta_{\rm Ein}) = \Sigma_{\rm cr} \times \pi\theta^2_{\rm Ein} \ . \tag{5.2}$$

This simple process is conducted for each value of $\theta_{\rm Ein}$ presented in Table 4.2. At this step, the results are cosmology-dependent. Indeed, the angular diameter distances $D_{\rm S}$, $D_{\rm LS}$ and $D_{\rm L}$ are evaluated thanks to the respective lens and source redshifts, and the redshift-distance conversion depends on the cosmological parameters $\Omega_{\rm m}$, Ω_Λ and the Hubble constant. In fact, so does the angular-linear distance conversion that we use for the Einstein radius, which is computed in arcseconds. We used the parameter values

Table 5.1: Integrated flux within an aperture of radius $\theta_{\rm Ein}$ before (F_λ) and after ($F_{\rm H}$) K-correction, for the SIE mass model with time delay constraints if available. The results are presented for both values of the Hubble constant. The latter mostly changes the conversion into solar units. Details of the error calculation on $F_{\rm H}$ can be found in Table 5.2.

	$H_0 = 73.24\ km/s/Mpc$				
	$\theta_{\rm Ein}$ (")	F_λ(erg/(s cm^{2}Å))	*K-correction*	$F_{\rm H}$(erg/(s cm^{2}Å))	$F_{\rm H}(10^{11}F_{\rm H\odot})$
MG0414	1.175	$8.156\ 10^{-18}$	0.50996	$4.160\ 10^{-18}$	2.940 ± 0.704
HE0435	1.200	$1.578\ 10^{-17}$	0.63701	$1.005\ 10^{-17}$	1.165 ± 0.170
RXJ0911	1.094	$7.127\ 10^{-18}$	0.54698	$3.898\ 10^{-18}$	1.592 ± 0.038
SDSS0924	0.874	$1.338\ 10^{-17}$	0.66599	$8.910\ 10^{-18}$	0.696 ± 0.137
PG1115	1.135	$2.074\ 10^{-17}$	0.70483	$1.462\ 10^{-17}$	0.667 ± 0.080
SDSS1138	0.665	$7.923\ 10^{-18}$	0.64090	$5.078\ 10^{-18}$	0.558 ± 0.065
B1422	0.771	$7.387\ 10^{-18}$	0.68946	$5.093\ 10^{-18}$	0.288 ± 0.085
WFI2033	1.119	$8.539\ 10^{-18}$	0.57381	$4.900\ 10^{-18}$	1.367 ± 0.246
	$H_0 = 62.3\ km/s/Mpc$				
	$\theta_{\rm Ein}$ (")	F_λ(erg/(s cm^{2}Å))	*K-correction*	$F_{\rm H}$(erg/(s cm^{2}Å))	$F_{\rm H}(10^{11}F_{\rm H\odot})$
MG0414	1.175	$8.156\ 10^{-18}$	0.50996	$4.160\ 10^{-18}$	4.063 ± 0.973
HE0435	1.200	$1,577\ 10^{-17}$	0.63701	$1.005\ 10^{-17}$	1.517 ± 0.222
RXJ0911	1.094	$7.167\ 10^{-18}$	0.54698	$3.920\ 10^{-18}$	2.212 ± 0.052
SDSS0924	0.874	$1.338\ 10^{-17}$	0.66599	$8.910\ 10^{-18}$	0.962 ± 0.189
PG1115	1.135	$2.074\ 10^{-17}$	0.70483	$1.462\ 10^{-17}$	0.920 ± 0.111
SDSS1138	0.665	$7.923\ 10^{-18}$	0.64090	$5.078\ 10^{-18}$	1.860 ± 0.217
B1422	0.771	$7.398\ 10^{-18}$	0.68946	$5.101\ 10^{-18}$	0.399 ± 0.118
WFI2033	1.119	$8.512\ 10^{-18}$	0.57381	$4.884\ 10^{-18}$	1.883 ± 0.339

Table 5.2: Error budget on $F_{\rm H}$ for Einstein radii obtained with an SIE mass model, with $H_0 = H1$. All quantities are expressed in units of $10^{11}F_{\rm H\odot}$. *From left to right*: total flux, dispersion, error from the uncertainty on the Einstein radius, on the X-, Y- position of the sources, on their intensities, on the half-light radius, on the sky and arc subtraction and the total error. "N.A." stands for "not applicable".

System	$F_{\rm H}$	$\sigma_{\rm rand}$	$\sigma_{\rm sky}$	$\sigma_{\rm arc}$	$\sigma_{\rm x_s}$	$\sigma_{\rm y_s}$	$\sigma_{\rm I_s}$	$\sigma_{\theta_{\rm eff}}$	$\sigma_{\theta_{\rm Ein}}$	$\sigma_{\rm tot}$
MG0414	2.940	0.070	0.286	N.A.	0.334	0.315	0.318	0.313	0.001	0.704
HE0435	1.165	0.024	0.077	0.073	0.067	0.067	0.067	0.060	3E-04	0.170
RXJ0911	1.592	0.021	0.026	N.A.	0.001	0.008	0.006	0.015	0.001	0.038
SDSS0924	0.696	0.004	0.059	0.034	0.059	0.061	0.061	0.057	3E-05	0.137
PG1115	0.667	0.004	0.028	0.045	0.031	0.031	0.031	0.028	3E-05	0.080
SDSS1138	0.558	0.009	0.015	0.048	0.019	0.020	0.020	0.021	3E-04	0.065
B1422	0.288	0.005	0.036	0.014	0.038	0.034	0.040	0.038	1E-04	0.085
WFI2033	1.367	0.058	0.029	N.A.	0.199	0.061	0.071	0.090	4E-04	0.246

of WMAP, and consider our usual two values of H_0 separately. All these dependencies yield several values of the mass: one for each Hubble constant, one for each mass model. They are expressed in solar units, one solar mass being 1.989 10^{30} kg (Mamajek et al. 2015, Prša et al. 2016). The error bar on $M(\theta_{\text{Ein}})$ comes only from the error on θ_{Ein} and is therefore relatively small. The $M(\theta_{\text{Ein}})$ results for the SIE mass models are shown in Table 5.3 with their error bars. The values are very similar for all other mass models, and so are the relative error bars. The results for all other combinations of mass model and Hubble constant are added in Table A1 at the end of this work.

Table 5.3: Mass within the Einstein radii from the SIE mass models, with their error bars. All masses are expressed in 10^{11} $M_{\odot}$.

SIE models, time delays (if any)				
	$H_0 = 73.24\ km/s/Mpc$		$H_0 = 62.3\ km/s/Mpc$	
System	θ_{Ein}	$M(\theta_{\text{Ein}})$	θ_{Ein}	$M(\theta_{\text{Ein}})$
MG0414	1.175	5.730 ± 0.011	1.175	6.737 ± 0.013
HE0435	1.201	3.254 ± 0.008	1.200	3.823 ± 0.009
RXJ0911	1.094	3.840 ± 0.006	1.062	4.254 ± 0.006
SDSS0924	0.874	1.491 ± 5E-04	0.874	1.753 ± 6E-04
PG1115	1.135	1.919 ± 0.002	1.137	2.265 ± 0.002
SDSS1138	0.665	0.881 ± 0.003	0.665	1.036 ± 0.004
B1422	0.771	0.867 ± 0.004	0.771	1.020 ± 0.004
WFI2033	1.119	4.358 ± 0.008	1.116	5.094 ± 0.009

5.3 Characterisation of mass-to-light ratios

Now in possession of the total mass and flux comprised within θ_{Ein}, both expressed in solar units with their error bars, we can compute the mass-to-light ratio at θ_{Ein} and proceed to the core analysis of this work. We produce a value of the mass-to-light ratio at θ_{Ein} for each system, under each considered mass model, for each Hubble constant. Each of these values is given in Table 5.5 with its error bar, at the end of this Chapter. The error bar on M/L stems from the propagated error bars on M and L. The result is quite independent from the mass model we consider in the lens modelling, and varies little with the Hubble constant. It seems thus reasonable to consider, for each lensing galaxy, only the best-constrained model. For that reason, in all further discussions, we will be considering M/L ratios coming from models with time delay constraints when available, and we will restrain the discussion to values measured with $H_0 = 73.24\ km/s/Mpc$. The validity of such a decision is discussed in Subsection 5.3.3.

As a first step, the M/L are compared to expected theoretical M/L values under a variety of hypotheses regarding the galaxies dark matter content, in Subsection 5.3.1. Then, the slope of M/L versus the galacto-centric distance is evaluated, because the M/L ratio is expected to increase outwards in a dark matter halo embedded galaxy, in Subsection 5.3.2.

5.3.1 Comparison to theoretical M/L

5.3.1.1 Computation of theoretical M/L

Figure 5.1 shows the measured M/L values on our lensing galaxies as a function of the Einstein radius expressed in half-light radii, $\theta_{\rm Ein}/\theta_{\rm eff}$. It has three panels, one for each mass model. The points coming from DVC mass profiles appear on all panels, in order to compare profiles with and without dark matter halos. The background of the graph displays three different coloured zones. They correspond to theoretical M/L under three different assumptions regarding the galactic dark matter distribution.

The green zone corresponds to constant M/L with respect to the galacto-centric distance. It is computed based on single stellar population models computed by Maraston (2005). The latter provides, among others, M/L values of stellar population models, in all spectral bands, depending on their age, metallicity, initial mass function (Kroupa IMF (Kroupa 2002) or Salpeter IMF (Salpeter 1955)) and horizontal branch morphology. They thus represent M/L from a stellar component only. The probable ranges for these quantities in our sample galaxies provide the width of the green zone of Figure 5.1. We considered ages of stellar populations between 5 and 10 Gyr, as well as a metallicity range $Z/H \subset [-1.35; 0.35]$. We focused on the H-band M/L only. We took both possible IMFs and horizontal branch morphologies into account.

The blue zone corresponds to galaxies with constant mass-to-light ratios, too, only this time, the upper M/L limit of the blue area is the double of that of the green area. Cosmological nucleosynthesis (Schramm and Turner 1998) predicts a baryonic matter density of 4% (Cyburt et al. 2016, Pitrou et al. 2018). Yet, the inventory of baryonic matter in the Universe reaches a density of 2% meaning that about half the baryonic matter in the Universe seems to be missing (Fukugita and Peebles 2004, Cen and Ostriker 2006, Shull et al. 2012, Nicastro et al. 2017). It could be hiding under the form of baryonic dark matter. If it were distributed in galaxies, in a "mass-follows-light" fashion, then the M/L value of galaxies could double. This is the hypothetical situation that the blue zone illustrates. This baryonic dark matter content calculation is rough and unorthodox: there is no good reason for all the missing baryonic matter to be hiding in elliptical galaxies only. In fact, the most likely solution to the missing baryons problem currently resides in the filaments of warm intergalactic medium (Davé et al. 2001, Tripp et al. 2004, Nicastro et al. 2018). Finally, even so, it might not be distributed like the regular baryonic matter at all and still present a dependency on the galacto-centric distance. The blue zone is but an approximation of this broad hypothesis. It is a visualisation of the assumption of homogeneously distributed dark matter, in a "mass-follows-light" manner.

The red zone corresponds to theoretical M/L of early-type galaxies with a light component that follows a de Vaucouleurs law and a dark matter component distributed as an NFW halo. The M/L dependency on the galacto-centric distance is computed analytically. A projected circular de Vaucouleurs profile (Prugniel and Simien 1997) is integrated in a circular region of increasing galacto-centric radius, yielding a quantity we label $M_{\rm L}$. Similarly, a projected NFW profile is integrated in the same region, yielding $M_{\rm D}$. The ratio between these two quantities, $M_{\rm D}/M_{\rm L}$, is linked to the M/L expressed in solar units

through the following :

$$\frac{M/L}{M_\odot/L_\odot} = 1 + \frac{M_\mathrm{D}}{M_\mathrm{L}} \tag{5.3}$$

where $M = M_\mathrm{D} + M_\mathrm{L}$. The curve is calibrated to match the M/L of NGC3198, one of the best studied spiral galaxies in terms of rotation curve (van Albada et al. 1985). It reaches 4 at 5.8 r_eff from its centre. The M/L value computed that way are in agreement with M/L measured on elliptical galaxies with kinematics data such as in Pierini et al. (2002), Cappellari et al. (2006b), Grillo et al. (2008) or Ferreras et al. (2008). Calibrating the M/L dependency on the radial coordinate on a single galaxy might seem a little abrupt, but the effect of such a choice is discussed in Subsection 5.3.2. NGC3198 is a spiral galaxy, whereas we are studying early-type galaxies. We are thereby restraining our search to "spiral-like" halos. Once again, the width of the red zone corresponds to a range of reasonable age, metallicity, IMF and horizontal branch morphologies for the stellar population of our sample of galaxies, the same as for the green zone, from Maraston (2005).

It should be emphasised that these three theoretical ranges for M/L rely on broad hypotheses and are quite approximative. For example, the green zone corresponds only to the stellar population contribution, and extrapolating it to the M/L of a galaxy without any dark matter would imply neglecting all of its gas and dust content, which contribute to the mass without changing the light very much. By extension, simply doubling its upper limit to account for the missing big bang nucleosynthesis predictions of baryons propagates that error. Moreover, since Maraston (2005) was published, the solar abundances in metals, used as a basis for many stellar populations evolutionary tools, have been revised downwards. These tools also depend on the stellar evolution models, which have a domain of validity. For example, Maraston (2005) did not consider any convective overshooting, which might extend the main sequence of some stars, increasing the total luminosity of the population at certain ages. We used results from single stellar population models, meaning that all the stars have the same age and initial chemical composition. This might not be valid for elliptical galaxies, particularly under the merger galaxy formation scenario. Some secondary star formation may interfere with the stellar populations M/L expected in ellipticals, and a mix of single stellar population models taking the formation history into account would have been more precise (Pierini et al. 2002, Cappellari et al. 2006b). Nevertheless, the relevance of the H-band for this work comes from a weaker dependance of the M/L on stellar evolution models or galaxy colour indices (Fioc and Rocca-Volmerange 1997, Grillo et al. 2008, McGaugh and Schombert 2014, Jun and Im 2008). It is shown in Maraston (1998) and Maraston (1999) (specifically in their Figure 1) that the M/L of their synthetic stellar populations in the H-band are quite stable regarding the age and metallicity of the population. At a given age (of 10 Gyr), it remains constant to 4% in the domain of metallicity considered in this work. It shows a 55% increase when the age of the population doubles from 5 Gyr to 10 Gyr, whereas it nearly doubles in the B-band, for example. To sum up, the coloured zones should be taken as a coarse visualisation of possible M/L ranges for some assumptions on the dark matter profiles, whereas a stronger statement on whether or not dark matter halos might exist around our sample galaxies is made in the next Subsection.

The M/L measurements all lie out of the green zone, except for the one from SDSS1138 lying at its upper edge. This implies that all the lensing galaxies of the sample have a mass-to-light ratio at least higher than the stellar population contribution only. Given that elliptical galaxies may contain more than only stars (some gas and dust for example), this result could be expected. They mostly lie at the intersection of the blue and the red zone. The majority of our lensing systems are only probing out to one or two half-light radii, as only three of them (SDSS0924, SDSS1138 and B1422) have an Einstein radius over 2.5 $\theta_{\rm eff}$. Out of these three, only one is time delay-constrained. These outermost points are the most relevant to the search for dark matter halos, and yet, SDSS1138 and B1422 yield M/L ratios that lie out of the red zone, indicating a lower M/L than might be expected if they had a spiral-like halo. The WFI2033 result is worth noticing on most panels of Figure 5.1, because it lies at the upper border of the red zone, meaning its M/L ratio is even higher than the prediction including a dark matter halo.

The range coming from the uncertainty on the stellar population metallicity, IMF and age is quite large. However, two of the factors contributing to this wide M/L range can be corrected for in a straightforward manner: its age and its IMF. This is done in the next few paragraphs.

Figure 5.1: Measured mass-to-light ratios compared to theoretical values based on single stellar population models and on the integration of a projected NFW dark matter profile. The thickness of the background zones represents the uncertainty coming from the nature of the IMF, metallicity and age of the stellar population. The successive panels, from top to bottom, left to right, respectively correspond to SIE, DVC + NFW and DVC + NFW* lens models.

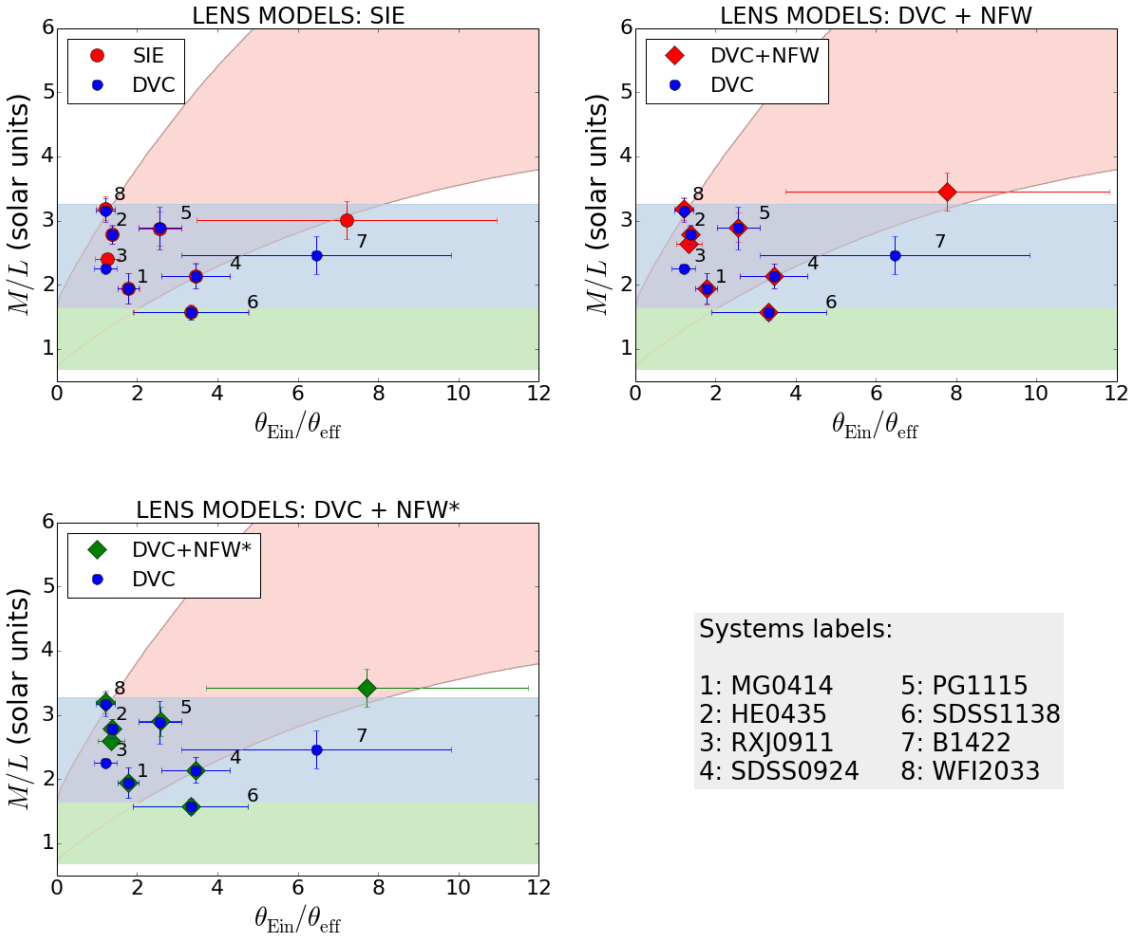

5.3.1.2 Effect of the age of the stellar population

The age of each galaxy can be estimated based on its redshift (Wright 2006), and the M/L values from Maraston (2005) can be interpolated to match each objects age instead of averaged over an age range. The width of the zones then only come from the uncertainty on metallicity, IMF and horizontal branch morphology. This implies that one theoretical M/L range should be computed for each object according to its age. A less tedious way to proceed would be to pick an age for the theoretical stellar population, e.g. 10 Gyr, and then apply a correction to the observed lenses M/L to account for the galaxy age. The measured M/L simply needs to be shifted of a value that can be estimated from Maraston (2005), so that it gives the M/L "as if" the galaxy was 10 Gyr. That correction is computed for both IMFs and for metallicities in the chosen range, then averaged to give one single correction per system.

The result of this process yields Figure 5.2, that is, the same graphs as in Figure 5.1, with slightly narrower zones and shifted measurements. In that case, one system moves out of the red zone after correction for its age, that is, MG0414. SDSS0924 changes from being at the border of the red zone to lying clearly out of its range. It might seem obvious that if the theoretical halo M/L range is reduced, fewer points will be compatible with it, but the observed M/L have been age corrected too, possibly changing that expectation. Therefore, the fact that MG0414 and SDSS0924 leave the red zone after correction for the galaxies age is a relevant observation, driving these systems further away from the possibility of a spiral-like dark matter halo model.

Figure 5.2: Same as Figure 5.1 but the thickness of the background zones represents the uncertainty coming from the nature of the IMF and metallicity of the stellar population, and the measurements are corrected for the age of the galaxy. The successive panels, from top to bottom, left to right, respectively correspond to SIE, DVC + NFW and DVC + NFW* lens models.

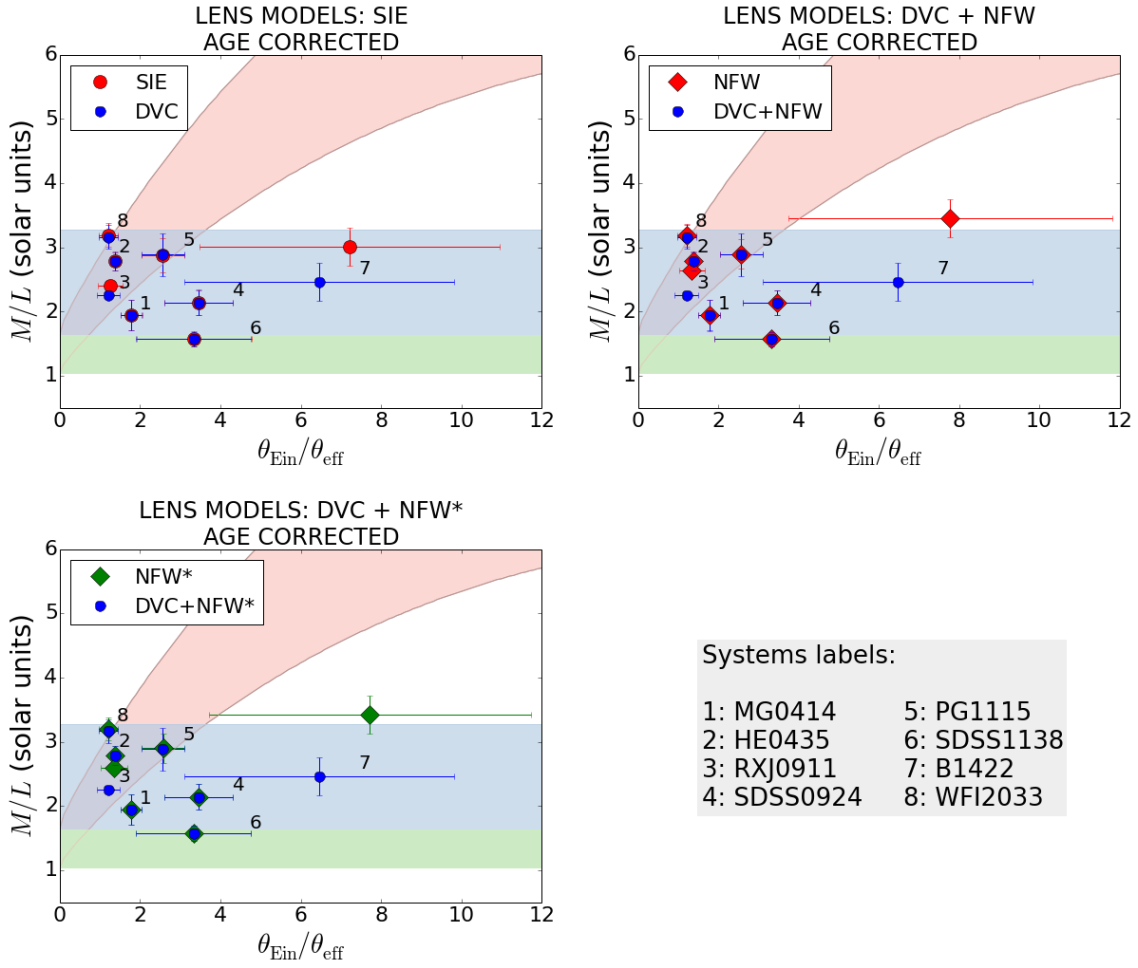

5.3.1.3 Effect of the IMF of the stellar population model

The size of the M/L range in the green zone is mostly defined by the difference between the results coming from both considered IMFs. The Kroupa IMF contains more high mass stars than the Salpeter IMF, producing a brighter population, and thus a lower M/L. A graph similar to Figure 5.2 can be produced with one IMF at a time, so that the width of the zones only come from the uncertainty on the population metallicity and horizontal branch morphology. In that case, the age correction is computed for one IMF at a time instead of averaged over both IMFs. Such plots are shown on Figure 5.3. The red and green zones still display some thickness coming from the M/L range defined by the stellar population metallicity and horizontal branch morphology. It is however drastically reduced compared to Figure 5.2, as stellar population M/L remains constant to 4% at 10 Gyr, given the chosen metallicity domain.

It can be seen that the Salpeter IMF predicts higher M/L than the Kroupa IMF. With the Salpeter IMF, only HE0435 and RXJ0911 are compatible with theoretical M/L that include a dark matter halo, whereas for the Kroupa IMF, only MG0414 and PG1115 are. SDSS0924, SDSS1138 and B1422 are below the red zone in both cases, and WFI2033, above. A study of the validity of these IMFs is beyond the scope of this work, but it illustrates the dependency of the theoretical M/L computation on galactic evolution models. It has been shown that neither of these IMFs match all early-type galaxies dynamics observations. In fact, the best-fitting IMF might depend on the mass regime (Cappellari et al. 2006b, Thomas et al. 2011, Tortora et al. 2013, 2014, Parikh et al. 2018, Barber et al. 2018).

Figure 5.3: Same as Figure 5.2 but the thickness of the background zones is drastically reduced by taking only one IMF into account. The first three panels correspond to the Salpeter IMF, the second three, to the Kroupa IMF. For readability, the blue zone equivalent on this plot has not been shown. The successive panels, from top to bottom, left to right, respectively correspond to SIE, DVC + NFW and DVC + NFW* lens models.

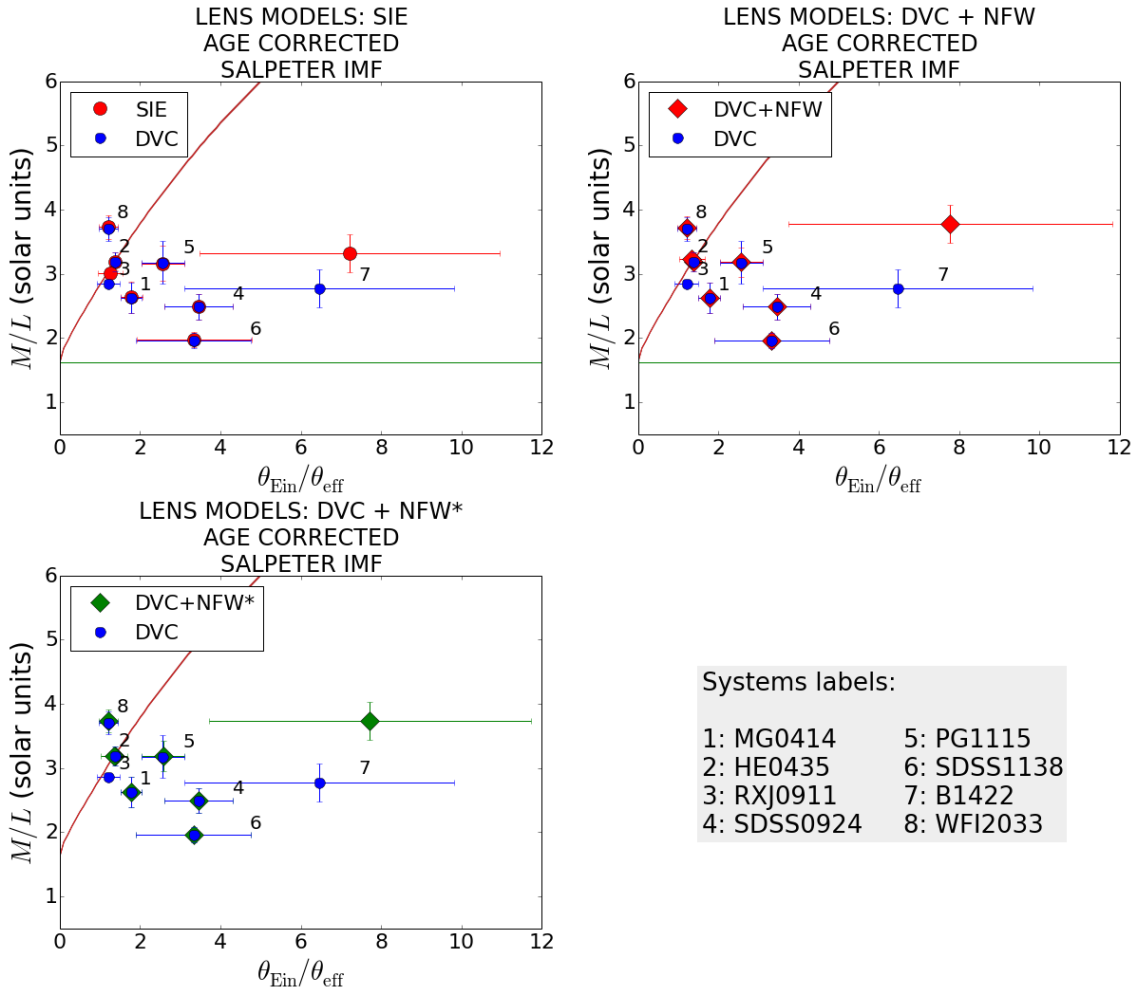

Figure 5.3: Continued.

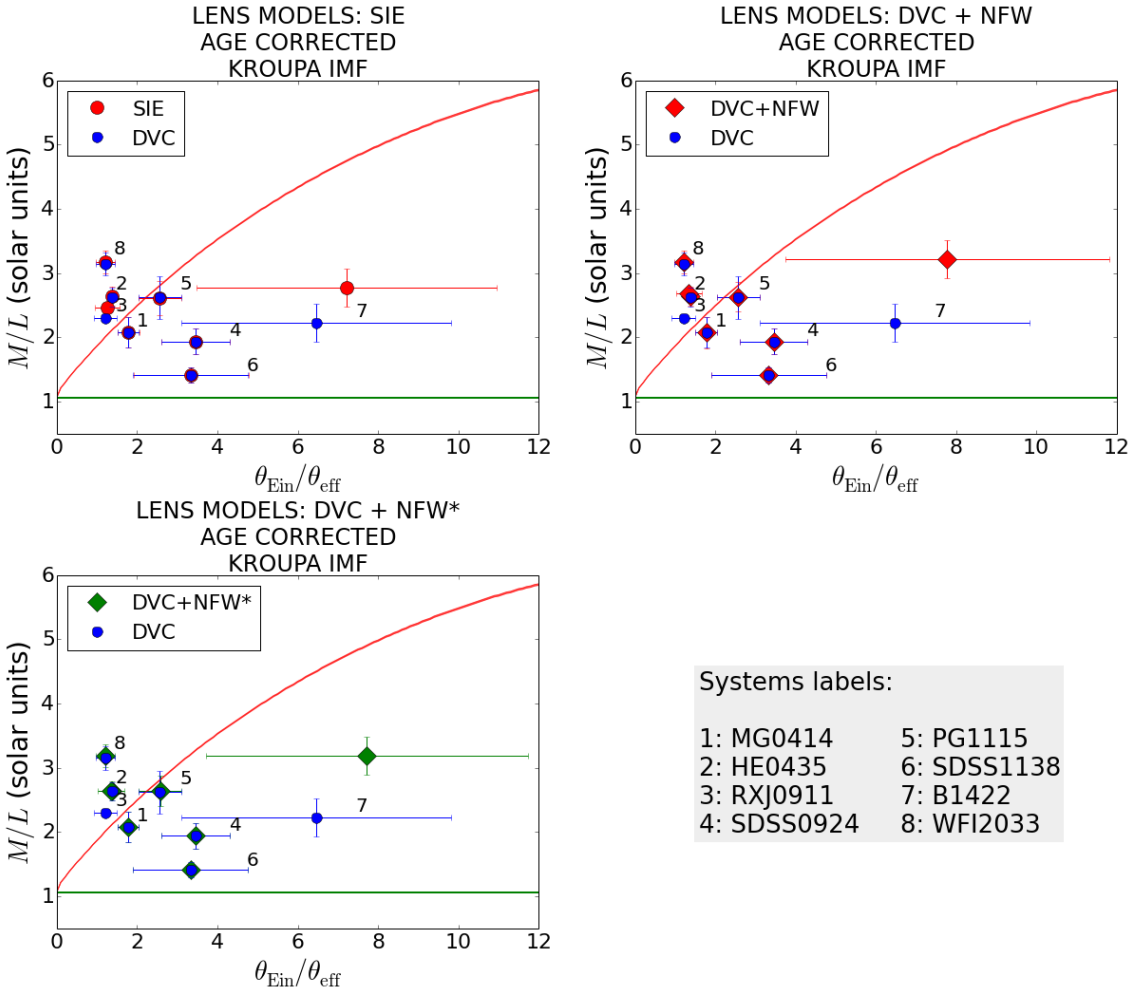

5.3.1.4 Effect of the choice of NFW for theoretical M/L computation

The red zones from Figures 5.1, 5.2 and 5.3 have been computed by integrating a projected NFW halo. In some lens modelling cases, we considered an SIE mass profile. Therefore, we have re-computed the theoretical M/L using an SIE mass profile, for comparison purposes. The process was similar to the one used with an NFW halo, that is, integrating a projected SIE profile along with a projected de Vaucouleurs profile for the light content, and calibrating it on NGC3198. Usually, the SIE profile is used to represent the total mass profile of galaxies, that is, the sum of luminous and dark matter. We are making the approximation of using an SIE for the dark matter content only, as we are only aiming at a coarse idea of the M/L range.

The change from NFW to SIE profile only affects the shape of the red zone on the aforementioned Figures, but as can be seen from Figure 5.4, it does not have a significant impact. The conclusions from previous subsections remain valid: nearly all systems lie at the intersection of the blue and SIE red zones, except for SDSS1138 and B1422 that lie below the lower limit of the SIE red zone. The WFI2033 M/L lies above its upper limit. The process of correcting from the stellar population age has also been re-conducted with the SIE red zone, but the same observations remained: MG0414 and SDSS0924 are driven away from being compatible with M/L including halos, although to a lower extent than with theoretical NFW halos for MG0414. Finally, the correction for the IMF still produces the exact same results. Both Figures 5.2 and 5.3 have been re-plotted using the SIE M/L ranges, yielding Figures 5.5 and 5.6, displaying the same outcome as with the NFW. As a result, switching from an NFW to an SIE mass profile to compute the M/L theoretical ranges does not affect the discussion, adding some security to our conclusions.

Figure 5.4: Same as Figure 5.1 but the red zone M/L are based on a projected SIE dark matter profile. The thickness of the background zones represents the uncertainty coming from the nature of the IMF, metallicity and age of the stellar population. The successive panels, from top to bottom, left to right, respectively correspond to SIE, DVC + NFW and DVC + NFW* lens models.

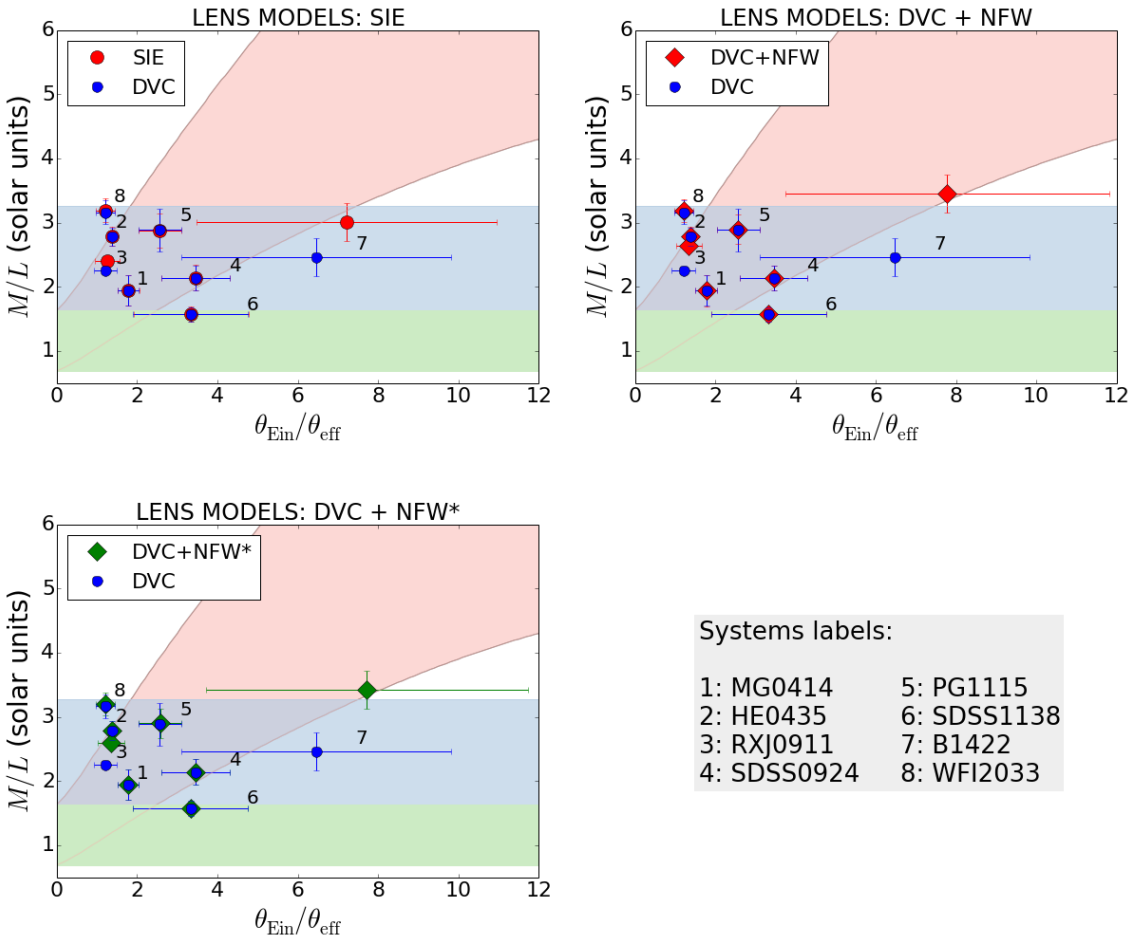

Figure 5.5: Same as figure 5.2 but the red zone M/L are based on a projected SIE dark matter profile. The thickness of the background zones represent the uncertainty coming from the nature of the IMF and metallicity of the stellar population. The successive panels, from top to bottom, left to right, respectively correspond to SIE, DVC + NFW and DVC + NFW* lens models.

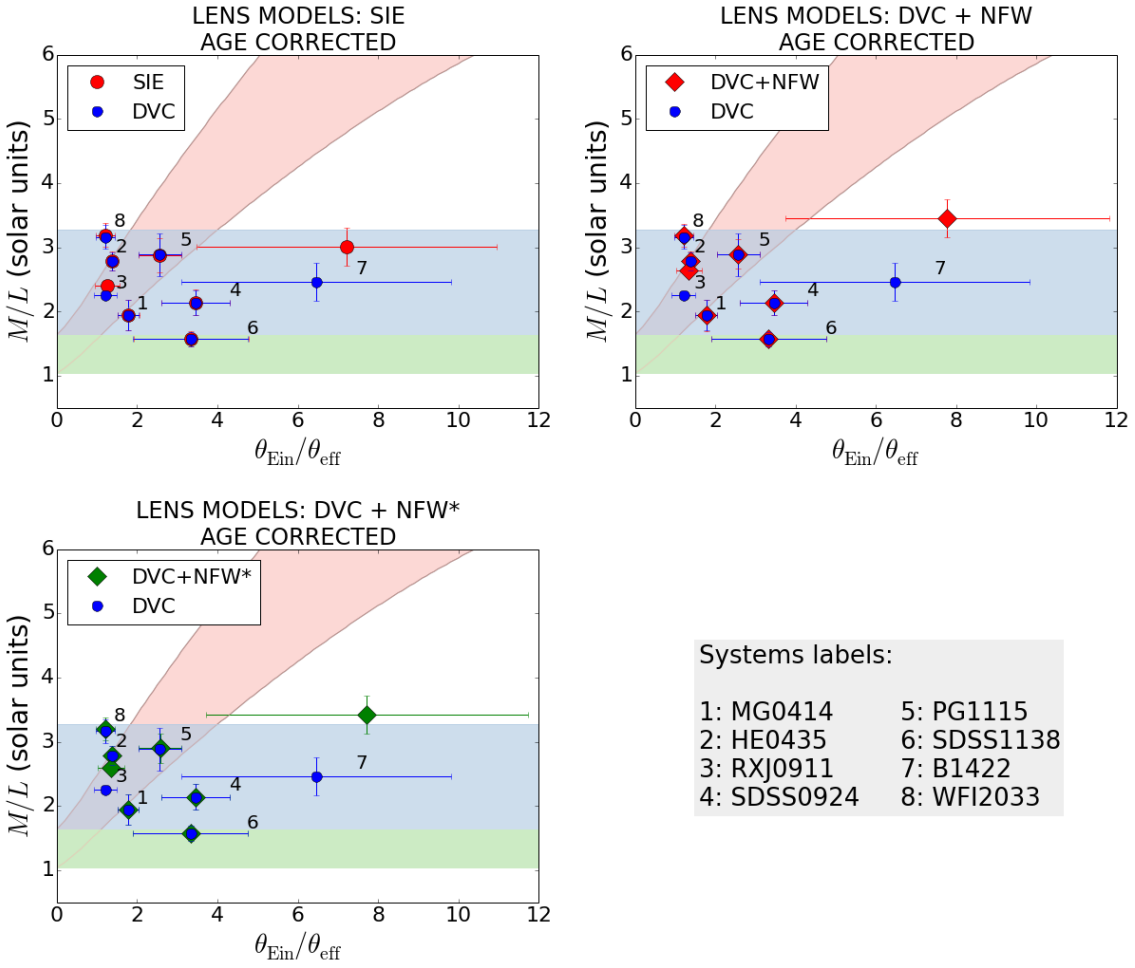

Figure 5.6: Same as Figure 5.3 but the red zone M/L are based on a projected SIE dark matter profile. The first three panels correspond to the Salpeter IMF, the second three, to the Kroupa IMF. The successive panels, from top to bottom, left to right, respectively correspond to SIE, DVC + NFW and DVC + NFW* lens models.

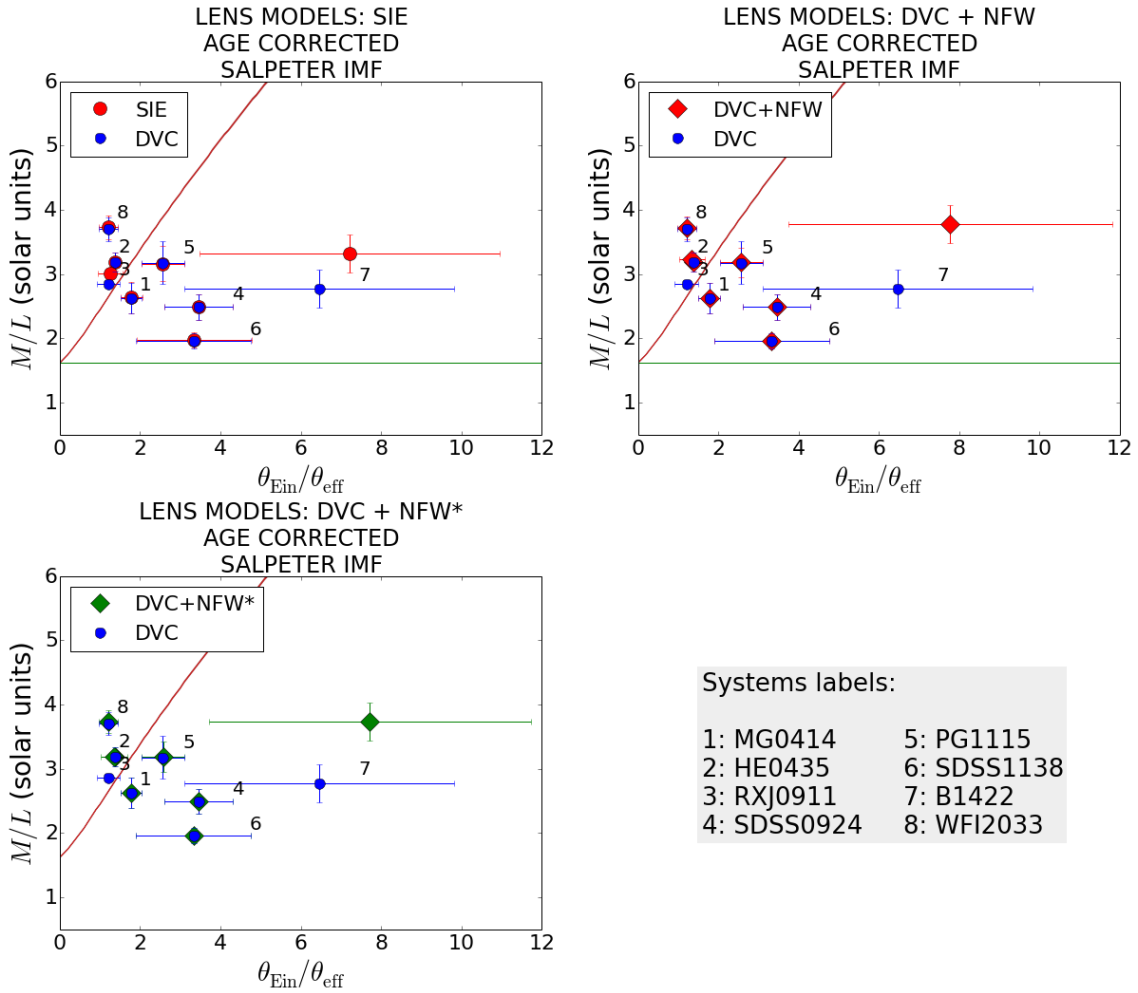

Figure 5.6: Continued.

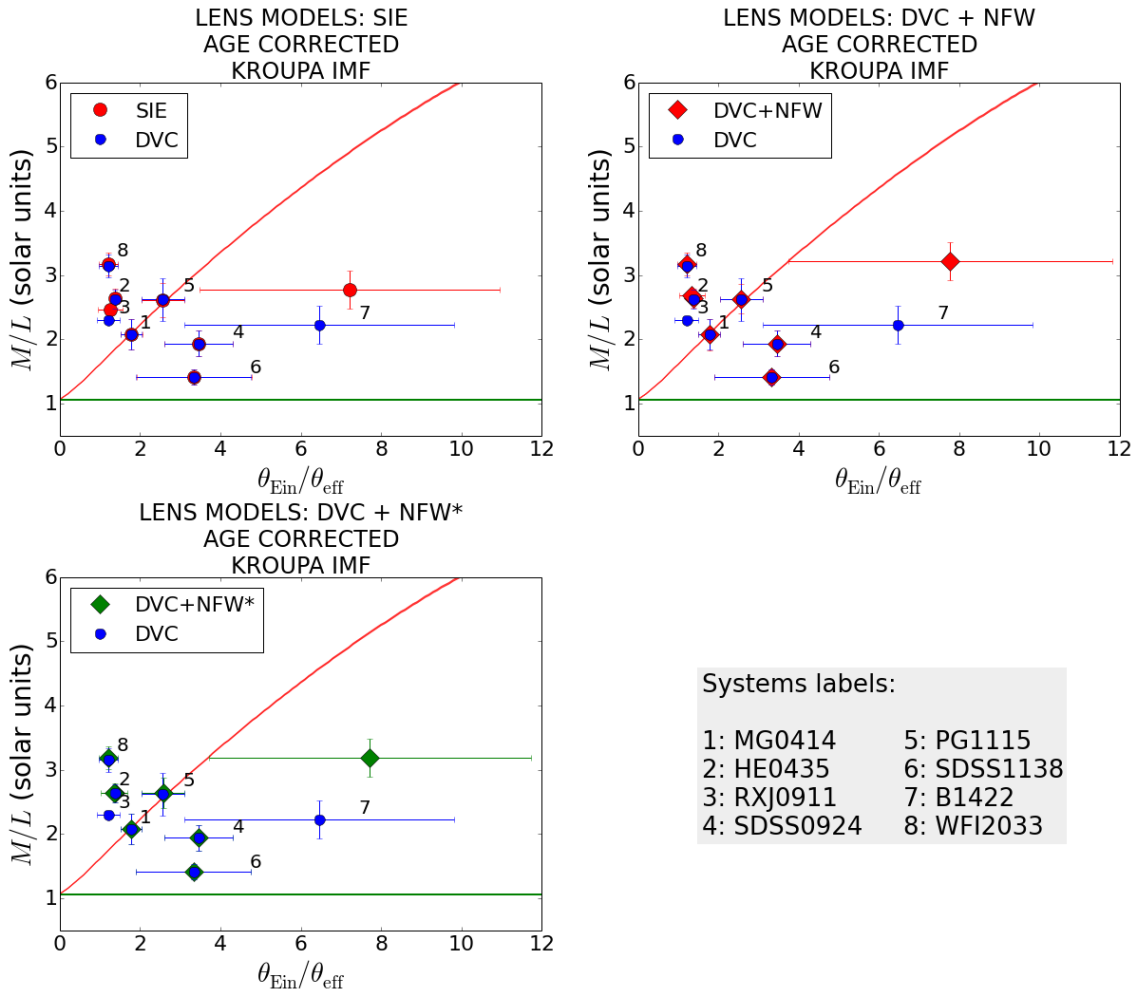

5.3.1.5 Comparison to literature M/L

Many previous studies have provided observed and theoretical mass-to-light ratios for ellipticals, based on a variety of data, from kinematics to lensing and stellar population model fitting. A great majority of studies combining two or more of these proxies have yielded core mass-to-light ratios below or around $\theta_{\rm eff}$ close to 1.5 solar units (Pierini et al. 2002, Cappellari et al. 2006b, Grillo et al. 2008, Ferreras et al. 2008). This indicates light-dominated inner parts of elliptical galaxies. In Meza et al. (2003), a galaxy formation simulation based on mergers yielded an approximate M/L of 1.35 at $1\theta_{\rm eff}$, matching these results. On the other hand, planetary nebulae kinematics and earlier velocity dispersion studies yielded higher M/L within $\theta_{\rm eff}$ roughly between 5 and 7[1] (Bertin et al. 1988, Bacon et al. 1985, Capaccioli et al. 2002). Even earlier studies based on X-ray fluxes predicted high mass-to-light ratios in the outer parts of ellipticals, around 10 (Fabricant et al. 1980, Trinchieri et al. 1986).

For HE0435, RXJ0911 and WFI2033 we obtained $\theta_{\rm Ein}/\theta_{\rm eff}$ of not much more than 1, so we are probing regions close to the galactic core. Their M/L reach around 2.5, or even 3.2 for WFI2033. Our results seem to lie between the results from kinematics and from planetary nebulae. We cannot exclude the existence of a dark matter core. However, our outermost point lies at about $7\theta_{\rm eff}$ and its M/L goes from 2.5 to 3.5 depending on the lens model, which is below the expected value from X-rays and planetary nebulae in those regions. At first glance, there is no evidence for high outer M/L ratios matching a dark matter halo hypothesis.

5.3.2 Dependency of M/L on the galacto-centric distance

Because of the uncertainties coming from stellar evolution models, comparing observed M/L to theoretical M/L is not the most secure way to draw a conclusion. A more robust analysis is obtained by observing the M/L behaviour with the galacto-centric distance. The M/L of a galaxy embedded in a dark matter halo is expected to increase with galacto-centric distance. That increase is expected even in galaxies with a dark matter rich core (Hibbard and Yun 2000, Chiosi and Carraro 2002).

We perform a linear regression on the M/L vs $\theta_{\rm Ein}/\theta_{\rm eff}$ we measured from each mass model, that is, the points of same shape and colour on Figure 5.1. The slope of each case is shown in the lower portion of Table 5.4. Their uncertainties come from the error bars on both M/L and $\theta_{\rm Ein}/\theta_{\rm eff}$. The linear regressions all have a negative slope that is compatible with a null slope at between 1.14σ and 1.40σ. A negative slope may seem nonsensical, because even if the galaxy only contained regular, baryonic matter, its mass-to-light ratio would be approximately constant with galacto-centric distance. Let us however notice that only three points out of eight have an Einstein radius higher than 2.5. This uneven distribution of the sample between inner and outer regions of the galaxy might make the

[1] In some of the aforementioned references, mass-to-light ratios are computed in the B-band. When that is the case, we use the Fioc and Rocca-Volmerange (1997) spectra to "K-correct" them towards the H-band, for comparison purposes.

linear regression uncertain. Moreover, the uncertainties on $\theta_{\rm Ein}/\theta_{\rm eff}$ are quite large, especially on the outermost point, which would be the most relevant in our context. Therefore, the negative quality of the slopes is probably an artefact due to these sources of uncertainties. Nevertheless, the best-constrained cases of all our mass models yield a slope that is close to zero, indicating that the mass-to-light ratio does not increase with galacto-centric distance. The large uncertainties prevent us from drawing a firm and conclusive result, but we find no evidence for the existence of spiral-like dark matter halos around the galaxies in this sample.

To secure that conclusion, we aim at quantifying the expected increase for a galaxy with a dark matter halo by computing the slope of the red zone from Figure 5.1. The M/L as a function of the distance in the red zone were obtained by integrating the sum of a projected de Vaucouleurs profile and of a projected SIE or NFW profile. This operation is quite secure, and the uncertain character of the theoretical M/L ranges does not affect the reliability of a linear regression on the red zone. The most important contributor to the uncertainty on the $M/L(r)$ function, with r representing the galacto-centric distance parameter, is its calibration[2]. We have chosen to calibrate $M/L(r)$ to match that of NGC3198, as explained in Subsection 5.3.1. The aim is to perform a linear regression on this numerically obtained $M/L(r)$ taking into account the uncertainty from the calibration. Let us remind that our numerical $M/L(r)$ also depends on the IMF, so the process will be conducted for both considered IMFs.

We choose to consider a coarse, deliberately large uncertainty of 25% on the NGC3198 M/L ratio at 5.8 $\theta_{\rm eff}$. The linear regressions are shown on Figure 5.7, where the red curves correspond to the analytical $M/L(r)$ for both IMFs: the lower values come from the Kroupa IMF, the higher, from the Salpeter IMF. Each red curve is surrounded by a light red cone-shaped zone that traces the error coming from the arbitrary ±25% on the calibration. The blue, dashed lines correspond to the linear regression on each IMF, where the error on the linear regression parameters, represented by the light blue zone, come from the calibration uncertainty. This process is conducted for SIE and NFW halos, for both IMFs. The four slopes are summarised in the upper portion of Table 5.4. They can then be compared to the linear regressions on observed M/L.

Figure 5.8 helps making that comparison. The red horizontal bands on the figure correspond to theoretical SIE mass profiles, the green ones, to NFW mass profiles, each one assuming one IMF or the other. The red, blue and green markers with their error bars are the observed M/L slopes from the sample, respectively with SIE, DVC and DVC+NFW(*) lens models. None of them match the expected rate of increase of M/L with distance in the case of a dark matter halo, even when considering a large uncertainty of the $M/L(r)$ function calibration. In fact, the observed slopes are on average compatible with their theoretical match at 1.63σ, whereas their "distance" with a null slope is on average 1.29σ.

[2]Another parameter is quite arbitrary in the halo profiles, that is, the halo core radius for the SIE model, and the scaling radius for the NFW model. The effect of both on the hypothetical $M/L(r)$ slope has been investigated and turned out to be negligible compared to that of a possible error on the calibration.

On that same figure is shown a grey, shaded slope value coming from the simulation work of Meza et al. (2003). Specifically, we used their detailed composed mass profile results to perform a linear regression on their $M/L(r)$ and obtained a slope of 0.056 ± 0.017. This is thus the approximate M/L dependency on the galacto-centric distance of a simulated elliptical galaxy based on a merger scenario. It is very close to a null slope, and the observed $M/L(\theta_{\rm Ein}/\theta_{\rm eff})$ trends match it at 1.17 to 1.45σ, that is 1.34σ on average. Although this match is better than for the stellar populations based $M/L(r)$, it is mildly convincing, and supports the conclusion that our sample of galaxy does not exhibit the M/L increase with radius expected in the presence of a dark matter halo. Let us also highlight that the simulated galaxy obtained in Meza et al. (2003) is atypical: it has a compact morphology, an unusually high surface brightness and important rotation velocities at almost all distances, as can be seen in their Table 1. Because the central stellar component concentration might be a little overestimated[3], the slope of the $M/L(r)$ trend might be underestimated. It should thus merely be considered as a lower limit on $M/L(r)$ trends for mergers simulations products.

Figure 5.7: Linear regressions on the theoretical M/L vs the galacto-centric distances for galaxies with dark matter halos modelled as SIE (left panel) and NFW (right panel). The red contours represent the arbitrary ±25% uncertainty on the calibration. The blue, dashed lines correspond to the linear regression on each IMF, where the error on the linear regression parameters, represented by the light blue zone, come from the calibration uncertainty. The upper curve correspond to the Salpeter IMF, the lower curve, to the Kroupa IMF.

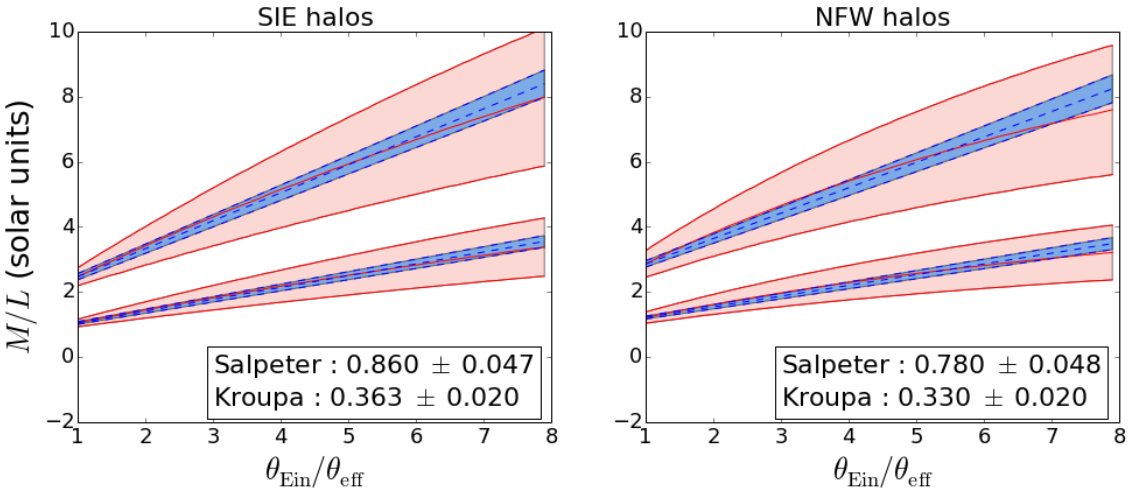

[3]The authors of Meza et al. (2003) attribute that overestimation to an efficient star formation process in their simulation algorithm.

Figure 5.8: A visual comparison of expected and measured slopes of the M/L trend with galacto-centric distance. The horizontal bands are the theoretically computed slopes, the markers are the observed slopes with 1σ error bars.

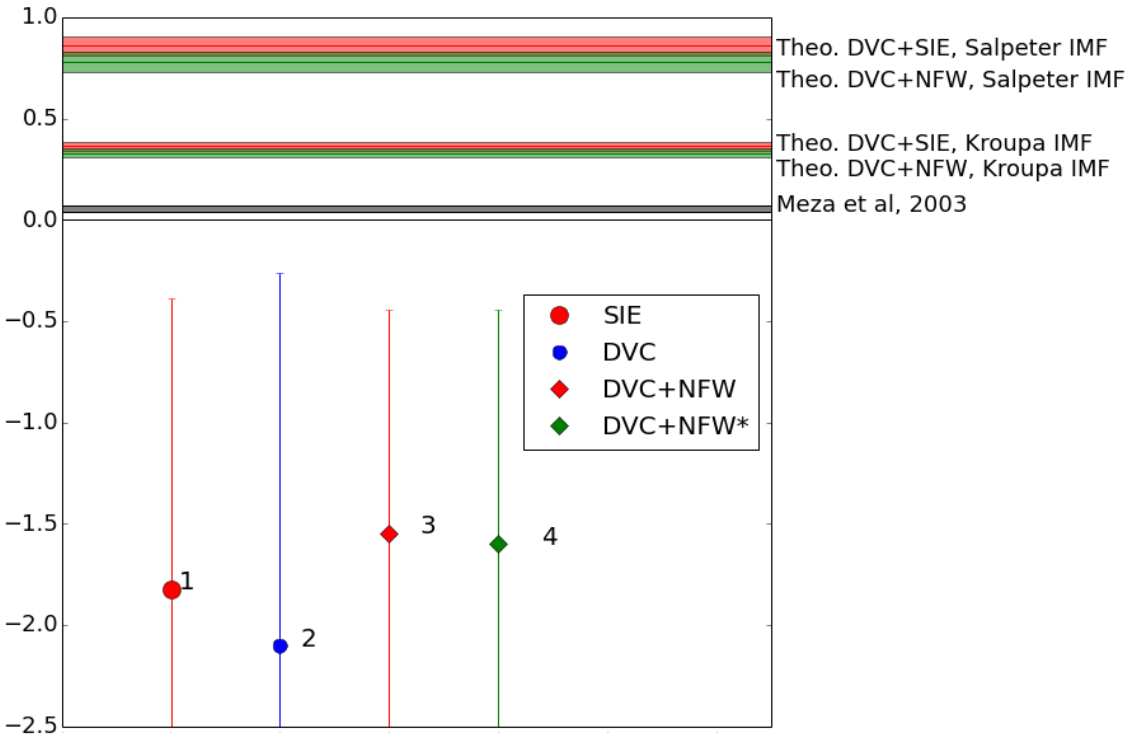

Table 5.4: A list of expected (upper panel) and measured (lower panel) slopes of the $M/L(r)$ trend, along with their 1σ error bars.

Mass model	**Slope**
Theoretical mass to light ratios	
SIE+DVC, Kroupa IMF	0.363 ± 0.020
SIE+DVC, Salpeter IMF	0.860 ± 0.047
NFW+DVC, Kroupa IMF	0.330 ± 0.020
NFW+DVC, Salpeter IMF	0.780 ± 0.048
Meza et al. (2003)	0.056 ± 0.017
Observed mass to light ratios	
SIE	-1.822 ± 1.436
DVC	-2.102 ± 1.839
NFW	-1.545 ± 1.102
NFW*	-1.599 ± 1.155

5.3.3 Studying subsamples

The whole analysis of M/L ratios has been conducted on a sample of measured M/L coming from the best-constrained mass models of lensing galaxies. However, in Chapter 4, we produce a variety of models, sometimes removing the time delays from our constraints list, considering two values of the Hubble constant. In Table 4.2, for example, we separate three subsamples: one containing all eight galaxies, rejecting the time delay constraints, and two including only time delay-constrained lenses, with two different values of H_0. The subsample without time delays includes more points, which may seem like an advantage for the linear regression, but mass models without time delays are subject to more degeneracies, especially the MSD. However, as can be seen from Table A1, the masses enclosed within $\theta_{\rm eff}$ are quite model-independent. For this M/L study, non time-delay constrained cases are thus also worth considering. The M/L characterisation has been conducted on the set of subsamples, and a linear regression has been performed on all mass model cases within each subsample. Each slope is given on an indicative basis in Table 5.5 (Page 121).

The conclusions remain the same, whether the work has been conducted on the best sample or on these subsamples: the observed M/L slopes versus galacto-centric distance are compatible with the absence of dark matter halos, although their error bars are sometimes extremely large. In the case of time delay-constrained lenses, the linear regression is performed on five points only, and nearly all of them have a $\theta_{\rm Ein}/\theta_{\rm eff}$ of below 2.5, so the slope is ill-constrained. Nevertheless, one case seems to stand out of the crowd : the observed, time delay-constrained DVC+NFW mass-to-light ratios yield a slope of 0.302 $\pm$ 0.333, which is still compatible with a null slope, but also with the expected, theoretical NFW increase of 0.330 $\pm$ 0.02 in the Kroupa IMF. Interestingly, for three out out of five of these systems (that is RXJ0911, B1422 and WFI2033), the dark matter fraction from the mass model is also compatible with its expected value. RXJ0911 is also the only one for which the DVC+NFW mass model comes in first in terms of reduced χ^2. Conversely, PG1115, which is part of the currently discussed subsample too, yields the best reduced χ^2 for a DVC only mass model. Therefore, if this result is definitely worth mentioning, it is not strongly conclusive, and we do not think it goes against the previous conclusion regarding the absence of strong evidence for spiral-like dark matter halos in the galaxies studied here.

5.4 Conclusion

The mass-to-light ratios of eight lensing galaxies have been evaluated with a secure error bar, including a careful processing of the systematics. They are compared to theoretical M/L values, based on different assumptions on the dark matter content. Despite correcting for factors of uncertainty on theoretical M/L from stellar populations, like their age or IMF, no clear preference between the "mass-follows-light" and "spiral-like dark matter halo" M/L ranges can be inferred from our sample. Five out of eight objects have a $\theta_{\rm Ein}/\theta_{\rm eff}$ ratio below 3, which means we are probing slightly less relevant regions in the search for dark matter halos. Previous studies based on planetary nebulae have provided

M/L for these inner regions between 5 and 7, indicating a dark matter rich core, whereas studies based on lensing and kinematics have yielded a lower core M/L of about 1.5. Our innermost points lie between these two limits and cannot exclude dark matter in the galaxies core. The three remaining systems, however, allow for probing outer regions, out to about $7\theta_{\rm eff}$, and happen to have some of the lowest M/L in the sample, which may seem incompatible with the existence of a dark halo. Nevertheless, the dispersed character of our results, the large uncertainties on $\theta_{\rm Ein}/\theta_{\rm eff}$ and the uneven distribution of our sample between inner and outer parts of galaxies prevent us from drawing any secure conclusion. The linear regressions on $M/L(\theta_{\rm Ein}/\theta_{\rm eff})$ have shown slopes that are compatible with a null slope at a 1.3σ level on average. A positive slope should be expected in case of a dark matter halo surrounding the lensing galaxies. Once again, large error bars on $\theta_{\rm Ein}/\theta_{\rm eff}$ yield large error bars on the $M/L(\theta_{\rm Ein}/\theta_{\rm eff})$ slopes, meaning they are only mildly conclusive.

The characterisation of M/L, whether the chosen indicator is its value itself or its behaviour with the galacto-centric distance, has shown no evidence for the existence of dark halos around the lensing galaxies in our sample, but large uncertainties make it impossible to produce a definitive answer to the core question of this study. The present work thus presents some room for progress. For example, the sample should be enriched with galaxies that have a higher Einstein radius for this result to become even more conclusive. These prospects, along with a brief summary of the present work, are discussed in the next Chapter.

5.5 Observational bias

An indirect result of this study makes it possible to highlight a selection bias in gravitational lensing observations. Figure 5.9 shows the masses of the galaxies in our sample as a function of their redshifts. It can be seen that the higher the redshift, the higher the mass. It seems indeed quite intuitive that for a given alignment between the observer, the lens and the quasar, if the lens-observer distance increases, the mass at the origin of the lensing potential needs to be more important to produce a detectable angular separation. This implies that at higher redshifts, lensing systems can only be detected if the lens has an important mass (or density).

This observational bias can be confirmed by plotting the lens mass versus the distances ratio $(D_{\rm L}D_{\rm S})/D_{\rm LS}$. Indeed, the definition of the Einstein radius, that roughly traces the angular separation of a quadruply imaged quasar, depends on that ratio

$$\theta_{\rm Ein} = \sqrt{\frac{4GM}{c^2}\frac{D_{LS}}{D_L D_S}}\,. \tag{5.4}$$

For the system to be detectable, $\theta_{\rm Ein}$ has to be higher than a threshold that depends, among others, on the instrument and the wavelength. The larger the distances, the higher the necessary M to reach that threshold. Figure 5.10 shows a clear correlation between M and the distances ratio in our sample, confirming that observational bias. A similar bias has

also been observed by, for example, Mandelbaum et al. (2009).

To a certain extent, a correlation has also been observed between the mass-to-light ratio and the redshift. Given the dispersion of our sample, as can be seen on Figure 5.11, this correlation is hardly significant. In fact, such correlations can be linked to the fundamental plane relations (Franx et al. 1999, van de Sande et al. 2015) and do not impair our conclusions.

Figure 5.9: A correlation between the masses and redshifts of the galaxies in our sample. Each panel shows masses that have been obtained with a different lens model, indicated in the legend box.

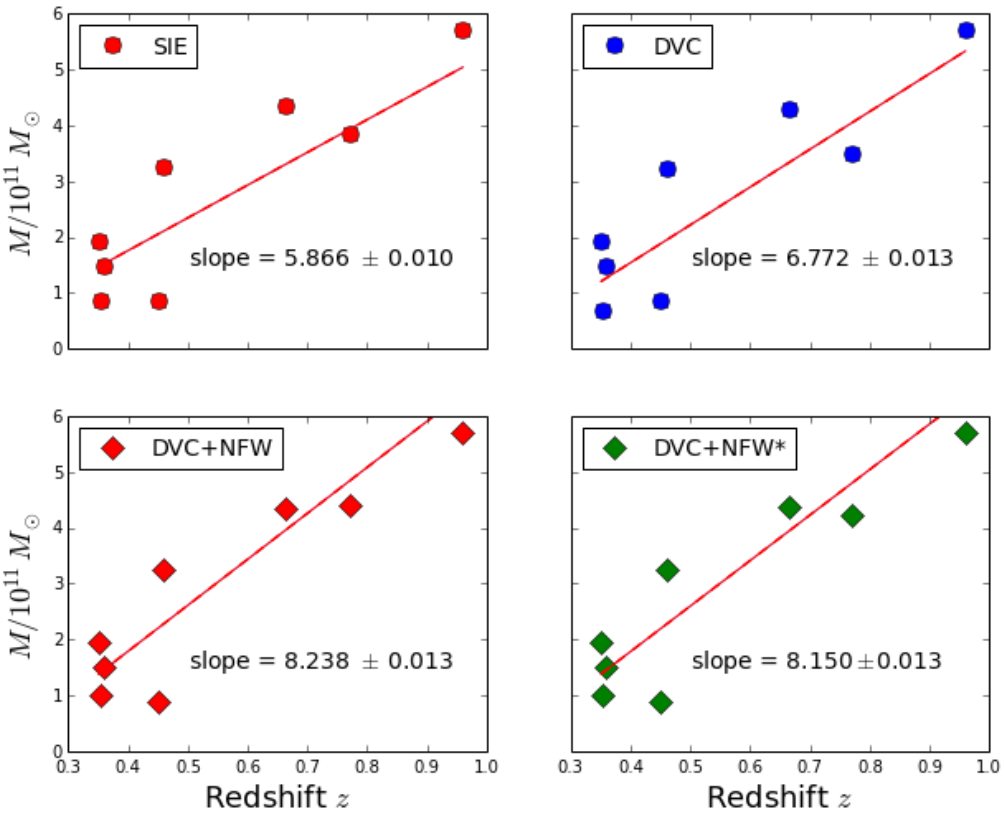

Figure 5.10: A correlation between the masses and distances ratio of the galaxies in our sample. Each panel shows masses that have been obtained with a different lens model, indicated in the legend box.

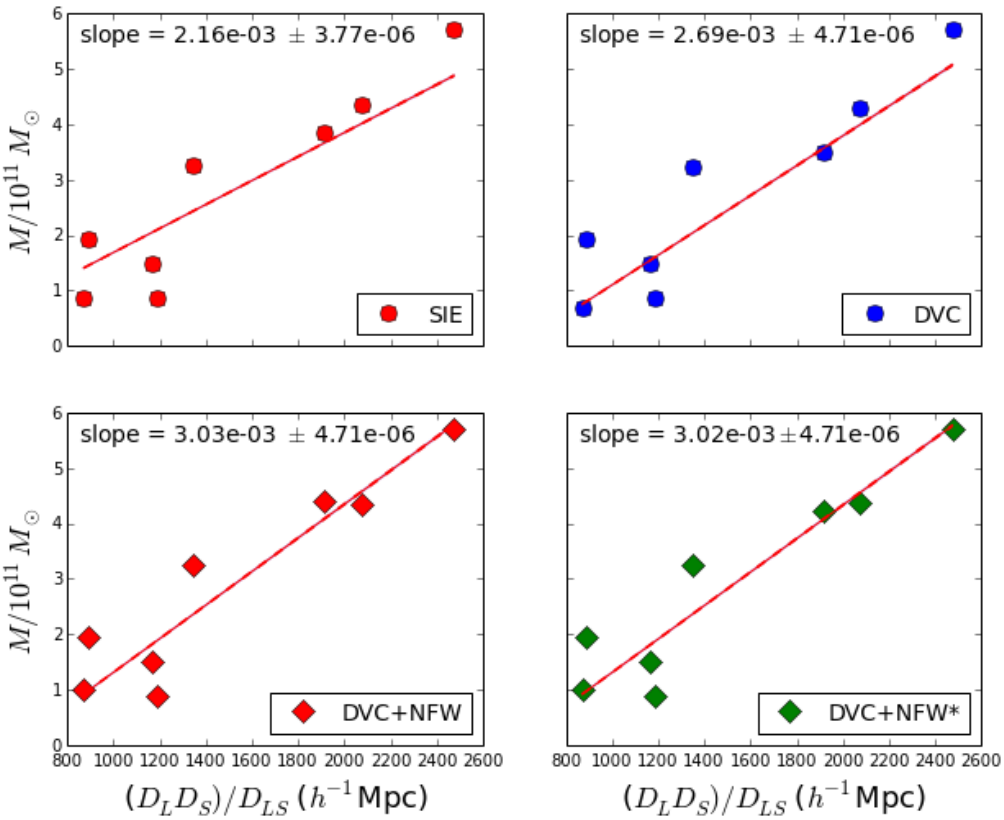

Figure 5.11: A weak correlation between the mass-to-light ratios and redshifts of the galaxies in our sample. Each panel shows masses that have been obtained with a different lens model, indicated in the legend box.

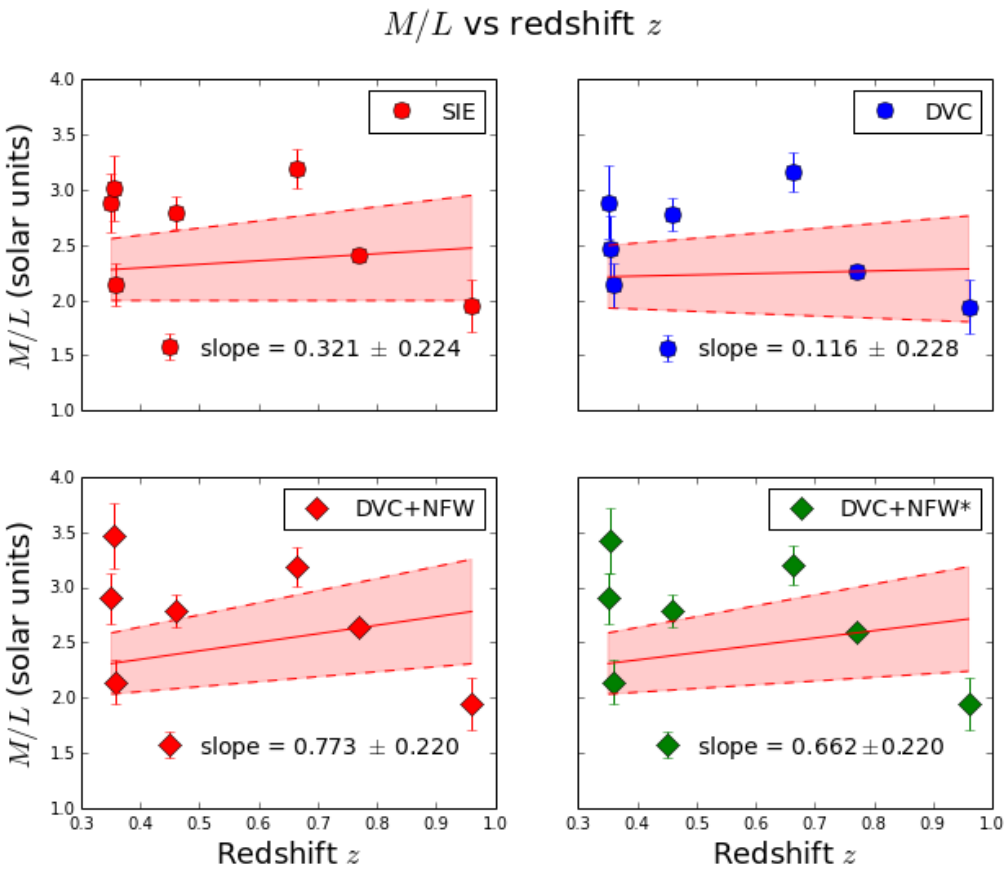

5.6 Complete Table

Table 5.5: Results of the $\theta_{\rm Ein}/\theta_{\rm eff}$ and M/L measurements with their 1σ error bars, for each case of lens model and Hubble constant. The slope of the linear regression on $M/L(\theta_{\rm Ein}/\theta_{\rm eff})$ is given at the bottom of each subtable.

Without taking Δt into account				
	SIE		DVC	
	$\theta_{\rm Ein}/\theta_{\rm eff}$	M/L	$\theta_{\rm Ein}/\theta_{\rm eff}$	M/L
MG0414	1.781 ± 0.270	1.949 ± 0.240	1.777 ± 0.270	1.943 ± 0.240
HE0435	1.377 ± 0.121	2.794 ± 0.146	1.374 ± 0.121	2.856 ± 0.146
RXJ0911	1.246 ± 0.297	2.377 ± 0.024	1.249 ± 0.297	2.385 ± 0.024
SDSS0924	3.454 ± 0.849	2.142 ± 0.197	3.452 ± 0.848	2.141 ± 0.197
PG1115	2.562 ± 0.533	2.878 ± 0.266	2.567 ± 0.534	2.890 ± 0.275
SDSS1138	3.342 ± 1.432	1.579 ± 0.117	3.331 ± 1.428	1.570 ± 0.117
B1422	7.210 ± 3.740	3.014 ± 0.295	7.114 ± 3.691	2.936 ± 0.295
WFI2033	1.218 ± 0.240	3.217 ± 0.180	1.204 ± 0.237	3.157 ± 0.180
Slope	-1.959 ± 1.612		-1.875 ± 1.485	
	DVC+NFW		DVC+NFW*	
	$\theta_{\rm Ein}/\theta_{\rm eff}$	M/L	$\theta_{\rm Ein}/\theta_{\rm eff}$	M/L
MG0414	1.779 ± 0.270	1.942 ± 0.240	1.778 ± 0.270	1.942 ± 0.240
HE0435	1.374 ± 0.121	2.856 ± 0.146	1.199 ± 0.105	2.705 ± 0.146
RXJ0911	1.355 ± 0.322	2.695 ± 0.024	1.363 ± 0.324	2.719 ± 0.024
SDSS0924	3.452 ± 0.848	2.141 ± 0.197	3.452 ± 0.848	2.141 ± 0.197
PG1115	2.567 ± 0.534	2.891 ± 0.274	2.567 ± 0.534	2.890 ± 0.275
SDSS1138	3.331 ± 1.428	1.570 ± 0.117	3.331 ± 1.428	1.570 ± 0.117
B1422	7.127 ± 3.697	2.946 ± 0.295	7.112 ± 3.690	2.934 ± 0.295
WFI2033	1.204 ± 0.237	3.148 ± 0.180	1.204 ± 0.237	3.156 ± 0.180
Slope	-1.313 ± 0.831		-0.990 ± 0.624	

Continued on next page

Table 5.5 – Continued

With Δt, $H_0 = 73.24\ kms^{-1}Mpc^{-1}$				
	SIE		DVC	
	$\theta_{\mathrm{Ein}}/\theta_{\mathrm{eff}}$	M/L	$\theta_{\mathrm{Ein}}/\theta_{\mathrm{eff}}$	M/L
HE0435	1.377 ± 0.121	2.794 ± 0.146	1.374 ± 0.121	2.784 ± 0.146
RXJ0911	1.259 ± 0.300	2.412 ± 0.024	1.204 ± 0.287	2.257 ± 0.024
PG1115	2.562 ± 0.533	2.879 ± 0.267	2.566 ± 0.534	2.888 ± 0.332
B1422	7.209 ± 3.740	3.013 ± 0.295	6.467 ± 3.355	2.464 ± 0.295
WFI2033	1.213 ± 0.239	3.194 ± 0.180	1.206 ± 0.238	3.166 ± 0.180
Slope	14.459 ± 165.825		11.344 ± 87.248	
	DVC+NFW		DVC+NFW*	
	$\theta_{\mathrm{Ein}}/\theta_{\mathrm{eff}}$	M/L	$\theta_{\mathrm{Ein}}/\theta_{\mathrm{eff}}$	M/L
HE0435	1.376 ± 0.121	2.791 ± 0.146	1.375 ± 0.121	2.788 ± 0.146
RXJ0911	1.346 ± 0.320	2.641 ± 0.024	1.353 ± 0.322	2.592 ± 0.024
PG1115	2.572 ± 0.535	2.898 ± 0.231	2.572 ± 0.535	2.899 ± 0.234
B1422	7.775 ± 4.034	3.462 ± 0.295	7.723 ± 4.007	3.419 ± 0.295
WFI2033	1.211 ± 0.239	3.188 ± 0.180	1.214 ± 0.240	3.201 ± 0.180
Slope	0.302 ± 0.333		13.760 ± 179.610	

Continued on next page

Table 5.5 – Continued

With Δt, $H_0 = 62.3\ kms^{-1}Mpc^{-1}$				
	SIE		DVC	
	$\theta_{\rm Ein}/\theta_{\rm eff}$	M/L	$\theta_{\rm Ein}/\theta_{\rm eff}$	M/L
HE0435	1.377 ± 0.121	2.521 ± 0.146	1.374 ± 0.121	2.514 ± 0.146
RXJ0911	1.222 ± 0.291	1.923 ± 0.024	1.149 ± 0.273	1.791 ± 0.024
PG1115	2.567 ± 0.534	2.461 ± 0.268	2.566 ± 0.534	2.470 ± 0.334
B1422	7.209 ± 3.740	2.559 ± 0.295	6.475 ± 3.359	2.101 ± 0.295
WFI2033	1.209 ± 0.239	2.705 ± 0.180	1.204 ± 0.237	2.686 ± 0.180
Slope	9.648 ± 71.681		3.849 ± 9.343	
	DVC+NFW			
	$\theta_{\rm Ein}/\theta_{\rm eff}$	M/L		
HE0435	1.376 ± 0.121	2.519 ± 0.146		
RXJ0911	1.362 ± 0.324	2.311 ± 0.024		
PG1115	2.571 ± 0.535	2.465 ± 0.231		
B1422	7.775 ± 4.034	2.945 ± 0.295		
WFI2033	1.213 ± 0.239	2.718 ± 0.180		
Slope	0.122 ± 0.133			

6 Conclusions and prospects

The core target of this work is the search for dark matter halos around elliptical galaxies through gravitational lensing. The main goal is to quantify the dark matter content of a sample of eight gravitational lenses, using, among others, their mass-to-light ratios. For that purpose, we propose an extensive analysis of their luminous matter content, and a study of their mass profile based on gravitational lens modelling. The combination of both these results yields the H-band mass-to-light ratio as a function of the Einstein radius. The sample we are focusing on comes from a larger sample processed by Chantry et al. (2010) and Sluse et al. (2012).

First, all 50 images of the selected quadruply-imaged quasars have gone through a careful pre-processing, specifically designed to disentangle lensed background quasar signal from relevant lensing galaxy signal. The source subtraction is based on the MCS deconvolution method, as it has proven to be particularly well suited to gravitational lensing images, where usually no point-like star is available to help computing the PSF. PSFs for each systems are taken from Chantry et al. (2010) and Sluse et al. (2012). A method to subtract the arc-shaped lensed images has been designed, requiring only a few reasonable hypotheses, and it has been applied to four out of the eight systems. For three of the remaining systems, no significant arc is visible and there is thus no need for subtraction. One system, WFI2033, presents an arc that is too diffuse to be securely subtracted, maybe because the background quasar host galaxy is rather spread out. Despite its drawbacks of sometimes creating some residual noise and artefacts on individual pixels, the lensed signal subtraction, both point-like and diffuse, has significantly improved the visibility of the galaxies: on average, the surface of the circular region of interest around the galaxy centre has increased by 37%. Reaching as far out from the centre of the galaxies as possible is relevant for the study of their morphology, as the value of $r_{\rm eff}$ is quite sensitive to the wings in a de Vaucouleurs profile. Moreover, convolution mostly affects their central regions.

After that pre-processing, the light profiles of the galaxies have been analysed with a newly designed method, different from classical fitting methods. Each de Vaucouleurs profile parameter has been estimated individually in order to work around the common

issue of local minima in the high-dimensional parameters space. The PA and ellipticity have been determined based on the computation of isophotes. The half-light radius and central intensity have been evaluated using a method based on a χ^2 minimisation in the $(\ln I \ ; r^{1/4})$ space. The latter is named the linear regression method or LRM. The effect of the PSF is taken into account by implementing an iterative procedure that tunes the parameters of a synthetic de Vaucouleurs profile until it yields, after convolution by the HST PSF, the same values of the shape parameters as the ones measured on actual data frames. The stability of the LRM has been tested versus that of GALFIT regarding crucial aspects of gravitational lenses image processing: the size of the region of interest, the size of the galaxy compared to that of the PSF, the signal-to-noise ratio, and the use of a wrong Sérsic index. The LRM has proved to be much more robust than GALFIT with respect to all these quantities. The biases of the $r_{\rm eff}$ estimates from GALFIT are in all cases a factor two or three larger than those from the LRM. The latter is thus less dependent on the Sérsic index and better suited to studying small galaxies compared to the PSF. For that reason, it is particularly well suited to analysing lensed images, as the study of lensing galaxies is often restricted to small, inner regions of the lens because of the lensed signal. Finally, by performing a quick residual curvature test, we have also verified that the de Vaucouleurs profile satisfactorily represents the physical light distribution of our sample of elliptical galaxies.

We have conducted lens modelling on our sample in order to obtain a robust estimate of their total mass content. We have used the *lensmodel* application to solve the lens equation for a variety of mass models, each corresponding to some different hypotheses on the lens dark matter distribution. We considered three families of mass profiles: SIE, DVC and DVC+NFW(*), where the star denotes a scaling relation between the light component and the NFW halo. We take into account any extra deflector detected along the line-of-sight, and we include a shear term in all the fits. We have used time delay constraints when available but have chosen not to include flux ratios in the lens modelling, as they are prone to being affected by microlensing. Keeping in mind that lens modelling suffers from well-known degeneracies and that some cases are poorly constrained, especially without time delay measurements, we conduct several fits on our sample and compare their individual goodness-of-fit as a first step towards assessing the existence of dark matter halos around our lensing galaxies. The SIE model has turned out to yield the most satisfactory fits on a χ^2 criterion for the majority of cases. However, for five out of eight systems, the addition of an NFW(*) dark matter halo to a DVC profile has not improved the fit. Although this is not in favour of dark matter halos existing around these galaxies, the low number of constraints, the probable degeneracies and the lack of clear trend in our sample call for further investigation using more robust, less model-dependent proxies.

To that aim, we have computed the mass-to-light ratios of our galaxies within their Einstein radii by combining the results from lens modelling and image processing. The Einstein radius and the total mass comprised within it have been computed using the *lensmodel* package. They are not tightly model-dependent, confirming that the M/L within $\theta_{\rm Ein}$ should give a more robust information about the dark matter content of the lenses. The total H-band flux has been computed thanks to the brightness distribution model from our image processing. The best-fitting de Vaucouleurs model obtained with our shape and in-

tensity parameters measurements has been integrated in a circle of a radius equal to $\theta_{\rm Ein}$. A K-correction has been added to that result to account for the redshift of the lenses. Both M and L have been estimated with secure error bars. The uncertainty on M stems from the (small) uncertainty on $\theta_{\rm Ein}$, stemming itself from the covariance matrices on the best-fitting mass models parameters. The error bars on L are evaluated in details, accounting for all the systematics we could identify.

The observed M/L values are plotted as a function of the Einstein radius in units of half-light radius. They are compared to theoretical M/L values, based on different assumptions on the dark matter content. First, the M/L of the stellar component only are taken into account. Using single stellar population synthesis results from Maraston (2005), a range of plausible M/L for the stellar content of elliptical galaxies is determined, with a width coming from the plausible domain of age, metallicity and IMF. They should mimic a dark-matter free galaxy. Then, a range of M/L for a spiral-like dark matter halo is computed by integrating projected de Vaucouleurs and NFW profiles, and calibrated on NGC3198. Even when correcting for the uncertainties on age and IMFs, the results are not conclusive enough to draw any conclusion on the lenses dark matter content. Indeed, most objects have a low $\theta_{\rm Ein}/\theta_{\rm eff}$ ratio (below 3), which is less relevant in the search for dark matter halos. Some studies combining lensing and kinematics data have provided an estimate for the core M/L around $\theta_{\rm eff}$ of some ellipticals of about 1.5 solar units (e.g. Pierini et al. 2002, Cappellari et al. 2006b, Grillo et al. 2008, Ferreras et al. 2008). Some other studies, based on planetary nebulae, have yielded higher estimates, of between 5 and 7 solar units (Bertin et al. 1988, Bacon et al. 1985, Capaccioli et al. 2002). For three systems in our sample, we are not probing much farther than $\theta_{\rm eff}$, and our M/L estimate lies between those two trends. They are thus not incompatible with a dark matter rich core. On the other hand, three systems have a $\theta_{\rm Ein}/\theta_{\rm eff}$ ratio above 3. Remarkably, their mass-to-light ratios lie out of the plausible dark halo-including M/L range, and are amongst the lowest of the sample. This does not seem compatible with the presence of a dark matter halo. The dispersed character of our results, as well as the broad hypotheses (for example on stellar populations M/L) they rely on, prevent us from drawing any secure conclusion.

Beyond its very value, the behaviour of M/L with galacto-centric distance constitutes a good proxy for the existence of a dark halo. An increase in the observed $M/L(r)$ function (with $r = \theta_{\rm Ein}/\theta_{\rm eff}$ in this case) would be expected in the presence of a dark halo. That increase has been quantified by the slope of linear regressions on M/L versus $\theta_{\rm Ein}/\theta_{\rm eff}$, for the hypothetical M/L obtained from our theoretical light and mass profile integration. We have taken the uncertainty coming from the NGC3198 calibration into account in the form of an error bar on the slope. We have then performed such linear regressions on the observed M/L versus $\theta_{\rm Ein}/\theta_{\rm eff}$ from our sample. We have obtained negative slopes with large error bars coming from uncertainties on both M/L and $\theta_{\rm Ein}/\theta_{\rm eff}$, regardless of the mass profile we considered for the lens modelling. The observed slopes are compatible with a null slope at 1.3σ on average, but the large uncertainties on $\theta_{\rm Ein}/\theta_{\rm eff}$ make this observation weakly conclusive. Their negative quality highlights the uncertainties coming from the uneven distribution of the M/L points between inner and outer parts of the galaxy.

All in all, the mass-to-light ratios of our sample have provided no evidence for dark matter halos in galaxies, but important uncertainties prevent them from bringing out any secure evidence against their existence. The large error bars on $\theta_{\rm Ein}/\theta_{\rm eff}$ seem to be responsible for an important contribution to the slopes 1σ error bars. Despite this lack of strong conclusion, the search for dark halos around lensing galaxies through their mass-to-light ratios ought to be carried out further. Indeed, the present result paves way for more research, particularly in order to reduce the $\theta_{\rm Ein}/\theta_{\rm eff}$ uncertainty.

It appears that the large $\theta_{\rm Ein}/\theta_{\rm eff}$ error bar is mainly due to $\sigma_{\theta_{\rm eff}}$. Reducing the uncertainty on the half-light radius thus seems to be the most direct way to achieve better constraint on the $M/L(r)$ slopes. However, $\sigma_{\theta_{\rm eff}}$ takes into account a lot of systematics that would be difficult to overcome, such as the astrometric uncertainties on the sources and lenses. It can be seen by examining Table 3.1 that no single source of uncertainty dominates the error budget. Therefore, reducing the error bar on $\theta_{\rm eff}$ would be a matter of improving the astrometry and/or the PSF determination. Moreover, despite significantly improving the area of the region of interest, the lensed signal subtraction comes with a few drawbacks that could be addressed. It sometimes produces artefacts, that are for the moment taken into account using weighting masks with a null weight on affected pixels. This only happened for B1422. In fact, B1422 is the system for which the $\theta_{\rm Ein}/\theta_{\rm eff}$ uncertainty is the largest: one of the sources is very close in projection to the lensing galaxy, and the difficulty of disentangling it from lens signal produces a large $\sigma_{\theta_{\rm eff}}$. The effect of a smoothing process on pixels affected by such artefacts, like an interpolation on neighbouring pixels for example, could be investigated. The only remaining strong hypothesis on the light profile is the use of a de Vaucouleurs profile. Switching to a Sérsic profile may change the value of $\theta_{\rm eff}$ and improve its error bar, particularly for B1422: its physical brightness distribution does not seem to be well represented by a de Vaucouleurs, as can be seen from the residual curvature test in Figure 3.16. An independent method to estimate the galaxies Sérsic index could be designed, along the same line of reasoning than the methods we designed in this work for the measurement of the shape parameters.

Besides reducing the error bars on $\theta_{\rm Ein}/\theta_{\rm eff}$, another way to better constrain the $M/L(r)$ trends would be to enlarge the sample, including more points preferably with higher $\theta_{\rm Ein}/\theta_{\rm eff}$. Owing to selection biases and instrument sensitivity limits, this issue could currently be solved by including doubly-lensed quasars, although they are less constrained than quadruply-imaged quasars and would probably produce large uncertainties on $\theta_{\rm Ein}$ and $M(\theta_{\rm Ein})$.

In the near future, new instruments like Euclid (Laureijs et al. 2014) should make it possible to survey a wealth of new lensing systems, providing a larger sample on which this kind of analysis could be conducted and opening the possibility of adding a statistical quality to this study (Amiaux et al. 2012, Collett 2015, Serjeant 2017). Future data may also include lenses probing farther out than in this work. Another improvement to this analysis could reside in combining lensing data to spectral energy distribution data, providing a more secure estimate of the flux in the H-band (or any other relevant band) without resorting to a K-correction. The redshift of far away galaxies tends to shift the bulk of their flux in the far infrared bands, so this sort of observation on high-redshift

lenses would require a great sensitivity in a variety of infrared wavebands that the James Webb Space Telescope may satisfy (Gardner et al. 2006, Dixon et al. 2016, Giardino et al. 2016).

Understanding the distribution of dark matter in elliptical galaxies is challenging but crucial to build accurate galaxy formation models. Under the merger hypothesis, the fate of the progenitors dark matter halos can be investigated mainly through simulations. They are thought to merge into a single, larger halo around the remnant, and its shape is defined by the mergers conditions (Steinmetz and Mueller 1993, Chiosi and Carraro 2002, Gonzalez Garcia 2003, Gerhard 2006, Mo et al. 2010, for example). Extended halos should then be detected around ellipticals. This work seems to lean slightly more towards the absence of dark halos around the members of our sample, which would contradict the mergers scenario. If this conclusion were to become more commonly reached by different dark matter proxies in ellipticals, it could shed a new light on galaxy formation and evolution, and potentially question dark matter halos in spirals, too. The evidence for dark matter halos around spiral galaxies is compelling. A viable alternative that does not require any modification of Newtonian dynamics is the hypothesis suggested by Pfenniger et al. (1994) and Pfenniger and Combes (1994) that at least some of the dark matter in spiral halos could be made up of cold gas with a high proportion of molecular and atomic hydrogen clouds. Indeed, such clouds could be made of primordial matter, presenting few spectral lines, making them hard to detect. The 21-cm line of atomic hydrogen has been observed at large galacto-centric distances, indicating the existence of cold gas clouds beyond the visible disk region. In that scenario, a merger could induce the contraction of such clouds, but because they could not cool down through radiation, the contraction would not be efficient and would not trigger star formation. If further investigation were in fact to confirm the existence of dark matter halos around elliptical galaxies, this would not invalidate the cold gas cloud hypothesis.

The present work opens up leads to continue investigating the existence of dark matter halos in ellipticals using robust, lensing-based proxies. We have highlighted biases in classical galaxy light profile fitting methods, and designed techniques to alleviate these issues, providing an accurate determination of the light content of eight lenses. We have extensively studied lens modelling results for a variety of mass models on these eight objects, and have shown that adding an NFW halo does not systematically improve the fit quality indicators compared to a "mass-follows-light" profile. We have characterised the lenses mass-to-light ratios, and despite the impossibility of bringing out a definitive answer to our initial question, have set forth to more accurate studies of dark matter in early-type gravitational lensing galaxies.

Appendix 1: Results of flux and mass measurements within $\theta_{\rm Ein}$

Table A1: $F_H(\theta_{\rm Ein})$ and $M(\theta_{\rm Ein})$ within the Einstein radius of each system from each mass model, with their 1σ error bars, for both Hubble constants.

System	$F_H(\theta_{\rm Ein})(in\ 10^{11} F_{H,\odot})$	$M(\theta_{\rm Ein})(in\ 10^{11} M\odot)$
No Δt		
SIE		
MG0414	2.940 ± 0.704	5.730 ± 0.011
HE0435	1.164 ± 0.170	3.253 ± 0.008
RXJ0911	1.584 ± 0.037	3.764 ± 0.006
SDSS0924	0.696 ± 0.137	1.491 ± 0.000
PG1115	0.666 ± 0.080	1.917 ± 0.001
SDSS1138	0.558 ± 0.065	0.881 ± 0.003
B1422	0.288 ± 0.085	0.868 ± 0.004
WFI2033	1.367 ± 0.246	4.397 ± 0.006
DVC		
MG0414	2.937 ± 0.704	5.706 ± 0.014
HE0435	1.134 ± 0.166	3.237 ± 0.008
RXJ0911	1.585 ± 0.037	3.781 ± 0.008
SDSS0924	0.696 ± 0.137	1.490 ± 0.002
PG1115	0.667 ± 0.080	1.926 ± 0.005
SDSS1138	0.558 ± 0.065	0.875 ± 0.004
B1422	0.288 ± 0.085	0.845 ± 0.003
WFI2033	1.360 ± 0.245	4.292 ± 0.007
DVC+NFW		
MG0414	2.939 ± 0.704	5.705 ± 0.014
HE0435	1.134 ± 0.166	3.237 ± 0.008
RXJ0911	1.651 ± 0.039	4.449 ± 0.010
SDSS0924	0.696 ± 0.137	1.490 ± 0.002
PG1115	0.666 ± 0.080	1.926 ± 0.005
SDSS1138	0.558 ± 0.065	0.875 ± 0.004
B1422	0.288 ± 0.085	0.848 ± 0.004
WFI2033	1.364 ± 0.245	4.292 ± 0.007

Continued on next page

Table A1 – continued from previous page

DVC+NFW*		
MG0414	2.938 ± 0.704	5.705 ± 0.014
HE0435	1.199 ± 0.175	3.243 ± 0.008
RXJ0911	1.655 ± 0.039	4.501 ± 0.010
SDSS0924	0.696 ± 0.137	1.490 ± 0.002
PG1115	0.667 ± 0.080	1.926 ± 0.005
SDSS1138	0.558 ± 0.065	0.875 ± 0.004
B1422	0.288 ± 0.085	0.844 ± 0.004
WFI2033	1.360 ± 0.245	4.292 ± 0.007
$H_0 = H1$		
SIE		
HE0435	1.165 ± 0.170	3.254 ± 0.008
RXJ0911	1.592 ± 0.038	3.840 ± 0.006
PG1115	0.667 ± 0.080	1.919 ± 0.002
B1422	0.288 ± 0.085	0.867 ± 0.004
WFI2033	1.364 ± 0.246	4.358 ± 0.008
DVC		
HE0435	1.163 ± 0.170	3.238 ± 0.008
RXJ0911	1.556 ± 0.037	3.511 ± 0.009
PG1115	0.666 ± 0.080	1.924 ± 0.005
B1422	0.283 ± 0.084	0.698 ± 0.003
WFI2033	1.361 ± 0.245	4.309 ± 0.008
DVC+NFW		
HE0435	1.164 ± 0.170	3.249 ± 0.000
RXJ0911	1.661 ± 0.039	4.387 ± 0.010
PG1115	0.667 ± 0.080	1.933 ± 0.005
B1422	0.292 ± 0.086	1.009 ± 0.001
WFI2033	1.364 ± 0.245	4.348 ± 0.008
DVC+NFW*		
HE0435	1.164 ± 0.170	3.244 ± 0.000
RXJ0911	1.630 ± 0.038	4.226 ± 0.010
PG1115	0.667 ± 0.080	1.933 ± 0.005
B1422	0.291 ± 0.086	0.996 ± 0.001
WFI2033	1.365 ± 0.246	4.370 ± 0.008

Continued on next page

Table A1 – continued from previous page

$H_0 = H2$		
SIE		
HE0435	1.517 ± 0.222	3.823 ± 0.009
RXJ0911	2.212 ± 0.052	4.254 ± 0.006
PG1115	0.920 ± 0.111	2.265 ± 0.002
B1422	0.399 ± 0.118	1.020 ± 0.004
WFI2033	1.883 ± 0.339	5.094 ± 0.009
DVC		
HE0435	1.515 ± 0.221	3.810 ± 0.010
RXJ0911	2.098 ± 0.050	3.759 ± 0.011
PG1115	0.922 ± 0.111	2.277 ± 0.006
B1422	0.392 ± 0.116	0.823 ± 0.003
WFI2033	1.879 ± 0.338	5.048 ± 0.009
DVC+NFW		
HE0435	1.516 ± 0.222	3.820 ± 0.000
RXJ0911	2.287 ± 0.054	5.285 ± 0.012
PG1115	0.922 ± 0.111	2.272 ± 0.006
B1422	0.403 ± 0.119	1.187 ± 0.001
WFI2033	1.886 ± 0.339	5.126 ± 0.009

Bibliography

Amiaux, J., Scaramella, R., Mellier, Y., Altieri, B., Burigana, C., Da Silva, A., Gomez, P., Hoar, J., Laureijs, R., Maiorano, E., Magalhães Oliveira, D., Renk, F., Saavedra Criado, G., Tereno, I., Auguères, J. L., Brinchmann, J., Cropper, M., Duvet, L., Ealet, A., Franzetti, P., Garilli, B., Gondoin, P., Guzzo, L., Hoekstra, H., Holmes, R., Jahnke, K., Kitching, T., Meneghetti, M., Percival, W., and Warren, S.: 2012, in *Space Telescopes and Instrumentation 2012: Optical, Infrared, and Millimeter Wave*, Vol. 8442 of *Proc. SPIE*, p. 84420Z

Bacon, R., Monnet, G., and Simien, F.: 1985, *A&A* **152**, 315

Bade, N., Siebert, J., Lopez, S., Voges, W., and Reimers, D.: 1997, *A&A* **317**, L13

Barber, C., Crain, R. A., and Schaye, J.: 2018, *ArXiv e-prints*

Barkana, R.: 1997, *ApJ* **489**, 21

Bartelmann, M.: 1996, *A&A* **313**, 697

Bertin, G., Bertola, F., Buson, L. M., Danzinger, I. J., Dejonghe, H., Sadler, E. M., Saglia, R. P., de Zeeuw, P. T., and Zeilinger, W. W.: 1994, *Astronomy and Astrophysics* **292**, 381

Bertin, G., Saglia, R. P., and Stiavelli, M.: 1988, *ApJ* **330**, 78

Bertone, G., Hooper, D., and Silk, J.: 2005, *Phys. Rep.* **405**, 279

Biernaux, J., Magain, P., and Hauret, C.: 2017, *A&A* **604**, A46

Biernaux, J., Magain, P., Sluse, D., and Chantry, V.: 2016, *Astronomy and Astrophysics* **585**, A84

Binney, J. and Merrifield, M.: 1998, *Galactic Astronomy*

Binney, J. J., Davies, R. L., and Illingworth, G. D.: 1990, *ApJ* **361**, 78

Blumenthal, G. R., Faber, S. M., Primack, J. R., and Rees, M. J.: 1984, *Nature* **311**, 517

Bolton, A. S., Brownstein, J. R., Kochanek, C. S., Shu, Y., Schlegel, D. J., Eisenstein, D. J., Wake, D. A., Connolly, N., Maraston, C., Arneson, R. A., and Weaver, B. A.: 2012, *Astrophysical Journal* **757**, 82

Bonvin, V., Chan, J. H. H., Millon, M., Rojas, K., Courbin, F., Chen, C. F., Fassnacht, C. D., Paic, E., Tewes, M., Chao, D. C.-Y., Chijani, M., Gilman, D., Gilmore, K., Williams, P., Buckley-Geer, E., Frieman, J., Marshall, P. J., Suyu, S. H., Treu, T., Hempel, A., Kim, S., Lachaume, R., Rabus, M., Anguita, T., Meylan, G., Motta, V., Magain, P., and Van Winckel, H.: 2018, *A&A*

Bonvin, V., Courbin, F., Suyu, S. H., Marshall, P. J., Rusu, C. E., Sluse, D., Tewes, M., Wong, K. C., Collett, T., Fassnacht, C. D., Treu, T., Auger, M. W., Hilbert, S., Koopmans, L. V. E., Meylan, G., Rumbaugh, N., Sonnenfeld, A., and Spiniello, C.: 2017, *MNRAS* **465**, 4914

Bonvin, V., Tewes, M., Courbin, F., Kuntzer, T., Sluse, D., and Meylan, G.: 2016, *A&A* **585**, A88

Bosma, A.: 1981, *AJ* **86**, 1791

Brimioulle, F., Seitz, S., Lerchster, M., Bender, R., and Snigula, J.: 2013, *Monthly Notices of the Royal Astronomical Society* **432(2)**, 1046

Burkert, A., Naab, T., Johansson, P. H., and Jesseit, R.: 2008, *ApJ* **685**, 897

Burud, I.: 2001, *Ph.D. thesis*, Institute of Astrophysics and Geophysics in Liege

Burud, I., Courbin, F., Lidman, C., Jaunsen, A. O., Hjorth, J., Østensen, R., Andersen, M. I., Clasen, J. W., Wucknitz, O., Meylan, G., Magain, P., Stabell, R., and Refsdal, S.: 1998, *ApJ* **501**, L5

Burud, I., Magain, P., Sohy, S., and Hjorth, J.: 2001, *A&A* **380**, 805

C. Renault, C. A. e. a.: 1997, *Astronomy and Astrophysics* 324

Capaccioli, M., Napolitano, N. R., and Arnaboldi, M.: 2002, *ArXiv Astrophysics e-prints*

Cappellari, M., Bacon, R., Bureau, M., Damen, M. C., Davies, R. L., de Zeeuw, P. T., Emsellem, E., Falcón-Barroso, J., Krajnović, D., Kuntschner, H., McDermid, R. M., Peletier, R. F., Sarzi, M., van den Bosch, R. C. E., and van de Ven, G.: 2006a, in G. A. Mamon, F. Combes, C. Deffayet, and B. Fort (eds.), *EAS Publications Series*, Vol. 20 of *EAS Publications Series*, pp 127–130

Cappellari, M., Bacon, R., Bureau, M., Damen, M. C., Davies, R. L., de Zeeuw, P. T., Emsellem, E., Falcón-Barroso, J., Krajnović, D., Kuntschner, H., McDermid, R. M., Peletier, R. F., Sarzi, M., van den Bosch, R. C. E., and van de Ven, G.: 2006b, *MNRAS* **366**, 1126

Cappellari, M., Emsellem, E., Krajnović, D., McDermid, R. M., Scott, N., Verdoes Kleijn, G. A., Young, L. M., Alatalo, K., Bacon, R., Blitz, L., Bois, M., Bournaud, F., Bureau, M., Davies, R. L., Davis, T. A., de Zeeuw, P. T., Duc, P.-A., Khochfar, S., Kuntschner, H., Lablanche, P.-Y., Morganti, R., Naab, T., Oosterloo, T., Sarzi, M., Serra, P., and Weijmans, A.-M.: 2011, *MNRAS* **413**, 813

Cappellari, M., McDermid, R. M., Alatalo, K., Blitz, L., Bois, M., Bournaud, F., Bureau, M., Crocker, A. F., Davies, R. L., Davis, T. A., de Zeeuw, P. T., Duc, P.-A., Emsellem, E., Khochfar, S., Krajnović, D., Kuntschner, H., Morganti, R., Naab, T., Oosterloo, T., Sarzi, M., Scott, N., Serra, P., Weijmans, A.-M., and Young, L. M.: 2013, *Monthly Notices of the RAS* **432**, 1862

Cappellari, M., Romanowsky, A. J., Brodie, J. P., Forbes, D. A., Strader, J., Foster, C., Kartha, S. S., Pastorello, N., Pota, V., Spitler, L. R., Usher, C., and Arnold, J. A.: 2015, *Astrophysical Journal, Letters* **804**, L21

Cardone, V. F.: 2004, *A&A* **415**, 839

Carollo, C. M., de Zeeuw, P. T., van der Marel, R. P., Danziger, I. J., and Qian, E. E.: 1995, *ApJ* **441**, L25

Cen, R. and Ostriker, J. P.: 2006, *ApJ* **650**, 560

Chae, K.-H., Bernardi, M., and Kravtsov, A. V.: 2014, *MNRAS* **437**, 3670

Chantry, V.: 2009, *Ph.D. thesis*, Unversity of Liège

Chantry, V. and Magain, P.: 2007, *Astronomy and Astrophysics* **470**, 467

Chantry, V., Sluse, D., and Magain, P.: 2010, *Astronomy and Astrophysics* **522**, A95

Chiosi, C. and Carraro, G.: 2002, *MNRAS* **335**, 335

Cole, S. and Lacey, C.: 1996, *MNRAS* **281**, 716

Colina, L., Bohlin, R. C., and Castelli, F.: 1996, *AJ* **112**, 307

Collett, T. E.: 2015, *ApJ* **811**, 20

Courbin, F.: 1999, *Ph.D. thesis*, Institut d'astrophysique, Universite de Liege, Belgium; Observatoire de Paris Meudon - DAEC, FRance

Courbin, F.: 2003, *ArXiv Astrophysics e-prints*

Courbin, F., Chantry, V., Revaz, Y., Sluse, D., Faure, C., Tewes, M., Eulaers, E., Koleva, M., Asfandiyarov, I., Dye, S., Magain, P., van Winckel, H., Coles, J., Saha, P., Ibrahimov, M., and Meylan, G.: 2011, *Astronomy and Astrophysics* **536**, A53

Cox, T. J., Dutta, S. N., Di Matteo, T., Hernquist, L., Hopkins, P. F., Robertson, B., and Springel, V.: 2006, *ApJ* **650**, 791

Cyburt, R. H., Fields, B. D., Olive, K. A., and Yeh, T.-H.: 2016, *Reviews of Modern Physics* **88(1)**, 015004

Davé, R., Cen, R., Ostriker, J. P., Bryan, G. L., Hernquist, L., Katz, N., Weinberg, D. H., Norman, M. L., and O'Shea, B.: 2001, *ApJ* **552**, 473

De Lorenzi, F., Gerhard, O., Coccato, L., Arnaboldi, M., Capaccioli, M., Douglas, N. G., Freeman, K. C., Kuijken, K., Merrifield, M. R., Napolitano, N. R., Noordermeer, E., Romanowsky, A. J., and Debattista, V. P.: 2009, *Monthly Notices of the Royal Astronomical Society* **395(1)**, 76

de Paolis, F., Ingrosso, G., and Strafella, F.: 1995, *ApJ* **438**, 83

de Vaucouleurs, G.: 1948, *Annales d'Astrophysique* **11**, 247

Dekel, A., Stoehr, F., Mamon, G. A., Cox, T. J., Novak, G. S., and Primack, J. R.: 2005, *Nature* **437**, 707

Diehl, S. and Statler, T. S.: 2007, *ApJ* **668**, 150

Dixon, W. V., Ravindranath, S., and Willott, C. J.: 2016, in S. Kaviraj (ed.), *Galaxies at High Redshift and Their Evolution Over Cosmic Time*, Vol. 319 of *IAU Symposium*, pp 11–11

D.P. Bennett, C. A. e. a.: 1997, *ArXiv Asrtrophysics e-prints, arxiv:astro-ph/9510104*

Dressler, A.: 1980, *ApJ* **236**, 351

Dubinski, J.: 1998, *ApJ* **502**, 141

Dutton, A. A. and Treu, T.: 2014, *MNRAS* **438**, 3594

Eichner, T.: 2013, *Ph.D. thesis*, Ludwig-Maximilians-Universität Münchene

Eigenbrod, A., Courbin, F., Dye, S., Meylan, G., Sluse, D., Vuissoz, C., and Magain, P.: 2006a, *Astronomy and Astrophysics* **451**, 747

Eigenbrod, A., Courbin, F., Meylan, G., Vuissoz, C., and Magain, P.: 2006b, *A&A* **451**, 759

Einstein, A.: 1936, *Science* **84**, 506

Emsellem, E., Cappellari, M., Peletier, R. F., McDermid, R. M., Bacon, R., Bureau, M., Copin, Y., Davies, R. L., Krajnović, D., Kuntschner, H., Miller, B. W., and de Zeeuw, P. T.: 2004, *MNRAS* **352**, 721

Eulaers, E.: 2012, *Ph.D. thesis*, Institute of Astrophysics and Geophysics in Liege

Eulaers, E. and Magain, P.: 2011, *A&A* **536**, A44

Fabricant, D., Lecar, M., and Gorenstein, P.: 1980, *ApJ* **241**, 552

Falco, E. E., Gorenstein, M. V., and Shapiro, I. I.: 1985, *ApJ* **289**, L1

Falco, E. E., Lehar, J., and Shapiro, I. I.: 1997, *AJ* **113**, 540

Ferreras, I., Saha, P., and Burles, S.: 2008, *MNRAS* **383**, 857

Fioc, M. and Rocca-Volmerange, B.: 1997, *A&A* **326**, 950

Forbes, D. A.: 1999, in G. Giuricin, M. Mezzetti, and P. Salucci (eds.), *Observational Cosmology: The Development of Galaxy Systems*, Vol. 176 of *Astronomical Society of the Pacific Conference Series*, p. 347

Forman, W., Jones, C., and Tucker, W.: 1985, *ApJ* **293**, 102

Franx, M., van Dokkum, P., Kelson, D., Illingworth, G., and Fabricant, D.: 1999, in J. E. Barnes and D. B. Sanders (eds.), *Galaxy Interactions at Low and High Redshift*, Vol. 186 of *IAU Symposium*, p. 447

Fukugita, M. and Peebles, P. J. E.: 2004, *ApJ* **616**, 643

Gardner, J. P., Mather, J. C., Clampin, M., Doyon, R., Greenhouse, M. A., Hammel, H. B., Hutchings, J. B., Jakobsen, P., Lilly, S. J., Long, K. S., Lunine, J. I., McCaughrean, M. J., Mountain, M., Nella, J., Rieke, G. H., Rieke, M. J., Rix, H.-W., Smith, E. P., Sonneborn, G., Stiavelli, M., Stockman, H. S., Windhorst, R. A., and Wright, G. S.: 2006, *Space Sci. Rev.* **123**, 485

Gavazzi, R., Treu, T., Koopmans, L. V. E., Bolton, A. S., Moustakas, L. A., Burles, S., and Marshall, P. J.: 2008, *ApJ* **677**, 1046

Gerhard, O.: 2006, in L. Stanghellini, J. R. Walsh, and N. G. Douglas (eds.), *Planetary Nebulae Beyond the Milky Way*, pp 299–310, Springer Berlin Heidelberg, Berlin, Heidelberg

Giardino, G., de Oliveira, C. A., Arribas, S., Beck, T. L., Birkmann, S. M., Boeker, T., Bunker, A. J., Charlot, S., Chevallard, J., De Marchi, G., Ferruit, P., Franx, M., Maiolino, R., Moseley, S. H., Rauscher, B. J., Rix, H.-W., Sirianni, M., and Willott, C. J.: 2016, in I. Skillen, M. Balcells, and S. Trager (eds.), *Multi-Object Spectroscopy in the Next Decade: Big Questions, Large Surveys, and Wide Fields*, Vol. 507 of *Astronomical Society of the Pacific Conference Series*, p. 305

Golse, G. and Kneib, J.-P.: 2002, *A&A* **390**, 821

Gonzalez Garcia, A.: 2003, *Ph.D. thesis*

Gorenstein, M. V., Shapiro, I. I., and Falco, E. E.: 1988, *ApJ* **327**, 693

Grant, C. E., Bautz, M. W., Chartas, G., and Garmire, G. P.: 2004, *ApJ* **610**, 686

Grillo, C., Gobat, R., Rosati, P., and Lombardi, M.: 2008, *A&A* **477**, L25

Hazard, C., Morton, D. C., Terlevich, R., and McMahon, R.: 1984, *Astrophysical Journal* **282**, 33

Hewitt, J. N., Turner, E. L., Lawrence, C. R., Schneider, D. P., and Brody, J. P.: 1992, *AJ* **104**, 968

Hibbard, J. E. and Yun, M. S.: 2000, in F. Combes, G. A. Mamon, and V. Charmandaris (eds.), *Dynamics of Galaxies: from the Early Universe to the Present*, Vol. 197 of *Astronomical Society of the Pacific Conference Series*, p. 349

Hjorth, J., Burud, I., Jaunsen, A. O., Schechter, P. L., Kneib, J.-P., Andersen, M. I., Korhonen, H., Clasen, J. W., Kaas, A. A., Østensen, R., Pelt, J., and Pijpers, F. P.: 2002, *ApJ* **572**, L11

Hook, R. and Krist, J.: 1997, *Space Telescope European Coordinating Facility Newsletter* **24**, 10

Huchra, J. and Brodie, J.: 1987, *AJ* **93**, 779

Humphrey, P. J., Buote, D. A., Gastaldello, F., Zappacosta, L., Bullock, J. S., Brighenti, F., and Mathews, W. G.: 2006, *ApJ* **646**, 899

Impey, C. D., Foltz, C. B., Petry, C. E., Browne, I. W. A., and Patnaik, A. R.: 1996, *ApJ* **462**, L53

Inada, N., Becker, R. H., Burles, S., Castander, F. J., Eisenstein, D., Hall, P. B., Johnston, D. E., Pindor, B., Richards, G. T., Schechter, P. L., Sekiguchi, M., White, R. L., Brinkmann, J., Frieman, J. A., Kleinman, S. J., Krzesiński, J., Long, D. C., Neilsen, Jr., E. H., Newman, P. R., Nitta, A., Schneider, D. P., Snedden, S., and York, D. G.: 2003, *AJ* **126**, 666

Inada, N., Oguri, M., Becker, R. H., Shin, M.-S., Richards, G. T., Hennawi, J. F., White, R. L., Pindor, B., Strauss, M. A., Kochanek, C. S., Johnston, D. E., Gregg, M. D., Kayo, I., Eisenstein, D., Hall, P. B., Castander, F. J., Clocchiatti, A., Anderson, S. F., Schneider, D. P., York, D. G., Lupton, R., Chiu, K., Kawano, Y., Scranton, R., Frieman, J. A., Keeton, C. R., Morokuma, T., Rix, H.-W., Turner, E. L., Burles, S., Brunner, R. J., Sheldon, E. S., Bahcall, N. A., and Masataka, F.: 2008, *AJ* **135**, 496

Janz, J., Cappellari, M., Romanowsky, A. J., Ciotti, L., Alabi, A., and Forbes, D. A.: 2016, *MNRAS* **461**, 2367

Jun, H. D. and Im, M.: 2008, *ApJ* **678**, L97

Keeton, C. R.: 2001, *ArXiv Astrophysics e-prints*

Keeton, C. R.: 2002, in N. Metcalfe and T. Shanks (eds.), *A New Era in Cosmology*, Vol. 283 of *Astronomical Society of the Pacific Conference Series*, p. 173

Keeton, C. R.: 2011, *GRAVLENS: Computational Methods for Gravitational Lensing*, Astrophysics Source Code Library

Keeton, C. R., Burles, S., Schechter, P. L., and Wambsganss, J.: 2006a, *ApJ* **639**, 1

Keeton, C. R., Burles, S., Schechter, P. L., and Wambsganss, J.: 2006b, *Astrophysical Journal* **639**, 1

Keeton, C. R., Kochanek, C. S., and Seljak, U.: 1997, *ApJ* **482**, 604

Keselman, A. and Nusser, A.: 2012, *ArXiv e-prints*

Klimov, Y. G.: 1963a, *AZh* **40**, 874

Klimov, Y. G.: 1963b, *Soviet Physics Doklady* **8**, 119

Klimov, Y. G.: 1963c, *Soviet Physics Doklady* **8**, 431

Kneib, J.-P., Cohen, J. G., and Hjorth, J.: 2000a, *ApJ* **544**, L35

Kneib, J.-P., Cohen, J. G., and Hjorth, J.: 2000b, *ApJ* **544**, L35

Kochanek, C. S., Falco, E. E., Impey, C. D., Lehár, J., McLeod, B. A., Rix, H.-W., Keeton, C. R., Muñoz, J. A., and Peng, C. Y.: 2000, *Astrophysical Journal* **543**, 131

Kochanek, C. S., Morgan, N. D., Falco, E. E., McLeod, B. A., Winn, J. N., Dembicky, J., and Ketzeback, B.: 2006, *Astrophysical Journal* **640**, 47

Kormann, R., Schneider, P., and Bartelmann, M.: 1994, *A&A* **284**, 285

Kormendy, J., Fisher, D. B., Cornell, M. E., and Bender, R.: 2009, *Astrophysical Journals* **182**, 216

Kravtsov, A. V.: 2013, *The Astrophysical Journal Letters* **764(2)**, L31

Krist, J. E. and Hook, R. N.: 1997, in S. Casertano, R. Jedrzejewski, T. Keyes, and M. Stevens (eds.), *The 1997 HST Calibration Workshop with a New Generation of Instruments*, p. 192

Kroupa, P.: 2002, in E. K. Grebel and W. Brandner (eds.), *Modes of Star Formation and the Origin of Field Populations*, Vol. 285 of *Astronomical Society of the Pacific Conference Series*, p. 86

Kundic, T., Hogg, D. W., Blandford, R. D., Cohen, J. G., Lubin, L. M., and Larkin, J. E.: 1997, *AJ* **114**, 2276

Lacey, C. and Cole, S.: 1993, *MNRAS* **262**, 627

Lagattuta, D. J., Fassnacht, C. D., Auger, M. W., Marshall, P. J., Bradač, M., Treu, T., Gavazzi, R., Schrabback, T., Faure, C., and Anguita, T.: 2010, *ApJ* **716**, 1579

Laureijs, R., Hoar, J., Buenadicha3, G., Mellier, Y., Pasian, F., Dabin, C., Sauvage, M., and Euclid Collaboration: 2014, in N. Manset and P. Forshay (eds.), *Astronomical Data Anaylsis Software and Systems XXIII*, Vol. 485 of *Astronomical Society of the Pacific Conference Series*, p. 495

Lawrence, C. R., Neugebauer, G., Weir, N., Matthews, K., and Patnaik, A. R.: 1992, *MNRAS* **259**, 5P

Leier, D., Ferreras, I., and Saha, P.: 2012, *MNRAS* **424**, 104

Leier, D., Ferreras, I., Saha, P., Charlot, S., Bruzual, G., and La Barbera, F.: 2016, *MNRAS* **459**, 3677

Lewis, A.: 2008, *Physical Review D* **78(2)**, 023002

Liebes, S.: 1964, *Physical Review* **133**, 835

Liesenborgs, J. and De Rijcke, S.: 2012, *MNRAS* **425**, 1772

Liesenborgs, J., de Rijcke, S., Dejonghe, H., and Bekaert, P.: 2009, *MNRAS* **397**, 341

Liller, M. H.: 1960, *Astrophysical Journal* **132**, 306

Liller, M. H.: 1966, *Astrophysical Journal* **146**, 28

Longair, M.: 2006, *The Cosmic Century: A History of Astrophysics and Cosmology*, Cambridge University Press

Lucy, L. B.: 1974, *Astronomical Journalj* **79**, 745

Magain, P., Courbin, F., Gillon, M., Sohy, S., Letawe, G., Chantry, V., and Letawe, Y.: 2007, *Astronomy and Astrophysics* **461**, 373

Magain, P., Courbin, F., and Sohy, S.: 1998, *Astrophysical Journal* **494**, 472

Magain, P., Surdej, J., Swings, J.-P., Borgeest, U., and Kayser, R.: 1988, *Nature* **334**, 325

Mamajek, E. E., Prsa, A., Torres, G., Harmanec, P., Asplund, M., Bennett, P. D., Capitaine, N., Christensen-Dalsgaard, J., Depagne, E., Folkner, W. M., Haberreiter, M., Hekker, S., Hilton, J. L., Kostov, V., Kurtz, D. W., Laskar, J., Mason, B. D., Milone, E. F., Montgomery, M. M., Richards, M. T., Schou, J., and Stewart, S. G.: 2015, *ArXiv e-prints*

Mandelbaum, R., van de Ven, G., and Keeton, C. R.: 2009, *MNRAS* **398**, 635

Mann, A. W. and von Braun, K.: 2015, *PASP* **127**, 102

Maoz, D. and Rix, H.-W.: 1993, *ApJ* **416**, 425

Maraston, C.: 1998, *MNRAS* **300**, 872

Maraston, C.: 1999, in P. Carral and J. Cepa (eds.), *Star Formation in Early Type Galaxies*, Vol. 163 of *Astronomical Society of the Pacific Conference Series*, p. 28

Maraston, C.: 2005, *MNRAS* **362**, 799

McGaugh, S. S., Lelli, F., and Schombert, J. M.: 2016, *Physical Review Letters* **117(20)**, 201101

McGaugh, S. S. and Schombert, J. M.: 2014, *AJ* **148**, 77

McLeod, B. A., Bernstein, G. M., Rieke, M. J., and Weedman, D. W.: 1998, *Astronomical Journal* **115**, 1377

Mediavilla, E., Munoz, J., Garzon, F., and Mahoney, T.: 2016, *Astrophysical applications of gravitational lensing: XXIV Canary Islands Winter School of Astrophysics*, Cambridge University Press

Meneghetti, M., Bartelmann, M., and Moscardini, L.: 2001, *ArXiv Astrophysics e-prints*

Meza, A., Navarro, J. F., Steinmetz, M., and Eke, V. R.: 2003, *ApJ* **590**, 619

Mo, H., van den Bosch, F., and White, S.: 2010, *Galaxy Formation and Evolution*, Cambridge University Press

Momcheva, I., Williams, K., Keeton, C., and Zabludoff, A.: 2006, *ApJ* **641**, 169

Momcheva, I. G.: 2009, *Ph.D. thesis*, The University of Arizona

Morgan, C. W., Kochanek, C. S., Morgan, N. D., and Falco, E. E.: 2006, *Astrophysical Journal* **647**, 874

Morgan, N. D., Caldwell, J. A. R., Schechter, P. L., Dressler, A., Egami, E., and Rix, H.-W.: 2004, *AJ* **127**, 2617

Morgan, N. D., Kochanek, C. S., Pevunova, O., and Schechter, P. L.: 2005, *AJ* **129**, 2531

Muñoz, J. A., Falco, E. E., Kochanek, C. S., Lehár, J., McLeod, B. A., Impey, C. D., Rix, H.-W., and Peng, C. Y.: 1998, *Astrophysics and Space Science* **263**, 51

Napolitano, N. R., Romanowsky, A. J., Coccato, L., Capaccioli, M., Douglas, N. G., Noordermeer, E., Gerhard, O., Arnaboldi, M., De Lorenzi, F., Kuijken, K., Merrifield, M. R., O'Sullivan, E., Cortesi, A., Das, P., and Freeman, K. C.: 2009, *Monthly Notices of the Royal Astronomical Society* **393(2)**, 329

Narayan, R. and Bartelmann, M.: 1996, *ArXiv Astrophysics e-prints*

Navarro, J. F., Frenk, C. S., and White, S. D. M.: 1996, *ApJ* **462**, 563

Nelder, J. A. and Mead, R.: 1965, *Computer Journal* **7**, 308

Nicastro, F., Kaastra, J., Krongold, Y., Borgani, S., Branchini, E., Cen, R., Dadina, M., Danforth, C. W., and Elvis, M.: 2018, *Nature* **558**, 406

Nicastro, F., Krongold, Y., Mathur, S., and Elvis, M.: 2017, *Astronomische Nachrichten* **338**, 281

Ofek, E. O., Maoz, D., Rix, H.-W., Kochanek, C. S., and Falco, E. E.: 2006a, *ApJ* **641**, 70

Ofek, E. O., Maoz, D., Rix, H.-W., Kochanek, C. S., and Falco, E. E.: 2006b, *ApJ* **641**, 70

Oguri, M., Rusu, C. E., and Falco, E. E.: 2014, *MNRAS* **439**, 2494

O'Sullivan, E., Vrtilek, J. M., Harris, D. E., and Ponman, T. J.: 2007, *ApJ* **658**, 299

Parikh, T., Thomas, D., Maraston, C., Westfall, K. B., Goddard, D., Lian, J., Meneses-Goytia, S., Jones, A., Vaughan, S., Andrews, B. H., Bershady, M., Bizyaev, D., Brinkmann, J., Brownstein, J. R., Bundy, K., Drory, N., Emsellem, E., Law, D. R., Newman, J. A., Roman-Lopes, A., Wake, D., Yan, R., and Zheng, Z.: 2018, *MNRAS* **477**, 3954

Patnaik, A. R., Browne, I. W. A., Walsh, D., Chaffee, F. H., and Foltz, C. B.: 1992, *MNRAS* **259**, 1P

Peng, C. Y., Ho, L. C., Impey, C. D., and Rix, H.-W.: 2002, *Astronomical Journal* **124**, 266

Peng, C. Y., Ho, L. C., Impey, C. D., and Rix, H.-W.: 2010, *Astronomical Journal* **139**, 2097

Persic, M., Salucci, P., and Stel, F.: 1996, *MNRAS* **281**, 27

Pfenniger, D. and Combes, F.: 1994, *A&A* **285**, 94

Pfenniger, D., Combes, F., and Martinet, L.: 1994, *A&A* **285**, 79

Pierini, D., Gavazzi, G., Franzetti, P., Scodeggio, M., and Boselli, A.: 2002, *MNRAS* **332**, 422

Pitrou, C., Coc, A., Uzan, J.-P., and Vangioni, E.: 2018, *ArXiv e-prints*

Planck Collaboration, Ade, P. A. R., Aghanim, N., Armitage-Caplan, C., Arnaud, M., Ashdown, M., Atrio-Barandela, F., Aumont, J., Baccigalupi, C., Banday, A. J., and et al.: 2013, *ArXiv e-prints*

Press, W. H., Teukolsky, S. A., Vetterling, W. T., and Flannery, B. P.: 1992, *Numerical recipes in FORTRAN. The art of scientific computing*

Prugniel, P. and Simien, F.: 1997, *Astronomy and Astrophysics* **321**, 111

Prša, A., Harmanec, P., Torres, G., Mamajek, E., Asplund, M., Capitaine, N., Christensen-Dalsgaard, J., Depagne, É., Haberreiter, M., Hekker, S., Hilton, J., Kopp, G., Kostov, V., Kurtz, D. W., Laskar, J., Mason, B. D., Milone, E. F., Montgomery, M., Richards, M., Schmutz, W., Schou, J., and Stewart, S. G.: 2016, *AJ* **152**, 41

Pu, S. B., Saglia, R. P., Fabricius, M. H., Thomas, J., Bender, R., and Han, Z.: 2010, *A&A* **516**, A4

Refsdal, S.: 1964a, *MNRAS* **128**, 307

Refsdal, S.: 1964b, *MNRAS* **128**, 295

Remus, R.-S., Burkert, A., Dolag, K., Johansson, P. H., Naab, T., Oser, L., and Thomas, J.: 2013, *ApJ* **766**, 71

Remy, M., Surdej, J., Smette, A., and Claeskens, J.-F.: 1993, *A&A* **278**, L19

Renn, J. and Tilman, S.: 2000, *Preprints of Max Planck Institute for the History of Science*

Richardson, W. H.: 1972, *Journal of the Optical Society of America (1917-1983)* **62**, 55

Riess, A. G., Li, W., Stetson, P. B., Filippenko, A. V., Jha, S., Kirshner, R. P., Challis, P. M., Garnavich, P. M., and Chornock, R.: 2005, *ApJ* **627**, 579

Roberts, M. S.: 1966, *ApJ* **144**, 639

Rogstad, D. H. and Shostak, G. S.: 1972, *ApJ* **176**, 315

Romanowsky, A. J., Douglas, N. G., Arnaboldi, M., Kuijken, K., Merrifield, M. R., Napolitano, N. R., Capaccioli, M., and Freeman, K. C.: 2003, *Science* **301**, 1696

Ros, E., Guirado, J. C., Marcaide, J. M., Pérez-Torres, M. A., Falco, E. E., Muñoz, J. A., Alberdi, A., and Lara, L.: 2000, *A&A* **362**, 845

Rubin, V. C., Ford, Jr., W. K., and Thonnard, N.: 1980, *ApJ* **238**, 471

S. Calchi Novati, S. M. e. a.: 2013, *Monthly Notices of the Royal Astronomical Society* 435

S. Calchi Novati, V. B. e. a.: 2014, *The Astrophysical Journal* 783

Saglia, R. P., Bertin, G., and Stiavelli, M.: 1992, *ApJ* **384**, 433

Saglia, R. P., Bertschinger, E., Baggley, G., Burstein, D., Colless, M., Davies, R. L., McMahan, Jr., R. K., and Wegner, G.: 1993, *MNRAS* **264**, 961

Saha, P.: 2000, *AJ* **120**, 1654

Saha, P., Courbin, F., Sluse, D., Dye, S., and Meylan, G.: 2006, *A&A* **450**, 461

Salpeter, E. E.: 1955, *ApJ* **121**, 161

Sandage, A., Tammann, G. A., Saha, A., Reindl, B., Macchetto, F. D., and Panagia, N.: 2006, *ApJ* **653**, 843

Schechter, P. L., Bailyn, C. D., Barr, R., Barvainis, R., Becker, C. M., Bernstein, G. M., Blakeslee, J. P., Bus, S. J., Dressler, A., Falco, E. E., Fesen, R. A., Fischer, P., Gebhardt, K., Harmer, D., Hewitt, J. N., Hjorth, J., Hurt, T., Jaunsen, A. O., Mateo, M., Mehlert, D., Richstone, D. O., Sparke, L. S., Thorstensen, J. R., Tonry, J. L., Wegner, G., Willmarth, D. W., and Worthey, G.: 1997, *ApJ* **475**, L85

Schechter, P. L. and Moore, C. B.: 1993, *AJ* **105**, 1

Schechter, P. L., Pooley, D., Blackburne, J. A., and Wambsganss, J.: 2014, *Astrophysical Journal* **793**, 96

Schmidt, M.: 1963, *Nature* **197**, 1040

Schneider, P. and Sluse, D.: 2013, *A&A* **559**, A37

Schneider, P. and Sluse, D.: 2014, *A&A* **564**, A103

Schramm, D. N. and Turner, M. S.: 1998, *Reviews of Modern Physics* **70**, 303

Schramm, T.: 1990, *A&A* **231**, 19

Serjeant, S.: 2017, *Publication of Korean Astronomical Society* **32**, 251

Sérsic, J. L.: 1963, *Boletin de la Asociacion Argentina de Astronomia La Plata Argentina* **6**, 41

Shannon, C. E.: 1949, *IEEE Proceedings* **37**, 10

Shapiro, I. I.: 1964, *Physical Review Letters* **13**, 789

Shimanovskaya, E., Oknyansky, V., and Artamonov, B.: 2015a, *ArXiv e-prints*

Shimanovskaya, E. V., Oknyanskii, V. L., and Artamonov, B. P.: 2015b, *Astronomy Reports* **59**, 12

Shull, J. M., Smith, B. D., and Danforth, C. W.: 2012, *ApJ* **759**, 23

Siegfried, T.: 2015, *Science News*

Sluse, D., Chantry, V., Magain, P., Courbin, F., and Meylan, G.: 2012, *Astronomy and Astrophysics* **538**, A99

Sluse, D., Sonnenfeld, A., Rumbaugh, N., Rusu, C. E., Fassnacht, C. D., Treu, T., Suyu, S. H., Wong, K. C., Auger, M. W., Bonvin, V., Collett, T., Courbin, F., Hilbert, S., Koopmans, L. V. E., Marshall, P. J., Meylan, G., Spiniello, C., and Tewes, M.: 2017, *MNRAS* **470**, 4838

Smith, R. J., Lucey, J. R., and Edge, A. C.: 2017, *MNRAS* **471**, 383

Spinrad, H.: 2005, *Galaxy Formation and Evolution*, Springer-Verlag Berlin Heidelberg

Steinmetz, M. and Mueller, E.: 1993, *ArXiv Astrophysics e-prints*

Stockton, A.: 1980, *ApJ* **242**, L141

Suyu, S. H., Bonvin, V., Courbin, F., Fassnacht, C. D., Rusu, C. E., Sluse, D., Treu, T., Wong, K. C., Auger, M. W., Ding, X., Hilbert, S., Marshall, P. J., Rumbaugh, N., Sonnenfeld, A., Tewes, M., Tihhonova, O., Agnello, A., Blandford, R. D., Chen, G. C.-F., Collett, T., Koopmans, L. V. E., Liao, K., Meylan, G., and Spiniello, C.: 2017, *MNRAS* **468**, 2590

Thomas, J., Saglia, R. P., Bender, R., Thomas, D., Gebhardt, K., Magorrian, J., Corsini, E. M., and Wegner, G.: 2007, *MNRAS* **382**, 657

Thomas, J., Saglia, R. P., Bender, R., Thomas, D., Gebhardt, K., Magorrian, J., Corsini, E. M., and Wegner, G.: 2009, *ApJ* **691**, 770

Thomas, J., Saglia, R. P., Bender, R., Thomas, D., Gebhardt, K., Magorrian, J., Corsini, E. M., Wegner, G., and Seitz, S.: 2011, *MNRAS* **415**, 545

Tonry, J. L.: 1998, *AJ* **115**, 1

Tonry, J. L. and Kochanek, C. S.: 1999, *AJ* **117**, 2034

Toomre, A.: 1977, in B. M. Tinsley and R. B. G. Larson, D. Campbell (eds.), *Evolution of Galaxies and Stellar Populations*, p. 401

Tortora, C., La Barbera, F., Napolitano, N. R., Romanowsky, A. J., Ferreras, I., and de Carvalho, R. R.: 2014, *MNRAS* **445**, 115

Tortora, C., Romanowsky, A. J., and Napolitano, N. R.: 2013, *ApJ* **765**, 8

Trinchieri, G., Fabbiano, G., and Canizares, C. R.: 1986, *ApJ* **310**, 637

Tripp, T. M., Bowen, D. V., Sembach, K. R., Jenkins, E. B., Savage, B. D., and Richter, P.: 2004, *ArXiv Astrophysics e-prints*

Turnbull, A. J., Carter, D., Bridges, T. J., and Thomson, R. C.: 1999, in J. E. Barnes and D. B. Sanders (eds.), *Galaxy Interactions at Low and High Redshift*, Vol. 186 of *IAU Symposium*, p. 191

Umnov, A. V., Krylov, A. S., and Nasonov, A. V.: 2015, *Lecture Notes in Computer Science* **9386**, 35

Unruh, S., Schneider, P., and Sluse, D.: 2017, *A&A* **601**, A77

Usher, C., Forbes, D. A., Brodie, J. P., Foster, C., Spitler, L. R., Arnold, J. A., Romanowsky, A. J., Strader, J., and Pota, V.: 2012, *MNRAS* **426**, 1475

Valls-Gabaud, D.: 2006, in J.-M. Alimi and A. Füzfa (eds.), *Albert Einstein Century International Conference*, Vol. 861 of *American Institute of Physics Conference Series*, pp 1163–1163

van Albada, T. S., Bahcall, J. N., Begeman, K., and Sancisi, R.: 1985, *ApJ* **295**, 305

van de Sande, J., Kriek, M., Franx, M., Bezanson, R., and van Dokkum, P. G.: 2015, *ApJ* **799**, 125

van de Ven, G., Mandelbaum, R., and Keeton, C. R.: 2009a, *MNRAS* **398**, 607

van de Ven, G., Mandelbaum, R., and Keeton, C. R.: 2009b, *MNRAS* **398**, 607

van der Marel, R. P., Binney, J., and Davies, R. L.: 1990, *MNRAS* **245**, 582

Vuissoz, C., Courbin, F., Sluse, D., Meylan, G., Chantry, V., Eulaers, E., Morgan, C., Eyler, M. E., Kochanek, C. S., Coles, J., Saha, P., Magain, P., and Falco, E. E.: 2008, *A&A* **488**, 481

Walsh, D., Carswell, R. F., and Weymann, R. J.: 1979, *Nature* **279**, 381

Weijmans, A.-M., Krajnović, D., van de Ven, G., Oosterloo, T. A., Morganti, R., and de Zeeuw, P. T.: 2008, *MNRAS* **383**, 1343

Wertz, O. and Orthen, B.: 2018, *ArXiv e-prints*

Wertz, O., Orthen, B., and Schneider, P.: 2017, *ArXiv e-prints*

Weymann, R. J., Latham, D., Roger, J., Angel, P., Green, R. F., Liebert, J. W., Turnshek, D. A., Turnshek, D. E., and Tyson, J. A.: 1980, *Nature* **285**, 641

White, M.: 2001, *A&A* **367**, 27

Wisotzki, L., Schechter, P. L., Bradt, H. V., Heinmüller, J., and Reimers, D.: 2002, *A&A* **395**, 17

Wright, E. L.: 2006, *PASP* **118**, 1711

Wucknitz, O.: 2002, *MNRAS* **332**, 951

Xu, D., Sluse, D., Schneider, P., Springel, V., Vogelsberger, M., Nelson, D., and Hernquist, L.: 2016, *MNRAS* **456**, 739

Xu, D., Springel, V., Sluse, D., Schneider, P., Sonnenfeld, A., Nelson, D., Vogelsberger, M., and Hernquist, L.: 2017, *MNRAS* **469**, 1824

Yıldırım, A., van den Bosch, R. C. E., van de Ven, G., Dutton, A., Läsker, R., Husemann, B., Walsh, J. L., Gebhardt, K., Gültekin, K., and Martín-Navarro, I.: 2016, *MNRAS* **456**, 538

Zwicky, F.: 1933, *Helvetica Physica Acta* **6**, 110

Zwicky, F.: 1937a, *Physical Review* **51**, 290

Zwicky, F.: 1937b, *Physical Review* **51**, 679

Publications and communications of Judith Biernaux [u220797]

Legend

Bibliometric indicators linked to the journal *(for those whose ISSN has been indicated by the author)*

- ***IF = Impact factor*** *Thomson ISI. Are indicated : IF of the year of publication and IF of the last edition of JCR* ***(last)****, « **?** » if not known by ORBi yet ; « **-** » if non-existent.*
- ***IF5 :*** *idem as IF but for a 5 year period (new indicator since 2009).*
- *Following the decision of the French-speaking rectors to stop subscribing to the JCR Impact Factor, IF and IF5 are no longer updated from 2015. The "last" index corresponds to the 2014 index of the journal, or of the last year of presence of the journal in the JCR.*
- ***EigenF = EigenFactor*** *(see : http://www.eigenfactor.org/).*
- ***Article Infl. = Article Influence :*** *EigenFactor divided by the number of articles published in the journal.*

➔ More information ? http://orbi.uliege.be/rpt#rev

Bibliometric indicators linked to the article

- ***ORBi viewed*** *= total number of visualizations of a reference on ORBi (of which X internally within the ULiège).*
- ***ORBi downloaded*** *= total number of downloads of the full text via ORBi, including requests copy.*
- ***SCOPUS®*** *= number of citations picked up by SCOPUS®.*

➔ More information ? http://orbi.uliege.be/rpt#art

(Warning : According to disciplines, some bibliometric indicators may not be relevant)

etc: full text of the document available in Open Access

etc: full text of the document available in restricted access

1. Published books, as author, co-author or editor

2. Books chapters, as author or co-author

3. Articles accepted in journals with committee (peer reviewed)

1) Hauret, C., Magain, P., & **Biernaux, J.** (2018). A cosmology-independent calibration of type Ia supernovae data. *Monthly Notices of the Royal Astronomical Society, 479*(3), 3996-4003.
http://hdl.handle.net/2268/226670
ORBi viewed: **12** ; downloaded: **0**
IF: — EigenF 2018: **?**; last: **0.303** — Article Infl. 2018: **?**; last: **1.6**

2) Hauret, C., Magain, P., & **Biernaux, J.** (2017). Cosmological Time, Entropy and Infinity. *Entropy, 19*(7).
http://hdl.handle.net/2268/213064
ORBi viewed: **30** (12 ULiège) ; downloaded: **23** (6 ULiège) — SCOPUS®: **0**
IF 2017: **?**; last: **1.743**; IF5: **1.78** — EigenF: — Article Infl.:

3) **Biernaux, J.**, Magain, P., & Hauret, C. (2017). Analysis of luminosity distributions of strong lensing galaxies: subtraction of diffuse lensed signal. *Astronomy and Astrophysics*.
http://hdl.handle.net/2268/210323
ORBi viewed: **20** (7 ULiège) ; downloaded: **11** (6 ULiège) — SCOPUS®: **0**
IF 2017: **?**; last: **5.185**; IF5: **4.4** — EigenF: — Article Infl.:

4) **Biernaux, J.**, Magain, P., Sluse, D., & Chantry, V. (2016). Analysis of luminosity distributions and shape parameters of strong gravitational lensing elliptical galaxies. *Astronomy and Astrophysics, 585*, 84-18.
http://hdl.handle.net/2268/184625
ORBi viewed: **36** (17 ULiège) ; downloaded: **43** (8 ULiège) — SCOPUS®: **1**
IF 2016: **?**; last: **5.185**; IF5: **4.4** — EigenF: — Article Infl.:

4. Articles accepted in journals without committee (non-peer reviewed)

5. Articles accepted in conference proceedings

6. Oral presentations in conferences with scientific selection committee

1) **Biernaux, J.** (2015, May 20). *Analysis of shape parameters of early-type lensing galaxies and testing the existence of dark matter haloes*. Paper presented at 4th CosPa Meeting, Université de Mons.
http://hdl.handle.net/2268/181716
ORBi viewed: **22** (8 ULiège) ; downloaded: **18** (1 ULiège) — SCOPUS®: **-**

2) **Biernaux, J.** (2015, May 13). *Gravitational lensing search for dark matter haloes (2)*. Paper presented at Annual Scientific Meeting of the Belgian Physical Society.
http://hdl.handle.net/2268/181580
ORBi viewed: **14** (1 ULiège) ; downloaded: **17** — SCOPUS®: **-**

3) **Biernaux, J.** (2014, November 19). *Gravitational lensing search for dark matter halos*. Paper presented at Third CosPa meeting.
http://hdl.handle.net/2268/174579
ORBi viewed: **21** (7 ULiège) ; downloaded: **20** — SCOPUS®: **-**

7. Patents